Two-dimensional Spectroscopic Study of Biological Photosynthetic Systems and the Solar Cell Functional Materials

Dissertation

zur Erlangung des Doktorgrades

des Fachbereichs Physik

der Universität Hamburg

vorgelegt von

Hong-Guang Duan

September 2017

Gutachter der Dissertation: Prof. Dr. Michael Thorwart
Prof. Dr. R. J. Dwayne Miller
Prof. Dr. Tõnu Pullerits

Gutachter der Disputation: Prof. Dr. R. J. Dwayne Miller
Prof. Dr. Michael Thorwart
Prof. Dr. Nils Huse
Prof. Dr. Michael Potthoff

Datum der Disputation: 16.02.2018

Vorsitzender des Prüfungsausschusses: Prof. Dr. Daniela Pfannkuche

Vorsitzender des Promotionsausschusses: Prof. Dr. Wolfgang Hansen

Abstract

This thesis focuses on the experimental and theoretical studies of molecular electronic dynamics by two-dimensional (2D) electronic spectroscopy in biologically relevant systems. The primary energy transport and charge separation in natural photosynthetic complexes such as light-harvesting complex II, Photosystem II Reaction Center and Fenna-Matthews-Olson (FMO) complex were studied. The energy-transfer and charge-separation pathways and the associated timescales were identified from the experiments in conjunction with theoretical modeling and a global fitting approach. In the FMO complex, the measured timescale of the electronic coherence was on the order of 60 fs at ambient temperature. No evidence was found that suggests that this plays a functional role for the process of natural energy transport. In a separate study, the exciton and free-carrier dynamics in hybrid lead perovskite thin films were investigated by 2D electronic spectroscopy after excitation with a 750 nm-laser. The ultrafast exciton dissociation and free-carrier scattering processes were identified in these measurements.

Moreover, theoretical study was undertaken of the dynamics of an electronic wave packet in the vicinity of a conical intersection (CI). It was found that the numerical simulation time can be significantly reduced by transforming the molecular vibrational modes into the bath and treating the full resulting non-Markovian dynamics numerically exactly. The presence of the CI was identified by the excited state absorption in the 2D spectrum. Furthermore, the impact of vibrational coherence on the electronic wave-packet dynamics was also studied near to the CI. It was shown that vibrational coherence is one of crucial factors to determine the quantum efficiency of the wave packet transfer at the CI.

Kurzfassung

Diese Arbeit konzentriert sich auf die experimentellen und theoretischen Untersuchung der molekularen elektronischen Dynamik durch zweidimensionale (2D) elektronische Spektroskopie in biologisch relevanten Systemen. Der primäre Energietransport und die Ladungstrennung in natürlichen Photosynthesekomplexen wie dem Light-Harvesting Complex II (LHCII), dem Reaktionszentrum des Photosystems II (PSII) und derm Fenna-Matthews-Olson (FMO) Komplex wurden untersucht. Die Reaktionspfade des Energietransfers und der Ladungstrennung und die damit verbundenen Zeitskalen wurden in Experimenten in Verbindung mit einer theoretischen Modellierung und einer globalen Fit-Methode identifiziert. Im FMO-Komplex liegt die gemessene Zeitskala der elektronischen Kohärenz im Bereich von 60 fs bei ambienter Umgebungstemperatur. Es wurde kein Hinweis dafür gefunden, dass dies eine funktionelle Rolle für den Prozess des Energietransports spielt. In einer weiteren Studie wurde die Dynamik der gebundenen Exzitonen und der freien Ladungsträger in Hybrid-Blei-Perowskit durch 2D Elektronenspektroskopie nach Anregung bei einer

Wellenlänge von 750 nm untersucht. In diesen Messungen wurden die ultraschnellen Exciton-Dissoziation und die Streuungprozesse der freien Ladungsträger identifiziert.

Darüber hinaus wurde eine theoretische Untersuchung der Dynamik eines elektronischen Wellenpakets in der Nähe einer konischen Durchschneidung durchgeführt. Es wurde festgestellt, dass die numerische Simulationszeit deutlich reduziert werden kann, indem man die molekularen Vibrationsmoden in das Bad transformiert und die volle resultierende nicht-Markovsche Dynamik numerisch exakt behandelt. Die Anwesenheit des konischen Durchschneidung wurde durch die Absorption im angeregten Zustand im 2D-Spektrum identifiziert. Darüber hinaus wurde auch der Einfluss der Vibrationskohärenz auf die elektronische Wellenpaketdynamik in der Nhe der Durchschneidung untersucht. Es wurde gezeigt, dass die Vibrationskohärenz einer der entscheidenden Faktoren ist, welcher die Quanteneffizienz des Wellenpakettransfers an der Durchschneidung bestimmt.

Acknowledgments

After five years of hard work, I finally have enough material to write this thesis with. There are many people to thank for the completion of this journey. Firstly, I want to thank my two supervisors, Prof. M. Thorwart and Prof. R.J. D. Miller. Under their able supervision, I had the chance to learn a lot and develop both theory knowledge and experimental skills. Their way to treat Science, their patience and their encouragement to overcome any barrier are truly exemplary. They have always supported my ambitions in trying different things and also kept me grounded and focused on the main task, i.e. do good science.

I also want to thank Dr.V. I. Prokhorenko who became my supervisor when I started out as an experimentalist. He was instrumental in teaching me how to properly treat the optics, laser and instilled in me the desire to always obtain super-high quality of signal. This I cherish very much and am grateful to him for teaching me the proper way to do experiments. I wish to also thank Dr. Ajay Jha and Miss Vandana Tiwari. They were my lab mates with whom I spent quality time doing experiments late into

the nights and sometimes staying overnights. Vandana always have some jokes, which helped me remain awake during those times. It is also surprising and impressive that Ajay seems to have an endless list of samples that he wants to measure and I had the pleasure to be part of the experiments for some of those samples. I also want to thank my office mate Dr. Khalid Siddiqui. We had many stimulating chats over science from basics to advanced stuff. We also spoke of other day-to-day matters and it was always great fun.

Next, I would like to acknowledge the help I got from the theoretical group at the University of Hamburg, especially I like to mention Prof. P. Nalbach who became my mentor at the beginning of my PhD studies.

I want to acknowledge the financial support from Joachim-Herz Stiftung for selecting me for the scholarship and giving me the chance to come to such vibrant community of scientists. I also am grateful for the financial support from CUI (The Hamburg Center for Ultrafast Imaging) that they provided towards the end of my PhD. Finally, I thank the University of Hamburg and Max-Planck institute for providing a perfect platform to do science.

Last but not least, I reserve a special and important thanks for my parents and my girlfriend for their endless love and support over the last five years.

Contents

List of Figures

List of Tables

Chapter 1

Introduction

1.1 Photosynthetic molecular systems

Photosynthesis is the process used by plants and other organisms to convert sunlight energy into chemical energy that can be latter released to fuel the organisms' activities [1]. It happens everywhere and everyday on Earth, from certain bacteria deep in the ocean to higher plants on land. After billion years of evolution, the biological functions in photosynthesis are largely optimized. Recently, it was found that in the initial steps of photosynthesis, pigment-protein complexes (PPCs) complete the light-energy transfer and charge separation with a near unity quantum efficiency [2], which is not currently possible for any artificial photosynthetic system. As such, it makes this research area very attractive.

1.1.1 Molecular structure and spectrum

In photosynthetic systems, the energy-transfer mechanism is mainly based on the molecular structure of the basic photo-excitation unit (pigment). Therefore, getting information of the molecular structure of the pigment is the most important task for the first steps of research. Based on scattering theory, the molecular structure has been resolved by X-ray crystallography, which significantly extends our understanding of the photosynthetic system. For instance, the crystal structure of the light-harvesting complex II (LHCII), one of the most important types of peripheral antenna complexes in the Photosystem II (PSII) of higher plants, was resolved with a resolution of 2.72 Å˙This is high enough to identify the chlorophyll species (8 chlorophyll a (Chla) and 6 chlorophyll b (Chlb) in each monomer unit) and the orientation of the chlorophylls within the protein matrix [3, 4]. The crystal structure of trimeric LHCII is shown in Fig. 1.1(a). The photons are captured by peripheral PPCs–LHCII and the excited energy is transferred through the network of antennas to the PSII reaction center, where the photon-excited energy is converted to chemical energy by splitting water molecules [1]. In the PSII reaction center, eight pigments (6 Chla and 2 pheophytins (Pheo)) are located on two sides along the center axis and are named as D1 and D2 branches. They absorb the photon-excited energy from core PPCs (CP43, CP47) for the charge separation. Due to the different protein environment of the two branches, charge separation is processed only by the active D1 branch [5].

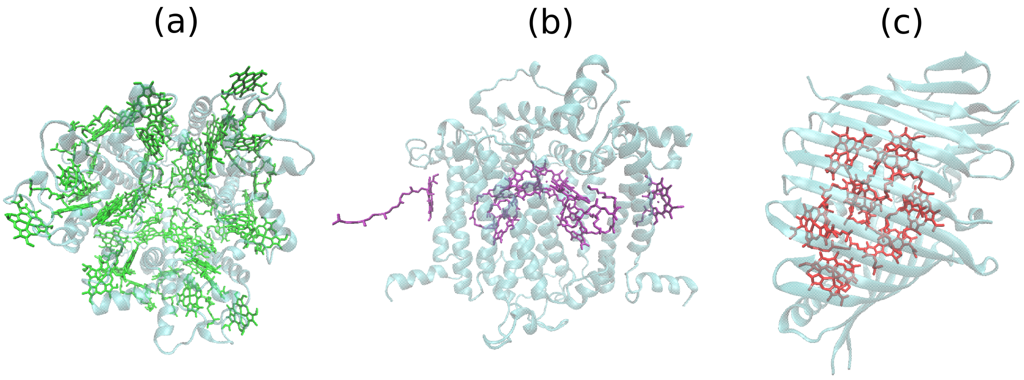

Figure 1.1: Molecular structure of three PPCs, the trimeric LHCII (a), reaction center (b) and FMO subunit (c). The pigments are emphasized in green in the LHCII, in purple in the reaction center, and in red in the FMO subunit. For clarity of the presentation, the carotenoids are not shown. VMD [9] was used to create the figures with PDB files (LHCII: 2BHW.pdb, reaction center: 3ARC.pdb, FMO: 1M50.pdb).

The arrangement of pigments in the PSII reaction center is shown in Fig. 1.1(b).

The FMO complex is another type of PPCs, which was named after Roger Fenna and Brian Matthews, who first determined its structure, and John Olson, who discovered the protein [6]. The FMO protein is sandwiched between the chlorosome and the bacteria reaction center in green sulfur bacteria [7]. Its structure consists of a trimeric complex of monomer subunits, each of which contains seven bacteriochlorophyll a (Bchla) molecules. Recently, the eighth molecule was resolved as well between the subunits [8]. The additional pigments in the three monomers are positioned towards the chlorosome and are probably the entry points for excitations from the chlorosome baseplate. The monomeric subunit of FMO PPCs is shown in Fig. 1.1(c).

The most obvious way to study the difference of PPCs in higher plants and in photosynthetic bacteria is to compare the chemical structure of chlorophylls. The name was first used by Pelletier and Caventou in 1818 to describe the green pigments that are involved in photosynthesis in higher plants [1]. In addition, three Nobel prizes were awarded to scientists for the studies of the structural determination and synthesis of chlorophyll (Richard Wilstätter, Hans Fischer and Robert Woodward).

Here, we choose typical Chla and Bchla for a first comparison. The molecular chemical formula for Chla is $C_{55}H_{72}N_4O_5Mg$ and the chemically structural formula is shown in Fig. 1.2(a). It is a squarish planar molecule with a width of about 10 Å. A Mg atom is in the center of plane and connects to 4 nitrogen atoms. Each nitrogen atom is part of a cyclic organic compound in a five-membered ring with four carbons. A fifth ring is formed in the lower right corner and a long hydrocarbon tail is attached to the lower left. The chemical structure of Bchla is shown in Fig. 1.2(b) and compared to Chla. It is the principal chlorophyll-type pigment in the majority of anoxygenic photosynthetic bacteria. The chemical difference between the structures of Chla and Bchla is the acetyl group at the left-top ring and the single bond in the right-top ring, instead of the double bond found in Chla. This reduces the degree of conjugation in the marcocycle and also reduces the symmetry of the molecule as compared to chlorophylls. These structural variations exert major effects in the spectral properties. The chlorophylls all contain two major absorption bands, one in the near ultraviolet (UV) and one in the near infrared (IR), named as Q_x and Q_y band in Fig. 1.2. The transition dipole moment in each band follows the direction of the molecular X- axis as defined as passing through the N atoms of the bottom-left ring to the up-right ring (green arrow), with molecular Y-axis rotated by 90 degrees (red arrow). The Z- axis is perpendicular to the plane of the macrocycle. The absorption (left) and fluorescence (right) of Chla and Bchla are shown with different transition frequencies. They are due to the structure variations mentioned above.

1.1.2 Energy transfer, charge separation and quantum coherence

In this part, I introduce the mechanism of excitation energy transfer (EET), charge separation and the electronic quantum coherence in the photosynthetic molecular systems.

The concept of energy transfer in photosynthetic systems is about 80 years old. In 1936, Gaffron and Wohl imagined that the energy was transferred from one pigment to another rather than by a movement of the products of photochemistry or the processing enzyme [10]. This photosynthetic unit consists of a connection of many

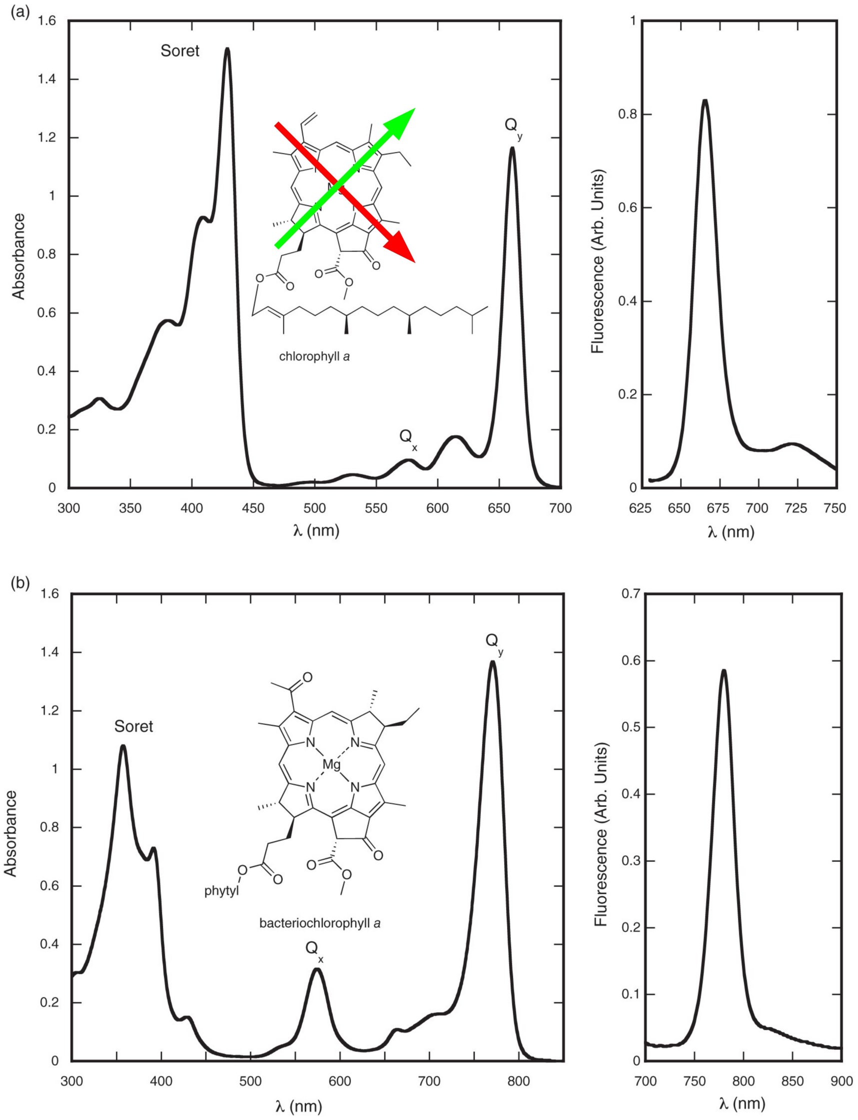

Figure 1.2: Molecular structure of Chla (a), Bchla (b) with absorption (left) and fluorescence spectra (right). The transition dipole direction in the Q_y range is labeled by the red arrow, Q_x is labeled by the green arrow. Picture taken from the Ref. [1].

pigments, among which the excitation energy could fluctuate before being trapped or stabilized. However, no physical mechanism was known at that time that could cause this energy transfer from one chlorophyll to another. This idea met with severe criticism from the other scientists since the efficiency of a one-dimensional diffusion process is very low [1]. Of course, today we know that the EET through the antenna pigments occurs in well-defined, three dimensional structures. By this way only few steps are needed to connect antenna and the reaction center.

The theoretical description of the energy transfer that is nowadays widely applied to photosynthetic systems was provided by Förster in the 1940s [11]. It is a non-radiative resonance transfer process. For the energy transfer, two pigments must have some couplings between them, which depends on the relative orientations and distance between the two pigments. Moreover, this kind of weak Coulomb interaction can be quantified by the overlap area of the absorption and emission spectrum. However, Förster theory breaks down for relatively strong Coulomb interaction when two antenna pigments are close to each other. Instead, in this case, the concept of a strong exciton coupling applies. Therefore, we have two pictures of the interaction of pigments: the Förster picture, applicable at long distances and weak interactions, and the exciton picture, applicable at short distances but strong interactions. A more sophisticated treatment reveals that the two viewpoints are really just two sides of the same coin, and that no fundamental difference exists [12].

The EET between two molecules can be conceptually described as

$$D^* + A \rightarrow D + A^*. \tag{1.1}$$

The donor of the excitation energy is labeled by D and the acceptor by A. The starting point is a situation where the donor molecule was excited (D^*), for instance, having received a photon, and the acceptor is in its ground state (A). Then the Coulomb interaction between them leads to reaction where the donor molecule is deexcited and the energy is transferred to the acceptor molecule and excites the molecule A (A^*). In Fig. 1.3, the excitation energy transfer between a donor molecule D and an acceptor A is illustrated. Furthermore, if the electronic coupling between them is sufficiently large, the quantum initial state $|D^*A\rangle$ and the final state $|DA^*\rangle$ may form a quantum superposition state $|D^*A\rangle\langle DA^*| + |DA^*\rangle\langle D^*A|$, which leads to quantum coherence between them. If it is generated in an arbitrary set of molecules, this state is known as the Frenkel exciton [13]. The light-harvesting complex of natural photosynthetic antenna systems is perhaps one of most fascinating examples of how the concept of Frenkel excitons can be applied.

To extend the concept of the energy transfer, we need to take into account the electron exchange contribution when the distance of donor and acceptor is small since short distance leads to an overlap of the molecular orbitals. If this contributes in a significant way, the EET is called a Dexter type of transfer [14]. During this type of EET process, a new intermediate charge-transfer (CT) state $|D^+A^-\rangle$ is formed and

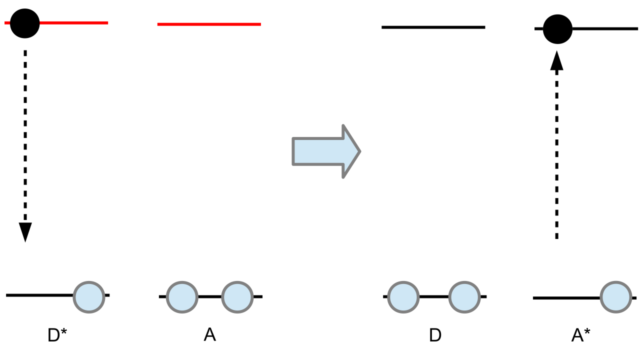

Figure 1.3: Excitation energy transfer between an energy donor D and an acceptor A. One LUMO-HOMO scheme was used to describe the molecule A and D.

becomes a bridge between the energy excited donor and acceptor states. The scheme is described in Fig. 1.4, and one may have

$$|D^*A\rangle \rightarrow \left|D^+A^-\right\rangle \rightarrow |DA^*\rangle\,, \tag{1.2}$$

or, alternatively,

$$|D^*A\rangle \rightarrow \left|D^-A^+\right\rangle \rightarrow |DA^*\rangle\,. \tag{1.3}$$

Here, we have briefly described the concept of energy transfer and charge separation. In the next chapter, we will introduce the details of the theoretical modeling of these process in the photosynthetic systems.

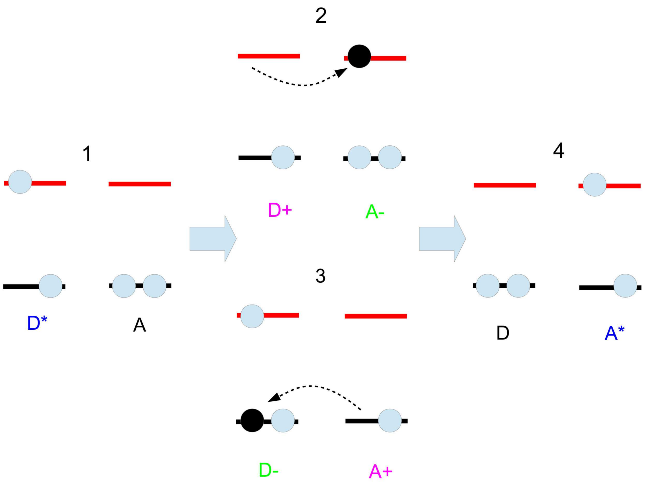

Figure 1.4: One LUMO-HOMO scheme of EET based on a two-electron exchange via the CT states.

Chapter 2

Theoretical background

In this chapter, I introduce the theoretical background for the description of energy transfers and charge separations in photosynthetic systems described in the last chapter. First, a quantum dissipative system is described by a system-bath Hamiltonian. Second, the general quantum master equation is derived with projection operators. For the numerical applications, the Markovian and Born approximations are applied to obtain the standard Redfield equation. Third, the non-Markovian master equation (time non-local equation) is derived based on the second-order perturbation theory. Last, several standard models for exciton dynamics (Frenkel-exciton, the vibronic and the tight-binding model) are briefly described.

2.1 Quantum dissipative systems

Generally, any quantum system is coupled to its environment and forms a quantum dissipative system. For many complex quantum systems, there is no clear picture of the microscopic origin of the environment-induced damping. For instance, chlorophyll interacts with a protein matrix environment in the photosynthetic system. It is often possible to measure the effective power spectrum of fluctuations in an experiment [15]. Thus, it is important to develop a phenomenological system-bath model, in which, on one hand, pursuits the full quantum mechanical treatment, and on the other hand, reduces in the classical limit to a stochastic dynamical system described in terms of the Langevin-like equation of motion [16].

The simplest model of a quantum dissipative system is a system oscillator which is linearly damped by a set of harmonic oscillators. The interaction with the reservoir can be modeled by its displacement coordinate coupling to the fluctuating collective coordinate of the dynamical harmonic bath. The equilibrium state of the reservoir is assumed to be only weakly perturbed by the central oscillator. Then, the noise statistics of the stochastic process induced by the harmonic reservoir is strictly Gaussian. This simple system-bath model has been introduced and discussed by Ullersma [17]. Zwanzig generalized the model to the case in which the central particle moves in an anharmonic potential and studied the classical regime [18]. Caldeira and Leggett were among the first who applied this model to a study of quantum mechanical tunneling of a macroscopic variable [19].

Let us consider a system with one or few degrees of freedom (DOF) which is coupled to a large number of DOFs of an environment and let us consider that the environment is represented by a set of harmonic oscillators. The interaction of the system with each individual bath oscillator is proportional to the inverse of the volume of the reservoir. Hence, the coupling to an individual bath mode is weak for a geometrically macroscopic environment. Therefore, it is physically reasonable for macroscopic global systems to assume that the system-bath interaction is modeled as a linear function of the bath coordinates. This property is favorable since it allows us to eliminate the environment exactly.

The general form of the system-bath model is given by the Hamiltonian

$$H = H_S + H_I + H_B. \tag{2.1}$$

Here, H_S is the Hamiltonian of relevant system of interest. For the discussion below, we assume a particle with mass M moving in the potential V_Q, i.e.,

$$H_S = \frac{P^2}{2M} + V(Q). \tag{2.2}$$

The reservoir is described by a set of harmonic oscillators,

$$H_B = \sum_{j=1}^{N} \left(\frac{p_j^2}{2m_j} + \frac{1}{2} m_j \omega_j^2 x_j^2 \right). \tag{2.3}$$

Here, N is the total number of oscillators in the bath and x_j, ω_j are the coordinate and the corresponding frequency of the jth oscillator with mass m_j. The system-bath interaction term has the form

$$H_I = -\sum_{j=1}^{N} F_j(Q)x_j + \Delta V(Q). \tag{2.4}$$

The special counter-term $\Delta V(Q)$ depends on the system-bath interaction form $F_j(Q)$ and on the parameters x_j, ω_j of the reservoir. The additional potential term $\Delta V(Q)$ is introduced in order to compensate a renormalization of the potential $V(Q)$ which is caused by the coupling in the interaction term H_I. This coupling induces the effective potential

$$V_{\text{eff}}(Q) = V(Q) - \sum_{j}^{N} \frac{F_j^2(Q)}{2m_j\omega_j^2}. \tag{2.5}$$

Then, $\Delta V(Q) = \sum_j^N \frac{F_j^2(Q)}{2m_j\omega_j^2}$ is added to compensate for the potential renormalization.

In the simplest case, the interaction form is independent of each individual bath mode and we can set $F_j(Q) = c_jF(Q)$. Therefore, the general form of a system-bath model Hamiltonian can be written as

$$H = \frac{P^2}{2M} + V(Q) + \sum_{j=1}^{N} \left[\frac{p_j^2}{2m_j} + \frac{1}{2}m_j\omega_j^2 \left(x_j - \frac{c_j}{m_j\omega_j^2}F(Q) \right)^2 \right]. \tag{2.6}$$

The properties of the bath can be fully described by the bath correlation function, which is defined as the correlation function of bath coordinates according to

$$\begin{aligned} C(t) &= \langle x_{j'}(t) x_j(0) \rangle \\ &= \left\langle \sum_{jj'} g_j g_{j'} (\alpha_j e^{-i\omega_j t} + \alpha_j^\dagger e^{i\omega_j t})(\alpha_{j'} + \alpha_{j'}^\dagger) \right\rangle, \\ &= \sum_j g_j^2 \langle e^{-\omega_j t} \left[1 + n_B(\omega_j)\right] + e^{i\omega_j t} n_B(\omega_j) \rangle, \\ &= \int_0^\infty J(\omega) d\omega \langle e^{-i\omega t}(1 + n_B(\omega)) + e^{i\omega t} n_B(\omega) \rangle. \end{aligned} \tag{2.7}$$

The coupling constants $g_j = \frac{c_j^2}{2m_j\omega_j^2}$ of each bath mode are encapsulated in the definition of the spectral density, which has the form $J(\omega) = \sum_j g_j^2 \delta(\omega - \omega_j)$. $\alpha_j^\dagger$ and α_j is the creation and annihilation operator of the jth harmonic oscillator. Using $\coth(\beta\omega/2) = 1 + 2n_B(\omega)$ and $n_B(\omega) = \frac{1}{e^{\beta\omega}-1}$ with $\beta = \frac{1}{k_B T}$, the final form of the bath correlation function is given as

$$C(t) = \int_0^\infty d\omega J(\omega) \left[\coth(\beta\omega/2)\cos(\omega t) - i\sin(\omega t)\right]. \tag{2.8}$$

We have set $\hbar = 1$.

2.2 Quantum master equations

The starting point of the derivation of the quantum master equation is the Liouville equation of motion for the global density operator $W(t)$, i.e.,

$$W(t) = -i\left[H, W(t)\right] = \mathcal{L}W(t). \tag{2.9}$$

Here, $\mathcal{L}$ is the global Liouville super-operator of the total system. Next, we exploit that the Hamiltonian H and Liouville operator $\mathcal{L}$ of the total system can be decomposed as

$$H = H_S + H_I + H_B; \qquad \mathcal{L} = \mathcal{L}_S + \mathcal{L}_I + \mathcal{L}_B. \tag{2.10}$$

Here, $\mathcal{L}_S$, $\mathcal{L}_I$ and $\mathcal{L}_B$ refer to the Liouville operators of the studied system, the interaction and reservoir part, respectively. Next, we define a projection operator P, which acts on the total density operator and reduces the full density operator to an operator living only in the Hilbert space of the relevant system variables, i.e.,

$$\rho(t) = PW(t). \tag{2.11}$$

The operator $\rho(t)$ is denoted as the reduced density operator. For the system with Hamiltonian Eq. 2.10, the projection operator contains a trace operator over the reservoir DOF. By means of the projection operator P, the total density operator can be decomposed into the relevant part $\rho(t)$ and the irrelevant part $(1-P)W(t)$, according to

$$W(t) = \rho(t) + (1-P)W(t); \qquad P^2 = P. \tag{2.12}$$

This decomposition can now be used in Eq. (2.9). After acting on the resulting equation with P and $1-P$, respectively, we obtain the two equations

$$\begin{aligned} P\dot{W}(t) &= P\mathcal{L}PW(t) + P\mathcal{L}(1-P)W(t), \\ (1-P)\dot{W}(t) &= (1-P)\mathcal{L}(1-P)W(t) + (1-P)\mathcal{L}PW(t). \end{aligned} \tag{2.13}$$

Solving the second equation, we obtain $(1-P)W(t) = e^{(1-P)\mathcal{L}t}(1-P)W(t=0) + \int_0^t dt' e^{(1-P)\mathcal{L}t'}(1-P)\mathcal{L}PW(t-t')$. This solution can be inserted into the first equation of Eq. (2.13). This yields the Nakajima–Zwanzig equation

$$\begin{aligned}\dot{\rho}(t) =& P\mathcal{L}\rho(t) + \int_0^t dt' \left[P\mathcal{L}e^{(1-P)\mathcal{L}t'}(1-P)\mathcal{L}\rho(t-t')\right] + \\ & P\mathcal{L}e^{(1-P)\mathcal{L}t}(1-P)W(0).\end{aligned} \tag{2.14}$$

The last term of the right part in Eq. (2.14) is called the inhomogeneous term, and contains the interference between the system and the reservoir at initial time. For simplicity, the Born approximation, which neglects the correlation between system and bath at the initial time $W(0) = \rho(0) \bigotimes \rho_B(0)$, is used next to simplify the master equation as

$$\dot{\rho}(t) = P(\mathcal{L}_S + \mathcal{L}_I)\rho(t) + \int_0^t dt' P\mathcal{L}_I e^{(1-P)\mathcal{L}t'}(1-P)\mathcal{L}_I\rho(t-t'). \tag{2.15}$$

Here ρ_B is the bath density operator. The first term describes the coherent motion of the relevant system while the second time-retarded term brings in irreversibility. It includes all effects the reservoir exerts on the system, such as relaxation, decoherence and an energy shift. Eq. (2.15) provides the exact result within the Born approximation. Yet, it is still too complicated to evaluate in practice. First, the kernel of Eq. (2.15) contains all orders of $\mathcal{L}_I$. Second, the dynamics of ρ at time t depends on the whole history of the density matrix. In order to surmount these difficulties, one usually considers the kernel in Eq. (2.15) only up to the second order in $\mathcal{L}_I$. Disregarding the retardation effects (Markovian approximation) and remaining with the second order approximation for the interaction term $\mathcal{L}_I$, one arrives at the quantum master equation in Born-Markovian approximation. It has the form

$$\dot{\rho}(t) = P(\mathcal{L}_S + \mathcal{L}_I)\rho(t) + \int_0^t dt' P\mathcal{L}_I e^{(1-P)(\mathcal{L}_S+\mathcal{L}_R)t'}(1-P)\mathcal{L}_I\rho(t). \tag{2.16}$$

This equation and variants were successfully used to describe phenomena with weak system-bath coupling.

Redfield equation. When Eq. 2.16 is projected onto the eigenstates of H_S, one obtains the Redfield quantum master equation [20]

$$\dot{\rho}_{nm}(t) = -i\omega_{nm}\rho_{nm}(t) - \sum_{k,l} R_{nmkl}\rho_{kl}(t), \tag{2.17}$$

where $\omega_{nm} = E_n - E_m$ is the energy gap between E_n and E_m in the energy eigenbasis. The coefficients R_{nmkl} describe the Redfield relaxation tensor associated to the effect of the bath. They are given by

$$R_{nmkl} = \delta_{lm}\sum_r \Gamma^+_{nrrk} + \delta_{nk}\sum_r \Gamma^-_{lrrm} - \Gamma^+_{lmnk} - \Gamma^-_{lmnk}, \tag{2.18}$$

with the underlying transition rates

$$\begin{aligned} \Gamma^+_{lmnk} &= \int_0^\infty dt\, e^{-i\omega_{nk}t}\langle \widetilde{H}_{I,lm}(t)\widetilde{H}_{I,nk}(0)\rangle_R, \\ \Gamma^-_{lmnk} &= \int_0^\infty dt\, e^{-i\omega_{lm}t}\langle \widetilde{H}_{I,lm}(0)\widetilde{H}_{I,nk}(t)\rangle_R. \end{aligned} \tag{2.19}$$

Here, $\widetilde{H}_I(t) = e^{iH_Rt/\hbar}H_I e^{-iH_Rt/\hbar}$ is the interaction Hamiltonian in the interaction picture and the angular brackets denote the thermal average over the bath DOF.

Time non-local master equation. For the study of the linear and 2D spectra performed in this work, we have applied the time non-local (TNL) quantum master equation. Here, we briefly describe how this can be derived. Based on Eq. 2.14, the time evolution of the reduced density operator can be re-written as

$$\begin{aligned}
\dot{\rho}(t) &= \mathcal{L}_S^{\text{eff}}\rho(t) + \int_0^t K(t,t')\rho(t') + \Gamma(t), \\
\mathcal{L}_S^{\text{eff}} &= \mathcal{L}_S + \text{tr}_\text{B}\mathcal{L}_\text{I}\rho_\text{B}^\text{eq} + \mathcal{L}_\text{ren}, \\
K(t,t') &= \text{tr}_\text{B}\mathcal{L}_\text{I}\left(\text{Te}^{\int_{\text{t}'}^{\text{t}}(1-\text{P})\mathcal{L}\text{dt}''}\right)(1-\text{P})(\mathcal{L}_\text{B}+\mathcal{L}_\text{I})\rho_\text{B}^\text{eq}, \\
\Gamma(t) &= \text{tr}_\text{B}\mathcal{L}_\text{I}\left(\text{Te}^{\int_0^{\text{t}}(1-\text{P})\mathcal{L}\text{dt}''}\right)(1-\text{P})\text{W}(0).
\end{aligned} \tag{2.20}$$

The reversible term, the memory term and the inhomogeneous terms are denoted by $\mathcal{L}_S^{\text{eff}}\rho(t)$, $\int_0^t K(t,t')\rho(t')$ and $\Gamma(t)$. The total Hamiltonian is $H = H_S + H_B + H_I + H_\text{ren}$. H_ren is the renormalization term associated to the additional potential term $\Delta V(Q)$ in Eq. (2.4). The Liouville superoperators $\mathcal{L}_\text{S}$, $\mathcal{L}_\text{I}$ and $\mathcal{L}_\text{ren}$ are associated with the corresponding Hamiltonian operators. Moreover, $\mathcal{L}_\text{S}^\text{eff}\cdot = -i[H_\text{S} + H_\text{ren}, \cdot]$ and T is the time ordering operator [21].

Next, we expand the correlated thermal equilibrium state ρ^eq up to the first order in the overall coupling strength and obtain

$$\rho^\text{eq} \approx \frac{1}{Z_\text{S}}\frac{1}{Z_\text{B}}e^{-\beta(H_\text{S}+H_\text{B})} - \frac{1}{Z_\text{S}}\frac{1}{Z_\text{B}}\int_0^\beta d\beta' e^{-(\beta-\beta')(H_\text{S}+H_\text{B})}H_\text{I}^{(1)}e^{-\beta'(H_\text{S}+H_\text{B})}, \tag{2.21}$$

with the respective partition functions $Z = \text{tr}\,\text{exp}(-\beta\text{H})$, $Z_\text{B} = \text{tr}_\text{B}\text{exp}(-\beta\text{H}_\text{B})$, and $Z_\text{S} = \text{tr}_\text{S}\,\text{exp}(-\beta\text{H}_\text{S})$. Next, we take the trace over the system DOF on both sides of

Eq. (2.21) and get

$$\rho_{\mathrm{B}}^{\mathrm{eq}} = \frac{1}{Z_{\mathrm{B}}} e^{-\beta H_{\mathrm{B}}} + \frac{\chi}{Z_{\mathrm{B}}} \int_0^{\beta} d\beta' e^{-(\beta-\beta')H_{\mathrm{B}}} \left(\sum_{i=1}^{N} c_i x_i \right) e^{-\beta' H_{\mathrm{B}}}. \tag{2.22}$$

Here, $\chi = (1/Z_{\mathrm{S}})\mathrm{tr_s}\left[\mathrm{F(Q)e^{-\beta H_s}}\right]$ with the system-bath coupling assumed in the form $F(Q)$.

The well-known bath correlation function

$$\begin{aligned} C(t) &= \int_{-\infty}^{\infty} \frac{d\omega}{2\pi} J(\omega) \cos(\omega t) \coth\left(\frac{\beta\omega}{2}\right) - i \int_{-\infty}^{\infty} \frac{d\omega}{2\pi} J(\omega) \sin(\omega t) \\ &= a(t) - ib(t) \end{aligned} \tag{2.23}$$

is given in terms of the standard bath spectral density $J(\omega)$ and has the real part $a(t)$ and imaginary part $b(t)$. After inserting Eqs. 2.22 into Eq. 2.20, we express the last three terms of Eq. 2.20 by $a(t)$ and $b(t)$ in the form

$$\begin{aligned} \mathcal{L}_{\mathrm{S}}^{\mathrm{eff}} &= \mathcal{L}_{\mathrm{S}} + \mu \mathcal{L}_{\mathrm{ren,S}} + \chi \mu \mathcal{L}^-, \\ K(t,t') &= \mathcal{L}^- \left(a(t-t') T e^{\int_{t'}^{t} \mathcal{L}_{\mathrm{S}}} \mathcal{L}^- + b(t-t') T e^{\int_{t'}^{t} \mathcal{L}_{\mathrm{S}}} \mathcal{L}^+ \right), \\ \Gamma(t) &= \mathcal{L}^- \int_{-\infty}^{0} dt' \left[a(t-t') T e^{\int_{t'}^{t} \mathcal{L}_{\mathrm{S}}} \mathcal{L}^- \rho_{\mathrm{S}}^{\mathrm{eq}} + b(t-t') T e^{\int_{t'}^{t} \mathcal{L}_{\mathrm{S}}} \mathcal{L}^+ \rho_{S}^{\mathrm{eq}} \right], \end{aligned} \tag{2.24}$$

with $\mathcal{L}^- = -i[H_{\mathrm{I}}, \cdot]$ and $\mathcal{L}^+ = [H_{\mathrm{I}}, \cdot]_+ - 2\chi$. The potential renormalization is given in terms of the spectral density by $\mu = \int_{-\infty}^{\infty} \frac{d\omega}{2\pi} J(\omega)/\omega$. In order to obtain an analytic form of the bath correlation function, we assume that a given spectral density can be decomposed into a sum of Lorentzian-like spectral terms according to

$$J(\omega) = \frac{\pi}{2} \sum_{k=1}^{n} \frac{p_k \omega}{[(\omega + \Omega_k)^2 + \Gamma_k^2][(\omega - \Omega_k)^2 + \Gamma_k^2]}. \tag{2.25}$$

The spectral amplitude p_k, the frequency Ω_k and the width Γ_k follow from the expansion of the original function in terms of the Lorentzian shapes. Inserting the expanded form of $J(\omega)$ into Eq. 2.23 results in

$$\begin{aligned} a(t) &= \sum_{k=1}^{n} \frac{p_k}{8\Omega_k\Gamma_k} \coth\left[\frac{\beta}{2}\left(\Omega_k + i\Gamma_k\right) e^{i\Omega_k t - \Gamma_k t}\right] \\ &\quad + \sum_{k=1}^{n} \frac{p_k}{8\Omega_k\Gamma_k} \coth\left[\frac{\beta}{2}\left(\Omega_k - i\Gamma_k\right) e^{-i\Omega_k t - \Gamma_k t}\right] + \frac{2i}{\beta}\sum_{k=1}^{n'} J(i\nu_k) e^{-\nu_k t}, \\ b(t) &= \sum_{k=1}^{n} \frac{ip_k}{8\Omega_k\Gamma_k}\left(e^{i\Omega_k t - \Gamma_k t} - e^{-i\Omega_k t - \Gamma_k t}\right), \end{aligned} \tag{2.26}$$

with the Matsubara frequencies $\nu_k = 2\pi k/\beta$.

Next, we rewrite the correlation functions as $a(t) = \sum_{k=1}^{n_r} \alpha_k^r e^{\gamma_k^r t}$ and $b(t) = \sum_{k=1}^{n_i} \alpha_k^i e^{\gamma_k^i t}$ with $n_i = 2n$, $n_r = 2n + n'$, where n' is the number of Matsubara frequencies used. Then, we define new auxiliary "density matrices" which incorporate both memory effects and initial correlations according to

$$\begin{aligned} \rho_k^r(t) &= T e^{\int_0^t dt' \mathcal{L}_\mathrm{S}} e^{\gamma_k^r t} \int_0^\infty dt' e^{\mathcal{L}_\mathrm{s} t'} e^{\gamma_k^r t'} \mathcal{L}^- \rho_\mathrm{s}^\mathrm{eq} + \int_0^t dt' e^{\gamma_k^r (t-t')} T e^{\int_{t'}^t L_\mathrm{s}} \mathcal{L}^- \rho(t'), \\ \rho_k^i(t) &= T e^{\int_0^t dt' \mathcal{L}_\mathrm{s}} e^{\gamma_k^i t} \int_0^\infty dt' e^{\mathcal{L}_S t'} e^{\gamma_k^i t'} \mathcal{L}^+ \rho_s^\mathrm{eq} + \int_0^t dt'\, e^{\gamma_k^i (t-t')} T e^{\int_{t'}^t L_\mathrm{s}} \mathcal{L}^+ \rho(t'). \end{aligned} \tag{2.27}$$

The first term of the time-retarded Eq. (2.20) can be then deconvoluted into a set of coupled first-order equations as

$$\begin{aligned} \dot\rho(t) &= \mathcal{L}_\mathrm{s}^\mathrm{eff}(t)\rho(t) + \left[\sum_{k=1}^{n_r} \alpha_k^r \mathcal{L}^- \rho_k^r(t) + \sum_{k=1}^{n_i} \alpha_k^i \mathcal{L}^- \rho_k^i(t)\right], \\ \dot\rho_k^r(t) &= \left[\mathcal{L}_\mathrm{S}(t) + \gamma_k^r\right] \rho_k^r(t) + \mathcal{L}^- \rho(t), \qquad k = 1, \ldots, n_r, \\ \dot\rho_k^i(t) &= \left[\mathcal{L}_\mathrm{S}(t) + \gamma_k^i\right] \rho_k^i(t) + \mathcal{L}^+ \rho(t), \qquad k = 1, \ldots, n_i. \end{aligned} \tag{2.28}$$

Here, I end the introduction of this section with the TNL quantum master equation. Compared to the Redfield equation, the TNL equation takes into account the non-Markovian effect by deconvoluting it into the coupled set of auxiliary density operators, as introduced above. The non-Markovian effect is considered as one of important effects in the process of energy transfer in photosynthetic systems since its interaction with the environment in the intermediate coupling region. In this region, the memory of the system can not be fully suppressed by the strength of thermal fluctuations from the environment. Next, I will introduce the theoretical model of the energy transfers in the photosynthetic system.

2.3 Frenkel-exciton model for the energy-transfer process

The energy of a molecular transition is mainly determined by the energy gap between lowest unoccupied molecular orbital (LUMO) and the highest occupied molecular orbital (HOMO). Both are obtained from the eigenvalues of the molecular orbitals. A possible way to obtain molecular orbitals via quantum chemistry calculations is via the well-known linear combination of atomic orbitals. Often, the study of organic molecules is hindered by the very complicated molecular energy spectrum obtained from the quantum chemistry calculations (semiempirical, ab initio . . .). For the study of the energy-transfer mechanism, a simplified two-level system model, the Frenkel-exciton model, has been introduced. This considerably simplifies the calculation and renders the investigation feasible. In Fig. 2.1, an example of simplified molecular electronic states and the orbital energies is shown in the diagram. It suggests that the exact electronic transition is replaced by a simple promotion of an electron from the HOMO to the LUMO. In reality, several different electronic configurations, including contributions from higher-energy molecular orbitals, can contribute to the electronic transition by the well-known configuration interaction. A simplification is that there is no one-to-one correspondence between orbital occupations and electronic transitions. The pigment is only phenomenologically modeled as an effective quantum two-level system consisting of the ground state $|g\rangle$ and the electronic excited state $|e\rangle$. The energy gap between the ground and excited state is defined as the site energy.

With the above simplified two-level system as an elementary building block, the molecular Hamiltonian of N molecular pigments is given by

$$H_S = \sum_{m=1}^{N} \epsilon_m \alpha_m^\dagger \alpha_m + \sum_{m=1}^{N} \sum_{n<m} J_{n,m} (\alpha_m^\dagger \alpha_n + \alpha_n^\dagger \alpha_m), \tag{2.29}$$

where ϵ_m is the m-th site energy and $J_{n,m}$ is the electronic coupling between two

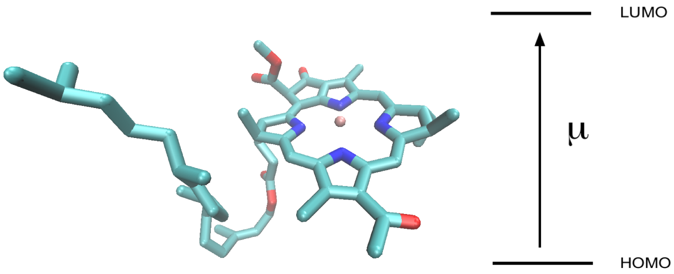

Figure 2.1: Simplified model of a molecular two-level system. It indicates that the full complicated electronic transition is replaced by a simple promotion of an electron from the HOMO to the LUMO. μ denotes the transition dipole moment.

pigments, n and m. The total Hamiltonian can be written as

$$\begin{aligned} H &= H_S + H_B + H_I, \\ H_B &= \sum_{m=1}^{N} \sum_{j}^{N_b^m} \left(\frac{p_{m_j}^2}{2m_j} + \frac{1}{2}\omega_{mj} x_{mj}^2 \right), \\ H_I &= \sum_{m=1}^{N} \sum_{j=1}^{N_b^m} c_{mj} x_{mj} \alpha_m^{\dagger} \alpha_m. \end{aligned} \tag{2.30}$$

Here, the system-bath interaction term H_I has been simplified in the form of a linear coupling to the bath coordinates.

2.4 Vibronic model

In the above Frenkel-exciton model, the electronic DOF are separated from the total Hamiltonian. All other DOFs can be described by a bath as a reservoir of harmonic oscillators. They provide Gaussian fluctuations around the thermal equilibrium state. This model has been widely used for the study of case with weak system-bath interaction. It forms the basis for the Born-Oppenheimer approximation. There, fast electron motion is compared to the slow dynamics of the nuclei. Then, the approximation that the nuclear dynamics can be seen as a perturbative fluctuating electric field acting on the electrons is useful. However, for certain systems, intramolecular vibrational modes are strongly coupled to the electronic DOF of the studied molecule and thus, strongly act on the electronic dynamics. Then, it is not appropriate to model such a strong vibrational mode as a fluctuating mode at thermal equilibrium. For such an active coupled vibrational mode, we introduce the vibronic model, in which the active vibrational mode is specified as part of the system Hamiltonian and the interaction between the electronic DOF and the vibrational mode is included explicitly. The vibronic model Hamiltonian has the form

$$H_S = H_g + H_e = |g\rangle \, h_g \, \langle g| + |e\rangle \, (h_e + E) \, \langle e| \, , \tag{2.31}$$

with $h_g = \Omega(b^\dagger b + 1/2)$, $h_e = \Omega(b^\dagger b + 1/2) + \kappa(b^\dagger + b)$ and Ω is the vibrational frequency. In the excited state, the electronic-vibrational (vibronic) coupling κ is related to the

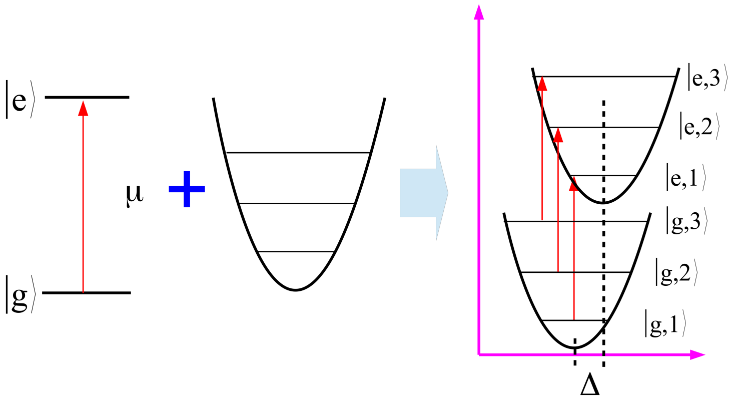

Figure 2.2: Electronic-vibrational coupling leads to the vibronic splitting. Δ indicates the dimensionless shift between the minimum of the ground and the excited state. The vibronic coupling can be evaluated by $\kappa = \Delta\Omega/\sqrt{2}$. μ is the transition dipole moment.

dimensionless displacement of the geometry between the potential energy surface (PES) of $|g\rangle$ and $|e\rangle$, and to Δ. In fact, $\kappa = \Omega\Delta/\sqrt{2}$. A sketch is shown in Fig. 2.2.

Electronic and vibronic transitions. Next, we introduce a quantum mechanical transition in the Frenkel-exciton model combined with a vibrational mode in order to distinguish the electronic transition from the vibrational transitions by the so called stick spectrum. It can be understood as the basis for the absorption spectrum of the molecule without the effect of a bath (gas phase). The magnitude of the stick spectrum can be calculated as $\langle\widetilde{\mu}^2\rangle$, here, $\widetilde{\mu} = \mathrm{U}^{-1}\mu\mathrm{U}$ and U is the matrix diagonalizing the model Hamiltonian, i.e., $\widetilde{\mathrm{H}} = \mathrm{U}^{-1}\mathrm{HU}$. The transition frequency in the spectrum can be evaluated by the frequency difference between the two exciton states associated to transition.

To illustrate the stick spectrum, we start from the two-level model with a ground ($|g\rangle$) and an excited state ($|e\rangle$). We assume one transition induced by, for instance, a laser pulse from the ground to the excited state (red arrow in Fig. 2.3). The corresponding transition dipole operator can be written as $\mu = |g\rangle \langle e|$. Therefore, one stick is located at the frequency $\omega = \omega_e - \omega_g$ to represent the corresponding transition signal. For the vibronic model, we have ordered main transitions from $|g, 1\rangle \rightarrow |e, 1\rangle$, $|g, 2\rangle \rightarrow |e, 2\rangle$ and $|g, 3\rangle \rightarrow |e, 3\rangle$, respectively. They can be represented by three transitions in the stick spectrum. Their peak height follows from the ratio of the magnitudes as 1, S, $S^2/2$, ... Here, S is the Franck-Condon factor and can be calculated as $S = \Delta^2$.

2.5 Tight-binding model for the charge-separation process

To study the charge separation in PSII reaction center, We introduce the tight-binding model. The charge separation can happen when the distance of two molecules is closed enough, which induce a significant overlap of molecular electronic wave functions. For the study of the charge-separation mechanism, each pigment is represented by two

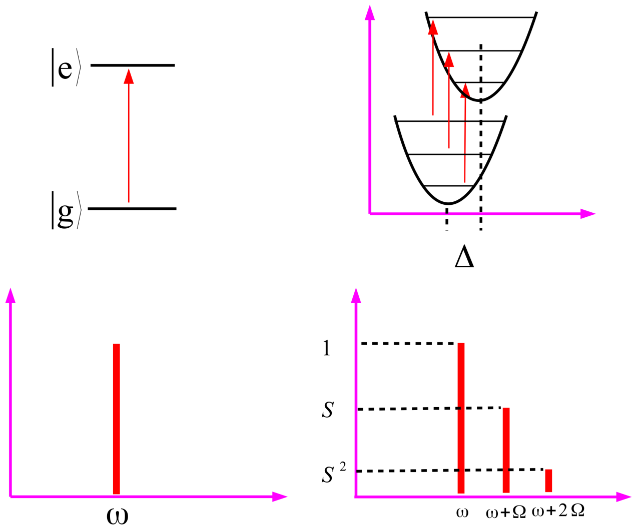

Figure 2.3: Stick spectrum of an electronic two-level system and the corresponding vibronic model. ω indicates the energy gap between ground $|g\rangle$ and excited state $|e\rangle$. Ω is the frequency of the active vibrational mode.

electronic orbitals, the HOMO and the LUMO. The construction of the model starts from operators $\hat{e}_m^\dagger$ ($\hat{e}_m$) that create (annihilate) an electron in the LUMO of site m and $\hat{h}_m^\dagger$ ($\hat{h}_m$) that create (annihilate) a hole in the HOMO. These operators satisfy the Fermi commutation relations

$$\{\hat{e}_m, \hat{e}_n^\dagger\} = \hat{e}_m\hat{e}_n^\dagger + \hat{e}_n^\dagger\hat{e}_m = \delta_{mn}, \ \{\hat{h}_m, \hat{h}_n^\dagger\} = \hat{h}_m\hat{h}_n^\dagger + \hat{h}_n^\dagger\hat{h}_m = \delta_{mn}. \tag{2.32}$$

When the electron in the LUMO and the hole in the HOMO reside at the same site m, we have the Frenkel excited (FE) state m^*, given by $\hat{e}_m^\dagger\hat{h}_m^\dagger\,|g\rangle$. Here, $|g\rangle$ is the ground state. On the other hand, when the electron and the hole are located on different sites m and n, we have the CT state n^-m^+, given by $\hat{e}_n^\dagger \hat{h}_m^\dagger |g\rangle$. The overall Hamiltonian is given by [22]

$$\begin{aligned}
H_s = &\sum_{m,n} t^e_{mn}\hat{e}^\dagger_m\hat{e}_n + \sum_{m,n} t^h_{mn}\hat{h}^\dagger_m\hat{h}_n + \sum_{m,n}^{m\neq n} W^d_{mn}\hat{e}^\dagger_m\hat{h}^\dagger_m\hat{h}_n\hat{e}_n - \sum_{m,n} V^{eh}_{mn}\hat{e}^\dagger_m\hat{h}^\dagger_n\hat{h}_n\hat{e}_m \\
&+ \frac{1}{2}\sum_{m,n}^{m\neq n} V^e_{mn}\hat{e}^\dagger_m\hat{e}^\dagger_n\hat{e}_n\hat{e}_m + \frac{1}{2}\sum_{m,n}^{m\neq n} V^h_{mn}\hat{h}^\dagger_m\hat{h}^\dagger_n\hat{h}_n\hat{h}_m \\
&+ \frac{1}{4}\sum_{k,m}^{k\neq m}\sum_{l,n}^{l\neq n} K_{kl,mn}\hat{e}^\dagger_k\hat{h}^\dagger_l\hat{e}^\dagger_m\hat{h}^\dagger_n\hat{h}_n\hat{e}_m\hat{h}_l\hat{e}_k.
\end{aligned} \tag{2.33}$$

Here t^e_{mn} (t^h_{mn}) is the electron (hole) hopping rate between the LUMO (HOMO) of different pigments. W^d_{mn} is the dipole-dipole type resonance interaction between m and n. V^{eh}_{mn} is the electron-hole interaction and V^e_{mn} (V^h_{mn}) is the electron-electron (hole-hole) Coulomb repulsion between the quaiparticles at sites m and n. The last term with $K_{kl,mn}$ is the interaction of static dipoles between FE states or the CT states and it is responsible for the energy shift of the double excited states.

The single-excitation manifold of the Hamiltonian matrix can be obtained by the projection

$$\langle e_k h_l| \hat{H}_S |e_m h_n\rangle = t^e_{km}\delta_{ln} + t^h_{ln}\delta_{km} - V^{eh}_{kl}\delta_{ln}\delta_{km} + W^d_{km}(1-\delta_{km})\delta_{lk}\delta_{mn}. \tag{2.34}$$

Therefore, the site energies of the FE and CT states are given by

$$\epsilon^*_m = t^e_{mm} + t^h_{mm} - V^{eh}_{mm}, \qquad \epsilon_{m^+n^-} = t^e_{nn} + t^h_{mm} - V^{eh}_{nm}, \tag{2.35}$$

and the electronic coupling between the FE-FE, FE-CT, CT-CT states can be written as

$$
\begin{aligned}
J_{m^*,n^*} &= W^d_{mn}, \\
J_{m^*,n^+k^-} &= t^e_{mk}\delta_{mn} + t^h_{mn}\delta_{mk}, \\
J_{m^+n^-,k^+l^-} &= t^e_{nl}\delta_{mk} + t^h_{mk}\delta_{nl}.
\end{aligned}
\tag{2.36}
$$

In the double-excited manifold, the Hamiltonian matrix elements are given by

$$
\begin{aligned}
&\langle e_k e_l h_m h_n | \, \hat{H}_S \, | e_{k'} e_{l'} h_{m'} h_{n'} \rangle = (t^e_{kk'}\delta_{ll'} + t^e_{kl'}\delta_{lk'} + t^e_{lk'}\delta_{kl'} + t^e_{ll'}\delta_{kk'})\delta_{mm'}\delta_{nn'} \\
&+ (t^h_{mm'}\delta_{nn'} + t^h_{mn'}\delta_{nm'} + t^h_{nm'}\delta_{mn'} + t^h_{nn'}\delta_{mm'})\delta_{kk'}\delta_{ll'} \\
&+ (V^e_{kl} + V^h_{mn} + V^{eh}_{km} + V^{eh}_{lm} - V^{eh}_{kn} - V^{eh}_{ln} + K_{km,ln})\delta_{kk'}\delta_{ll'}\delta_{mm'}\delta_{nn'} \\
&+ W^d_{kk'}(1 - \delta_{kk'})\delta_{ll'}\{\delta_{mk}(\delta_{k'm'}\delta_{nn'} + \delta_{k'l'}\delta_{nm'}) + \delta_{nk}(\delta_{k'm'}\delta_{mn'} + \delta_{k'n'}\delta_{mm'})\} \\
&+ W^d_{kl'}(1 - \delta_{kl'})\delta_{lk'}\{\delta_{mk}(\delta_{l'm'}\delta_{nn'} + \delta_{l'n'}\delta_{nm'}) + \delta_{nk}(\delta_{l'm'}\delta_{mn'} + \delta_{l'n'}\delta_{mm'})\} \\
&+ W^d_{lk'}(1 - \delta_{lk'})\delta_{kl'}\{\delta_{ml}(\delta_{k'm'}\delta_{nn'} + \delta_{k'n'}\delta_{nm'}) + \delta_{nl}(\delta_{k'm'}\delta_{mn'} + \delta_{k'n'}\delta_{mm'})\} \\
&+ W^d_{ll'}(1 - \delta_{ll'})\delta_{kk'}\{\delta_{ml}(\delta_{l'm'}\delta_{nn'} + \delta_{l'n'}\delta_{nm'}) + \delta_{nl}(\delta_{l'm'}\delta_{mn'} + \delta_{l'n'}\delta_{mm'})\}.
\end{aligned}
\tag{2.37}
$$

Hence, the site energies of the double-excited manifold are given by

$$
\begin{aligned}
\epsilon_{m^*n^*} &= \epsilon_{m^*} + \epsilon_{n^*} + K_{mm,nn}, \\
\epsilon_{m^*,n^+k^-} &= \epsilon_{m^*} + \epsilon_{n^+k^-} + K_{mm,kn}, \\
\epsilon_{m^+n^-,k^+l^-} &= \epsilon_{m^+n^-} + \epsilon_{k^+l^-} + V^e_{nl} + V^h_{mk} - V^{eh}_{nk} - V^{eh}_{ml} + K_{nm,lk},
\end{aligned}
\tag{2.38}
$$

and the electronic coupling elements between double-excited states are given by

$$\begin{aligned}
J_{m^*n^*,m'^*n'^*} &= J_{m^*,m'^*}(1-\delta_{mm'})\delta_{nn'} + J_{m^*,n'^*}(1-\delta_{mn'})\delta_{nm'} + \\
&J_{n^*,m'^*}(1-\delta_{nm'})\delta_{mn'} + J_{n^*,n'^*}(1-\delta_{nn'})\delta_{mm'}, \\
J_{m^*n^+k^-,m'^*n'^*} &= \delta_{mm'}J_{m'^*,m^+k^-} + \delta_{mn'}J_{m'^*,n^+k^-}, \\
J_{m^+n^-k^+l^-,m'^*n'^*} &= 0, \\
J_{m^*n^+k^-,m'^*n'^+k'^-} &= \delta_{mm'}J_{n^+k^-,n'^+k'^-} + \delta_{nn'}\delta_{kk'}(1-\delta_{mm'})J_{m^*,m'^*} + \\
&\delta_{mn'}\delta_{nm'}\delta_{kk'}J_{m^*,m^+m'^-} + \delta_{mk'}\delta_{nn'}\delta_{km'}J_{m^*,m'^+m^-}, \\
J_{m^+n^-k^+l^-,m'^*n'^+k'^-} &= \delta_{nk'}\delta_{kn'}J_{m'^*,m^+l^-} + \delta_{kn'}\delta_{lk'}J_{m'^*,m^+n^-} + \\
&\delta_{mn'}\delta_{lk'}J_{m'^*,k^+n^-} + \delta_{mn'}\delta_{nk'}J_{m',k^+l^-}, \\
J_{m^+n^-k^+l^-,m'^+n'^-k'^+l'^-} &= \delta_{kk'}\delta_{ll'}J_{m^+n^-,m'^+n'^-} + \delta_{mm'}\delta_{nn'}J_{k^+l^-,k'^+l'^-} + \delta_{kk'}\delta_{ln'}J_{m^+n^-,m'^+l'^-} \\
&+ \delta_{mm'}\delta_{nl'}J_{k^+l^-,k'^+n'^-} + \delta_{mk'}\delta_{ll'}J_{k^+n^-,m'^+n'^-} + \delta_{km'}\delta_{ln'}J_{m^+n^-,k'^+l'^-} \\
&+ \delta_{mk'}\delta_{nl'}J_{k^+l^-,m'^+n'^-} + \delta_{nn'}\delta_{km'}J_{m^+l^-,k'^+l'^-}.
\end{aligned} \tag{2.39}$$

This completes the description of theoretical models used for the study of energy transfer and charge separation in photosynthetic complex. Due to the large size of PPCs, the Frenkel-exciton model was introduced to study the dynamics of energy transfer in PPC, which is based on the modeling of pigment as quantum two-level system. The vibronic model was illustrated to treat the special case of vibrational DOF that are strongly acting on the electronic wave functions. The active vibrational DOFs interact with electronic DOFs to construct the system part of Hamiltonian instead of modeling it as part of the bath as equilibrium state. Moreover, the tight-binding model was introduced to study the charge-separation dynamics in the PSII reaction center.

2.6 Spectroscopic methods

After introducing the models, we summarize in this part the tools applied to perform spectroscopy of different molecular systems, which will be used in the following chapters. Linear spectra, here, in the form of absorption and circular dichroism (CD) spectra, are introduced to measure the absorption features of molecules and the time-resolved nonlinear spectroscopic techniques, transient absorption and 2D electronic spectroscopy.

Linear spectra. Absorption spectroscopy is one type of general spectroscopic techniques, which measures the absorption properties of the studied materials. The calculation of linear absorption spectrum is based on linear response theory [23]. It follows from the Fourier transform of the dipole-dipole autocorrelation function, i.e.,

$$I(\omega) \propto \frac{1}{2\pi}\omega \int_{-\infty}^{+\infty} dt\, e^{i\omega t} \langle \vec{\mu}(t)\vec{\mu}(0)\rangle_g, \tag{2.40}$$

where $\vec{\mu}$ is the electronic transition dipole moment of the studied molecule, and the subscript g indicates that the initial state to calculate the correlation function is the ground electronic state, $\rho_g = |0\rangle\langle 0| \bigotimes e^{-\beta H_{ph}}/\mathrm{Tr}e^{-\beta H_{ph}}$, ($\beta = 1/k_B T$ is inverse thermal energy). Since the dipole operator $\vec{\mu}$ does not depend on the bath DOF, the dipole autocorrelation function can be calculated as

$$\langle\vec{\mu}(t)\vec{\mu}(0)\rangle_g = \mathrm{Tr}_S\{\vec{\mu}\,\mathrm{Tr}_B[e^{-iHt}\vec{\mu}\rho_g e^{iHt}]\}. \tag{2.41}$$

We notice that $\rho(t) = \mathrm{Tr}_B[e^{-iHt}\vec{\mu}\rho_g e^{iHt}]$ is the system reduced density matrix at time t when assuming the initial density matrix $\rho(0) = \vec{\mu}\rho_g$. The absorption spectrum in Eq. (2.40) can be obtained by propagating the system reduced density matrix $\rho(t)$ and calculating the dipole autocorrelation function using Eq. (2.41).

Moreover, circularly polarized light can be used to measure the spectrum. The CD spectrum is the difference spectrum in the absorption of left-handed and right-handed circularly polarized light. It occurs when a molecule contains one or more chiral chromophores and can be calculated by propagating the time-dependent transition dipole autocorrelation function as well. In particular, it is given as

$$CD(\omega) \propto \omega \int_{-\infty}^{+\infty} dt\, e^{i\omega t}\langle\vec{R}_{m,n}\cdot\vec{\mu}_m \times \vec{\mu}_n\rangle, \tag{2.42}$$

where $\vec{R}_{m,n}$ is the vector from the center of molecule m to n.

Transient absorption spectroscopy. Transient absorption spectroscopy is a technique based on a two-pulse configuration. It is an extension of the steady-state absorption spectroscopy. The first pulse excites the molecule to excited states and the second pulse probes the excited-state dynamics with different waiting times [24]. Therefore, it detects the time-resolved absorption-difference signal. For the theoretical description of two pulses interacting with matter, the semi-classical Hamiltonian of the matter-field interaction is given as

$$\begin{aligned} H_{\text{int}}(t) &= -\sum_{\alpha=1}^{2} \left(X^{\dagger} \xi_{\alpha}(t) + X \xi_{\alpha}^{*}(t) \right), \\ X &= |g\rangle \langle e|, X^{\dagger} = |e\rangle \langle g|, \\ \xi_{\alpha}(t) &= A_{\alpha} E_{\alpha}(t - \tau_{\alpha}) \exp\{i(\vec{k}_{\alpha}\vec{r} - \omega_{\alpha} t)\}. \end{aligned} \tag{2.43}$$

Here, α =1, 2 indicates the pump and the probe pulse, respectively. A_{α}, $\vec{k}_{\alpha}$, ω_{α} and τ_{α} denote the amplitude, the wave vector, the frequency and the center time of the pulse. The dimensionless pulse envelope is given by

$$E_{\alpha}(t) = \exp\{-(\Gamma_{\alpha} t)^2\}, \tag{2.44}$$

with $\tau_{\alpha}^{P} = 2(\ln 2)^{1/2}/\Gamma_{\alpha}$ being the pulse duration.

To obtain the transient absorption spectrum, we need to use a dynamical equation of motion. The quantum master equation for the system density matrix $\rho(t)$ reads ($\hbar = 1$)

$$\dot{\rho}(t) = -i[H + H_{\text{int}}(t), \rho(t)] - \Re\{\rho(t)\}. \tag{2.45}$$

Here, $\Re$ is a superoperator to describe dissipative effect from environment. The total complex nonlinear polarization

$$P(t) = \text{tr}\langle X^{\dagger} \rho(t) \rangle \tag{2.46}$$

contains contributions corresponding to all possible values of the wave vector $\vec{k} = l_1\vec{k}_1 + l_2\vec{k}_2$, with l_α being arbitrary integers. The pump-probe polarization $P_{PP}(t)$ corresponds to the phase-matching condition $l_1 = 0$, $l_2 = 1$. $P_{PP}(t)$ can be retrieved from the total polarization $P(t)$ by the formula

$$P_{PP}(t) = \frac{1}{2\pi} \int_0^{2\pi} d\phi_2 \exp\{-i\phi_2\} P(\phi_2, t). \tag{2.47}$$

Here, $P(\phi_2, t)$ is computed via Eq. (2.45) and Eq. (2.46) for specific values of the phase angles ($\vec{k}_1\vec{r} = 0$ and $\vec{k}_2\vec{r} = \phi_2$) in the matter-field interaction Hamiltonian. Once $P_{PP}(t)$ has been determined, the transient absorption integral PP signal is obtained according to

$$S_{PP}(T) = \mathrm{Im} \int_{-\infty}^{\infty} dt\, \xi_2(t) \left[P_{PP}(t) - P_{PP}^{\mathrm{off}}(t)\right]. \tag{2.48}$$

Here, $P_{PP}^{\mathrm{off}}(t)$ is the polarization induced solely by the probe pulse and $T = \tau_2 - \tau_1$ is the waiting time between pump and probe pulse.

2D electronic spectroscopy. 2D electronic spectroscopy is a four-wave mixing technique (experimental details are described in chapter. 3), where three interactions between the incident laser fields with the sample induce the emission of a signal field. The experiment can be performed with a variety of pulse geometries, methods of delay control and pulse orderings. In order to produce a 2D spectrum, four pulses impinge on a sample. Pulse 1, 2 and 3 generate the signal and pulse 4, called the 'local oscillator', is used for the heterodyne detection. As described in Fig. 2.4, the delay τ between pulse 1 and 2 is named as coherence time, the time T between pulse 2 and 3 is known as the waiting time, and the delay t between pulse 3 and signal emission is known as the detection time. Traditionally, Fourier transform with respect to τ and t for a given value of T produces a 2D spectrum, which indicates the dynamical behavior of the studied system as a function of both the excitation and the emission frequency. This is particularly useful in examining the photosynthetic system in which the manifold of closely spaced electronic states and the broadening due to static disorder yield highly congested spectra. By the measurement of the second frequency dimension, the previously unresolved dynamical evolution and peak locations can be identified.

When the pulse 1 impinges on the sample, the fast oscillation of the electric field under the envelope of the laser pulse induces oscillations of transition dipoles within the ensemble of molecules in the sample. This process is named dephasing between ground and the excited state ($|g\rangle \langle e|$). Interaction of the sample with the second laser pulse converts the coherent state of the molecule to the population of the excited state or the ground state. Phase can be accumulated during the waiting time until the third laser pulse arrives. The arrival of the third pulse again produces a coherence in the ensemble, $|g\rangle \langle e|$. The resulting oscillatory macroscopic polarization in the sample drives the emission of a signal in the form of an electric field [25].

For the calculation of 2D spectra in this work, we have applied the equation of

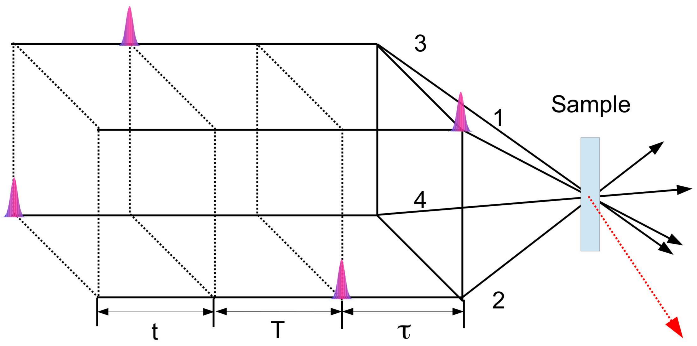

Figure 2.4: Photon-echo signal generated based on the four-wave-mixing technique. The coherent time τ is defined between the first and the second pulse, the waiting time T is the one between the second and third pulse. The time interval between the third pulse and the echo signal is the detection time t. The photon-echo signal (red arrow) is artificially separated from the beam direction of the local oscillator.

motion-phase matching approach (EOM-PMA) established in Ref. [26]. In the EOM-PMA, the induced polarization in the direction of the photon-echo signal is calculated by the simultaneous propagation of three auxiliary density matrices, $\rho_1(t)$, $\rho_2(t)$, and $\rho_3(t)$ after the rotating-wave approximation has been applied. Each of those obeys a modified effective equation of motion according to

$$\begin{aligned}
\dot{\rho}_1(t) &= -i[H_S - V_1(t,t_1) - V_2^\dagger(t,t_2) - V_3^\dagger(t,t_3), \rho_1(t)] - \Re(t)\rho_1(t), \\
\dot{\rho}_2(t) &= -i[H_S - V_1(t,t_1) - V_2^\dagger(t,t_2), \rho_2(t)] - \Re(t)\rho_2(t), \\
\dot{\rho}_3(t) &= -i[H_S - V_1(t,t_1) - V_3^\dagger(t,t_3), \rho_3(t)] - \Re(t)\rho_3(t),
\end{aligned} \tag{2.49}$$

where the pulse function is $V_\alpha(t,t_\alpha) = XAe^{-(t-t_\alpha)^2/2\Gamma^2}e^{i\omega_\alpha t}$, X is the transition dipole operator, Γ is the pulse duration, and $\Re$ is a relaxation superoperator. All three equations can be calculated in connection with quantum master equations to obtain the time-dependent auxiliary density operators. Eventually, the third-order induced polarization signal is calculated as

$$P_{PE}(t_1,t_2,t_3,t) = \langle X(\rho_1(t) - \rho_2(t) - \rho_3(t))\rangle + c.c., \tag{2.50}$$

where the brackets $\langle \ldots \rangle$ indicate the evaluation of the trace.

The total 2D Fourier-transformed spectrum is then given by the double Fourier transform of the photon-echo polarization signal with respect to the delay time $\tau = t_2 - t_1$ and t according to

$$S(\omega_\tau, T, \omega_t) \sim \int_{-\infty}^{+\infty} d\tau \int_{-\infty}^{+\infty} dt\, e^{-i\omega_\tau \tau} e^{i\omega_t t} P_{PE}(\tau, T, t). \tag{2.51}$$

Here, ω_τ is the coherence frequency, ω_t is the detection frequency, and T is waiting time given by the difference between t_3 and t_2. For the concrete simulations of the 2D spectrum, a multi-processing interface can be used to minimize the simulation time.

2D decay-associated spectrum Normally, the kinetics of the studied system are present on 2D electronic spectra with varying waiting times. A collection of the 2D spectra can be used to generate a three dimensional data $S(\omega_\tau, \omega_t, T)$ and the kinetics along the waiting time can be fitted by several exponential components, i.e.,

$$S(\omega_\tau, \omega_t, T) = \sum_i A_i(\omega_\tau, \omega_t) \exp(-T/\tau_i). \tag{2.52}$$

Here, $A(\omega_\tau, \omega_t)$ is the amplitude spectrum of one particular exponential decay component associated to the decay time τ_i. Therefore, a positive peak in the amplitude spectrum indicates the exponential decay along waiting time T with the resolved time scale τ_i. In contrast, a negative peak denotes the exponential increase along waiting time T.

Double-side Feynman diagram. Based on the temporal sequence of pulse 1 and 2, the 2D signal can be classified as rephasing (pulse 1 before 2, $\tau > 0$) and nonrephasing (pulse 2 before 1, $\tau < 0$) spectrum. In Fig. 2.5, the signatures of the electronic coupling are represented by the cross peaks in 2D map. The associated double-side Feynman diagram (ground state bleaching and excited state absorption) are shown with the respective transitions. Let us consider, e.g., the left rephasing diagram shown in Fig. 2.5(a). The first laser pulse interacts with system and induces electronic coherence between the ground and the excited state e_1, which induce a transition signal at ω_1 on the excitation-frequency axis. The interaction with the second pulse transfers the coherent state to the population dynamics of ground state

($|g\rangle\langle g|$). After the interaction with the third pulse, the induced coherence between ($|e_2\rangle$) and ($\langle g|$) generate a signal at ω_2 on the detection-frequency axis. Therefore, the dynamical information of left diagram in Fig. 2.5(a) can be represented on the 2D map with (ω_τ, $\omega_t = \omega_1$, ω_2). Following the same explanation, the excited absorption diagram (right) of Fig. 2.5(a) can be fully described by the peak at (ω_τ, $\omega_t = \omega_1$, $\omega_f - \omega_1$) in the 2D spectrum. It follows the same way to read the ground state bleach (left) and excited absorption peak (right) in the nonrephasing part of the 2D spectrum, which is shown in Fig. 2.5(b).

Besides the ground state bleach and excited state absorption diagram, the excitonic population dynamics can be represented as well in the 2D spectrum. In left part of Fig. 2.6(a), the coherent state ($|g\rangle\langle e_2|$) is generated by the interaction with first laser pulse. After interaction with the second pulse, the molecule undergoes an exciton state ($|e_2\rangle\langle e_2|$). The exciton state starts transfer to the excitonic energy to the neighbor states, e.g., ($|e_1\rangle\langle e_1|$) during the waiting time due to the electronic interaction. After the waiting time period, the molecule is converted to the coherent state again by the third pulse. Therefore, the information of the population dynamics during the waiting time can be represented on the 2D map at the frequencies ($\omega_\tau = \omega_2$, $\omega_t = \omega_1$). It follows the same way to read the population dynamics in the excited absorption diagram in rephasing and nonrephasing part of Fig. 2.6.

2D spectroscopy also shows the ability to detect the information of electronic

Rephasing

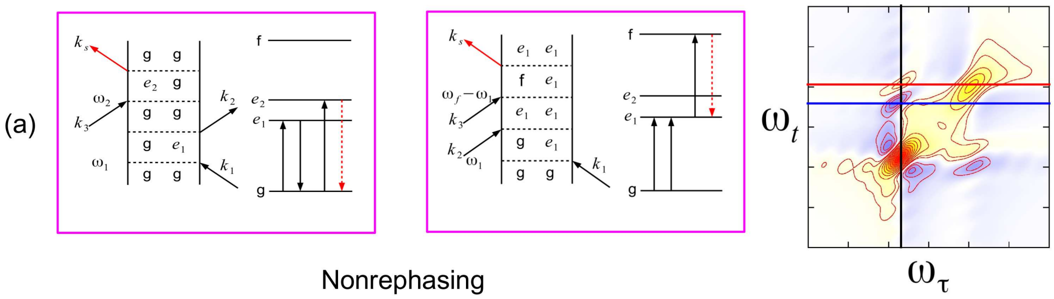

Nonrephasing

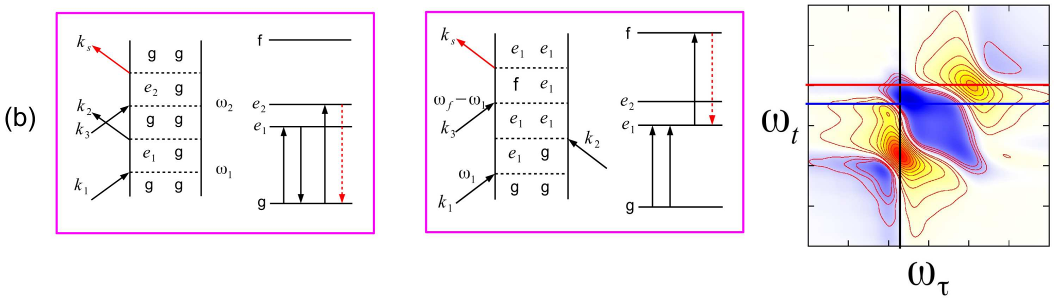

Figure 2.5: Double-side Feynman diagram which represent the Liouville space pathways contribution to the cross peaks (ω_τ, ω_t)=(ω_1, ω_2) and (ω_1, $\omega_f - \omega_1$) in the 2D electronic spectrum, ω_f denotes the transition from the ground state g to the double exciton state f. The corresponding energy-level diagrams are shown. In the 2D map, the black, red and blue lines denote the transition frequencies ω_1, ω_2 and $\omega_f - \omega_1$, respectively.

coherence. Take the left part of Fig. 2.7(a) as an example. The first and second laser pulses excite the molecule to the coherent state ($|e_1\rangle \langle e_2|$) in the same way we described before. Therefore, the electronic coherence between two exciton states (e_1 and e_2) can be detected with the evolution of the waiting time. This electronic

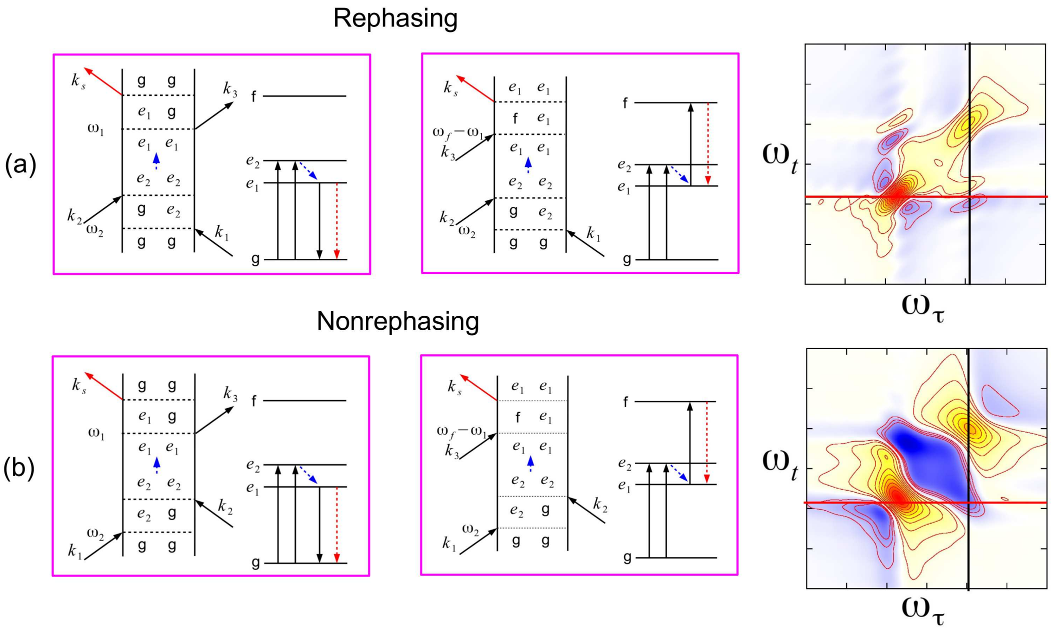

Figure 2.6: Double-side Feynman diagrams representing the population dynamics between exciton levels. In the 2D map, the signature of the energy transfer is visible at (ω_τ, ω_t)=(ω_2, ω_1) both in the rephasing and the nonrephasing part.

coherence can be located at the transition frequency in the coherence period at ω_{e_2} and the detection period ω_{e_1}. Based on the same explanation, the coherent dynamics can be seen in the excited state absorption diagram (right) and the nonrephasing part in Fig. 2.7(b).

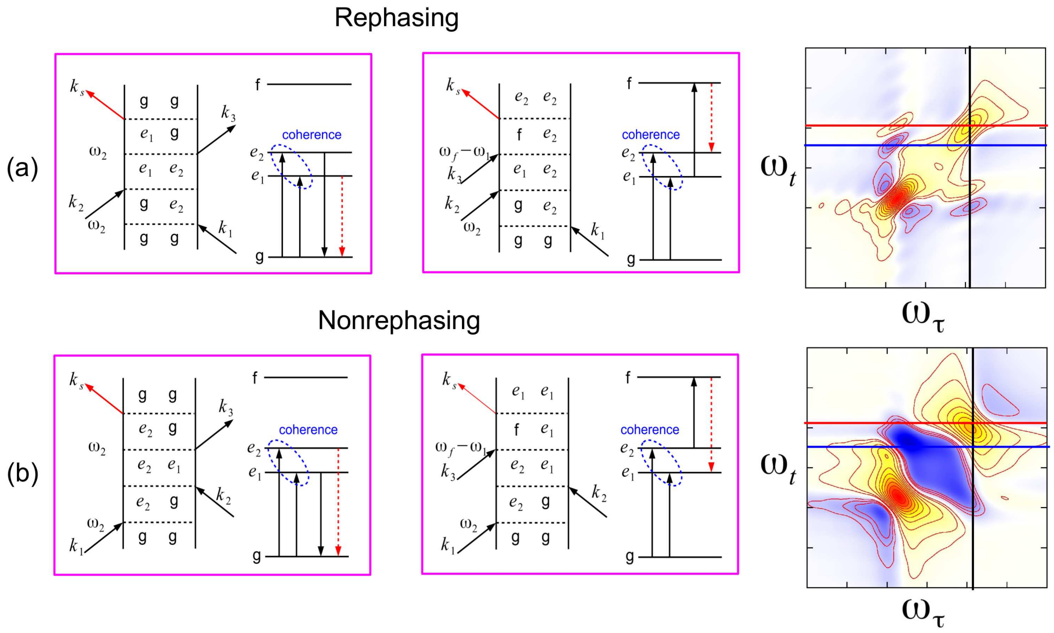

Figure 2.7: Double-side Feynman diagram representing electronic quantum coherence over the waiting time in the 2D map.

Chapter 3

Experimental techniques

In this section, I will describe the spectroscopic techniques used to measure the 2D electronic spectrum. First, I introduce the configuration of the nonlinear optical parametric amplifier (NOPA) and the critical steps, for instance, the stability of the generated white light, the polarization of the pump and the seed part of the laser pulse. I then discuss the pulse compression and the characterization by combining a prism pair and a deformable mirror (DM). The configuration of the 2D experimental setup is described at the end of this chapter.

3.1 Nonlinear optical parametric amplifier (NOPA)

The setup of the entire constructed apparatus is described below and is schematically shown in Fig. 3.1. The incident beam is first split by using a 90:10 beam-splitter (BS), with 10% of the light energy going to the seed arm and 90% to the pump arm. The beam in the seed part then passes through the retro-reflector (RR) and an attenuator (AT). After being reflected by the dielectric mirror (M1), the seed beam is focused on the YAG crystal by a convex lens (L1) with a focus length of $f = 30$ mm to generate a super continuum spectrum. The lens is mounted on a translation stage to control the focusing conditions in the YAG, while the attenuator controls the power. The beam is then promptly collimated by a thin lens (L2) with focus length $f = 20$ mm. The beam is then reflected off two silver mirrors (M3 and M4) and send to the NOPA BBO crystal for the amplification.

In the pump arm, the beam first passes through a half wave plate (WP2) to convert the polarization direction and, then, goes through the type I BBO crystal (23.4^o) for the second harmonic generation (SHG). After the SHG, 515 nm pump light is generated and focused by lens (L3) to the BBO crystal after being reflected by two dielectric mirrors. Mirrors M5 and M6 highly reflect 515 nm and anti-reflect at 1030 nm to filter residual fundamentals from the pump beam. The two focused seed and pump beams are then mixed inside the NOPA BBO (cut angle 22.05^o). The polarization of the amplified output signal is then rotated by an achromatic half waveplate to horizontally (p) polarized before heading to the compressor.

Stabilizing the super continuum spectrum. The white light generation by the femtosecond laser pulse has become an invaluable tool for the ultrafast spec-

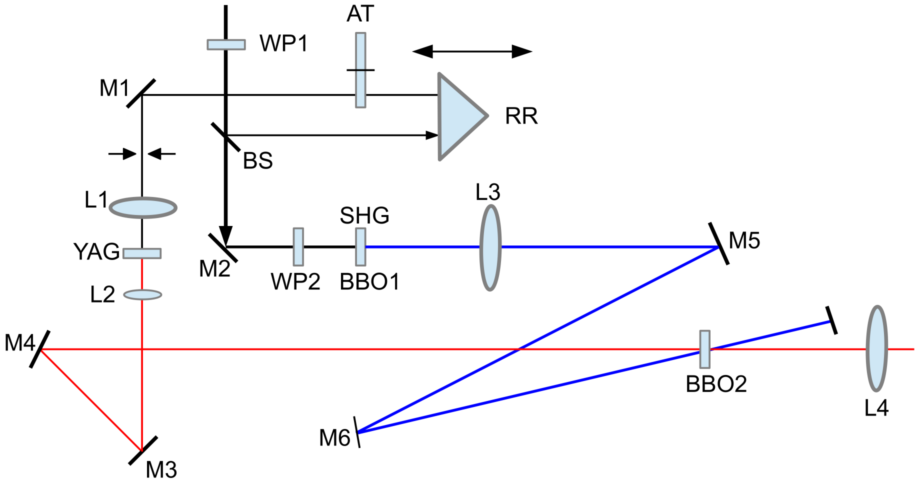

Figure 3.1: Aligned configuration of the NOPA apparatus used in the current 2D setup. The pump beam is generated by SHG (denoted by the blue line) and the super continuum spectrum is indicated by the red line.

troscopic study, both as the seed to generate the ultrabroad laser spectrum in the optical parametric amplifiers, and, as the probe in the transient absorption or 2D spectroscopic measurements. In principle, any dielectric medium, from water [27] to the crystal fiber [28] can be used as the source for the white-light generation. Among them, sapphire crystal is perhaps the most common source due to its high thermal conductivity.

The stability of the white-light generation is the most important task for stabilizing the NOPA output. For this, the central aim is to find the appropriate power and the optimal focusing condition to generate a single stable beam from the self-focusing.

A second issue is the stability of the input beam. Generation of the super continuum is a highly nonlinear process, and it amplifies any instability of the input beam. To first partially reduce the instability of the input, an aperture is necessary to be placed before the focusing lens (L1) since noise in the beam is always present at the edges of the beam. Then, the task is finding the optimal power and focusing condition for the lens L1. At the beginning, the power is raised by tuning the attenuator to generate the super continuum signal which is obviously above the needed threshold, while moving the focal lens to find the position where the beam is focused inside the crystal. This generated unstable white light with multiple filamentation served as a starting point. Then, one lowers the power while optimizing the lens position to get the maximum output of the super continuum spectrum until the power is below the threshold of white light generation. After this, one slowly increases the input power to recover the white light again until the uniform white spot appears. This indicates that the power is slightly higher than the lowest power needed to generate white light.

Polarization of the pump and the seed pulse. Another important issue is the polarization in the configuration of the NOPA. In the original NOPA of Gale *et al.* [29], the pump laser beam was oriented out of the horizontal plane of the optical table and their phase matching plane was vertically oriented. Having vertically propagating laser beams is experimentally unfavorable. Thus, in order to have a horizontal phase matching plane for the NOPA, it must simply be arranged such that the pump is horizontally polarized while the seed is vertically polarized. In Fig. 3.1, the incoming 1030 nm beam was initially horizontally polarized and the polarization was oriented to the vertical by the first half wave plate (WP1). After the beam was separated by the beam-splitter, the vertically polarized pump arm was oriented to the horizontal for the NOPA BBO amplification by the double frequency process (type I BBO). The second half wave plate (WP2) at the front of the BBO crystal was used to tune the pump energy by rotating the polarization direction. For the seed arm, the vertically polarized beam is kept to generate the white light until the NOPA BBO amplification. Based on this NOPA configuration, we employ the type I phase matching, where the pump and seed photons are orthogonally polarized (type: $o_{signal} + o_{idler} \rightarrow e_{pump}$).

Achieving spatial and temporal overlap. The achievement of the spatial and temporal overlap is perhaps the most difficult task of the building a NOPA. Based on the theoretical calculation, the pump, seed and idler beams should fulfill the condition of $\Delta k = k_p - k_s - k_i = 0$. For a broadband phase matching, the expansion

$$\Delta k = \Delta k_0 + \left(\frac{\partial \Delta k}{\partial \omega_s} - \frac{\partial \Delta k}{\partial \omega_i} \right) \Delta \omega + H.O.T. \tag{3.1}$$

Therefore, the first and the second order phase matching conditions are

$$\begin{aligned} \Delta k_0 &= 0, \\ \frac{\partial \Delta k}{\partial \omega_s} - \frac{\partial \Delta k}{\partial \omega_i} &= 0. \end{aligned} \tag{3.2}$$

To achieve the higher-order phase matching in the case of a collinear configuration

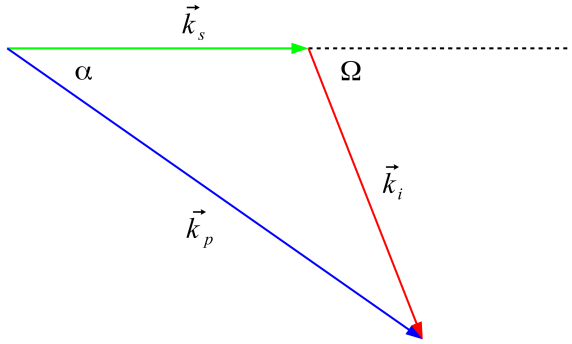

Figure 3.2: Geometry of the wave vectors for non-collinear optical parametric amplification. α is the angle between the pump vector ($\vec{k}_p$) and the signal vector ($\vec{k}_s$) inside the crystal and Ω' is the angle between $\vec{k}_s$ and the idler vector $\vec{k}_i$.

is generically impossible, a non-collinear geometry is needed by adding another new DOF, which is shown in Fig. 3.2.

Based on the derivation of Ref. [30], the first-order phase matching condition becomes a vector equation. Then, the parallel and perpendicular directions follow as

$$\begin{aligned} \Delta k_{par} &= k_p \cos\alpha - k_x - k_i \cos\Omega', \\ \Delta k_{perp} &= k_p \sin\alpha - k_i \sin\Omega'. \end{aligned} \tag{3.3}$$

The the second-order phase matching condition becomes

$$\begin{aligned} -\frac{\partial k_s}{\partial \omega_s} + \frac{\partial k_i}{\partial \omega_i}\cos\Omega' - k_i \sin\Omega' \frac{\partial \Omega'}{\partial \omega_i} &= 0, \\ \frac{\partial k_i}{\partial \omega_i} + k_i \cos\Omega' \frac{\partial \Omega'}{\partial \omega_i} &= 0. \end{aligned} \tag{3.4}$$

These two equations can be combined and simplified to yield an equivalent single condition for the group velocities of the signal and idler [30] according to

$$\nu_s = \nu_i \cos \Omega'. \tag{3.5}$$

Here, Ω' is the angle between signal and idler. Since the pump tilt, not the idler angle, is varied in practice, it is more useful to solve for the angle α between the pump and the seed. Using Eq. (3.5) and Eq. (3.3), the angle α inside the crystal follows as

$$\alpha = \arcsin \left[\frac{1 - \nu_s^2/\nu_i^2}{1 + 2\nu_s n_s \lambda_i/\nu_i n_i \lambda_i + n_s^2 \lambda_i^2/n_i^2 \lambda_s^2} \right]^{1/2}. \tag{3.6}$$

Here, ν_s and ν_i are the velocities of signal and idler pulse, respectively. n_s is the reflective index along the signal direction and λ_i is the wavelength of the idler signal. Considering the complicated forms, it is a quite involved job to calculate the appropriate crystal cutting angle for the broadband phase matching. Luckily, there is an excellent public software package, well known as SNLO, for such nonlinear optics calculations [31]. In Fig. (3.3), the phase matching angles of the BBO crystal (22.05°) was calculated using the SNLO package with a 515 nm pump beam.

Based on the above theoretical prediction, we know the proper cut-off angle for the amplification crystal (BBO2) with the internal angle of 22.05°. We can easily estimate that the external angle for the mixing of the pump and seed arm is around 6∼7°. Depending on this, we have enough information to achieve the spatial and temporal overlap. First, the BBO2 crystal can be aligned to face vertically to the seed beam (red line in Fig. 3.1) by checking the reflections to the pinhole. Afterwards, the mirror M6 can be roughly mounted on an estimated position with the mixing angle to achieve the overlap. Then, the NOPA output can be optimized by slightly changing the reflection direction of mirror M6.

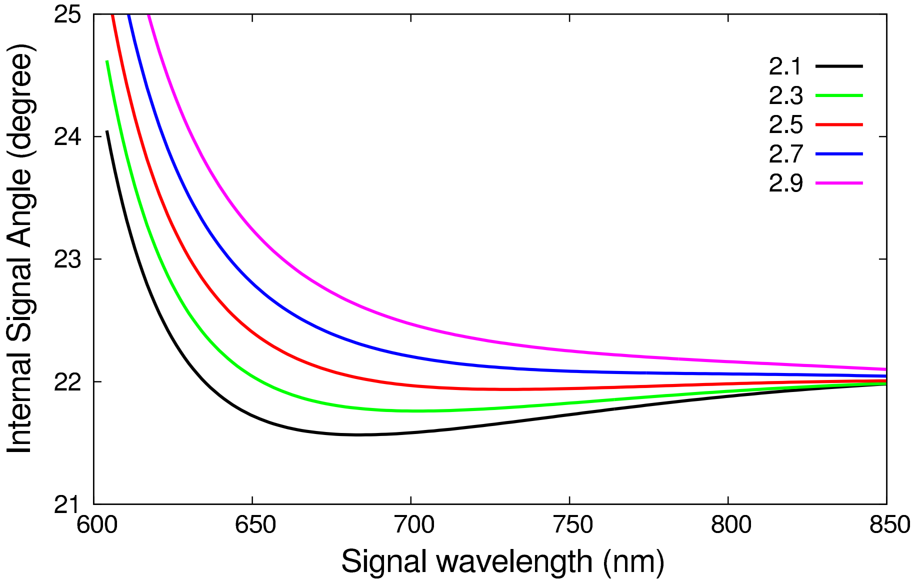

Figure 3.3: Phase matching curves as a function of the amplitude signal wavelength for a $\lambda = 515$ nm pump source for a variety of internal angles as indicated. A significant dependence of the shape of the phase matching condition on the noncolinear angle between the pump and the seed can be observed with changes as small as 0.2^o.

3.2 Pulse compression and characterization

Due to the highly nonlinear process of the super continuum generation, the NOPA output possesses an intrinsic chirp. Moreover, the NOPA beam traverses a number of dispersive optics, which introduce an additional group velocity dispersion to the pulse. For the 2D electronic spectroscopy, the stability of the pulse phase is extremely important to achieve the phase matching. Therefore, it is necessary to compress the pulse to a Fourier transform limited form before using it as the light source of the 2D spectroscopic experiment. Here, we use a prism pair and DM for the pulse compression. The pulse information (phase stability, pulse duration) is detected by a frequency-resolved optical grating (FROG).

Pulse compression. The different orders of the spectral phase can be expressed in terms of the Taylor expansion of the complex function $E(\omega) = A(\omega)\exp[-i\omega t + \phi(\omega)]$ and the spectral phase $\phi(\omega)$ can be expanded around the central laser frequency ω_0 according to

$$\phi(\omega) = \phi_0 + \frac{d\phi}{d\omega}(\omega - \omega_0) + \frac{d^2\phi}{d\omega^2}\frac{(\omega - \omega_0)^2}{2!} + \frac{d^3\phi}{d\omega^3}\frac{(\omega - \omega_0)^3}{3!} + \ldots. \tag{3.7}$$

The schematic of our compressors is presented in Fig. 3.4. The NOPA output is first diffracted by the grating (DG, slit 25 μm) and then collimated by the spherical mirror (SM) and directed to the deformable mirror (DM, 19x4 actuators, OKO Technologies). The reflected beam is subsequently focused by the spherical mirror again and finally focused by the diffraction grating. The output of this compressor is subsequently picked off and sent to the folded prism pair compressor (25 mm equilateral F2), where the prism P1 disperses the beam and prism P2 acts as both a collimation optic and the major source of phase correction via the increased optical path length of the prism material itself. A folding mirror steers the beam back through the prism pair allowing for the reconstruction by prism P1. The distance between the dispersive element and the collimation source acts as the critical component of the phase correction, for which the complete mathematical treatment of the phase correction factors can be found in Ref. [32].

The compressor is required for several purpose. First, in this compressor, the linear chirp can be easily eliminated by a grating or a prism pair. They induce a different optical path length for the red and blue part of the spectral component of a given pulse, as schematically indicated in the ray-tracing of Fig. 3.4. The second-order chirp can be primarily corrected by a diffraction grating. In addition, it is known that a grating compressor also induces normal third-order dispersion (additional positive third-order chirp to the spectral phase) and it can be compensated by a prism pair. For the final fine adjustment, a DM is used. In principle, it corrects arbitrary phase distortions by change of the shape of the mirror surface. As such, it is possible to find the stable phase, Fourier transform-limited pulse by combining a diffractive grating, a prism pair and the DM. It is worth to note that there is no single apparatus which can be used to correct the specific order of the chirp. They need to work together and find the optimal conditions to compensate the chirp. It always can be achieved by searching the optimal conditions. For instance, in the current work, we search for the maximum signal by using the genetic algorithm (MATLAB) combination with changing the position of the prism compressor (P2) and the shape of the DM. During this complicated searching process, the linear and nonlinear chirp can be eliminated effectively.

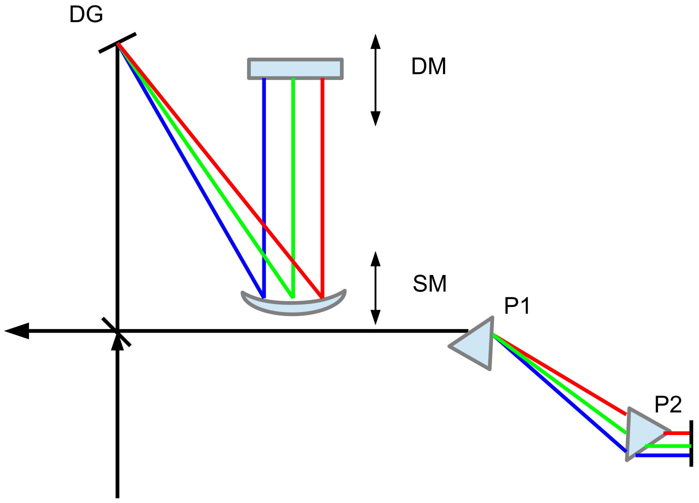

Figure 3.4: Geometry of pulse compression. It consists of a DM, grating compressor and a pair of prism compressors. DG: 300 g/mm, SM: 50 mm diameter, f=250 mm spherical mirror; P1, P2: 25 mm equilateral F2 prisms.

Pulse characterization by transient grating FROG. In order to characterize the pulse compression, transient grating FROG is used to measure the pulse duration and phase stability. The scheme of the FROG is shown in Fig. 3.5 and can be described as follows: three pulses are generated by two beam splitters (70:30 and 50:50) after go through three retro-reflectors. The difference in the optical path length between beam 1 and 2 is compensated by the compensating block (CB). The retorreflector (RR) 1 and 2 are static while RR3 is mounted on a translation stage to allow for the temporal characterization of the pulse.

The configuration of three beams are aligned as BOXCAR geometry and focused by an off-axis parabolic mirror (OAPM, f=40 mm) to the glass plate (usually SF11 or fused silica) to generate the signal. Beams 1 and 2 are coincident in space and time in nonlinear medium and form a grating in the index of refraction of the medium via the nonlinear optical Kerr effect. Pulse 3 is used to diffract off the transiently formed grating by the movable RR3 and to map out at all times the diffracted frequencies of the optical pulse as measured by the spectrometer (SPEC).

3.3 2D photon-echo spectrometer

The experimental scheme of a 2D photon-echo spectrometer used in this thesis is shown in Fig. 3.6. The Fourier-transform limited pulse is first reflected by a small-size mirror and send to the OAPM1. The beam is subsequently reflected to a customized diffractive optics (DO), which was designed to generate $\pm 1^{st}$ order beams with an

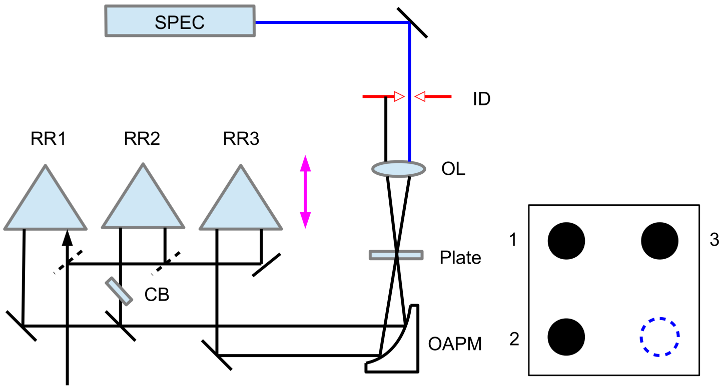

Figure 3.5: Configuration of the transient grating FROG. RR1–3: retro-reflectors; CB: compensating block; OAPM: f=50 mm off-axis parabolic mirror; OL, f=50 mm objective lens; ID, iris diaphragm; SPEC, spectrometer.

overall efficiency of 60%. A CARBOX geometry of four beams is generated and the arrangement is described in the top-left of Fig. 3.6. Thereafter, four beams are transversed through different translation stages (MTS1 and MTS2) and focused by the OAPM2 to the sample to generate the photon-echo signal, which is illustrated as a red point in the CARBOX geometry. It overlaps with the local oscillator. During the optical traverse, the delay between pulse 1 and (2) can be achieved by moving the MTS2, which allows for the delay scan of the waiting time T. For the same reason, the delay of the coherent time period τ can also be changed by moving the translation stage MTS1. An optical chopper is mounted in the optical path of beam 1, which allows for the differential measurement.

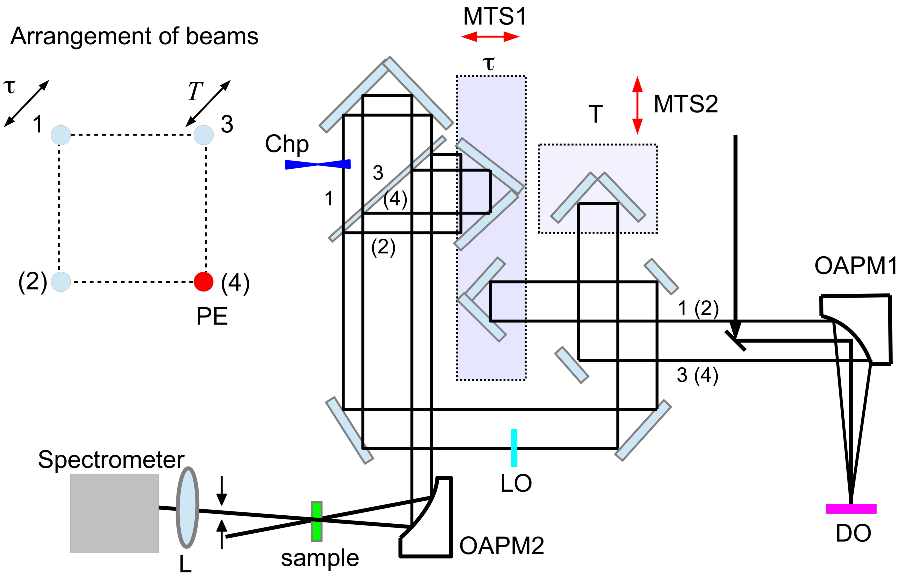

Figure 3.6: Schematic configuration of the instruments used in the 2D optical photon-echo spectroscopy.

Phase stability of 2D-PE spectrometer. The phase stability of the 2D PE setup is of central importance for the measurement. First, the phase stability should be checked before use [36].

The spectrometer measures the spectrum $S(\omega)$ of the incoming electric field E(t),

$$S(\omega) = \widetilde{E}(\omega)\widetilde{E}^{*}(\omega), \tag{3.8}$$

where the electric field is the sum of the signal from the PE and the local oscillator (LO), thus,

$$E(t) = PE(t) + LO(t - \Delta T - \tau - \delta t). \tag{3.9}$$

Heren ΔT is the time delay generated from the neutral density filter, which is mounted in the optical path of the LO (see 'LO' in Fig. 3.6). τ is the delay between the first and second pulse. δt is the jitter mainly caused by the air fluctuation and the mechanical vibrations of the setups. The measured spectrum contains the contributions from the PE, LO and their interaction terms,

$$S(\omega) = |PE(\omega)|^2 + |LO(\omega)|^2 + PE(\omega)LO^*(\omega)e^{i\omega(\Delta T+\tau)+i\delta\phi} + c.c. \tag{3.10}$$

The phase fluctuations are given by $\delta\phi = \omega\delta t$. In addition, the chopping technique in the experiment can remove the PE and the mixing signals after blocking one beam in the 2D setup (see 'Chp' in Fig. 3.6). Then, the measured spectrum can be written as

$$\Delta S(\omega) = \widetilde{A}(\omega)e^{i\omega(\Delta T+\tau)} + \widetilde{A}^*(\omega)e^{-i\omega(\Delta T+\tau)} + S_{PE}(\omega). \tag{3.11}$$

where $\widetilde{A}(\omega) = PE(\omega)LO^*(\omega)e^{i\delta\phi}$. Then, the inverse Fourier transform of the spectrum S_ω can be written in the time domain as

$$\Delta\widetilde{S}(t) = A(t - \Delta T - \tau) + A^*(t + \Delta T + \tau) + \widetilde{S}_{PE}(t). \tag{3.12}$$

Here, the signal is separated as negative and positive part in the time domain and the homodyne contribution of the PE signal can be blocked by zeroing the $\Delta\widetilde{S}(t)$ around t=0. The delay of the LO pulse should be large enough to completely separate the terms in Eq. (3.11) in the time domain, i.e., $\Delta T \gg \tau_{PE}$. Here, τ_{PE} is the maximum delay period of the PE signal. After the separation, one can obtain two complex-conjugated terms

$$\Delta S_{+}(\omega) = \widetilde{A}(\omega)e^{i\omega(\Delta T+\tau)}, \qquad \Delta S_{-}(\omega) = \widetilde{A}^{*}(\omega)e^{-i\omega(\Delta T+\tau)}. \tag{3.13}$$

The oscillatory part can be removed by multiplying $\exp[-i\omega(\Delta T + \tau)]$ with the first term in Eq. (3.13) and the inversed signal of the second term. We can obtain the phase information

$$\phi_s = \mathrm{Im}\left\{\ln\left[\widetilde{A}(\omega)\right]\right\} = \phi_0 + \delta\phi, \tag{3.14}$$

where $\phi_0 = \mathrm{Im}\left\{\ln\left[PE(\omega)LO^{*}(\omega)\right]\right\}$ reflects the sum of the phase spectra of the PE and LO. We assume that ϕ_0 does not change. The magnitude of the phase instability will be characterized by the standard deviation (STD) of the monitored actual phase: $|\delta\phi| = \mathrm{std}(\phi_{\mathrm{s}})$.

The measurement of the phase stability was performed at $\tau = 0$, $T = 0$ with a glass window at the sample position. The signal was monitored for 60 minutes, the measured phase stability is shown in Fig. 3.7.

Phasing the 2D PE spectrum. The directly measured 2D electronic spectrum shows the absolute magnitude and it should be separated into the real and imaginary part to extract the absorption and transmission information. The well-known protocols for the phasing in PE spectroscopy can be divided into interferometric [33, 34] and comparative based approaches [35]. In this work, we applied a simple scheme

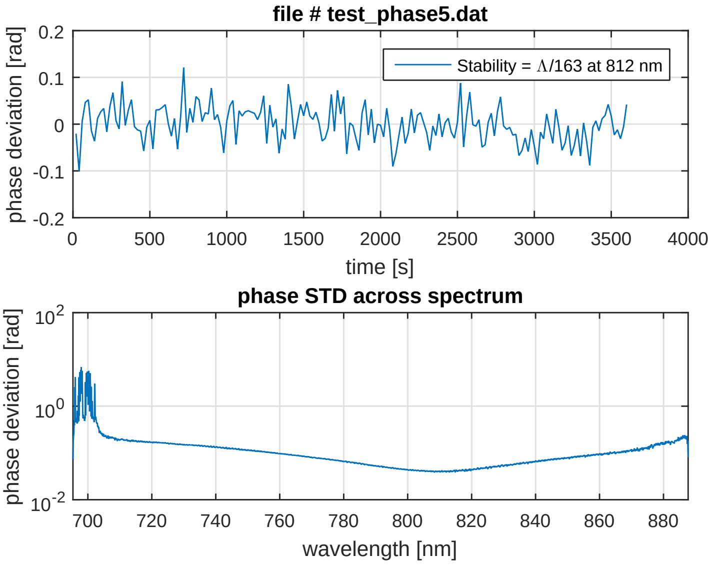

Figure 3.7: Phase stability of the 2D-PE spectrometer monitored within 60 minutes. The STD of the phase fluctuations is shown as $\Lambda/163$.

and the theory can be found in Ref. [36]. It is based on the direct comparison of the spectral profile obtained from transient absorption at zero delay and the PE spectrum, which is retrieved from the heterodyne detection of the PE signal measured at $\tau = 0$, $T = 0$. For this method, it is necessary to know the precise temporal delay of the LO filter and it only works for the measurement excited by the same pulse spectra. In our 2D spectrometer, a 1 mm neutral density filter is mounted in the LO optical path. First, the differential signal measured from the transient absorption (also named as pump-probe (PP)) without the LO filter can be written as

$$\Delta S_{pp}(\omega) = \widetilde{A}_{pp}(\omega) + \widetilde{A}^*_{pp}(\omega) + S_{pp}(\omega), \tag{3.15}$$

where $\widetilde{A}_{pp}(\omega) = PP(\omega)LO^*(\omega)$ is the spectral product of the PP signal and the LO, and the last term corresponds to the homodyne part of the PP signal. On the other hand, the measured differential PE signal at $\tau = 0$ is measured as

$$\Delta S_{pe}(\omega) = \widetilde{A}_{pe}(\omega)e^{i\omega\Delta T} + \widetilde{A}^*_{pe}(\omega)e^{-i\omega\Delta T} + S_{pe}(\omega), \tag{3.16}$$

where $\widetilde{A}_{pe}(\omega) = PE(\omega)LO^*(\omega)$ and $S_{pe}(\omega) = |PE(\omega)|^2$. We assume the LO-delay to be $\Delta T = \Delta T_0 + \delta t$ and ΔT_0 is the delay induced by the LO filter. We can remove the fast oscillations in the measured interferograms by multiplying the heterodyne term by factors $\exp(\pm i\omega\Delta T_0)$. This procedure requires the splitting of the measured PE spectrum into two complex-conjugated interferograms, which is already described in Eq. (3.13). Then, the PE spectrum can be obtained as

$$S_{pe}(\omega) = \Delta S_+(\omega)\Delta S_-(\omega)/S_{LO}(\omega). \tag{3.17}$$

After removing the fast oscillations, we have

$$\Delta S_{pe}(\omega) = \widetilde{A}_{pe}(\omega)e^{i\omega\delta t} + \widetilde{A}^*_{pe}(\omega)e^{-i\omega\delta t} + S_{pe}(\omega). \tag{3.18}$$

Due to the invariance of the third order polarization signal, $P^{(3)}$ at $T = 0$, all terms in Eqs. (3.15) and (3.18) are identical since $PP(\omega) = PE(\omega)$. The direct relation of both spectra is given as

$$\widetilde{A}_{pe}(\omega)e^{i\omega\delta t} + \widetilde{A}^*_{pe}(\omega)e^{-i\omega\delta t} + S_{pe}(\omega) = \Delta S_{pp}(\omega). \tag{3.19}$$

Data collection and processing. The spectrum collected from the measurement is given by

$$S(t_1, \omega_3) = S_{LO}(\omega_3) + S_{PE}(t_1, \omega_3) + E_{PE}(t_1, \omega_3)E^*_{LO}(t_1, \omega_3)e^{i\omega_3(\Delta T_{LO}+t_1)} + c.c.. \tag{3.20}$$

Based on the chopper technique, the PE and PE-LO mixing signal can be blocked and leads to the differential spectrum written as

$$\Delta S(t_1, \omega_3) = S_{PE}(t_1, \omega_3) + \widetilde{A}(t_1, \omega_3)e^{i\omega_3(\Delta T_{LO}+t_1)} + \widetilde{A}^*(t_1, \omega_3)e^{-i\omega_3(\Delta T_{LO}+t_1)}. \tag{3.21}$$

By performing an inverse Fourier transform with respect to ω_3, we obtain the signal in the time domain as

$$\Delta S(t_1, t_3) = \widetilde{S}_{PE}(t_1 + t_3) + A(t_3 - \Delta T - t_1) + A^*(t_3 + \Delta T + t_1). \tag{3.22}$$

The negative and positive signals in the frequency domain can be obtained by performing Fourier transforms after separating the signal in the time domain, which is described in detail above. We obtain

$$\begin{aligned} S'_+(t_1, \omega_3) &= \widetilde{A}(t_1, \omega_3)e^{i\omega_3(\Delta T_{LO}+t_1)}, \\ S'_-(t_1, \omega_3) &= \widetilde{A}^*(t_1, \omega_3)e^{-i\omega_3(\Delta T_{LO}+t_1)}. \end{aligned} \tag{3.23}$$

The fast oscillation components can be removed by multiplying the factor $e^{\mp i\omega_3\Delta T_{LO}}$, i.e.,

$$\begin{aligned} S_+(t_1,\omega_3) &= E_{PE}(t_1,\omega_3)E^*_{LO}(t_1,\omega_3)e^{i\omega_3 t_1}, \\ S_-(t_1,\omega_3) &= E^*_{PE}(t_1,\omega_3)E_{LO}(t_1,\omega_3)e^{-i\omega_3 t_1}. \end{aligned} \tag{3.24}$$

We define a modulus and a phase of the spectra, according to

$$\begin{aligned} |E_{PE}(t_1,\omega_3)| &= \sqrt{\frac{S_+(t_1,\omega_3)S_-(t_1,\omega_3)}{I_{LO}(t_1,\omega_3)}}, \\ \phi_{PE}(t_1,\omega_3) &= \arg(S_+) - \omega_3 t_1. \end{aligned} \tag{3.25}$$

Since $I_{LO}(t_1,\omega_3)$ is measured for each t_1 due to the chopper, the spectrum is normalized along ω_3 for each time point. Here, the real and imaginary part of the spectrum can be generated and associated to the absorptive and dispersive parts of the third-order signal. The 2D spectrum is generated by performing the inverse Fourier transform along ω_3. The procedure above emphasizes the proper way to determine the phase ΔT_{LO} which is a crucial step of the experiment.

Chapter 4

Excitation energy flow in Light-harvesting Complex II

Based on the description of theoretical models and the experimental techniques, we apply the 2D spectroscopic approach to study the primary step of energy transfer in the photosynthetic complex of higher plants. In this chapter, the 2D spectra of the peripheral antenna LHCII are measured at room temperature and combined with a theoretical analysis. First, based on the global analysis, multi-pathways of the energy transport are resolved with the associated different time scales. Second, for interpreting the measured data, an advanced theoretical model is constructed to simulate the 2D electronic spectra. We find shows a good agreement of the decay-associated spectra to the experiment. In the end, the electronic coherence is analyzed, for which we find the time scale of < 100 fs.

4.1 Introduction

LHCII, as introduced in Chapter 1, is one of the most abundant complexes in nature and is responsible for capturing sun light and the transfer of its energy to the reaction center with nearly unity efficiency. Since long, the central importance of the LHCII has been realized and thus, it has been investigated extensively by almost all available steady-state spectroscopic techniques, such as absorption, linear and circular dichroism (CD), fluorescence [37, 38, 39] and single-molecule spectroscopy [40], and also by Stark spectroscopy [41]. The electron-vibrational coupling and the involved intramolecular vibrational modes have been revealed using low-temperature non-photochemical hole burning [42] and fluorescence line-narrowing spectroscopies. Also energy transfer processes in LHCII have been extensively studied in the past. For this, ultrafast spectroscopies such as transient absorption and time-resolved fluorescence [43, 44, 45], and three pulse photon echo peak shift (3PEPS) [46, 47] spectroscopy have been used. More recently, also 2D photon echo spectroscopy [48, 49, 50] was applied.

In particular, in the femtosecond transient absorption spectroscopy carried out at low temperature (77 K), different time scales of the energy transfer have been addressed [43]. Various Chla absorption bands have been selectively excited and the induced changes over the entire Qy region have been detected. A subsequent global fit together with a target analysis on the basis of a sequential energy transfer model has revealed different time scales on which the energy transfer dynamics between the pigments in monomeric LHCII occurs. Within this excitation range, the population kinetics of the Chla pool involves the time scales of 0.28 ps, 11.5 ps, 160 ps and a long-lived component with the time scale of 3.4 ns. At room temperature, a transient absorption study of LHCII-trimers has been performed at very low excitations in the Chlb spectral region [44]. The measured kinetics showed lifetimes of 175 fs, 625 fs, 5 ps and a long-lived component. The shortest lifetimes were assigned to the energy transfer between the Chlb and Chla pools. Notably, a 300 fs lifetime component was not found in the measured kinetics of the LHCII trimers. However, this 300 fs lifetime was reported in Ref. [46] in the 3PEPS-kinetics in the Chlb absorption band. It was attributed to the energy transfer within the Chlb molecules, whereas a 4 ps component reflects the energy transfer from Chlb to Chla. Together with this, the 150 fs and the 600 fs lifetimes were also found in the 3PEPS-kinetics.

In the subsequent 3PEPS experiment reported in Ref. [47] from the same lab, this 300-fs component was observed in the 3PEPS kinetics and was then attributed to the energy transfer between Chlb and Chla. In a recent 2D spectroscopy study of LHCII trimers, only the Chlb pool was excited with excitation pulses with a relatively narrow spectrum (14 nm), however, with a spectrally broad reading pulse. This allowed then to resolve the 300-fs component in a sequence of 2D spectra taken at different waiting times. It was attributed, as well as the 2.4-ps component, to the energy transfer from Chlb to Chla. However, questions remained open: the excitation level was too high for annihilation-free conditions in view of the changes in the differential absorbance up to 50 mOD. Moreover, the interpretation of the Fourier-transformed photon-echo signals in terms of transient absorption changes, which involve changes in populations, is debatable.

In general, there is consensus about basically four timescales of the energy transfer in the LHCII (see, e.g., the reviews [51, 52]): a very fast one with the characteristic lifetime of 100-150 fs, a slower one with a 300-600 fs lifetime (whose appearance depends on the excitation wavelength and excitation spectrum), 1.5-2.5 ps which is generally accepted to be a lifetime of the energy transfer between the Chlb and Chla pools, and a 5-10 ps component.

In addition to the extended experimental investigations of the LHCII, great efforts have been made on the side of theoretical simulations of both stead-state and time-resolved spectroscopic data. It should be emphasized that the identification of the energy levels of the excitonic states and the energy transfer pathways in experimental data is not a trivial task and is often limited by typically highly congested linear spectra, homogeneous broadening, by the presence of static disorder and inhomogeneous broadening. The most refined exciton model of the LHCII was established by

Novoderezhkin et al. [53] on the basis of the crystal structure with a spatial resolution of 2.72 Å [3]. They performed a simultaneous fit of the absorption, linear dichroism, steady-state fluorescence, and transient absorption spectra at different delay times and at different excitation wavelengths (notice that the CD spectrum was not included in the fit to the set of data). The excitonic interactions between the pigments (i.e., the off-diagonal terms in the Hamiltonian matrix) were calculated in the dipole-dipole approximation [3]. The model describes reasonably well the linear spectra and the transient absorption data. The time scales and pathways of the energy transfer have been identified upon using modified Redfield theory and an experimental exciton-phonon spectral density [53]. According to this advanced model, the initial, fast Chlb → Chla energy transfer is due to a good spatial connection of the Chlb to strongly coupled Chla clusters. Long-lived components of the energy transfer are determined by the population of red-shifted monomeric Chl a604 (according to the pigment arrangement in Fig. 4.1), followed by a very slow (12 ps) flow of excitation energy from this bottleneck site to the remaining low-lying exciton states. The dynamics of the population within the Chla pool was found to be governed by fast (sub 100 fs) excitonic relaxation within the a610-a611-a612 trimer, followed by slower relaxation within a602-a603 and a613-a614 dimers on the time scale of 200-300 fs. An even slower migration on a time scale of 300-800 fs between these clusters then sets in, and, finally, a very slow transfer from a604 to the quasi-equilibrated sites terminates the transfer [52] (we use the nomenclature of Ref. [3]). The homogeneous broadening was described within Redfield theory, implying that this approach has no capacity for a proper description of the 2D electronic spectra. The dominating effect is fast dephasing which clearly has a non-Markovian behavior in general. It should also be noted that the dipole approximation for calculating the excitonic interactions is the simplest one and is actually applicable when the distances between the chromophores are large enough as compared to their spatial dimensions. A more accurate approach is the transition density cube (TDC) method [54] which includes the Coulomb interaction of the chromophore molecular charge densities. The site energies of the pigments (i.e., the diagonal terms in the Hamiltonian matrix) were obtained by fitting the calculated spectra to the experimental data. They also can be calculated independently by ab-initio, semi-empirical, or other quantum chemistry methods and by accounting for the energy level shifts due to the interaction of the chromophores with the local protein environment. Such an approach has been followed in Ref. [55] and may yield values of the site energies which can be used as very good initial values for a fitting procedure.

In addition to the traditional transient absorption and time-resolved fluorescence spectroscopies, the 2D photon-echo electronic spectroscopy was also applied to study the LHCII. Up to present, only a few investigations using this relatively new technique have been performed [56, 57, 58]. Moreover, the only theoretical analysis devoted to

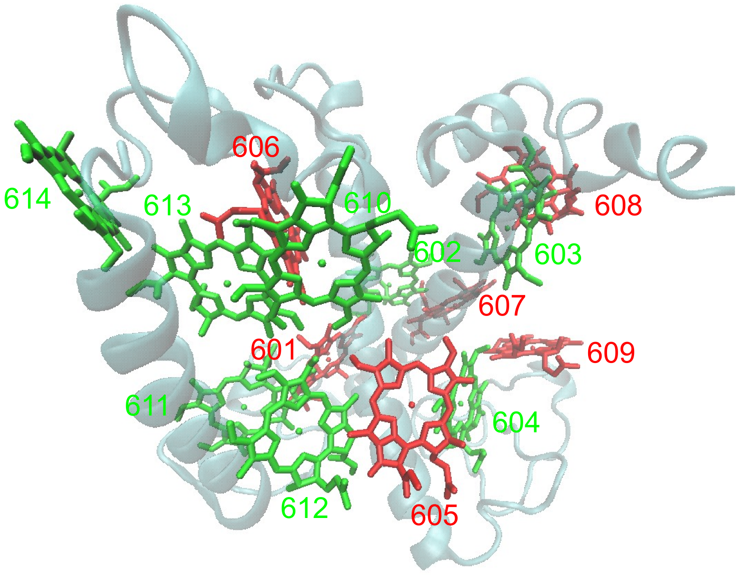

Figure 4.1: Spatial structure of the LHCII monomer from the stromal side (PDB file 2BHW) with labeling of pigments according to Ref. [4]. For clarity of presentation, the carotenoids are not shown. The figure was created using the VMD package [9].

the modeling of 2D spectra of the LHCII [48] is based on a modified Redfield master equation and uses a simplified technique [59] for creating 2D spectra. Extending the measurements of signals to the second frequency dimension allows identifying the locations of excitonic states and mapping the pathways of the energy transfer among them. The first report of 2D spectroscopy of the LHCII at 77 K has been provided in Ref. [48]. Several cross peaks between excitonic states were visualized and thus some energy transfer routes were identified. In a subsequent work of the same group, the authors have analyzed oscillations arising on the diagonal sections of 2D spectra measured at consecutive waiting times. From the power spectra of the Fourier-transformed oscillations, all exciton states in the LHCII have been identified [49]. The energies of the excitonic transitions were in excellent agreement with the values predicted earlier in Ref. [53], however, not with the energies defined later in a newly refined LHCII model by the same authors [60]. Furthermore, polarized 2D electronic spectroscopy was applied to reveal the angles between the transition dipole moments of some excitonic states [61]. The so-called coherence-specific pulse polarization sequence [62] isolates cross-peaks and suppresses diagonal peaks. It was also used to investigate dephasing in a 2D study of the LHCII [63]. The coherence of cross-peaks was reported to decay at 77 K on two distinguishable time scales of $\sim$50 and 800 fs. However, it remained unclear how these dephasing times relate to electronic dephasing and to the dephasing of exciton states in the LHCII. All 2D spectroscopy studies of the LHCII cited above were performed at low temperature (77 K). Up to present, only one published work applied this tool to the LHCII at room temperature [50]. However, a relatively narrow excitation spectrum, which covers only the Chlb absorption band, was used.

4.2 Experimental measurements

Experimental setups. The measurements reported here were performed using a 2D electronic spectroscopic setup described in Ref. [36] (also present in Chapter 3). In these experiments the 2D setup was used in a 'mono-beam' fashion, without involving a second beam passing through a deformable mirror compressor (see Fig. 3 in Ref. [36]). Heterodyne detection of the photon-echo signal was achieved by placing a thin neutral-density filter with OD 2 into the fourth (reference) beam which delays the local oscillator pulse by $\sim$ 400 fs. The spot size of all beams at the sample position was $\sim$ 60 μm.

Ultrashort light pulses where generated by a home-build NOPA, tuned to the red side of the visible spectrum and centered at 670 nm. Since at that position the NOPA spectrum is very broad, and in order to increase the spectral brightness, its spectral width was reduced to $\sim$ 60 nm by placing a 3-mm thick fused silica window into the white-light channel of the NOPA. Further, in order to avoid excitation of high-lying vibrational states in the Chl's, the wings of the NOPA spectrum were suppressed using an appropriate amplitude mask applied to an acousto-optic modulator Dazzler (Fastlite, France) which was placed into the first beam of the 2D setup (see in Ref. [36]). The resulting laser spectrum is shown in Fig. 4.2 together with the absorption spectrum of the LHCII sample used in the experiments. The light pulses were compressed to the transform-limited level (22 fs FWHM) using a corresponding phase mask applied to the Dazzler. The pulses were characterized by a home-build third-order FROG described in the last chapter. The energy of the excitation pulses was controlled by the Dazzler and limited up to 10-15 nJ per beam at the sample position. The laser repetition rate of 900 Hz was used. The measurements was preformed by Dr. Valentyn I. Prokhorenko at the University of Toronto.

Sample preparation and measuring conditions. The LHCII sample was provided by Prof. R. van Grondelle. It was isolated from the spinach according to the procedure described in Ref. [64], dissolved in a HEPES buffer, and stored at -40°C. Directly before the measurements, the samples were filtered using a 0.2 μm micropore filter in order to reduce unwanted light scattering which affects significantly the 2D spectra especially around zero waiting time. Measurements were performed at room temperature using a 0.4 mm thick closed cell with an inner volume of 1.5 mL, mounted onto a precise home-build X-Y motorized translator with a moving speed of $\approx$ 6 mm/sec. The actual spectrum of the sample is shown in the left panel of Fig. 4.2 together with the laser spectrum measured at the sample position. The OD in the maximum of absorbance of the Q_y band was 0.33. For minimizing unwanted contributions of the non-resonant response to the PE signal, a 0.2 mm fused silica cover slip was used as an input window in the cell. In order to avoid the so-called annihilation of excitons in LHCII trimers, the excitation energy was kept below 5 nJ. At these excitation conditions, the magnitude of the homodyne PE was proportional to the third power of the incoming energy (see PE power dependence on the right panel in Fig. 4.2) which ensures the linear regime of excitation. Deviations from the linear regime occur at energies > 6 nJ per beam. It was checked that under these illumination conditions the maximal degradation of absorbance of the LHCII-sample in the cell was $\sim 5\%$ within 12 hours of operation.

The photon-echo spectra were collected at each fixed 'waiting time' T by scanning the delay time τ in a range of [-100,+150] fs with the step of 1 fs, and 280 spectra were averaged at each delay point. The waiting time T was linearly scanned within 0-2 ps with a step of 25 fs, and with logarithmically spaced steps up to 50 ps. Since the accumulation of a large amount of photon-echo scans takes a couple of hours, the NOPA spectrum was actively stabilized using an appropriate feedback.

4.3 Theoretical model

We consider a molecular system coupled to the electric field which time-dependent Hamiltonian, which is written as

$$H(t) = H_{mol} - \boldsymbol{\mu} \cdot \mathbf{E}(t), \tag{4.1}$$

where H_{mol} is the Hamiltonian of the monomeric LHCII (our model is restricted to the LHCII monomers due to limitations in the available computer power), $\boldsymbol{E}(t)$ is the semi-classical electric field of the laser pulse, and $\boldsymbol{\mu}$ is the transition dipole operator.

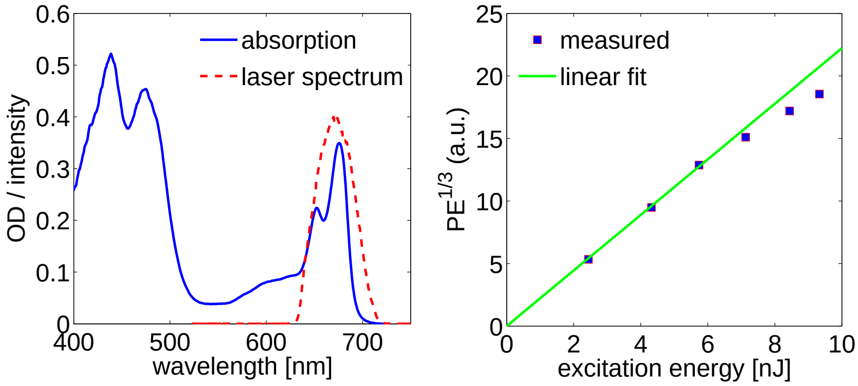

Figure 4.2: The left panel shows the absorption spectrum of the LHCII sample in overlap with the spectrum of the excitation laser. Right: Power dependence of the homodyne PE signal measured at waiting time T = 0. To better see the deviation from the linear regime, the PE magnitude is plotted as a cubic root vs. the excitation energy.

The total dipole operator $\boldsymbol{\mu}$ is expressed via the transition dipole moments of the individual molecules $\boldsymbol{\mu}_m$, i.e.,

$$\boldsymbol{\mu} = \sum_{m=1}^{N} \boldsymbol{\mu}_m \left(\alpha_m + \alpha_m^\dagger\right), \tag{4.2}$$

with $\alpha_m^\dagger$ and α_m being the creation and annihilation operators of the electronic excitation on the mth molecule. The molecular Hamiltonian H_{mol} is defined as

$$H_{mol} = H_e + H_{ph} + H_{e-ph}. \tag{4.3}$$

Here, the Frenkel-exciton Hamiltonian

$$H_e = \sum_{m=1}^{N} \epsilon_m \alpha_m^\dagger \alpha_m + \sum_{m=1}^{N} \sum_{n<m} J_{n,m} \left(\alpha_m^\dagger \alpha_n + \alpha_n^\dagger \alpha_m \right), \tag{4.4}$$

describes the electronic DOF, where ϵ_m are the site transition energies of the molecules, and $J_{n,m}$ is the inter-molecular excitonic coupling between them. H_{ph} describes nuclear (phonon) DOFs. In our model, we assume that the electronic excitation on the mth molecule couples independently to its own harmonic bath given by the Hamiltonian

$$H_{ph} = \sum_{m=1}^{N} \sum_{j=1}^{N_b^m} \left(\frac{p_{mj}^2}{2} + \frac{1}{2} \omega_{mj} x_{mj}^2 \right), \tag{4.5}$$

where N_b^m is the number of bath modes coupled to the molecule m, x_{mj} and p_{mj} are the mass weighted position and momentum of the jth harmonic oscillator with the frequency ω_{mj}. The bath spectral density has the form

$$J_m(\omega) = \frac{\pi}{2} \sum_{j=1}^{N_b^m} \frac{c_{mj}^2}{\omega_{mj}} \delta \left(\omega - \omega_{mj} \right). \tag{4.6}$$

For an infinite number of bath modes, the frequency distribution can be modeled by using a continuum-distributed spectral density for which we use the Ohmic model. The electron-phonon coupling H_{e-ph} is assumed to cause only electronic energy fluctuations and is the same for each molecule. Each molecule is also assumed to be linearly coupled to the phonons and the coupling Hamiltonian has the form

$$H_{e-ph} = \sum_{m=1}^{N} \sum_{j=1}^{N_b^m} c_{mj} x_{mj} \alpha_m^\dagger \alpha_m. \tag{4.7}$$

For the parametrization of the model, the site energies ϵ_m of the mth chromophore was pre-calculated by the ab-initio method in the gas phase. We have found higher transition energies ($S_0 \rightarrow S_1$) for Chlb than for Chla due to an additional carbonyl group in Chlb, which is known from the linear spectroscopic data. Then, the site energies have been optimized by fitting to the experimental linear spectra (absorption and CD) at different temperatures. The intermolecular excitonic couplings $J_{n,m}$, calculated by the transition density cube method [54], have been directly taken from Ref. [65] without any further modifications. To take the system-bath interaction into account, the Ohmic spectral density $J(\omega) = \gamma\omega e^{-\omega/\omega_c}$ was fitted by three artificial spectral densities using Eq. (15) of Ref. [66] which significantly speeds up numerical calculations. Quantum dynamical calculations were performed using the TNL quantum master equation [66, 67] (see Chapter 2 for details). The inhomogeneous broadening, or effects of low frequency nuclear motions, were accounted for by a convolution of simulated homogeneous spectra with a Gaussian-shaped distribution having a width of $\sigma = 106$ cm^{-1}. The dipole strengths and the orientations of the chromophores have also been taken from Ref. [65]. The relative strength of the transition dipole moments for the Chla and Chlb molecules was set to $|\mu_a|$=1.0 and $|\mu_b|$=0.85, respectively. More details about the Hamiltonian matrix and the numerical calculation procedures can be found in the Appendix A.

The calculated room-temperature absorption and CD spectra are shown in Fig. 4.3

in comparison with the experimentally measured ones (dots). The bars represent the calculated stick-spectrum. In order to fit the CD spectrum, the transition dipoles for the Chla molecules were rotated counter-clockwise by 8° and for the Chlb molecules, their directions were kept [68].

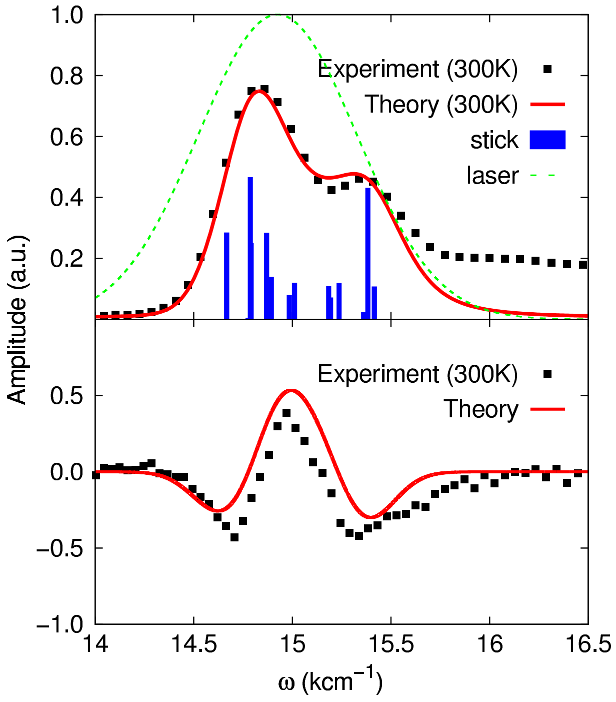

Figure 4.3: Stick, absorption (top) and CD spectrum (bottom) calculated by the TNL method. The parameters $\gamma = 0.6$ and $\omega_c = 400\ \text{cm}^{-1}$ are used for the Ohmic spectral density. The result has been convoluted with a Gaussian shaped distribution with $\sigma = 106\ \text{cm}^{-1}$ for the simultaneous fit of the width of the absorption and the CD spectrum.

4.4 Energy-transfer timescales and pathways

In this section, we will first show the selected 2D spectra for different waiting times and compare them to the theoretical calculations. Then, the pathways and the associated timescales of energy transfer in LHCII will be analyzed by 2DDAS [69]. Four different pathways can be clearly resolved. At last, the oscillations in 2D spectra are shown and their origin will be discussed.

4.4.1 Dephasing and inhomogeneous broadening

Figure 4.4 (left panel) shows several representative experimental 2D spectra collected at different waiting times as indicated. The shapes of the 2D spectra calculated on the basis of our theoretical model (right panel) are in very good agreement with the experimental ones which supports the developed LHCII model and justifies the theoretical approach used for simulations. At the initial waiting time T = 0, the 2D spectrum is significantly stretched along the diagonal direction which manifests a strong inhomogeneous broadening in the LHCII. Antidiagonal direction of the spectrum is related to homogeneous broadening. Its FWHM of 170 cm^{-1} corresponds to an electronic dephasing time of 62 fs (assuming the Lorentzian line shape). It is much shorter than the dephasing time estimated for the LHCII at low temperatures (77K) also from 2D spectroscopy [48], but still slightly longer than the typical electronic dephasing time for, e.g., organic dyes (40-50 fs). The degree of inhomogeneous broadening can be estimated by the ratio of the width of the diagonal and anti-diagonal parts. We find it to be ≈ 3.1 (FWHM of diagonal section is 530 cm^{-1}). However, this estimate is not strictly valid for an excitonic system having several transitions distributed over a wide spectral range (cf. stick spectrum on Fig. (4.3)). Even without inhomogeneous broadening, the 2D spectrum of such a system will display some diagonal stretch due to the spectral distribution of the excitonic transitions. We can deduce the degree of the inhomogeneous broadening by comparison of the diagonal width for the measured (inhomogeneous) and calculated homogeneous 2D spectrum (FWHM $\sim$ 410 cm^{-1}, not shown). From this comparison follows that the degree of the inhomogeneous broadening at T=0 is approximately 120 cm^{-1} which is actually close to the inhomogeneous parameter of 106 cm^{-1} used in the calculations of all spectra.

The feature visible in the left-top corner of the 2D spectrum (label C) can be associated with the cross-peak arising due to interference of exciton states associated with the manifolds of Chla and Chlb molecules. However, at this waiting time the corresponding diagonal peaks are not well resolved since they are ‘blurred’ by fast dephasing processes. They become much better resolved at waiting times starting from $\sim$ 100 fs, where dephasing is over, and the magnitude of the diagonal peak, associated with the Chlb pool (label B) then decays with increasing waiting time due to the energy transfer to the manifold of the exciton states associated with the Chla pool (label A). This energy transfer manifests itself as a growing of the cross-peak C

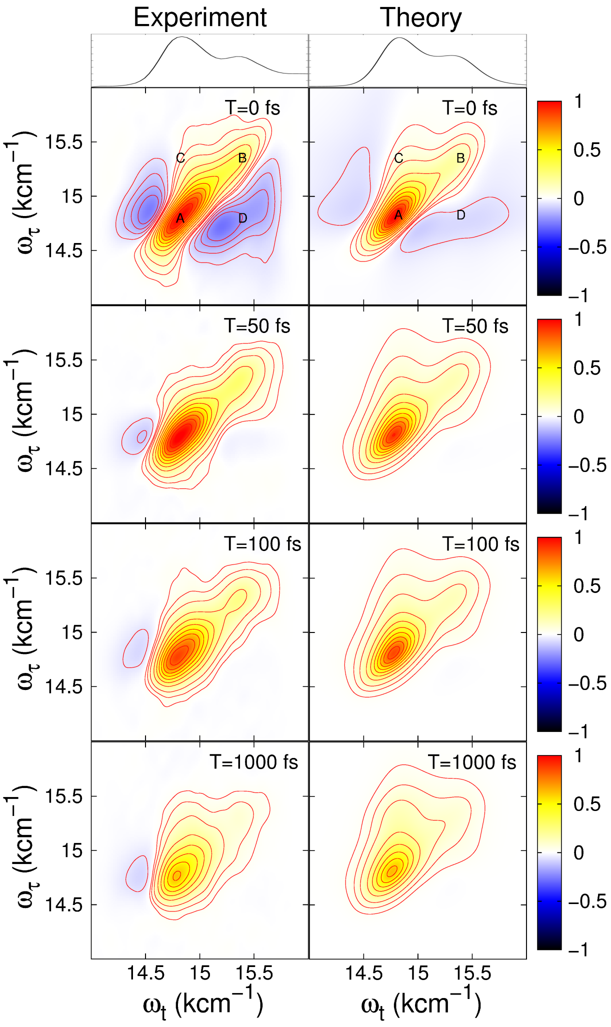

Figure 4.4: Real part of experimental (left) and theoretical (right) 2D photon-echo spectra of the LHCII at different waiting times. The theoretical result is calculated with the model and parameters obtained by fitting the linear absorption and CD spectra (see text). The diagonal and cross peaks are labeled by capital letters in the frame $T = 0$ fs.

which becomes clearly visible at waiting times larger than 100 fs and up to a few tens of ps. Fig. 4.5 displays different kinetics in the decay traces for the diagonal (A,B) and cross-peaks (C,D) caused by the energy transfer basically between the Chlb and Chla pools.

4.4.2 Energy transfer pathways in LHCII

The energy transfer pathways and the associated lifetimes can be resolved by applying a multidimensional global fit approach to the series of consecutive 2D spectra acquired at different waiting times. The global fitting of frequency- and time-resolved data is applicable only if the kinetics is not dispersive, i.e., has no significant wavelength (frequency) dependence of the lifetimes. To validate the applicability of the global fitting to our experimental LHCII 2D data, we independently have fit each decay trace (a single fit) in the set of 2D spectra which contains about of 26000 traces, and found that the retrieved lifetimes form 3 distinguishable groups with quite narrow distributions of lifetimes. For the probability of the occurrence of the lifetimes retrieved from the fit of individual trace, was shown in Fig. 4.6. The quality of the 3D global fits can be inspected by comparing the experimental and fitted decay traces shown in Fig. 4.5. The global fitting provides a 2DDAS, which is shown in the left panel of Fig. 4.7.

We find the lifetimes of 100 fs, 1.1 ps, 9.8 ps and a long lived component with

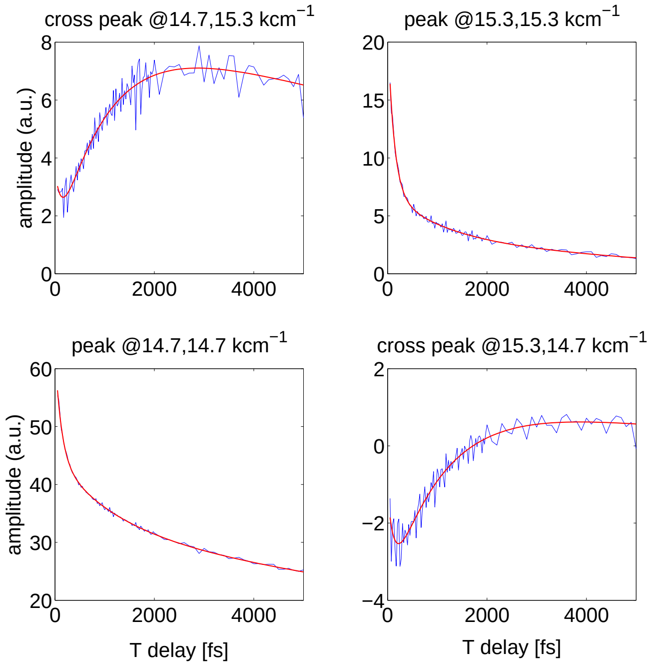

Figure 4.5: Representative time traces taken at the indicated positions of the diagonal- and off-diagonal peaks in 2D-spectra measured at different waiting times T.

a lifetime $>$ 100 ps, which is not resolved in the delay time window used (marked as ‘Inf’ in Fig. 4.7). This long-lived component in the 2DDAS can be associated with the trapping of excitation energy in low-lying exciton states after a fast energy transfer between excited states. A corresponding DAS with a long lifetime of a few ns was previously observed in numerous transient absorption and time-resolved fluorescence studies. The fastest resolved 2DDAS can be associated with the fast electronic dephasing, i.e., it appears due to the decay of coherence among excited exciton states (note that our excitation spectrum covers a whole Q_y band so that all

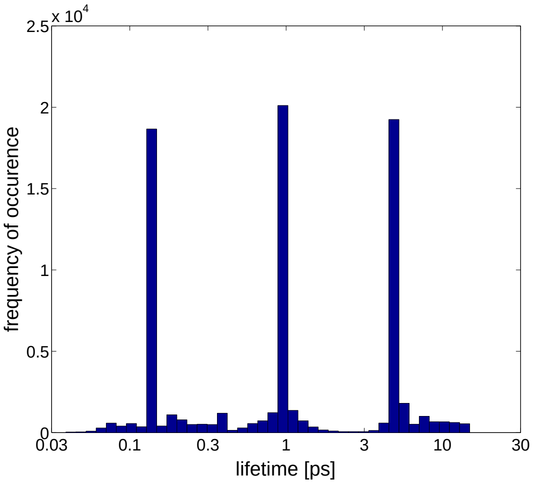

Figure 4.6: Lifetime distribution obtained from the fits of individual traces in the sequence of 2D spectra of LHCII.

exciton states are excited). This 2DDAS shows a smaller degree of inhomogeneity as compared to the 2D spectrum collected at T = 0 (Fig. 4.4), and a red-shifted cross-peak is also present there. Section of the 100-fs 2DDAS along ω_τ = 15340 cm^{-1} clearly visualizes it. Some energy transfer is also observed in the 100 fs 2DDAS along ω_τ = 14900 cm^{-1} which appears as a negative shoulder around ω_t = 14600 cm^{-1}. This energy transfer is associated with the main diagonal peaks (Chla) but it can be attributed to the energy transfer from the exciton states located at 14500 cm^{-1} to low-lying state(s) located around 14600 cm^{-1} (see in Fig. 4.7). In contrast to the experimental one, the corresponding 2DDAS with the comparable lifetime (70 fs) retrieved from the calculated 2D spectra has a rather different shape. It displays a negative peak around 15000 cm^{-1} which can be associated with an efficient energy transfer between the Chlb-Chla pools or with contributions of the excited state absorption.

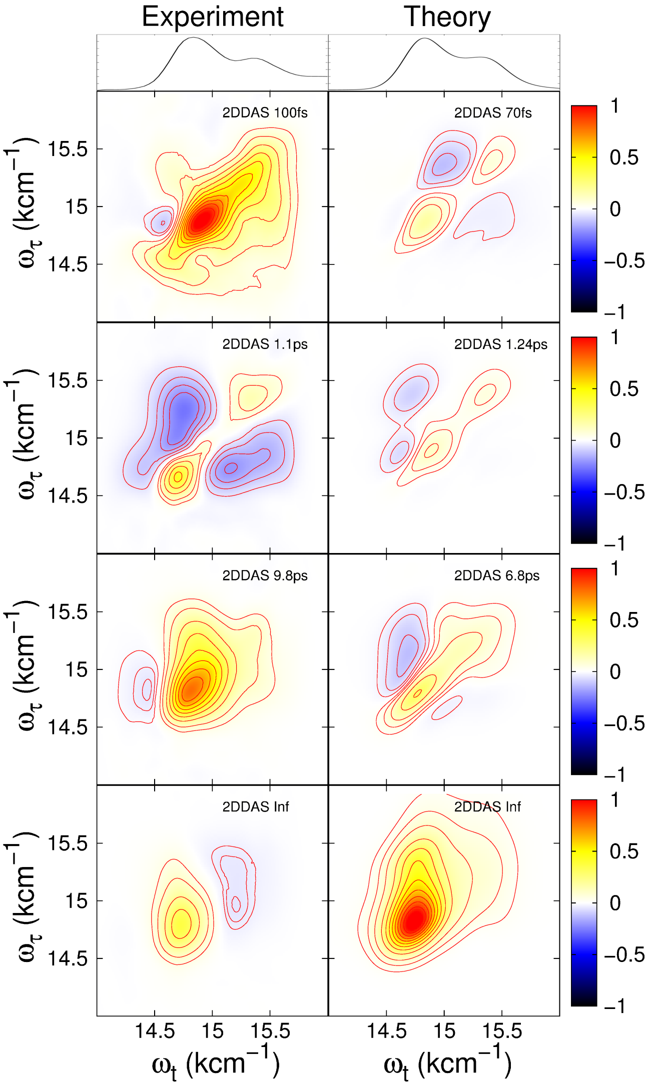

Figure 4.7: The experimental (left) and theoretical (right) lifetime components of the energy transport in LHCII by the global fitting analysis of 2DDAS.

We have not found a component with a lifetime 300 fs in neither the single nor the global fit analysis of the experimental data. Such a component was intensively discussed in several experimental papers [46]. It should be noted that in the performed separate conventional pump-probe experiment, this component was neither detected in the measured kinetics of our LHCII sample. However, the 2DDAS with the lifetime of 400 fs is resolved in our modeled 2D spectra (see Fig. 4.8). We would like to note that there is no direct link between transient spectroscopy and electronic 2D spectroscopy in terms of the observed spectra due to the difference in the measured signals and the dimensionality. Therefore, a direct comparison of the one-dimensional DAS obtained from the transient absorption and two-dimensional DAS retrieved from the 2D photon-echo spectroscopy experiments is not so straightforward, especially taking into account different excitation conditions. (Usually, a narrow excitation spectrum located at the blue side of the absorption spectrum is present in the pump-probe experiments, while a broad excitation spectrum is used covering a whole absorption Q_y band in the photon echo experiment reported here). However, if 2DPE spectroscopy is conducted under similar excitation conditions as the pump-probe experiment, i.e., with a narrow and blue-located excitation spectrum, the similarity in the retrieved DAS is much higher, but such conditions lead to loss of useful information which can be obtained from 2D spectroscopy (e.g., excitonic interaction visualized via cross-peaks). These excitation conditions were realized in the recently reported experiment

[50]. In particular, this difference in the excitation conditions can explain the absence of the 300 fs component in our experimental data.

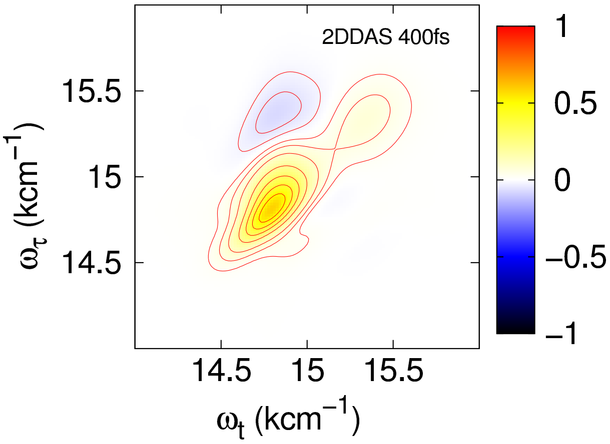

Figure 4.8: 2DDAS resolved 400 fs theoretical component. It is not in the found in the experimental data.

The overall energy transfer from the Chlb to the Chla pools is clearly resolved in the 2DDAS with the lifetime of 1.1 ps (see Fig. 4.7). Also, the corresponding Chla and Chlb diagonal peaks are fully separated and much better resolved in this decay-associated spectrum as compared to the 2D-spectra at different T as shown in Fig. 4.4. To illustrate this further, we show in Fig. 4.9 cuts along the horizontal axis through the 2DDAS. In particular, the viewgraph for the waiting time of 1.1 ps shows a section along $\omega_\tau = 15340$ cm^{-1} which belongs to the Chlb pool and whose 'butterfly' shape is similar to the decay-associated spectra in conventional time-resolved pump-probe spectroscopy. It reveals the "downhill" Chlb → Chla energy transfer, whereas

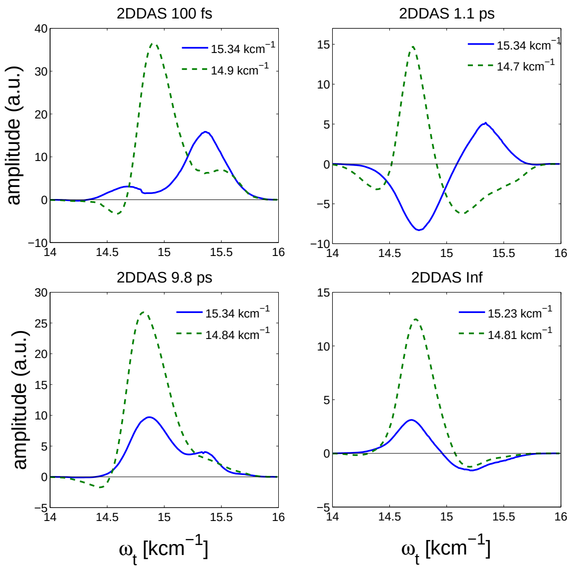

Figure 4.9: Lineshape of global fitting components for the 2DDAS.

the "uphill" Chla → Chlb transfer is observed in the cut along $\omega_\tau = 14700$ cm^{-1}. It crosses the diagonal peak associated with the Chla pool. For the given spectral split between the positive and the negative maximum (~ 400 cm^{-1}), the ratio of their amplitudes could be estimated on the basis of a Boltzmann distribution and yields 0.14. On the other hand, the observed ratio is 0.4. However, taking into account that in 2D spectroscopy the measured signal is proportional to the polarization rather than to the population as in the transient spectroscopy, this ratio has a reasonable magnitude ($\sqrt{0.14} = 0.38$). Hence, we can conclude that the overall shapes of the spectra are similar and the same energy transfer pathways are resolved. Moreover, the lifetimes in the 2DDAS retrieved from the experimental and from the calculated 2D spectra are similar, although the uphill energy transfer is not present in the calculated spectra.

The 2DDAS associated to the lifetime of 9.8 ps displays a significant cross peak C with a less populated diagonal peak B. The latter is associated with the exciton states corresponding to the Chlb pool. This cross peak is well resolved in the section of the 2DDAS at $\omega_\tau = 15340$ cm^{-1}. The shape of this 2DDAS does not show a signature of inhomogeneous broadening, and we thus can conclude that the inhomogeneous broadening in LHCII has diffusive character. Clearly, it has died out after $\sim$ 10 ps. The calculated 2DDAS with a similar lifetime ($\sim$ 7 ps) shows a strong elongation along the diagonal direction. This is associated with a strong inhomogeneous broadening even after $\sim$ 10 ps. This discrepancy between the measured and the calculated spectra is due to limitations in accounting for the inhomogeneous broadening while calculating the 2D spectra (see discussion in Theoretical Modeling). In particular, the effective inclusion of the inhomogeneous broadening via a convolution with a Gaussian distribution seems insufficient here. Therefore, the measured and the calculated 2DDAS cannot be directly compared for lifetimes longer then a few ps. This also holds for the shapes of the 2D spectra. In addition to the inhomogeneous broadening, the energy transfer between the exciton states located around $\omega_t = 14900$ cm^{-1} and the low-lying state(s) at 14500 cm^{-1} is also resolved in the 2DDAS associated to the lifetime of 9.8 ps, see the negative shoulder in the section at $\omega_t = 14840$cm^{-1} in Fig. 4.7. This allows us to conclude that there are two energy transfer pathways from the exciton states located around 14900 cm^{-1} to the low-lying "energy trap" states at the red shoulder of the absorption spectrum (14500-14600 cm^{-1}) with very different lifetimes of 100 fs and $\sim$ 10 ps.

4.4.3 Oscillations in the 2D spectra and their origin

The residuals of the experimental decay traces shown in Fig. 4.5 show several periodic oscillations within the first 2 ps of the delay time. A Fourier analysis of all residuals provides the 3D spectrum where the axes are ω_t, ω_τ and ω_T. Several 2D slices from this 3D spectrum taken at different frequencies ω_T overlap with the positions of the main diagonal peaks or the cross-peaks in the 2D spectra (see Fig. 4.10), but the overlap does not occur simultaneously. In addition, the spectral positions of the resolved "cross-peaks" with respect to the diagonal do not match the corresponding frequencies ω_T at which they are measured. Thus, we can conclude that the origin of these well-resolved peaks in the 3D spectrum has rather intramolecular character and involve vibrational states in the chromophores. This is in contrast to the interference beatings between excitonic states. In an additional analysis of the oscillations along the diagonal, we also were not able to attribute the resolved frequencies to particular excitonic states, as has been done in the 2D experiment at 77 K [48]. In fact, this is not surprising since almost all peaks associated with the oscillations of notable

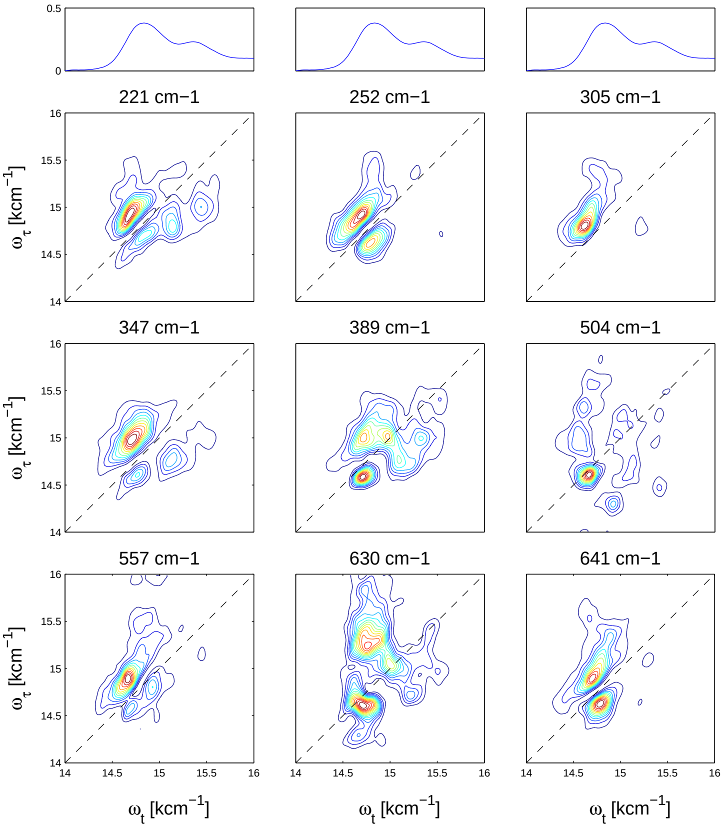

Figure 4.10: Two-dimensional spectra of the distribution of the oscillations in the residuals at different ω_T as indicated. The top row shows the measured absorption spectra of LHCII.

magnitudes are located away from our diagonal region (see Fig. 4.10).

To verify the origin of the oscillations observed in the 2D spectra, we have performed a cross-correlation analysis of the residuals across the diagonal $\omega_\tau = \omega_t$. In particular, we have calculated the correlation coefficients C between the residuals

R for each pair of conjugated spectral positions in the delay time window up to 2 ps. The delay time steps were equally distributed and the correlation coefficients are given as

$$C(\omega_t, \omega_\tau) = \mathrm{corr}\left[\mathrm{R}(\omega_\mathrm{t}, \omega_\tau, \mathrm{T}), \mathrm{R}(\omega_\tau, \omega_\mathrm{t}, \mathrm{T})\right] , \tag{4.8}$$

where corr evaluates the correlation with respect to T. This yields a correlation 2D spectrum which is plotted in Fig. 4.11. Negative values correspond to anticorrelated residuals, whereas positive values correspond to correlated residuals. We find strong correlations and anticorrelations between different areas of the 2D spectrum. Many cross-peaks can be resolved in this correlation spectrum and the positions of some of them are correlated with the Fourier-components in the 3D spectrum. In particular, peaks in the 630 cm^{-1} slice of the 3D spectrum overlap with the main correlated areas and the 252 cm^{-1} slice overlaps with the main anticorrelated areas (see Fig.4.10). The anticorrelated cross peaks in the correlation spectrum show that the oscillations contained in the corresponding residuals have opposite phases. According to the theoretical investigations in Ref. [70], this confirms the intramolecular or vibrational origin of these oscillations. There is only one area of positively correlated residuals around $\omega_t = 14700$ cm^{-1}, $\omega_\tau = 15200$ cm^{-1}. It can be associated with the beatings between excitonic states located within the Chlb and the Chla pools, especially when taking into account the 630-cm^{-1} oscillations in the residuals at these spectral positions. This is consistent with the Chlb-Chla spectral splitting.

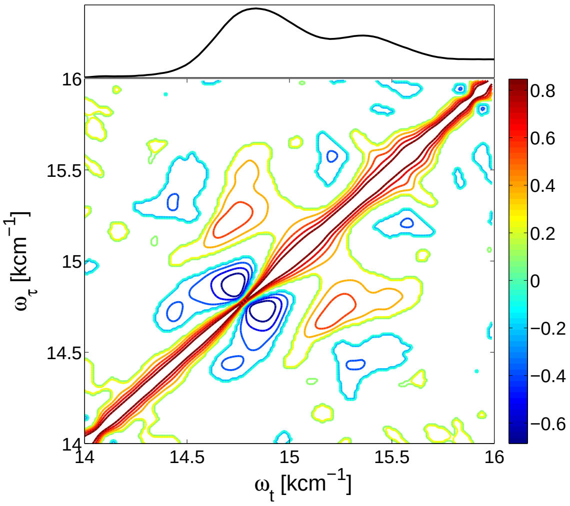

Figure 4.11: Correlation spectrum of residuals obtained after 3D global fitting of 2D-spectra. The color bar shows the magnitudes of correlation coefficients.

In our theoretical model, localized vibrational states of the chlorophylls were not included due to the exponential growth of the associated Hilbert space and the demanding size of the required computer hardware. Therefore, if oscillations appear in the sequence of the 2D spectra calculated within our model, they safely can be attributed only to beatings between exciton states. This clearly allows us to uniquely determine the origin of the oscillations observed in the experimental spectra. In the calculated 2D spectra, we find only strongly damped oscillations of small amplitudes within the initial waiting time window up to $\sim$ 200 fs for the spectral positions of the cross peaks C and D. The corresponding signals are shown in Fig. 4.12. Their underlying period can be estimated to $\sim$50 fs (ω_T=667 cm^{-1}). This frequency matches well the energy gap between the exciton transitions 14666 cm^{-1} and 15333 cm^{-1}. They belong to the Chla and the Chlb pools, respectively (see the stick spectrum in Fig. 4.3). Therefore, we can conclude that the 630-cm^{-1} oscillation observed in the experimental 2D spectra is associated with the beatings between exciton states, while all other resolved oscillations originate from the involved vibrational states of the chlorophylls. We cannot exclude that some of them could belong to vibronic states as well which would require a strong coupling between the electronic and the vibrational DOF. This plausible line of reasoning should be tested theoretically by explicitly including vibrational states to our model Hamiltonian and a subsequent dynamical description of the vibrational degrees of freedom in the corresponding calculations.

4.5 Conclusions

In this Chapter, we report the results of a broadband 2D electronic spectroscopic study of LHCII trimers at room temperature. Dephasing of the electronic excitation at room temperature is much faster as compared to low temperatures and occurs within a 60-fs range. Our data directly visualize the significant impact of strong inhomogeneous broadening in the LHCII. Equally important is the loss of inhomogeneity observed at longer waiting times. This allows us to conclude that the inhomogeneous broadening in the LHCII at room temperature has diffusive character and dies out after a few tens of ps. An analysis of the experimental data is given in terms of an

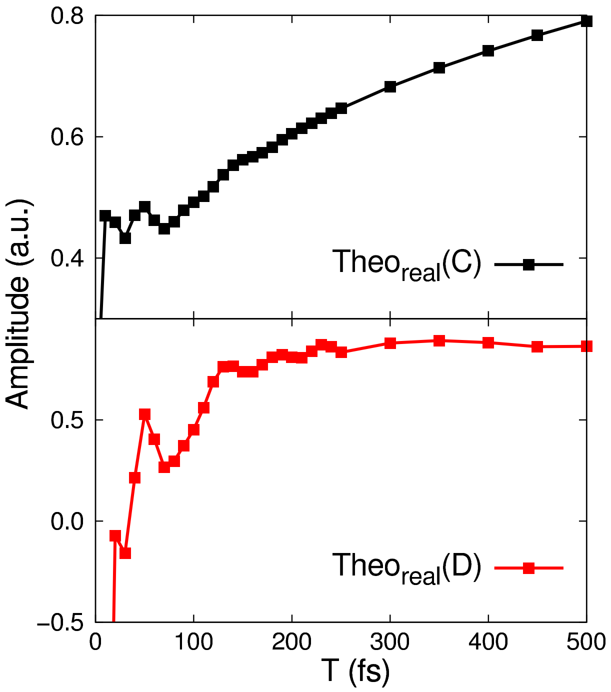

Figure 4.12: The time evolution of the cross peaks located at (ω_τ=14810 cm^{-1}, ω_t=15370 cm^{-1}). The estimated period is 50 fs (ω=667 cm^{-1}) according to the oscillation in the frequency range T=100 $\sim$ 250 fs.

exciton model of the LHCII-monomer and an explicit treatment of the dynamics.

The numerically calculated 2D spectra coincide with the experimentally measured ones in the range of waiting times of up to several ps. Together with the advanced global fit analysis, this relatively new spectroscopic technique allows us to reveal and literally visualize the energy transfer pathways of one of the most important light harvesting complexes of higher plants. Our analysis for ambient temperature conditions allows us to identify which of the channels, active at low temperatures, do contribute predominantly in the living species. We have safely resolved the energy transfer channels from the Chlb to the Chla pools in both the experimental and the modeled spectra. These transfer dynamics occur within 1.1 - 1.2 ps as retrieved from the 2D spectra. Moreover, the fastest 2DDAS with a lifetime of $\sim$ 100 fs can be attributed to the loss of coherence among excited exciton states. It also resolves the energy transfer pathway from the exciton states associated with the main absorption peak to the exciton states lying at its low-energy edge. The main diagonal peaks associated with the Chla and Chlb pools are resolved in the 2D spectra and even a cross peak between them is visible within a waiting time up to 1 ps. Yet, these peaks and cross peaks are much better visualized in the 2DDAS obtained after applying the multidimensional global fit to the sequence of 2D-spectra collected at different waiting times.

Besides resolving the energy transfer pathways and visualizing the diagonal as well as the cross peaks in the 2D spectra, also long-lasting oscillations in the kinetics of the coherence appear. The analysis of these oscillations and the cross correlations applied for the first time to 2D spectroscopy together with the comparison to the results of the numerical simulations show that almost all of them are associated with vibrational transitions of individual chlorophylls or corresponding vibronic states. Only one component of the oscillations with a frequency of $\sim$ 630 cm^{-1} can be attributed to the beatings between excitonic states located in the Chla and Chlb pools. The dephasing time of these oscillations can be estimated to be $\sim$ 100 fs (Fig. 8) which is consistent with the electronic dephasing in LHCII.

Despite some simplifications, our developed and carefully fitted exciton model matches well the linear spectra of the LHCII (both absorption and CD spectra). It properly simulates the 2D spectra on the basis of one set of model parameters. It is limited by a simplified accounting of the effects of the inhomogeneous broadening. By this, the calculated kinetics of the coherence deviates from the experimentally observed data for times greater than 2 ps where spectral diffusion begins to significantly affect the spectra.This leads to differences between the shapes and the lifetimes of some 2DDAS. Finally it should be mentioned that in additional computer simulations of simpler model systems, we have found that the proper accounting of the inhomogeneous broadening via an ensemble averaging of 2D spectra calculated with disordered site energies can lead to significant changes in retrieved lifetimes (up to a factor of 1.5 - 3) and in the shapes of the 2DDAS.

Chapter 5

Charge-separation dynamics in the PSII reaction center

In chapter, we study the charge transfer and separation process in the PSII reaction center. The 2D electronic spectra of the reaction center are measured and revealed spectral components with different lifetimes. On the basis of the theoretical investigation of a simple dimer model, the signature of charge separation can be well resolved with the assistance of a global fitting approach. Then, the vibrational modulation of the charge separation in the PSII reaction center is discussed.

5.1 Introduction

PSII is a unique biological system that is capable of collecting photon-excited energy and transferring it to the reaction center for the oxidation of water. PSII shows a rather complicated structure, containing chlorophyll-protein 43 (CP43), CP47 and branches 1 (D1) and 2 (D2) of the reaction centers. The peripheral complex, such as the LHCII, absorbs the sunlight energy and transfers it to the D1-D2 reaction center, where the initial charge separation occurs. The molecular structure of the PSII reaction center has been well resolved by X-ray crystallography [3, 4]. The D1, D2 branch of the reaction center contains eight pigments: two primary chlorophylls P_{D1} and P_{D2}, two accessory chlorophylls Chl_{D1} and Chl_{D2}, two pheophytins $Pheo_{D1}$ and $Pheo_{D2}$ and two peripheral chlorophylls $Chlz_{D1}$ and $Chlz_{D2}$. The simplified picture of the arrangement of the pigment molecules is presented in Fig. 5.1. Only the active D1 branch is responsible for the charge separation [5].

The importance of the PSII reaction center has been realized and thus, it has been extensively studied over several decades by almost all the available steady-state spectroscopic techniques, such as absorption, linear and circular dichroism and fluorescence spectroscopy [72, 73]. In order to resolve its biological function, namely the separation of charges, the primary charge separation of the D1/D2-cytb559 complex has been studied at low temperature by combining the photon-echo measurement with pump-probe spectroscopy [74]. Based on a theoretical modeling of the kinetics re-

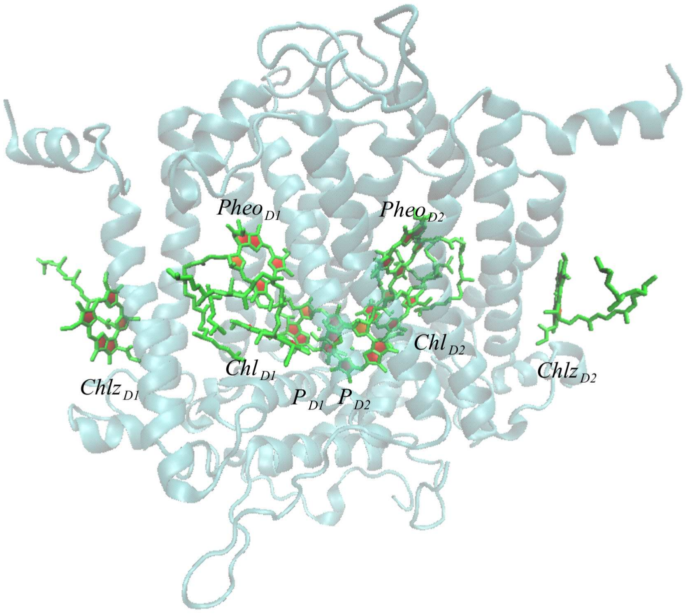

Figure 5.1: Pigment arrangement in PSII reaction center. The data are taken from 3ARC.pdb [71]. The VMD package [9] was used to generate the figure.

solved by pump-probe spectra, the primary charge separation timescale was retrieved to be 1.5 ps and the secondary charge separation process was estimated to occur within 25 ps. Moreover, the mechanism and kinetics of the electron transfer in the intact PSII core and the isolated D1/D2-cytb559 PSII reaction center have been investigated at low temperature as well by femtosecond transient absorption spectroscopy and analyzed by a decay-associated spectrum [75]. For the intact PSII reaction center, lifetime components of 5.5 ps and 35 ps were resolved as the timescales of the primary and the secondary charge separation, respectively. In addition, a long lifetime component (200 ps) was resolved and associated to the rate of the electron transfer from the cofactors to the Q_A acceptor. In the isolated reaction center, however, the primary and secondary charge separation were studied and revealed quite different rates (primary charge separation: 3 ps, secondary charge separation: 11 ps). In this study, the pigment Chl_{D1} was identified as the electron donor for the first charge separation process. The isolated PSII reaction center was measured again by transient absorption spectroscopic methods at 77 K with a larger spectral range (425 nm to 730 nm) and an extended time range (<3 ns) [76]. Multiply charge-separation pathways were identified with lifetimes, which differ from the former studies. For instance, the primary charge separation happens within sub-400 fs and 1.8 ps. The secondary charge separation process shows slower timescales (65 ps and 585 ps). Based on the theoretical modeling, the authors proposed that a huge static disorder acts on the CT state to induce multiple charge separation processes.

Among the techniques used, 2D electronic spectroscopy is a powerful tool which allows for direct mapping of excitation energy pathways and the coherent dynamics as a function of the optical absorption and emission wavelength [36]. This is particularly useful in examining the photosynthetic system in which the manifold of closely spaced electronic states and broadening through static disorder yields highly congested spectra. The first experimental 2D electronic spectroscopic study of the PSII reaction center complex at 77 K observed the energy transfer and charge separation process occurring with different timescales [77]. A new 2DDAS-resolved rapid lifetime (50-150 fs) was identified and proposed to be associated to fast down-hill energy transfer. Furthermore, the fast timescale component (sub-400 fs) was assumed to be associated to the rapid formation of a radical pair, $P_{D1}^{-}P_{D2}^{+}$. A mixed population transfer and charge separation component was resolved with timescales of 1-3 ps and 10-60 ps, respectively. The longest component (>2 ns) was resolved and proposed to correspond to the lifetime of CT states since it consistent with the transient absorption studies [76]. However, the authors did not provide any effective way to distinguish the energy transfer and charge separation process in 2DDAS-resolved lifetime components. Despite extensive studies have been done, the pathways and the corresponding timescales in the PSII reaction center still need to be clarified.

Due to the inconsistency of the experimental observations, it is still not entirely clear for the theoretical study of molecular identities of the functional states and the mechanistic and kinetic details of PSII reaction center. For instance, (i) which pigment is the electron donor and the acceptor which starts the primary charge separation? (ii) What are the pathways for the charge separation? Answering these questions allows to proceed how to model the charge separation dynamics and transport. In Ref. [74], the charge transfer process was modeled as the annihilation of the population of exciton states since the population is transferred to the dark CT state. Novoderezhkin and coworkers [78] found that one additional CT state is to be included in the model to simultaneously fit various kinds of linear and nonlinear spectra (steady-state absorption, linear dichroism, CD, steady-state fluorescence spectra, transient absorption with different excitation wavelengths, and time-resolved fluorescence). Due to the insensitivity of the linear spectroscopy to the CT state, the Stark spectra together with the spectra of the pheophytin-modified reaction center that lack one of the peripheral chlorophylls, were used for a quantitative fit. The site energies of the pigments and the first CT state were purified since the fluorescence and Stark spectra are more sensitive to the assignment of the primary CT state [79]. The absorption difference spectra were calculated and compared to measurements in Ref. [80] and the authors proposed that the D1-branch Chl_{D1} is likely to be the electron donor at cryogenic temperature but the electron transfer could start from both pigments, Chl_{D1} and P_{D1} at physiological temperature. Moreover, multiple CT states were needed to fit the transient absorption kinetics measured for the isolated reaction center of PSII at 77 K [81]. This revealed the multiple charge separation pathways with corresponding timescales: the ultrafast formation of a radical pair $P_{D2}^{+}P_{D1}^{-}$ and the initial charge separation of the electron donor and acceptor $(\mathrm{Chl_{D1}Pheo_{D1}})^{*} \rightarrow \mathrm{Chl_{D1}^{+}Pheo_{D1}^{-}}$ were retrieved with sub-ps timescale, and multiple pathways exist with a primary charge separation within ∼3 ps. The longest secondary charge separation results in populating the final radical pair with a time constant of 20 ps. In order to properly account for the Fermi property of the electron and the hole, a tight-binding model was applied to the study of the charge separation in the PSII reaction center and the corresponding 2D electronic spectra were calculated at 77K [22]. Furthermore, calculated results were used to examine the low-temperature kinetics in the PSII reaction center by comparing to measured data [82]. The analysis of the 2D spectra kinetics showed that the inclusion of the two electron transfer pathways helps to obtain an improved agreement with experimental data.

In order to identify the signature of the charge separation, first, we theoretically study a simple dimer model with one CT state. The charge-separation signature can be clearly identified by combining the 2D spectroscopy and 2DDAS technique. Then, we present the measured 2D electronic spectra of the PSII reaction center at physiological temperature. The theoretical model of the PSII reaction center is constructed and parametrized by fitting the temperature-dependent absorption (77 and 300 K) and CD spectra. Three decay-associated components with different lifetimes (200 fs, 1.5ps and 14 ps) are well resolved by a global fitting approach.

5.2 Sample preparation and measuring conditions

The sample was prepared by Dr. Emilie Wientjes and Prof. Roberta Croce at the University of Amsterdam according to the following procedure. Thylakoid membranes were isolated from A. thaliana plants as described in Ref. [83] till the centrifugation step at 6000 g. Thylakoid membranes were solubilized with 0.6% dodecyl-D-maltoside

(DDM) at a final chlorophyll concentration of 0.5 mg/ml. The sucrose density ultracentrifugation was used to obtain PSII core particles as described in Ref. [84]. The purification of the PSII reaction center from PSII core particles proceeds as follows: the PSII core particles were diluted in BTS200 buffer (20 mM Bis Tris pH 6.5, 20 mM MgCl2, 5 mM CaCl2, 10 mM MgSO4, 0.03% DDM, 0.2 M sucrose) to a chlorophyll concentration of 0.15 mg/ml and solubilized with an equal volume of 10% Triton X-100 in BTS200 buffer for 20 min; then the material was loaded on a HiTrap Q Sepharose HP 1 ml column (GE Healthcare) and washed with a BTS buffer until the eluate became colorless. Finally, the PSII RC particles were eluted from the column with 75 mM MgSO4 in a BTS200 buffer.

2D electronic spectroscopy in the regime of visible light is well established [36]. As in previously reported experiments [85], in order to suppress the excitation of high-lying vibrational states of chlorophylls and pheophytines, the spectrum of the excitation laser pulses is explicitly restricted to the spectral region $630 - 720$ nm.

Directly before measurements, the RC-sample was filtered using a 0.2-μm micropore filter and placed into a 0.8-mm thick closed cell with the inner volume of 2 mL, mounted onto a precise home-build X-Y motorized translator allowing a continuous changing of the excitation spot position. The spot size of all beams at the sample position was $\sim 60\mu$m. For minimizing unwanted of non-resonant response to the photon echo signal, the input cell window was made from a 150μm fused silica cover slip. To ensure annihilation-free excitation conditions, the energy of the laser pulses was kept below 5 nJ (except of the local oscillator beam which was attenuated with a neutral-density filter by a factor of 100).

The heterodyne-detected photon echo spectra were collected at each fixed waiting time T by scanning the τ delay in a range of $[-100, +150]$ fs, with a delay time step of 1 fs. At each delay point, $320 - 440$ spectra were averaged (depending on T) to achieve a high SNR. The waiting time T was linearly scaled within the first 2 ps delay and then logarithmically spaced up to 80 ps. The measured data were processed according to the procedure described in detail in Ref. [85]. The 2D global analysis [69] of the series of 2D spectra was performed using 4 life times and starting from a $T = 25$ fs delay. The 2D measurement was carried out by Dr. Valentyn I. Prokhorenko at the University of Toronto.

5.3 Predicted signature of the charge separation

Energy transfer and charge separation revealed by a dimer model. We describe the 2DDAS-resolved signature of the energy transfer and charge separation based on a simple model. First, based on the global fitting approach, the sequence of 2D spectra can be decomposed by a sum of exponential components: the amplitude spectrum $A_i(\omega_\tau, \omega_t)$ indicates the kinetics of the 2D spectra along the waiting time, as described in chapter 2. Second, we choose a dimer model composed of monomer

A and B with site energies $\epsilon_1 = 270$ cm^{-1} and $\epsilon_2 = 210$ cm^{-1}, respectively. The excitonic coupling between the two monomers is set to be $J = 150$ cm^{-1}. The bath parameters are obtained from the model of the PSII reaction center. The 2D spectra of the dimer were calculated for a time up to 5 ps and analyzed by the global analysis. One component with a lifetime of 60 fs is revealed and a second component with a infinite lifetime results. Both are shown in Fig. 5.2(a). On the basis of this simple dimer model, we have clear evidence of the energy transfer in the first amplitude spectrum (60 fs): one diagonal positive peak located at 400 cm^{-1} and two negative cross peaks (up-left: $\omega_t = 0$ cm^{-1}, $\omega_\tau = 400$ cm^{-1}. lower-right: $\omega_t = 400$ cm^{-1}, $\omega_\tau = 0$ cm^{-1}). It indicates that, in the 2D spectra, the magnitude of the diagonal peak at $\omega_t = \omega_\tau = 400$ cm^{-1} follows an exponential decay with a corresponding time constant of 60 fs. For the same reason, the magnitudes of the upper-left and the lower-right cross peaks follow an exponential increase with the same time constant. Moreover, the upper-left cross peak shows a much stronger increase than the lower-right part, which clearly manifests the ratio of down-hill and up-hill energy transfer between two excitonic states in the 2D map.

In order to study the charge transfer dynamics, one additional CT state (A^+B^-) has been included in the dimer model and we calculate the 2D spectra again within 5 ps. The site energy of the charge transfer state is set to be 150 cm^{-1} and the interaction with monomer A and B are set to the same value of 45 cm^{-1}. The

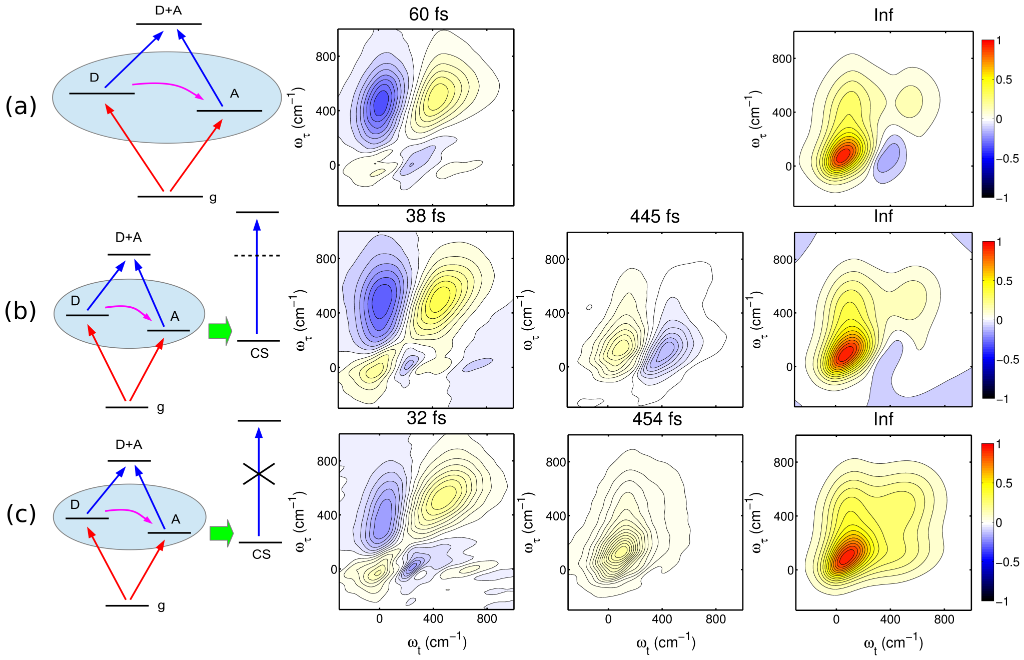

Figure 5.2: 2D spectra (T=0 fs) and 2DDAS resolved lifetime components of a simple dimer model. (a) shows the case of the excitonic dimer without the CT state. (b) is the case of the dimer with one additional CT state $A^{+}B^{-}$. (c) is the dimer model with one CT state, but the double excited block is artificially excluded.

2DDAS-resolved lifetime components are shown in Fig. 5.2(b). It clearly shows one additional component (445 fs) besides the typical energy transfer (38 fs) and the 'Inf' component. It shows a positive peak and a negative peak located at the two sides of the diagonal. The position of the negative peak is $\omega_t = 400$ cm^{-1}, $\omega_\tau = 100$ cm^{-1}, which is the same position as the location of the excited state absorption in the 2D spectrum (it is shown in the first column of Fig. 5.2). It indicates that the magnitude of the excited states absorption increases along the waiting time. It can be reasonably explained by the shift of the excited state absorption peak, which is induced by the interaction of the permanent dipole of the CT states. In order to support this picture, we investigate the dimer model with the CT state, however, in absence of the double excited state. The resulting calculated 2D spectrum (T=0 fs) and 2DDAS resolved lifetime components are shown in Fig. 5.2(c). We clearly observe one component with a comparable lifetime (454 fs) and find the same characteristics of the signature of charge separation in Fig. 5.2(c), but without the negative peak. This confirms the explanation of the 2DDAS-resolved charge-separation signature.

Based on the current dimer model, the signature of the energy transfer and the charge separation can be clearly resolved by the 2DDAS with different timescales. It clarifies that the charge-separation process leads to the strong shift of the charge-transfer-related double excited states in the dimer model, which cannot be revealed in the simple FE model.

In order to study the multiple charge separation processes, we calculate the kinetics and the 2D electronic spectra of a tetramer model. In this model, 4 charge-transfer-coupled pigments are selected with two CT states: (a) realizes the primary charge separation of donor and acceptor $(\mathrm{Chl_{D1}Pheo_{D1}})^* \rightarrow \mathrm{Chl_{D1}^{+}Pheo_{D1}^{-}}$ and (b) models the secondary charge separation $\mathrm{Chl_{D1}^{+}Pheo_{D1}^{-}} \rightarrow \mathrm{P_{D1}^{+}Pheo_{D1}^{-}}$. First, the kinetics of the CT states was calculated with an initial population distributed according to their transition dipole strength. The transfer process has been fitted yielding two time constants: the primary transfer occurs with 250 fs, and the secondary transfer with 5.0 ps.

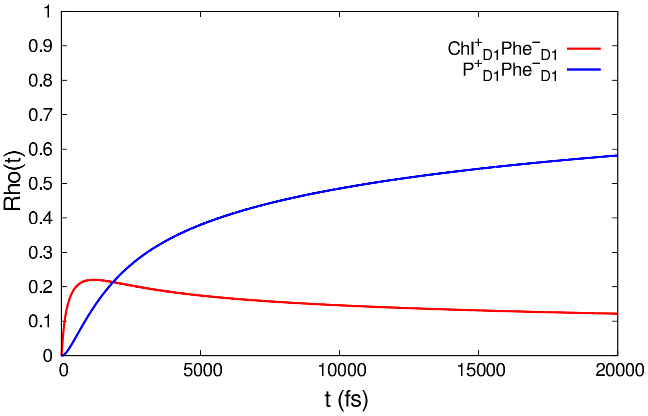

Figure 5.3: Kinetics of the CT states $\mathrm{Chl}^+_{\mathrm{D1}}\mathrm{Pheo}^-_{\mathrm{D1}}$ and $\mathrm{P}^+_{\mathrm{D1}}\mathrm{Pheo}^-_{\mathrm{D1}}$ calculated by the reduced tetramer model. The transfer process has been analyzed and the time constants of 250 fs (red) and 5.0 ps (blue).

Multiply charge transfer pathways revealed by tetramer model. After the dynamical calculation, the 2D electronic spectra of the tetramer model are calculated as well and the 2DDAS-resolved components with the different lifetime have been generated. Two charge transfer components (500 fs, 5.1 ps) are clearly resolved as shown in Fig. 5.4. The secondary charge separation process (5.1 ps) yields a time constant which agrees with that obtained from the dynamical calculation. The primary charge transfer component (500 fs) shows a difference from the dynamically calculated result (250 fs) since it is strongly disturbed by the fast dephasing component (60 fs). Here, this demonstrates that the multiple charge separation processes can be well resolved by the combination of the 2D spectroscopy and the 2DDAS technique.

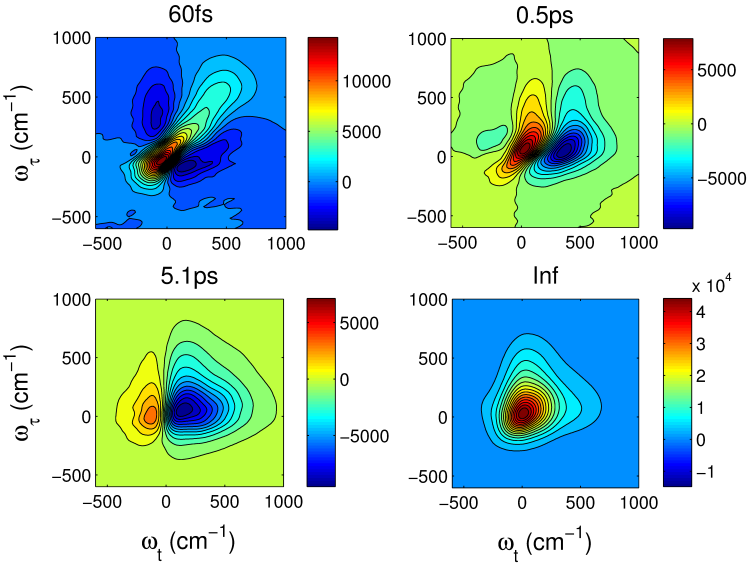

Figure 5.4: Multiple pathways of the charge separation revealed by the tetramer model with two CT states. Two charge separation components of 0.5 ps and 5.1 ps are resolved by the global fitting approach.

5.4 Energy transfer and charge separation in the PSII reaction center

Having formulated the expected signature of the charge separation on the basis of the simpler dimer and tetramer models, we next turn to the full analysis of the charge separation dynamics in the full model of reaction center. For this, we present a 2D spectroscopic study of the PSII reaction center at physiological temperature, which reflects the nature of the charge separation and the transfer process which happens in daily life. The energy transfer, charge separation and CT states are modeled within a tight-binding model, which is described in Chapter 1. Four primary CT states are taken from Ref. [81]: $\mathrm{P}_{\mathrm{D2}}^{+}\mathrm{P}_{\mathrm{D1}}^{-}$, $\mathrm{Chl}_{\mathrm{D1}}^{+}\mathrm{Pheo}_{\mathrm{D1}}^{-}$, $\mathrm{P}_{\mathrm{D1}}^{+}\mathrm{Chl}_{\mathrm{D1}}^{-}$ and $\mathrm{P}_{\mathrm{D1}}^{+}\mathrm{Pheo}_{\mathrm{D1}}^{-}$, which were resolved by fitting the kinetics of the transient absorption measurements. We need to specify the elements of the single excitation Hamiltonian. First, the Coulomb interaction terms J_{m^*,n^*} between two FE states were calculated by the TrESP method [80]. The Dexter-type exchange component was properly included in the interaction term between P_{D1} and P_{D2}. We use those parameters without any modifications. Second, the initial site energies of the FE states ϵ_{m^*} are taken from Ref. [79]. Besides, these site energies were further optimized by the simultaneous fit of the linear spectra (absorption and CD) at different temperatures (77 and 300 K). Third, the initial value of site energies of CT states and the corresponding interaction of FE–CT, CT–CT states was obtained from Ref. [81]. There, the site energies of the CT states were optimized by simultaneously fitting of the charge-sensitive time-resolved fluorescence and Stark spectra [79]. The interaction constants between the FE and CT, CT and CT were determined by fitting the kinetics of the transient absorption with different wavelength excitations.

For the system-bath interaction, the parameters of the Ohmic spectral density $J(\omega) = \gamma\omega e^{-\omega/\omega_c}$ were fit by assuming three artificial spectral densities, thereby using Eq. (15) of Ref. [66]. This approach significantly speeds up the numerical calculations. The quantum dynamical calculations were performed using the TNL method [66, 67]. Inhomogeneous broadening is generated by low frequency nuclear motion and static disorder. In this work, we have accounted for inhomogeneous broadening by an ensemble average over Gaussian-distributed site energies with width of 110 cm^{-1} for the FE states and 200 cm^{-1} for the CT states. In particular, to account for the spatially correlated disorder and the fluctuations of the CT states, the Cholesky decomposition scheme was used to generate the cross-correlated heat baths and static disorder [86]. The dipole strengths and orientations of the chromophores were taken from the direction of NA–NC atom on the pigments (3ARC.pdb). In particular, the relative strengths of the transition dipole moments of the chlorophylls and pheophytin molecules were set to $|\mu_{Chl}| = 1.0$ and $|\mu_{Pheo}| = 0.773$, respectively.

To verify the parameters, we have calculated the linear absorption and CD spectra,

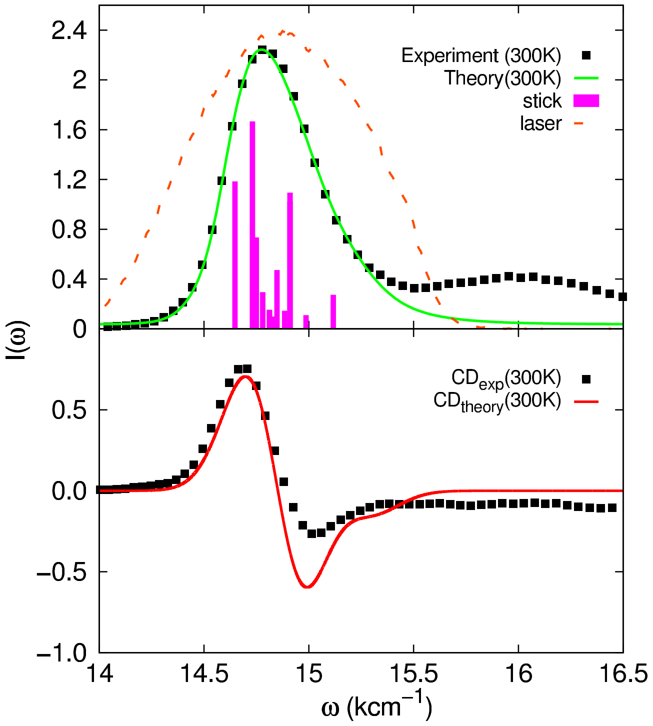

Figure 5.5: The experimental and associated theoretical absorption and CD spectra at 300 K.

and compare them to the experimental ones. To achieve the optimal fit both for the absorption and CD spectra, the site energies of the FE states, CT states and also the coupling terms of FE–CT and CT–CT need to be optimized. In Fig. 5.5, we show the absorption and CD spectra calculated at 300 K, together with the experimentally measured spectra. The calculated stick spectra are presented as well. In order to calculate the 2D electronic spectrum, we apply the EOM-PMA [87]. Therefore, all the parameters used for the final 2D spectral calculation are: site energies, $\epsilon_{\mathrm{P_{D1}}} = 14950$

cm^{-1}, $\epsilon_{\mathrm{P_{D2}}} = 14890$ cm^{-1}, $\epsilon_{\mathrm{Chl_{D1}}} = 14700$ cm^{-1}, $\epsilon_{\mathrm{Chl_{D2}}} = 14840$ cm^{-1}, $\epsilon_{\mathrm{Pheo_{D1}}} = 14835$ cm^{-1}, $\epsilon_{\mathrm{Pheo_{D2}}} = 14760$ cm^{-1}, $\epsilon_{\mathrm{Chlz_{D1}}} = 14910$ cm^{-1}, $\epsilon_{\mathrm{Pheo_{D2}}} = 14910$ cm^{-1} and CT states $\epsilon_{\mathrm{P^-_{D1}P^+_{D2}}} = 14840$ cm^{-1}, $\epsilon_{\mathrm{Chl^+_{D1}Pheo^-_{D2}}} = 14680$ cm^{-1}, $\epsilon_{\mathrm{P^+_{D1}Chl^-_{D1}}} = 14600$ cm^{-1}, $\epsilon_{\mathrm{P^+_{D1}Pheo^-_{D1}}} = 14180$ cm^{-1}. The parameters for the Ohmic spectral density are set to, $\gamma = 0.68$ and $\omega_c = 350$ cm^{-1}.

Dephasing and inhomogeneous broadening. In Fig. 5.6, representative experimental 2D electronic spectra of the reaction center are shown (left column) for different waiting times, T=0 fs, 100 fs, 500 fs and 1 ps. The corresponding theoretical calculations are presented as well in the right column, calculated for the same waiting times. Both results show good agreement. At the initial waiting time, the 2D spectra are significantly stretched along the diagonal direction which indicates strong inhomogeneous broadening present in the PSII reaction center. The anti-diagonal cross section in the 2D spectrum is related to the homogeneous line broadening, which is determined by fast electronic dephasing. Moreover, two negative-amplitude cross peaks appear at initial time which indicate the double excited states absorptions. They disappear very fast (<50 fs). At T=1 ps, there is no evidence of the inhomogeneous broadening and a similar bandwidth along the diagonal and the anti-diagonal cross section appears.

Charge separation revealed by the calculation of the population dynamics. The kinetics of the charge separation are calculated based on our theoret-

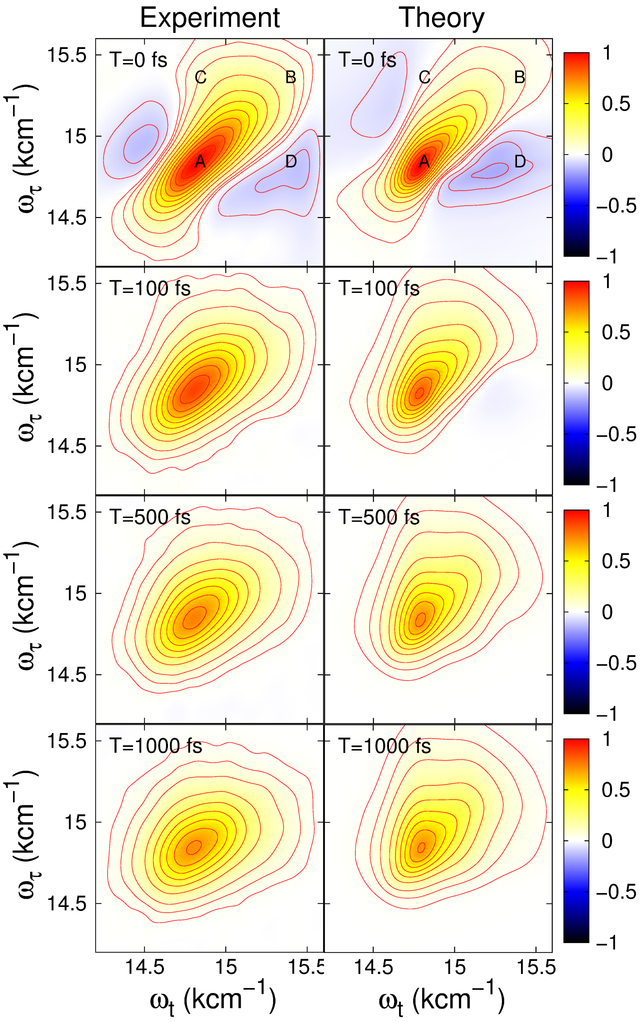

Figure 5.6: Real part of the experimental (left) and theoretical (right) 2D photon echo spectra of the PSII reaction center at different waiting times. The theoretical result is calculated with the model parameters obtained by simultaneously fitting the linear absorption and CD spectra. The diagonal and cross peaks are labeled by capital letters in frame T=0 fs.

ical model and plotted in Fig. 5.7. For the first calculation, the initial population is assumed to be equally located at the two peripheral chlorophylls $Chlz_{D1/D2}$ since they are close to the core antenna complexes CP43 and CP47. It is shown at top of the Fig. 5.7. We observe that at short time, the initial charge separation follows the order as: $\mathrm{Chl}^{+}_{\mathrm{D1}}\mathrm{Pheo}^{-}_{\mathrm{D1}}$, $\mathrm{P}^{+}_{\mathrm{D1}}\mathrm{Pheo}^{-}_{\mathrm{D1}}$, $\mathrm{P}^{+}_{\mathrm{D1}}\mathrm{Chl}^{-}_{\mathrm{D1}}$ and $\mathrm{P}^{-}_{\mathrm{D2}}\mathrm{P}^{+}_{\mathrm{D1}}$. The first starting CT state $\mathrm{Chl}^{+}_{\mathrm{D1}}\mathrm{Pheo}^{-}_{\mathrm{D1}}$ is mainly caused by the lowest FE state $\mathrm{Chl}_{\mathrm{D1}}$, which trap the excitons for the initial charge separation. After that, other two CT states $\mathrm{P}^{+}_{\mathrm{D1}}\mathrm{Pheo}^{-}_{\mathrm{D1}}$ and $\mathrm{P}^{+}_{\mathrm{D1}}\mathrm{Chl}^{-}_{\mathrm{D1}}$, which relate to the pigment $\mathrm{Chl}_{\mathrm{D1}}$, start to become populated. $\mathrm{P}^{+}_{\mathrm{D2}}\mathrm{P}^{-}_{\mathrm{D1}}$ is the last state for the initial charge separation.

It is important to realize that the charge-separation process revealed by the above population dynamics is quite different from the one revealed by the 2D spectroscopic study. The reason is that the excitation mechanisms are different. In the 2D experiment, a finite population of all pigments is generated simultaneously by the broadband laser pulse. In the present work, we have used a bandwidth from 14000 cm^{-1} to 15500 cm^{-1}. This can be roughly simulated by assigning an initial population to each pigment according to the magnitude of its transition dipole strength. The corresponding dynamics is calculated and presented at bottom of the Fig. 5.7. The population of each CT state is analyzed and the associated rates are shown in the figure.

Charge separation versus energy transfer. The kinetics and the associated lifetimes can be resolved by applying a multidimensional global fit approach to the series of consecutive 2D spectra acquired at different waiting times. The procedure for a global fitting of frequency- and time-resolved data is applicable only when the dynamics is not dispersive, i.e., when the lifetimes do not significantly depend on the wavelengths and the frequencies. To validate the applicability of the global fitting to our experimental PSII reaction center 2D data, we have independently fitted each decay trace in the set of the 2D spectra which contains about 28561 traces. We have found that the retrieved lifetimes can be classified into three clearly distinguishable groups with quite narrow distributions of lifetimes, except for the shortest component. The quality of the 3D global fits can be inspected by comparing the experimental and the fitted decay traces.

The experimental 2D data of the PSII reaction center are analyzed in terms of 2DDAS. The lifetime components are shown in the left column of Fig. 5.8. Three different lifetimes (132 fs, 1.5 ps and 13.9 ps) are extracted from the global fitting. In order to properly interpret the experiment, the theoretical lifetime components (148 fs and 1.98 ps) also resolved with 2DDAS by fitting the collection of the calculated 2D spectra with different waiting times. Before analyzing the decay associated lifetime components, we need to clarify the output of the information from the amplitude spectrum $A_i(\omega_\tau, \omega_t)$ of the 2DDAS. A positive peak in amplitude spectrum indicates an exponential decay along the waiting time T with the resolved time constant τ_i. In contrast, a negative peak denotes an exponential growth along the waiting time with the time constant τ_i.

For the shortest experimental lifetime component – 132 fs, a broadband positive peak located at $\omega_t = \omega_\tau = 14800$ cm^{-1} along the diagonal direction is formed, which is associated to fast electronic dephasing. In addition, a negative cross peak ($\omega_t = 14700$ cm^{-1}, $\omega_\tau = 15000$ cm^{-1}) indicates the increase of amplitude in that region, which is a typical signature of the energy transfer as revealed by using the simple dimer model described in Sec. 5.3. The comparably shortest lifetime component of 148 fs is resolved in the calculated 2D spectra. It shows a positive peak located on the diagonal ($\omega_t = \omega_\tau = 14800$ cm^{-1}), which indicates fast electronic dephasing. However, two negative cross peaks are shown in the amplitude spectrum. One fast energy transfer component is revealed as the energy transfer signature ($\omega_t = 14800$ cm^{-1}, $\omega_\tau = 15000$ cm^{-1}). In addition, the other component of charge separation is uncovered by the lower-right cross peak ($\omega_t = 15200$ cm^{-1}, $\omega_\tau = 14800$ cm^{-1}). Its meaning is clarified by comparing the 2D spectra calculated with the dimer model plus one additional CT state as done in Sec 5.3. In contrast to the experiment, the fastest theoretical component is associated to the mixing signature of electronic dephasing, fast energy transfer and charge separation. This charge-separation component can be associated to the rapid formation of the CT state $(\mathrm{P_{D1}P_{D2}})^* \rightarrow \mathrm{P_{D1}^{+}P_{D2}^{-}}$ since it agrees with the charge-separation rate of $\mathrm{P_{D1}^{+}P_{D2}^{-}}$ resolved by dynamical calculations. In Sec. 5.3, we have demonstrated the coincidence of the rates revealed by the dynamical calculation and the 2DDAS-resolved rate of the tetramer model. The absence of this charge separation in the current room-temperature measurement may be due to the interruption of noise or fast electronic dephasing. A charge-separation component (1.5 ps) is well resolved in the experimental part. The theoretical calculation shows a quantitative agreement with the experiment with 2DDAS. The lifetime of 1.98 ps is resolved by the 2DDAS. This lifetime component fits well with the rate of the primary charge separation between the electron donor and acceptor ($(\mathrm{Chl}_{\mathrm{D1}}\mathrm{Pheo}_{\mathrm{D1}})^* \rightarrow \mathrm{Chl}^+_{\mathrm{D1}}\mathrm{Pheo}^-_{\mathrm{D1}}$) predicted by the dynamical calculation. In contrast, the 2D experiment at 77K [77] resolved the component of a mixture of energy transfer and charge separation with a timescale of 1$\sim$3 ps. This may be caused by the different temperature or by the impossibility to effectively distinguish the energy transfer and the charge separation component. Moreover, a well-resolved component with a time constant of 13.9 ps is shown in Fig. 5.8(a) with only one positive diagonal peak located at $\omega_t = \omega_\tau = 14800$ cm^{-1}. It is not revealed by the theoretical counterpart since only short waiting times (<6 ps) are calculated, which is not enough to resolve the 14 ps lifetime component. It does not show any feature of an energy transfer or charge separation, in contrast to the shorter 2DDAS components. We assume that this lifetime component is associated with the slow energy transport from the two peripheral chlorophylls ($\mathrm{Chlz}_{\mathrm{D1}}$ and $\mathrm{Chlz}_{\mathrm{D2}}$) to the central cofactors since the electronic couplings are small due to the large distance.

$$
\begin{aligned}
&(\mathrm{Chl_{D1}Pheo_{D1}})^{*}\textcolor{red}{\rightarrow}\mathrm{Chl_{D1}^{+}Pheo_{D1}^{-}}\textcolor{blue}{\rightarrow}\mathrm{P_{D1}^{+}Pheo_{D1}^{-}},\\
&(\mathrm{P_{D1}P_{D2}})^{*}\textcolor{red}{\rightarrow}\mathrm{P_{D2}^{+}P_{D1}^{-}}\textcolor{blue}{\rightarrow}\mathrm{P_{D1}^{+}Chl_{D1}^{-}}\textcolor{blue}{\rightarrow}\mathrm{P_{D1}^{+}Pheo_{D1}^{-}}.
\end{aligned}
\tag{5.1}
$$

Here, we did not resolve any long-lifetime component associated to the secondary charge separation, which is indicated by the blue arrows in Eq. 5.1. The charge-separation process $\mathrm{P_{D2}^{+}P_{D1}^{-}} \rightarrow \mathrm{P_{D1}^{+}Chl_{D1}^{-}}$ is not well resolved in the measured data since the contribution of this CT pathway is small due to the relatively high site energy of the $\mathrm{P_{D2}^{+}P_{D1}^{-}}$-state in the current model. It is well described in the calculated results shown at the bottom of Fig. 5.7.

It is possible to resolve any long lifetime component associated to the secondary charge separation, which is denoted by the blue arrows in Eq. (5.1). One reason is that the secondary charge separation takes longer and exceeds the waiting-time window we have addressed. In this experiment, we have measured the 2D spectra up to ~ 80 ps, and it appears still shorter than the timescale of the secondary charge separation. In Ref. [76], the PSII reaction center has been measured up to 3 ns, with the result that the secondary charge separation takes up to 65 ps or even 585 ps. Both timescales are hard to resolve with a collection of 2D spectra up to 80 ps and 2DDAS technique from the presently available data.

Oscillations in 2D spectra and their origin. In Fig. 5.9, long-lived oscillations are clearly visible in the selected diagonal (A and B) and off-diagonal peaks (C and

D) of the measured 2D spectra. Interestingly enough, this indicates evidence of quantum coherence. However, it is still under debate that it belongs to the electronic or vibrational coherence [88, 89]. In the present work, we do not find any strong oscillations of the off-diagonal peaks in our simulated 2D electronic spectra, in which we did not include a vibrational mode. This points to a vibrational origin of the observed coherent oscillations. Recently, the vibronic coherence was observed in the PSII reaction center at cryogenic temperature and it has been well explained [90, 91] by a strong vibrational coupling.

In this chapter, the dynamics of the charge transfer has been studied by the 2D electronic spectroscopy. The pathways and corresponding timescales of the energy and the charge transfer have been resolved by the global fitting approach. Based on the simple dimer model, the charge transfer signature was identified by the DAS. Moreover, this signature with a time constant 1.5 ps was observed from the DAS, which is retrieved from the measured 2D spectra of the PSII reaction center. To our knowledge, this is the first time of directly revealing the charge-transfer signature from the reaction center. In Ref. [77], the 2D spectra of the reaction center have been measured at cryogenic temperature and the timescales of energy and charge transfer have been resolved. However, the direct evidence to distinguish the charge separation from energy transfer has still be missing.

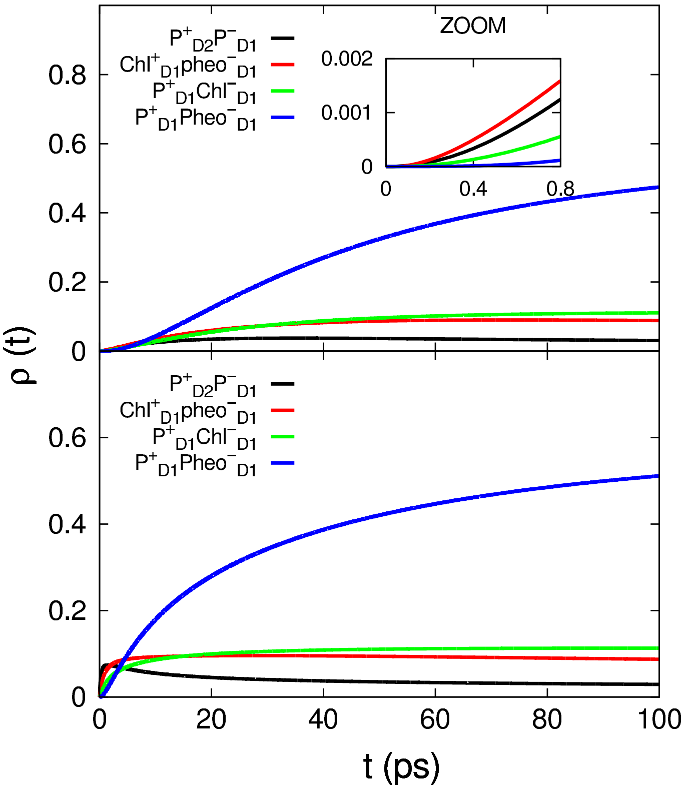

Figure 5.7: Top: population dynamics of the CT states within 100 ps. The initial population is assumed to be located at two peripheral chlorophylls $\mathrm{Chlz}_{\mathrm{D1/D2}}$ with equal probability of 1/2. The initial time window of 800 fs has been magnified in the inset. Bottom: dynamics calculated with initially distributed population according to the transition dipole strength of each pigment, which is used to mimic the 2D broadband excitation in the experiment. The transfer rates are fitted and yield $\mathrm{P}^+_{\mathrm{D2}}\mathrm{P}^-_{\mathrm{D1}}$: 238 fs, $\mathrm{Chl}^+_{\mathrm{D1}}\mathrm{Pheo}^-_{\mathrm{D1}}$: 1.84 ps, $\mathrm{P}^+_{\mathrm{D1}}\mathrm{Chl}^-_{\mathrm{D1}}$: 9.0 ps, $\mathrm{P}^+_{\mathrm{D1}}\mathrm{Pheo}^-_{\mathrm{D1}}$: 51 ps. The strength of static disorder was obtained from the fit of the absorption and CD spectra. The results were calculated by averaging 500 samples.

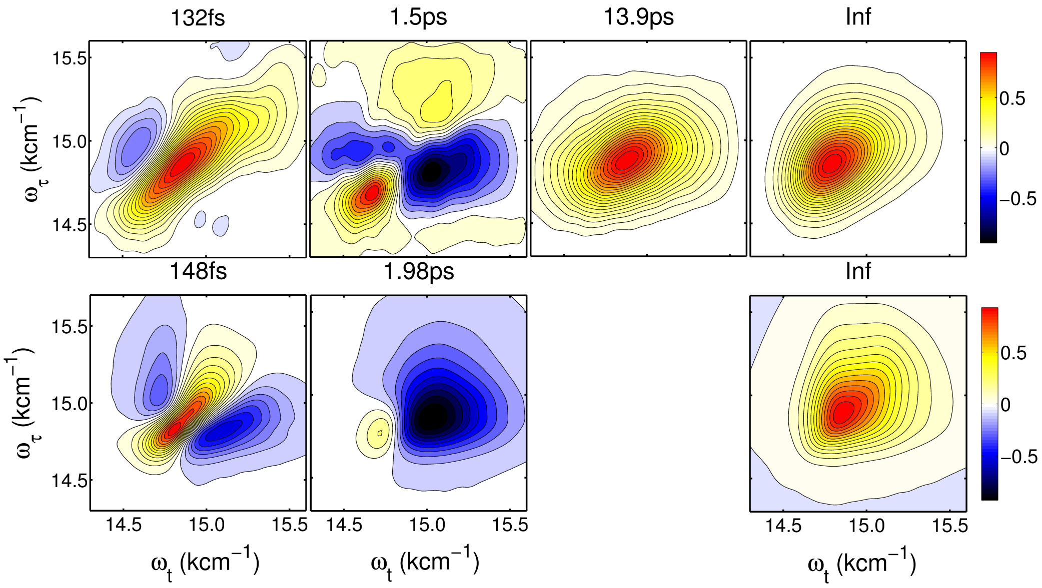

Figure 5.8: Experimental (top) and theoretical (bottom) DAS resolved by the global analysis of the time sequence of the 2D electronic spectra of the PSII reaction center. Note: one time component 13.9 ps can not be produced by theoretical calculation since the limitation of the computer hardware, all the calculations of 2D spectra are ended within the waiting time of 6 ps.

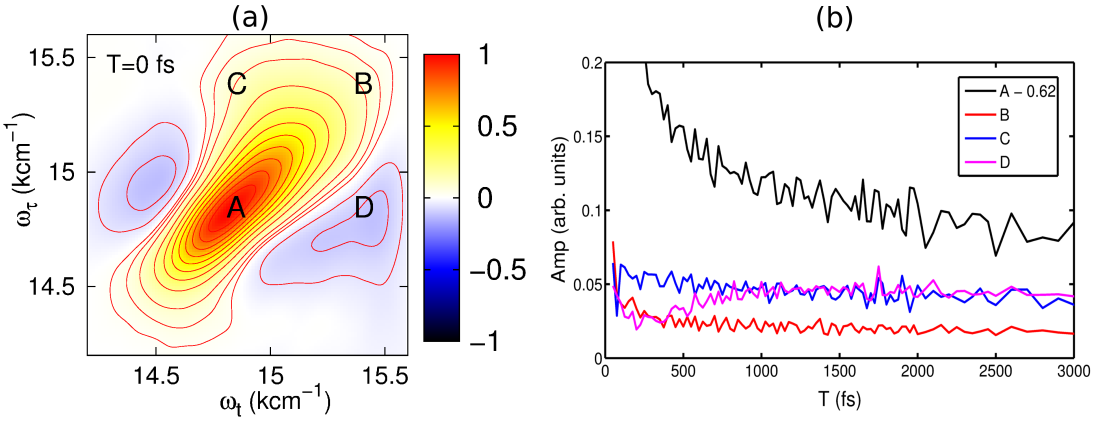

Figure 5.9: Time-dependent populations (b) of the selected peaks in the 2D electronic spectrum (a) at T=0 fs. Long-lived vibrational coherence can be seen in the traces of selected peaks.

Chapter 6

Quantum coherence in the Fenna-Matthews-Olson complex

In the last two chapters, the energy transfer in the LHCII and the charge separation in the PSII reaction center have been studied by 2D electronic spectroscopy. In this chapter, I report the study of the energy transport in a particular simple type of PPC, the Fenna-Matthews-Olson complex at room temperature. Its principal features were described in Chapter 1. Here, the process of energy transfer is analyzed by the global fitting approach. The retrieved lifetime components show timescales from hundreds of femtoseconds to tens of picoseconds. The subsequent theoretical model shows good agreement with the experimental results. More important, based on the contribution of experiment and theory, the retrieved timescale of the electronic coherence is found to be within ~ 60 fs, which is even shorter than the fastest energy-transfer component. This clearly manifests that, at room temperature, the electronic coherence is hardly to play any functional role in the process of energy transfer in PPCs.

6.1 Introduction

The FMO complex of *Prosthecochloris aestuari* was the first PPC for which the structure was determined by X-ray crystallography [92]. Since its discovery, the resolution of the electron density map has been refined down to 1.9 Å [93] and the structure of the FMO complex of the closely related bacterium *Chlorobium tepidum* has been determined as well [94, 95]. The two structures are very similar, but interestingly, the spectra look different. The molecular origin of this difference is still unknown. The structure of the FMO complex consists of a trimer, formed by three identical monomers of which each contains eight Bchl a. The molecular structure of the trimeric FMO complex (extracted from *Chlorobium tepidum*) is shown in Fig. 6.1.

The FMO trimer complex mediates the exciton energy from the antenna complex and the chlorosomes to the reaction center in the green sulfur bacteria [96]. Due to the structural simplicity, the FMO PPC has been extensively studied by various kinds of spectroscopies [97, 98]. In recent years, the ultrafast optical 2D spectroscopic approach was first extended to the visible range [57] and evidence of the electronic couplings between the pigments in FMO complex has been provided directly by the

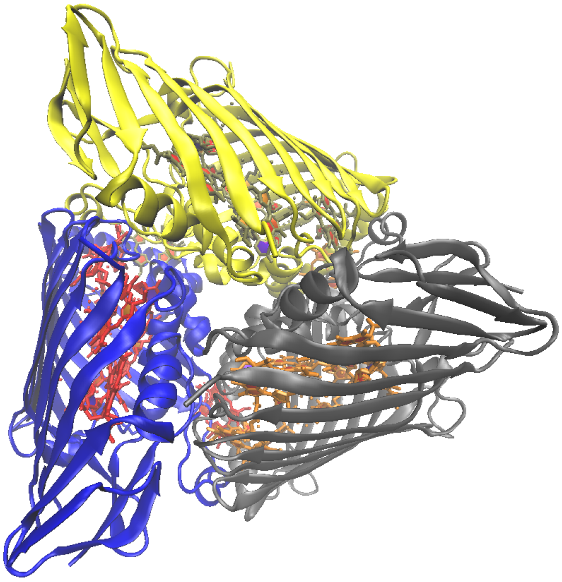

Figure 6.1: Pigment arrangement of Bchl a in the trimeric FMO complex of *C. tepdium*. Eight pigments are included in each monomer. The structure is generated from 3ENI.pdb [8] by using VMD package [9].

observation of the off-diagonal peaks in the 2D spectra [58]. Moreover, the exciton energy transfer has been investigated with higher temporal resolution. The oscillatory beatings observed in the off-diagonal signals of 2D optical spectra have been reported to survive for longer than 600 fs at cryogenic temperature (77 K) [99]. They were interpreted as the signature of long-lived electronic quantum coherent exciton dynamics in the FMO network. The same conclusion was drawn also from an experiment at higher temperature up to 277 K [100], and similar beatings have been reported for marine cryptophyte algae as well [101]. These experiments have triggered an enormous interest in a potential new field of "quantum biology" [2, 102, 103, 104, 105], with far reaching consequences even for the functionality of the human brain [106] and for technological applications [107]. The cornerstone experiments [99, 100, 101] were repeated to identify the excitonic energy transfer pathways [108] at 77 K. However, observation of long-lived electronic coherence in the 2D off-diagonal signals was even not mentioned in Ref. [108].

Theoretical simulations play an important role in interpreting the experimental observations. The electronic couplings of the pigments in the FMO complex were calculated by using quantum chemistry method [55]. With these parameters, Ishizaki *et al.* calculated the energy transfer dynamics in the FMO complex using the exciton model. The lifetime of electronic coherence agreed with those reported in experiments [109], but the used value of the reorganization energy [110] is clearly too small. 2D electronic spectra have been calculated using the HEOM approach, with the result that the oscillations are much weaker than the experimental observations [111]. The dynamics of the exciton transfer has been calculated with the numerically exact QUAPI method. It was found that the coherent oscillations are shorter than those in the experimental observations [112]. To fit the experiment, the long-lived vibrational coherence has been considered as a resource to enhance and prolong the electronic coherence, especially in the resonant case [88, 113, 114]. However, an atomic model was subsequently used to investigate the corresponding excitonic dynamics in FMO complex. In this approach, no evidence of long-lived quantum electronic coherence was observed by the calculation of the population dynamics under the spectral density obtained from a quantum mechanics/molecular mechanics (QM/MM) approach [115]. Based on the experimental and theoretical studies, clear evidence to support the long-lived electronic coherence in the FMO complex is still missing, especially at physiological temperature.

6.2 Materials and methods

Experimental setup. All the reported measurements were performed using the 2D setup, which was described in the third Chapter and built by the author of this thesis. Ultrafast light pulses were generated by a home-built NOPA. It was tuned to the near infrared spectrum and centered at 800nm. The broadband spectrum was compressed by using the combination of grating, prism pair and a deformable mirror as described. The pulse duration has been reduced to 16 fs, which was characterized by FROG. The energy of the excitation pulse was controlled by a neutral density filter (OD=1.0) and limited to 10-15 nJ for each beam at the sample position.

Sample preparation and measurement condition. The FMO sample was prepared in the laboratory of Prof. Richard Cogdell (University of Glasgow, UK). The FMO trimers were isolated from green sulfur bacteria (*C. tepidum*), dissolved in a Tris (PH=8.0) buffer, and stored at −80 °C. Before the measurement, the sample was filtered in order to reduce unwanted scattering, which significantly affects the 2D spectral measurements. The absorption spectrum was measured using an Avantes mini lamp in a 1mm cell and the result is shown in the left of Fig. 6.2. In order to check the linearity of the photon excitation, the relation between the exciton energy and the PE signal has been measured and is shown in the right part of Fig. 6.2. It clearly shows the linear relation between $\mathrm{PE}^{1/3}$ and the excitation energy when the excitation energy is below 15 nJ. The sample was provided by Dr. Khuram Ashraf and Prof. Richard Cogdell at the University of Glasgow, UK.

6.3 Theoretical modeling

We consider a molecular model of the FMO monomer described by the Hamiltonian H_{mol} consisting of seven chlorophylls in a quantum two-level approximation. Recently, the eighth pigment was found in the FMO complex. However, it is located far away from the other seven pigments and it is likely that this pigment is lost in the majority of the complexes during the isolation procedure [108, 116]. Thus, it is viable to restrict to seven sites. Moreover, we only consider the monomer due to principle limitations in computer hardware. The total transition dipole operator $\boldsymbol{\mu}$ of the molecule is coupled to the semiclassical electric field $\boldsymbol{E}(t)$ of the laser pulse, which results in the

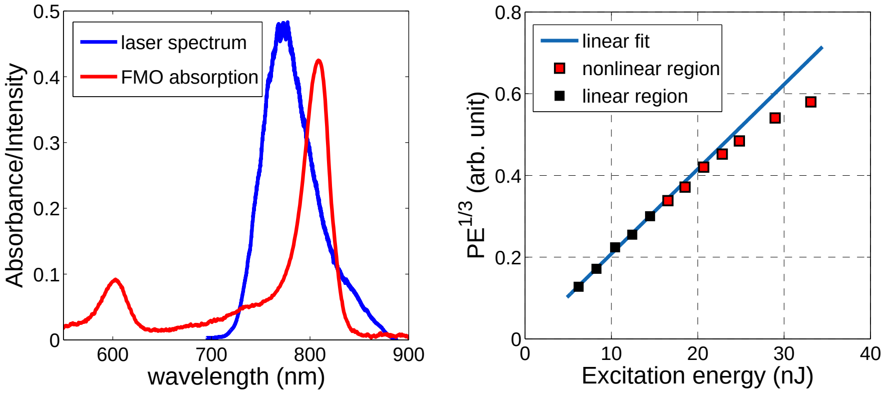

Figure 6.2: Left: measured linear absorption spectrum of the FMO trimer *C. tepidum* (red line) with the excitation laser spectrum (blue line). Right: The dependence of the homodyne PE signal on the excitation energy. To distinguish the nonlinear region of the excitation, a linear fit was applied to the measured data to confirm the linear dependence of PE∼E^3 upto the excitation energy of 15 nJ.

time-dependent Hamiltonian

$$H(t) = H_{mol} - \boldsymbol{\mu} \cdot \mathbf{E}(t)\,. \tag{6.1}$$

The total dipole operator is expressed via the transition dipole moments of individual molecules $\boldsymbol{\mu}_m$ according to

$$\boldsymbol{\mu} = \sum_{m=1}^{N} \boldsymbol{\mu}_m \left(\alpha_m + \alpha_m^\dagger\right), \tag{6.2}$$

with α_m and $\alpha_m^\dagger$ being the creation and annihilation operators of the electronic excitation on the mth molecule. The molecular Hamiltonian H_{mol} is given by

$$H_{mol} = H_e + H_{ph} + H_{e-ph}. \tag{6.3}$$

Here, the Frenkel Hamiltonian H_e describes the electronic DOF, and is given by

$$H_e = \sum_{m=1}^{N} \epsilon_m \alpha_m^\dagger \alpha_m + \sum_{m=1}^{N} \sum_{n<m} J_{n,m} \left(\alpha_m^\dagger \alpha_n + \alpha_n^\dagger \alpha_m \right) ,$$

where ϵ_m are the site transition energies of the molecules, and $J_{n,m}$ is the intermolecular excitonic coupling. H_{ph} describes the nuclear (phonon) DOF. We consider a continuous distribution of phonon modes which can be modeled as a bath of harmonic oscillators. In our model, we assume that the electronic excitation on the mth molecule couples independently to its own harmonic bath given by

$$H_{ph} = \sum_{m=1}^{N} \sum_{j=1}^{N_b^m} \left(\frac{P_{mj}^2}{2} + \frac{1}{2} \omega_{mj} x_{mj}^2 \right) . \tag{6.4}$$

Here, N_b^m is the number of bath modes which couple to the molecule m, x_{mj} and p_{mj} are the mass-weighted position and momentum of jth harmonic oscillator mode with the frequency ω_{mj}. The system-bath spectral density has the form

$$J_m(\omega) = \frac{\pi}{2} \sum_{j=1}^{N_b^m} \frac{c_{mj}^2}{\omega_{mj}} \delta \left(\omega - \omega_{mj} \right) . \tag{6.5}$$

As usual, we assume a continuous distribution of the frequencies of the bath modes for $N_b^m \to \infty$ and, in particular, we assume an Ohmic spectral density with parameters carefully determined from experimental data, see below. The electron-phonon coupling H_{e-ph} is assumed to cause only fluctuations of the electronic energy and is independent for each molecule, such that

$$H_{e-ph} = \sum_{m=1}^{N} \sum_{j=1}^{N_b^m} c_{mj} x_{mj} \alpha_m^\dagger \alpha_m \, . \tag{6.6}$$

For the parametrization of the model, the site energies ϵ_m and the electronic couplings $J_{n,m}$ are obtained from Ref. [55]. We keep the electronic coupling elements as constant without further modifications and use the site energies as the starting point for the calculations. The site energies are further optimized according to the fitting of the absorption and CD spectrum at different temperatures. To fit the absorption and CD spectra simultaneously, we optimize the parameters of the site energies and the inhomogeneous broadening, which accounts for the static disorder with a Gaussian distribution (FWHM 90 cm^{-1} except site 3). In order to obtain a converged result, 500 spectra are calculated for the disorder average. We found that it is necessary to reduce the static disorder of site 3 (FWHM 54 cm^{-1}) to fit the absorption peak of 12150 cm^{-1} at 77 K. The low-temperature calculations are shown in Fig. 6.3(a). The transition dipole orientation are taken from PDB file (3ENI) [8] and the strength are all assumed as equal to 1. In Fig. 6.3(b), we calculated the absorption and CD spectrum at room temperature and compare to the measured spectra. Both show excellent agreement. To fit the vibrational progression in the absorption spectrum, we add one broadband underdamped vibrational mode in the spectral density besides the continuous form of the Ohmic spectral density and the spectral density has the form

$$J(\omega) = \gamma w e^{-\omega/\omega_c} + \frac{2}{\pi} S \Omega^3 \frac{\omega \Gamma}{(\Omega^2 - \omega^2)^2 + \omega^2 \Gamma^2}, \tag{6.7}$$

with the parameters $\gamma = 0.7$, $\omega_c = 350$ cm^{-1}, $S = 0.12$, $\Omega = 900$ cm^{-1} and $\Gamma = 700$ cm^{-1}. The details of the spectral density are shown in Fig. 6.4.

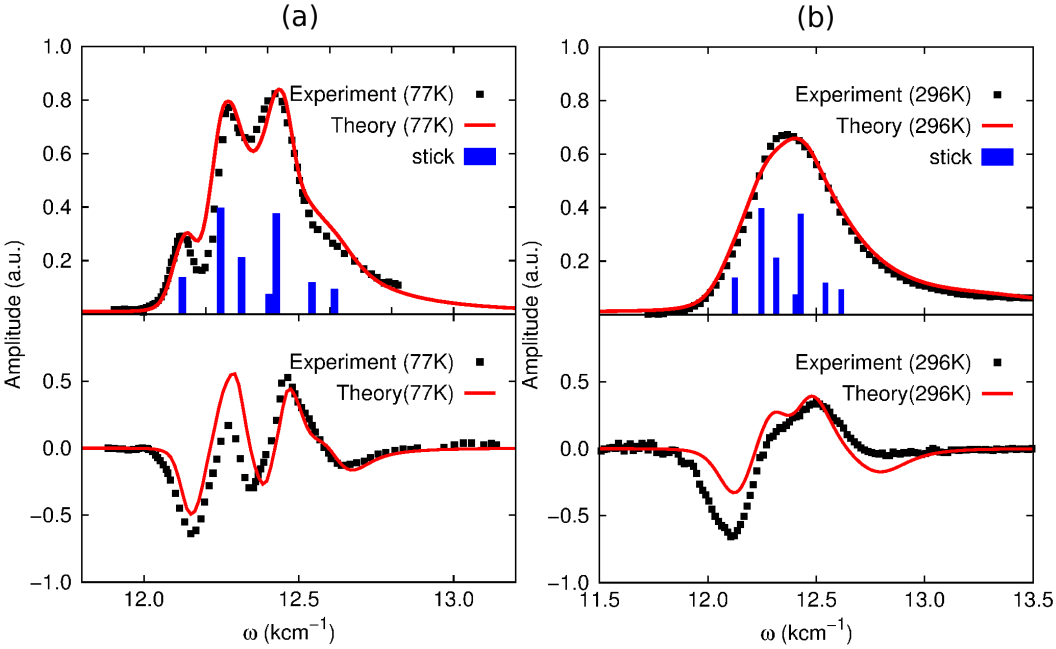

Figure 6.3: Experimental (square dots) and theoretical (red line) absorption and CD spectra of FMO complex. The spectra measured and calculated at 77 K (a) and 296 K (b). The experimental data in (a) are taken from Ref. [117]. For all four cases, the same parameters are used.

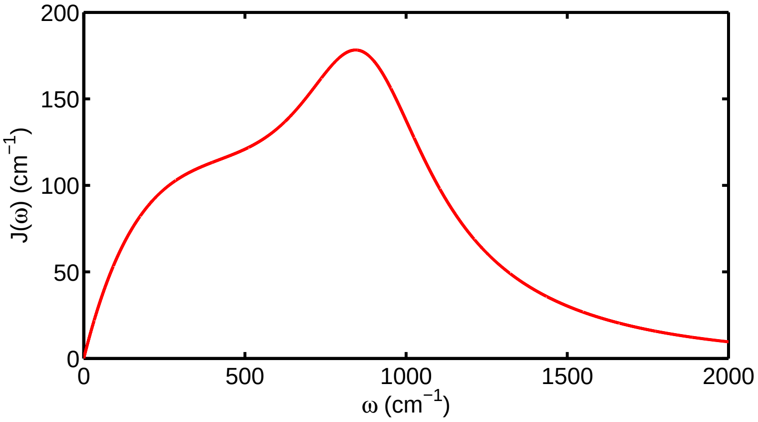

Figure 6.4: The spectral density used for the modeling of the FMO complex. One additional broadband peak is included to fit the vibrational progression in the absorption spectrum.

6.4 Energy flow in the FMO complex

We calculated the 2D photon echo spectra of the FMO complex and compare them to the experimental data for different waiting times in Fig. 6.5. We find good agreement between theory and experiment. At initial waiting time, the spectrum is significantly stretched along the diagonal which manifests rather strong inhomogeneous broadening in the FMO complex. With longer waiting time, the inhomogeneous broadening decays rapidly and is hard to be observed at T=1000 fs. Furthermore, the magnitude of the off-diagonal peaks on the up-left part of the 2D spectra increased during the evolution of the waiting time. The spectrum becomes strongly elongated along the

ω_τ coordinate. It indicates the energy transfer of pigments inside the FMO complex. Moreover, the long progressions from the central peak ($\omega_\tau = \omega_t = 12400$ cm^{-1}) to ($\omega_\tau = 13500$ cm^{-1}, $\omega_t = 12400$ cm^{-1}) manifests the vibrational relaxation of the localized vibrational modes of the chlorophylls. In addition, we clearly observe the decay of the central peak during the waiting time which is induced by thermal relaxation.

The energy transfer pathways and the associated timescales can be resolved by applying the global fitting approach to the series of consecutive 2D spectra with different waiting times. We construct the three dimensional data and fit by four exponential functions with different decay times, which is illustrated in Eq. 2.52. On the left part of Fig. 6.6, the DAS from the measured data show four different timescales of the energy transfer. The shortest one, 90 fs, shows one positive diagonal peak located at (12500 cm^{-1}) and one strong negative off-diagonal peak at ($\omega_\tau = 12500$ cm^{-1}, $\omega_t = 12000$ cm^{-1}). It clearly shows the evidence of the energy transfer from the chlorophylls with high site energy (12500 cm^{-1}) to the lower ones (12000 cm^{-1}). It is interesting to point out that the theoretical calculation of the shortest component shows the exactly same features and the timescale (90 fs) with higher resolution. The second component (750 fs) of the measured data shows a similar character as the first one but with somewhat boarder peaks. It indicates the second energy transfer pathways from the higher site-energy pigments to the lower ones with longer transfer

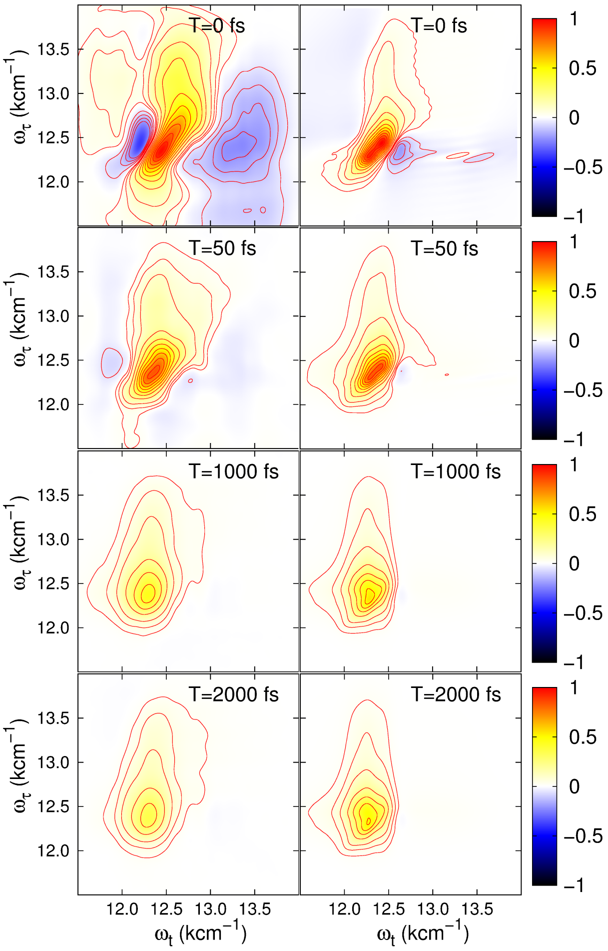

Figure 6.5: Real part of the experimental (left) and theoretical (right) 2D photon echo spectra of the FMO complex at different waiting times. The theoretical parameters are obtained from the fitting of the linear absorption and CD spectrum.

times. Theoretical calculations predict the same feature, however, with narrower peaks. The third and fourth DAS only show one diagonal peak at the central position 12200 cm^{-1} with a rather broad band, which indicates thermal relaxation of the pigments inside the FMO complexes. The DAS from our model also shows the same features with slightly different decay times of 6 ps. Hence, our model works well to fit the experimental 2D electronic spectra and the 2DDAS based on one set of parameters.

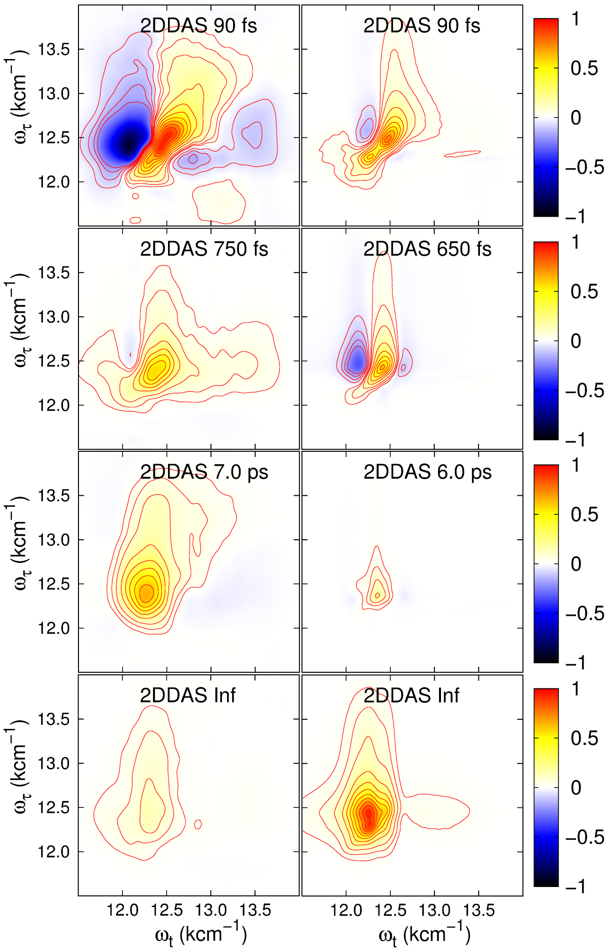

Figure 6.6: Experimental (left) and theoretical (right) decay-associated spectra. They show clearly four different time components for the energy transfers.

6.5 Oscillations in the 2D spectra and their origin

The residuals of the 2D spectra show oscillations within the first 2 ps. A Fourier analysis of all residuals provides the 3D spectrum of the vibrational maps. To verify the origin of the oscillations in the 2D spectra, we have performed a cross-correlation analysis of residuals across the diagonal $\omega_\tau = \omega_t$. We calculated the correlation coefficients C between the residuals R for each pair of conjugated spectral positions in the delay time window up to 2 ps, where the correlation coefficients are calculated as

$$C(\omega_t, \omega_\tau) = \mathrm{corr}(\mathrm{R}(\omega_\mathrm{t}, \omega_\tau, \mathrm{T}), \mathrm{R}(\omega_\tau, \omega_\mathrm{t}, \mathrm{T})). \tag{6.8}$$

This yields a correlation 2D spectrum, which is plotted in Fig. 6.7. Negative peaks indicate anticorrelated residuals and positive ones correspond to correlated residuals. We find strong correlations and anticorrelations of different areas in the correlation map. We know that all the pigments of the FMO complex have energies in the frequency region 12000∼12600 cm^{-1}. In this frequency range, two strong negative peaks are found in the correlation map. Based on Ref. [118], this shows that the oscillations in this region are related to the vibrational coherence. Moreover, we clearly observe two negative peaks located at 12400 cm^{-1} and 13300 cm^{-1}, which are related to the localized vibrational modes of bacteriochlorophylls in the FMO. This is rationalized by the vibrational progression in the absorption spectrum of Fig. 6.3.

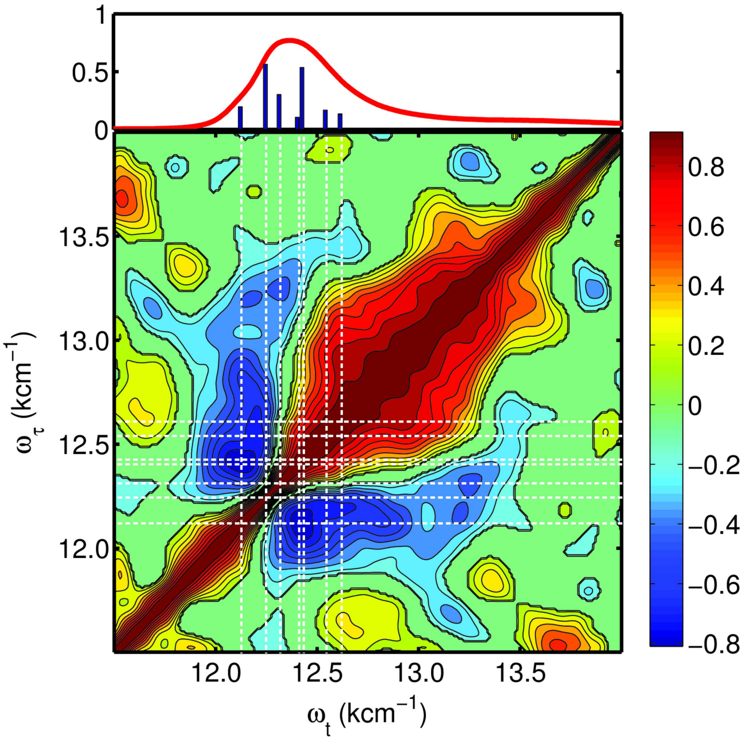

Figure 6.7: Correlation map of residuals obtained after subtracting the kinetics obtained by global fitting. White dots indicate the energy eigenvalues of the FMO Hamiltonian.

In our model, we didn't include the localized vibrational states of the bacteriochlorophyll due to the limitation of computational resource. However, in our modeling, any calculated oscillations originate from the beatings of the electronic coupling between excitons. This clearly allows us to uniquely determine the origin of the oscillations observed in the experimental spectra. In the calculated 2D spectra, we find the strongest oscillation position at the off-diagonal peaks located at 12300 cm^{-1} and

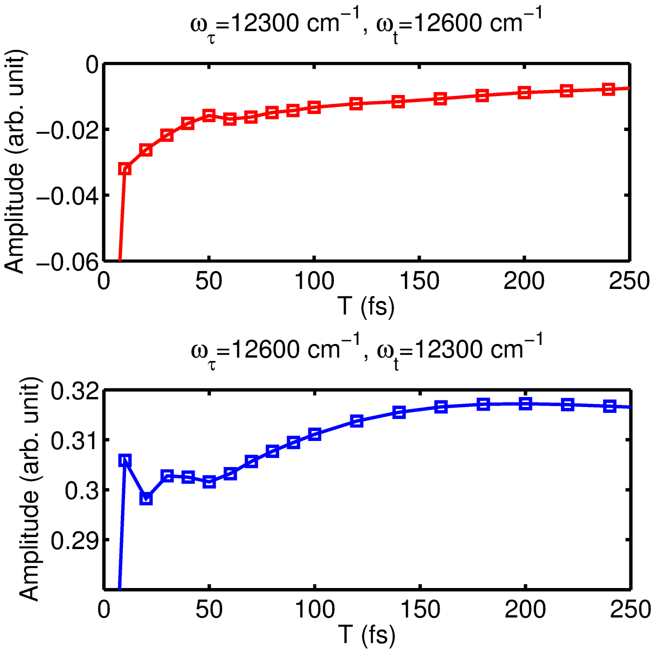

Figure 6.8: Evolution of the cross peak (real part) from the calculated spectra. The two peaks are located at the positions ω_τ=12300 cm^{-1}, ω_t=12600 cm^{-1} and ω_τ=12600 cm^{-1}, ω_t=12300 cm^{-1}, respectively. It shows that electronic coherence only survive for ∼80 fs.

12600 cm^{-1} and indicates electronic coherence within 80 fs. The trace of these two positions are shown in Fig. 6.8.

For a better comparison with previous works [100], we extracted the trace at same the position as the measured 2D spectra and plotted in Fig. 6.9. We did not observe any large-magnitude oscillations with features of electronic coherence. We observe the oscillations in real and imaginary parts with small magnitude and high frequency.

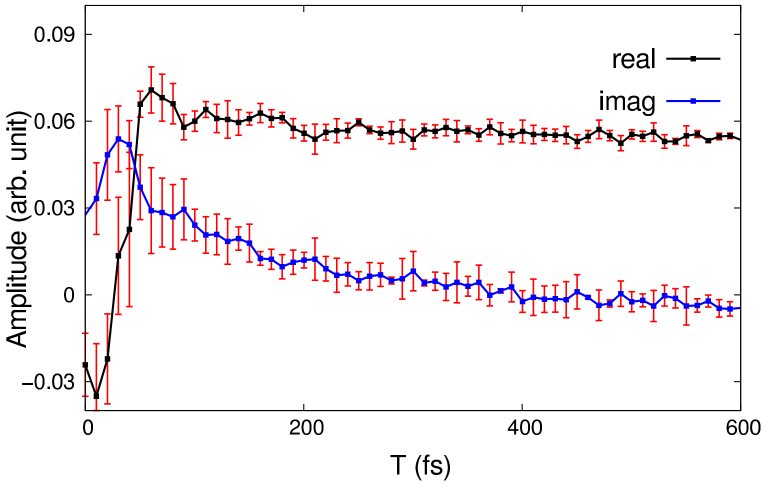

Figure 6.9: The real, imaginary and absolute value of trace at ($\omega_\tau = 12350$ cm^{-1}, ω_t=12200 cm^{-1}) from experimental 2D spectra. No long-lived electronic coherence are observed at 296 K. The error bars are obtained from averaging the experimental data over 4 data sets.

It clearly shows features of vibrational coherence.

6.6 Exciton dynamics at low temperature

In order to check the performance of the modeling and the reliability of the approach, we consider in this section the impact of varying the temperature, but keeping all other parameters unchanged. For this, we have calculated the linear absorption and CD spectra at 77 K. The calculated results are shown in Fig. 6.3 (red solid lines) together with the experimentally measured data taken from Refs. [58, 108]. We find

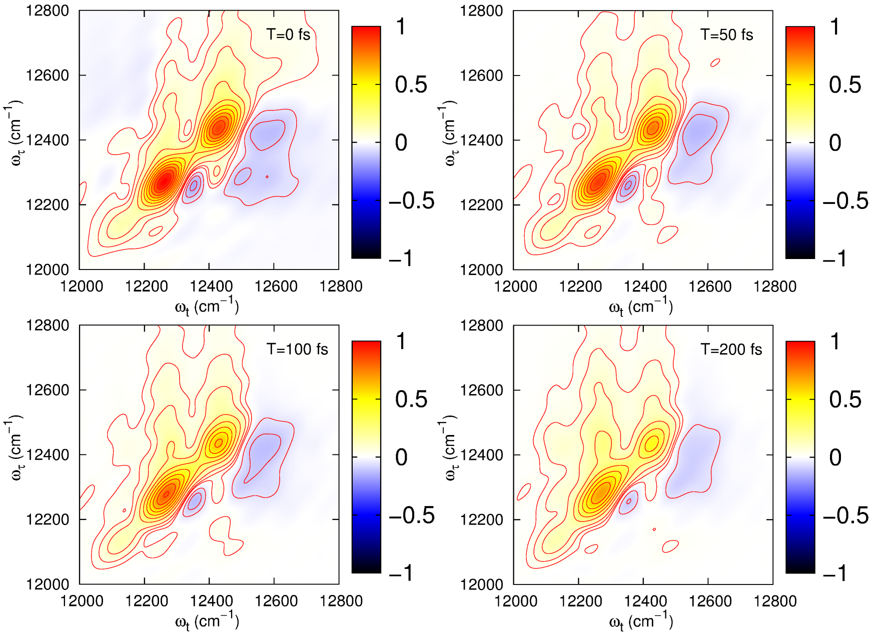

Figure 6.10: Real part of the 2D photon echo spectra calculated for a temperature of 77 K for selected waiting times as indicated. Notice that the two axes for ω_τ and ω_t are swapped as compared to Ref. [108].

a good agreement given the fact that the only varied parameter is temperature. In addition, we have calculated the 2D electronic spectra of the FMO complex at 77 K as well with the same set of parameters. The results for different waiting times are shown in Fig. 6.10. The spectra are in good agreement with the experimental results reported in Refs.[58, 108]. The energy transfer dynamics and pathways can be clearly observed by the kinetics of the off-diagonal peaks.

Moreover, we have calculated the time evolution of the off-diagonal signal at the spectral position ($\omega_\tau = 12350$ cm^{-1}, $\omega_t = 12200$ cm^{-1}) considered in Ref. [100], but now also for 77 K. Apart from changing temperature, we use the same parameters as before. The results for the real and imaginary parts are shown in Fig. 6.11. We find only weak electronic coherence which vanishes within the dephasing time of less than 200 fs. As a consistence check, we also measure the homogeneous linewidth provided by the anti-diagonal in Fig. 6.10 for zero waiting time. We find a FWHM of $\Delta_{\text{hom}} = 90$ cm^{-1}. This corresponds to an electronic dephasing time of $\tau_{\text{hom}} = 120$ fs at 77 K, in agreement with the previous results. Hence, we cannot confirm long-lived electronic coherence at a temperature of 77K reported up to times beyond 1 ps.

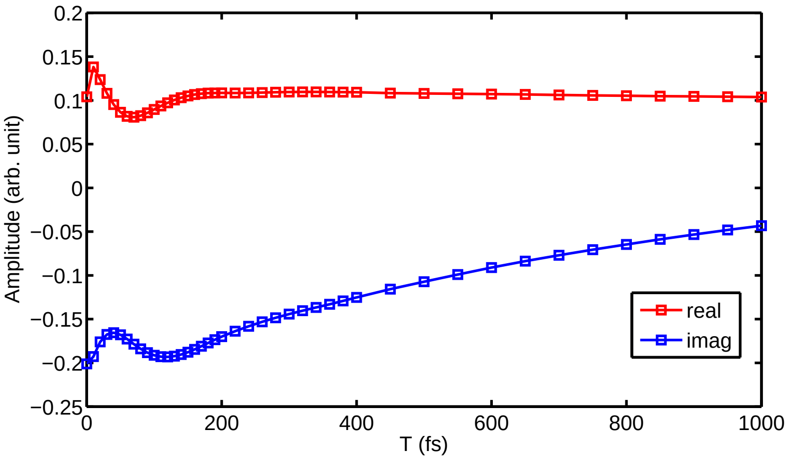

Figure 6.11: Calculated time-dependent off-diagonal signal (red: real part, blue: imaginary part) at the spectral position ($\omega_\tau = 12350$ cm^{-1}, $\omega_t = 12200$ cm^{-1}) considered in Ref. [100] at 77 K.

6.7 Simulating long-lived electronic coherence

We did not observe long-lived electronic coherence in the present experimental and theoretical results of the FMO complex. However, we can consider the question how a long-lived electronic coherence would show up in an optical 2D spectrum at low temperature and, consistently, in the time-dependent off-diagonal signal. To answer this question, we have used the simplest possible model of a pure Ohmic spectral density, i.e., only the first term of Eq. (6.7) and mimic long-lived electronic coherence by a very weak system-bath interaction. We set $\gamma = 0.35$ and $\omega_c = 100$ cm^{-1}, and set the temperature again to 77 K. In Fig. 6.12 (a), we show the result of the 2D spectrum of the FMO under these artificial weak-coupling conditions. The weak system-bath coupling induces a very narrow central peak with a small homogeneous broadening visible in the anti-diagonal band width. We extract a FWHM of $\Delta_{\text{hom}} = 25$ cm^{-1}. This corresponds to an electronic dephasing time of $\tau_{\text{hom}} = 420$ fs.

Correspondingly, we show in Fig. 6.12 (b) the time-dependent off-diagonal signal at the spectral position ($\omega_\tau = 12350$ cm^{-1}, $\omega_t = 12200$ cm^{-1}) considered in Ref. [100]. We find (artificially created) long-lived electronic coherence up to times beyond 450 fs, in agreement with the findings from the homogeneous line width. However, the measured 2D spectra of the real FMO complex do not show these sharp ridges with a very narrow diagonal peaks at zero waiting times.

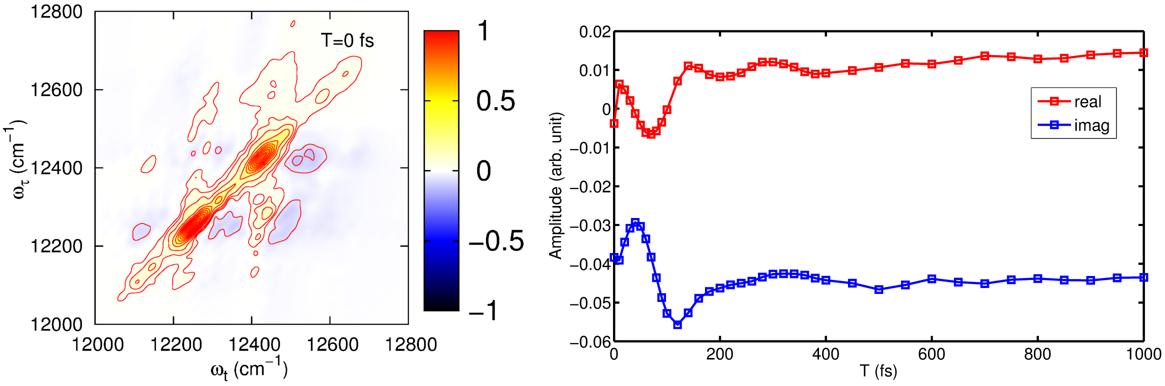

Figure 6.12: (a) Calculated 2D spectrum of the FMO under artificially assumed weak system-bath conditions with an Ohmic spectral density with $\gamma = 0.35$ and $\omega_c = 100$ cm^{-1}, and temperature of 77 K. Notice that the two axes for ω_τ and ω_t are swapped as compared to Ref. [108]. (b) Extracted time-dependent off-diagonal signal at the spectral position ($\omega_\tau = 12350$ cm^{-1}, $\omega_t = 12200$ cm^{-1}) considered in Ref. [100].

6.8 Correlation revealed by the diagonal and anti-diagonal bandwidth

In the 2D electronic spectra, the correlation $M(T)$ can be revealed by the time evolution of the diagonal and anti-diagonal bandwidth, $M(T) = \frac{(a^2-b^2)}{(a^2+b^2)}$, which is strongly related to the non-Markvoianity of the system interact to the environment [119, 120]. Here, we measured the time-evolved diagonal (a) and anti-diagonal (b) bandwidth from the 2D spectra with different waiting time, T. The correlation function $M(T)$ is plotted in Fig. 6.13 and it shows one exponential decay at the short time range ($<$ 500 fs). Based on the correlation analysis, it clearly shows the Markovian dynamics and it agrees with the previous works [121]. This proves that the FMO exciton dynamics occurs in the fast modulation limit and the T_2-time is reflected in the anti-diagonal bandwidth.

6.9 Transport timescales of the photosynthetic complexes

We have studied the energy transfer of the LHCII and FMO complexes. Both are two typical photosynthetic proteins resolved from higher plants and the sulfur bacteria. Despite their protein structure being rather different, it is interesting that both measurements reveal similar timescales of the energy transport: The shortest time constant of $\sim$100 fs is related to electronic dephasing. There, a fast energy transfer within $\sim$1 ps occurs and a relatively slower energy transfer with a timescale of several ps is formed. It is well known that the speed of the energy transfer is strongly related to the long-range electrostatic interaction. So, the distance of the pigments located inside the protein pocket is relevant. Nowadays, the distance between pigments can be well resolved by high-resolution X-ray crystallography. It shows that the averaged distance in the LHCII and the FMO complex are similar and in the range of 4$\sim$12Å. This leads to similar timescales of the electronic coupling between the pigments (5$\sim$80

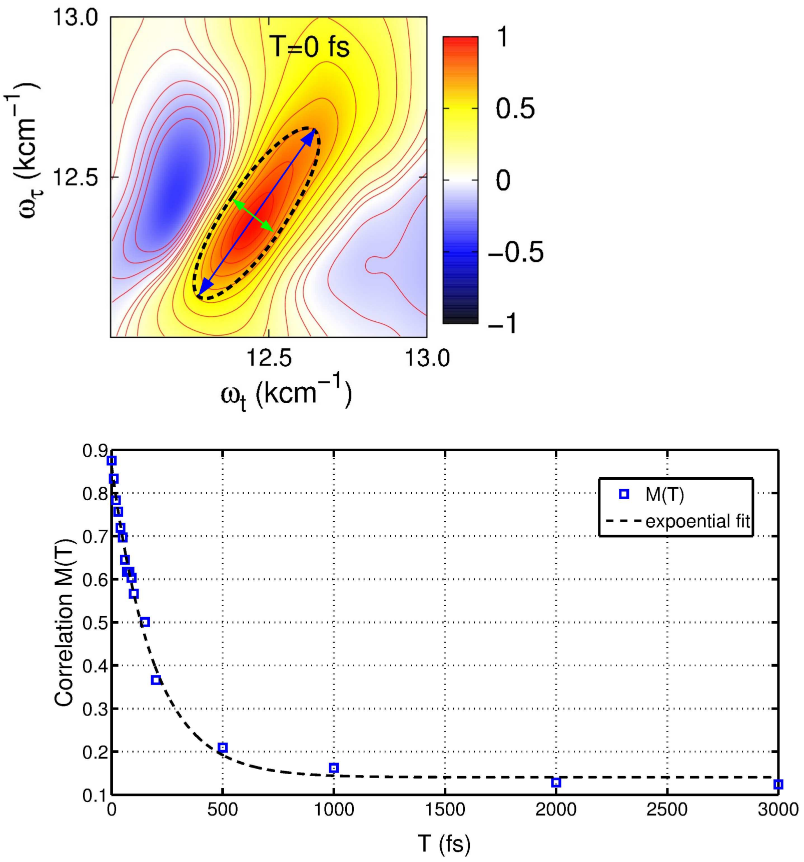

Figure 6.13: Time-evolution of the correlation function $M(T)$ calculated from the diagonal and anti-diagonal bandwidth. The dynamics can be well fitted by one exponential function, which clearly manifests the Markovian dynamics and it proves the exciton dynamics to occur in the fast modulation limit.

cm^{-1}). It is now easy to understand why the nature chooses this distance of the pigments for the energy transfers. On one hand, a larger distance definitely decreases the speed of energy transport. On the other hand, it is hard to avoid the overlap of molecular orbitals if the distance of pigments is shorter than 3Å. There, the overlap will induce the charge separation between different pigments, the same feature as we reported for the reaction center in Chapter 5. However, the reaction center is a functional protein, which separates the charges for the splitting of water. In addition, the energy transfer direction and the rates are also strongly related to the energetic gap between different pigments, which is induced by the different local protein environment. It is interesting to note that one argument suggests that the biological function of the photosynthetic complex is determined by the surrounding helices, i.e., the backbone architecture of the molecular complex and their exciton dynamics [122].

Chapter 7

Vibronic quantum coherence in artificial photoactive molecules

So far, we have addressed natural biological photosynthetic complexes, i.e., the antenna complex LHCII in higher plants, the FMO complex in the green sulfur bacteria and the charge separation in the PSII reaction center. With the help of theoretical studies, we have unravelled the short-lived electronic coherence, which is convoluted with the vibrational quantum coherence during the processes of energy transfer and charge separation. A central question is whether the electronic coherence can be prolonged by long-lived vibrational coherence via the vibronic coupling? It is well known that the mechanism of the energy transfer is completely different when the electronic coherence persists for a time longer or at least comparable to the timescale of the energy transport. It induces a spatially coherent energy transfer between pigments, while the vibrational coherent do not considered to strongly influence the energy transport since it usually originates from the local vibrations of pigments. Due to the complexity of natural pigment-protein complexes (strong static disorder, congested excitonic energies), the congested and strongly overlapping peaks in the 2D spectrum hardly provide a clear picture. For better identifying the origin of quantum coherence, we study the transfer dynamics in an artificial indocarbocyanine dye molecule using 2D electronic spectroscopy. This type of laser dye molecule shows a clear vibrational progression in its absorption spectrum. Moreover, two monomers can form a dimer by two linking butyl chains separated by $\sim$10 Å. This rather small distance allows for strong electronic interaction and clearly separated excitonic transition peaks in the 2D spectra. Moreover, the dynamics of each peak can be accurately traced over time. It is an ideal sample to be used to understand the relation and the dynamical interplay between electronic and vibrational coherence.

7.1 Molecular structure of the indocarbocyanine dye

In this section, we analyze the details of the structure of the monomer and the dimer molecule of indocarbocyanine dye. For the design of the molecule and in order to obtain its structural and spectroscopic parameters for the modeling of the absorption and 2D spectra, we have used the HyperChem package (version 7, HyperCube Inc., U.S.A.). First we have constructed a monomer molecule, the indocarbocyanine dye, and have optimized it using (sequentially) the PM3 and MM+ HyperChem toolboxes. Then, by means of the ZINDO/S tool, we have calculated the electronic absorption spectrum and have defined the magnitude of the transition dipole moment for the $S_0 \rightarrow S_1$ electronic transition. The obtained value of $\mu = 12.83$ Debye is close to the one found experimentally ($\mu = 11$ Debye) from the absorption spectrum and from the value of the extinction coefficient (Ref. [123], compound $A - 1$) using the well-known relation from Ref. [124].

For the dimer, we have used two identical indocarbocyanine monomers and have connected them by two butyl chains. Again, we have performed the structural optimization with PM3 and MM+. It is important to note that we have added two free $\mathrm{ClO_4}$ ions in order to realize the electrostatic equilibrium. The resulting geometry of the bis-indocarbocyanine dimer is shown in Fig. 7.1. The distance between monomers in this dimer is ≈ 10 Å (the lines in Fig. 7.1 have been drawn through the centers of the electronic densities of the monomers), and the twist angle between them is 15 degrees.

The excitonic interaction energy between the two monomers was calculated in the point-dipole approximation according to (see, e.g., Ref. [125])

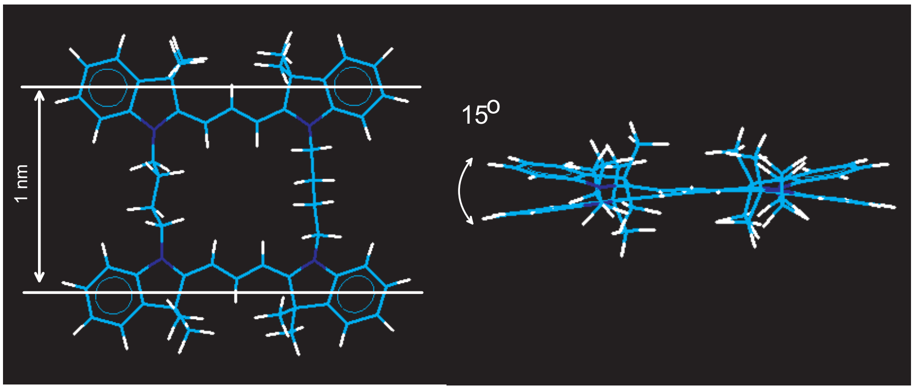

Figure 7.1: The structure of the bis-indocarbocyanine dimer, obtained after the HyperChem optimization. Left: front view, right: top view.

$$J_{12} = \frac{\vec{\mu}_1 \cdot \vec{\mu}_2}{|\vec{r}_{12}|^3} - 3\frac{(\vec{\mu}_1 \cdot \vec{r}_{12})(\vec{\mu}_2 \cdot \vec{r}_{12})}{|\vec{r}_{12}|^5} \,. \tag{7.1}$$

For the monomer dipole moment, we have $\mu_1 = \mu_2 = 13$ Debye. The distance between monomers is $r_{12} = 10$ Å, and the angle between the transition dipole moments is 15 degrees. We obtain the electronic coupling between two monomers as $J_{12} = 822$ cm^{-1}.

7.2 Electronic and vibrational component

Next, we discuss details of the mixed electronic and vibrational components of the wave functions of the molecule. Let us start with the simplest electronic two-level model as illustrated on the left side of Fig. 7.2. The population of the ground state $|g\rangle$

of the system is pumped to the excited state $|e\rangle$ which generates one single transition frequency in the stick spectrum. The transition frequency in the stick spectrum is determined by the energy gap between the ground and the excited state in the exciton basis. After adding a vibrational degree of freedom, more transitions can arise, see right-hand side of Fig. 7.2. The original electronic levels $|g\rangle$ and $|e\rangle$ are now split by the vibrational coupling.

To be more precise, let us consider the monomer Hamiltonian H with a vibrational mode coupled to it. We can define the wave function of this system as a direct product of electronic and vibrational states, i.e., $|\psi\rangle = |\alpha\rangle |n\rangle = |\alpha, n\rangle$ with $\alpha = g, e$ for the ground or the excited state of the electronic degree of freedom and with $n = 0, 1, \ldots$ being the vibrational quantum number. This wave function refers to the site basis. To calculate the stick spectrum, we need to diagonalize H by a unitary transformation. The resulting exciton basis with basis states $|k\rangle$ is defined by $H|k\rangle = E_k |k\rangle$. The transformation reads

$$|\alpha, n\rangle = \sum_k |k\rangle \langle k|\alpha, n\rangle \quad \text{or} \quad |k\rangle = \sum_{\alpha, n} |\alpha, n\rangle \langle \alpha, n|k\rangle \,. \tag{7.2}$$

The location of the sticks in the stick spectrum for the transition between the exciton states $|k\rangle$ and $|l\rangle$ is at the frequency $\omega_{k,l} = E_k - E_l$. For the height of the sticks and the ratio of the electronic and the vibrational parts, we need to have the dipole operator μ in the excitonic basis. It is given by

$$\begin{aligned}\mu &= |g\rangle\langle e| + |e\rangle\langle g| \equiv (|g\rangle\langle e| + |e\rangle\langle g|)\otimes \mathrm{Id}_{\mathrm{vib}} \\ &= |g\rangle\langle e| \otimes \sum_n |n\rangle\langle n| + |e\rangle\langle g| \otimes \sum_n |n\rangle\langle n| \\ &= \sum_n \left[|g,n\rangle\langle e,n| + |e,n\rangle\langle g,n|\right] ,\end{aligned} \tag{7.3}$$

where we have inserted the identity operator in the Hilbert subspace of the vibrational DOF. Next, we perform the transformation to the excitonic basis and insert Eq. (7.2) in Eq. (7.3) and obtain $\mu = \sum_{k,l} \mu_{k,l} |k\rangle\langle l|$ with

$$\mu_{k,l} = \sum_n \left[\langle k|g,n\rangle\langle e,n|l\rangle + \langle k|e,n\rangle\langle g,n|l\rangle\right] . \tag{7.4}$$

The total height of the sticks is given by $|\mu_{k,l}|^2$ since $I(\omega) \sim \mu(0)\mu(t)$. Hence, we have

$$\begin{aligned}|\mu_{k,l}|^2 = \mu_{k,l}\mu_{k,l}^* = &\sum_{n,m} \left[\langle k|g,n\rangle\langle e,n|l\rangle + \langle k|e,n\rangle\langle g,n|l\rangle\right] \\ &\left[\langle l|e,m\rangle\langle g,m|k\rangle + \langle l|g,m\rangle\langle e,m|k\rangle\right] .\end{aligned} \tag{7.5}$$

In order to distinguish between the electronic and the vibrational parts of the transition, we may write

$$|\mu_{k,l}|^2 = \left(|\mu_{k,l}|^2\right)_{\mathrm{el}} + \left(|\mu_{k,l}|^2\right)_{\mathrm{vib}} , \tag{7.6}$$

where the electronic part is defined by those terms which involve no vibrationally excited states, i.e., with $n = m = 0$. Hence,

$$\left(|\mu_{k,l}|^2\right)_{\mathrm{el}} = \left[\langle k|g,0\rangle\langle e,0|l\rangle + \langle k|e,0\rangle\langle g,0|l\rangle\right]\left[\langle l|e,0\rangle\langle g,0|k\rangle + \langle l|g,0\rangle\langle e,0|k\rangle\right] , \quad (7.7)$$

while the vibrational part is defined as the corresponding rest.

For the dimer Hamiltonian with one vibrational mode coupled to each monomer, we can define the wave function again as a direct product of electronic and vibrational states, i.e.,

$$|\psi\rangle = |\alpha\rangle_1 |n\rangle_1 |\beta\rangle_2 |m\rangle_2 = |\alpha,n\rangle_1 |\beta,m\rangle_2 = |\alpha,n;\beta,m\rangle , \quad (7.8)$$

with $\alpha, \beta = g, e$ for the ground or the excited state of the electronic degree of freedom and with $n, m = 0, 1, \ldots$ being the vibrational quantum number. This wave function again refers to the site basis.

The Hamiltonian is diagonalized by the transformation

$$|\alpha,n;\beta,m\rangle = \sum_k |k\rangle \langle k|\alpha,n;\beta,m\rangle \quad \text{or} \quad |k\rangle = \sum_{\alpha,\beta,n,m} |\alpha,n;\beta,m\rangle \langle \alpha,n;\beta,m|k\rangle . \quad (7.9)$$

For the electronic dipole operator of the dimer with $\hat{e}_1 = \hat{e}_x$ and $\hat{e}_1 = (\cos(\alpha)\hat{e}_x + \sin(\alpha)\hat{e}_y)$ with the angle α between the dipole moments and $\hat{e}_j$ the unit vectors in the coordinate system of the dimer, we have

$$
\begin{aligned}
\mu =&\hat{e}_1(|gg\rangle\langle eg| + |ge\rangle\langle ee|) + \hat{e}_2(|gg\rangle\langle ge| + |eg\rangle\langle ee|) + h.c. \\
\equiv& [\hat{e}_1(|gg\rangle\langle eg| + |ge\rangle\langle ee|) + \hat{e}_2(|gg\rangle\langle ge| + |eg\rangle\langle ee|) + h.c.] \otimes \mathrm{Id}_{\mathrm{vib},1} \otimes \mathrm{Id}_{\mathrm{vib},2} \\
=& [\hat{e}_1(|gg\rangle\langle eg| + |ge\rangle\langle ee|) + \hat{e}_2(|gg\rangle\langle ge| + |eg\rangle\langle ee|) + h.c.] \\
&\otimes \sum_n |n\rangle\langle n|_1 \otimes \sum_m |m\rangle\langle m|_2 \\
=& \sum_{n,m} [\hat{e}_1(|g,n;g,m\rangle\langle e,n;g,m| + |g,n;e,m\rangle\langle e,n;e,m|) \\
&+\hat{e}_2(|g,n;g,m\rangle\langle g,n;e,m| + |e,n;g,m\rangle\langle e,n;e,m|) + h.c.]\ .
\end{aligned}
\tag{7.10}
$$

As before, we perform the transformation to the exciton basis and with $\mu = \sum_{k,l} \mu_{k,l} |k\rangle\langle l|$, we obtain

$$
\begin{aligned}
\mu_{k,l} \;=\; & \sum_{n,m} [\hat{e}_1(\langle k|g,n;g,m\rangle\langle e,n;g,m|l\rangle + \langle k|g,n;e,m\rangle\langle e,n;e,m|l\rangle) \\
&+\hat{e}_2(\langle k|g,n;g,m\rangle\langle g,n;e,m|l\rangle + \langle k|e,n;g,m\rangle\langle e,n;e,m|l\rangle) + h.c.]\,.
\end{aligned}
\tag{7.11}
$$

From this, the electronic part $(|\mu_{k,l}|^2)_{\mathrm{el}}$ again follows by taking the square and setting all vibrational quantum numbers to zero ($n = m = 0$). As before, the "rest" is the vibrational part.

7.3 Theoretical model

The goal is to study the excitonic dynamics in terms of 2D optical spectroscopy and in the presence of strong vibronic coupling. For a theoretical description, we first

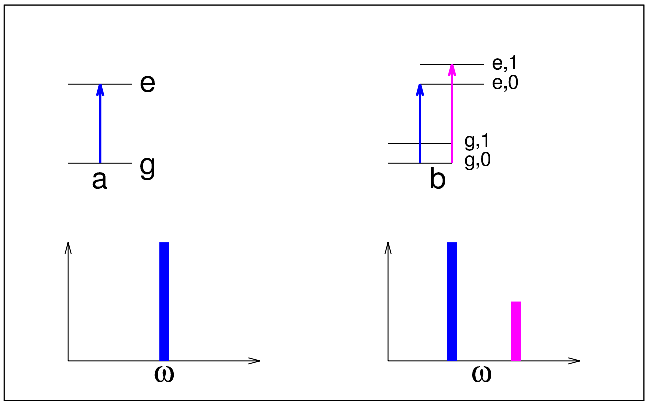

Figure 7.2: Sketch of a simple electronic (left) and vibronic (right) model with the associated stick spectra. The blue and pink sticks represent the electronic and vibrational components, respectively.

set-up a model Hamiltonian which includes vibrational states (see vibronic model in Chapter 1). By an accurate fit to the experimental absorption spectrum, we determine its parameters. We consider an electronic transition between the electronic ground S_0 ($|g\rangle$) and first excited state S_1 ($|e\rangle$), separated by the energy gap E. The electronic states are coupled to the excitations of a single vibrational harmonic mode with the frequency Ω and with the bosonic creation and annihilation operators, $b^\dagger$ and b, respectively. We denote the exciton-phonon coupling constant by κ. The monomer Hamiltonian thus reads ($\hbar = 1$)

$$H_{\text{mono}} = H_g + H_e = |g\rangle\, h_g\, \langle g| + |e\rangle\, (h_e + E)\, \langle e| \ , \tag{7.12}$$

with $h_g = \Omega\left(b^\dagger b + 1/2\right)$ and $h_e = \Omega\left(b^\dagger b + 1/2\right) + \kappa(b^\dagger + b)$. We further couple the monomer Hamiltonian to a fluctuating Gaussian quantum mechanical environment described by the standard bath Hamiltonian $H_B = \sum_{j,\nu=\mathrm{el,vib}} \omega_{j,\nu}(a^\dagger_{j,\nu} a_{j,\nu} + 1/2)$ [16]. The bilinear coupling is given by $H_{SB} = |e\rangle\langle e|\, \xi_{\mathrm{el}}(t) + (b^+ + b)\xi_{\mathrm{vib}}(t)$. The excited electronic state is coupled to the quantum statistical fluctuations $\xi_{\mathrm{el}}(t) = \sum_j c_{j,\mathrm{el}}(a^\dagger_{j,\mathrm{el}} + a_{j,\mathrm{el}})$, while the vibrational motion is coupled to a different harmonic bath via $\xi_{\mathrm{vib}}(t) = \sum_j c_{j,\mathrm{vib}}(a^\dagger_{j,\mathrm{vib}} + a_{j,\mathrm{vib}})$. Both baths have the same Ohmic spectral density, i.e., $J_{\mathrm{el/vib}}(\omega) = \gamma_{\mathrm{el/vib}}\omega e^{-\omega/\omega_c}$. We assume a large cut-off frequency ω_c taken to be equal for both branches. We calculate first the absorption spectrum [126]

$$I(\omega) \propto \omega \int_{-\infty}^{+\infty} dt\, e^{i\omega t} \langle \mu(t)\mu(0)\rangle_g \,, \tag{7.13}$$

where $\mu = |g\rangle\langle e| + |e\rangle\langle g|$ is the transition dipole moment of the monomer written in the Heisenberg picture. The quantum dynamics was calculated by means of the TNL master equation [66] for the system's reduced density operator $\rho(t)$ after tracing out the bath DOF. The subscript g in Eq. (7.13) indicates a tracing with respect to the initial state given by the equilibrium density operator ($k_B = 1$) $\rho(0) = |g\rangle\langle g| \otimes e^{-\Omega(b^\dagger b + 1/2)/T_0}/Z_{\mathrm{ph}}$ where the vibrational mode is in thermal equilibrium at temperature $T_0 = 300$ K. Z_{ph} is the phonon equilibrium partition function. The electronic and the vibrational bath are held at the same temperature. Inhomogeneous broadening is included by convoluting the calculated homogeneous absorption spectrum of Eq. (7.13) with a Gaussian-shaped inhomogeneous broadening function.

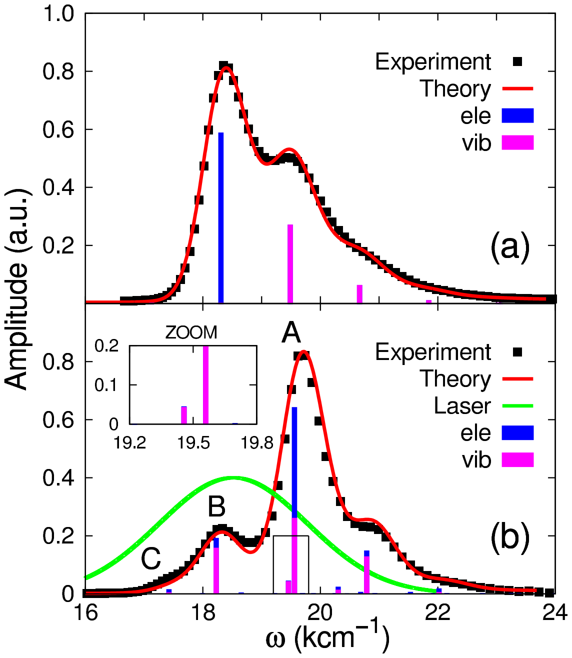

Figure 7.3: Measured (symbols) and calculated (lines) absorption spectra of the monomer (a) and dimer (b). In addition, the stick spectra are shown. The electronic and vibrational contributions to the eigenstates are indicated by the different colors. The main electronic transition in the monomer spectrum (the "zero-zero" transition), as well as the vibrational progressions, are clearly resolved. In the dimer spectrum (b), a clear electron-vibrational coherent coupling is present. The green line in (b) indicates the power spectrum of the excitation pulse of the laser used in the simulations.

Furthermore, the obtained spectra are averaged over 500 random orientations. From the fitting of the calculated absorption spectrum to the experimental one, we obtain the complete set of parameters for our model: $E = 18850$ cm^{-1}, $\Omega = 1180$ cm^{-1}, $\kappa = 800$ cm^{-1}, $\gamma_{\mathrm{el}} = 0.9$, $\gamma_{\mathrm{vib}} = 0.01$, $\omega_c = 700$ cm^{-1}, and the FWHM of the inhomogeneous broadening of 300 cm^{-1} which is typical for the dissolved organic dyes at room temperature. Our model reproduces the monomer experimental absorption spectrum very well as shown in Fig. 7.3a, together with the calculated stick spectrum. For achieving convergent results, we have included $n_{\mathrm{ph}} = 6$ vibrational eigenstates. To estimate the vibrational dephasing rate, we first set $\gamma_{\mathrm{el}} = 0$ and kept the off-diagonal elements of the vibrational coupling in the exciton representation. Then, using an estimated vibrational lifetime of 1 ps, we have adjusted the vibrational dephasing rate to $\gamma_{\mathrm{vib}} = 0.01$. The stick spectrum in Fig. 7.3a clearly shows that the main peak is purely electronic, while the three well resolved side peaks have a vibrational origin.

Having obtained the monomer model parameters, we next turn to the dimer. It consists of two identical indocarbocyanine monomers, covalently bounded by two butyl chains (the homodimer) with an in-plane angle of $\alpha = 15°$. To extend the model to the dimer, we use the Hamiltonian

$$H_{\mathrm{dim}} = \sum_{j,k=g,e} |jk\rangle \, (h_j^{(1)} + h_k^{(2)}) \, \langle jk| + |ge\rangle \, U \, \langle eg| + |eg\rangle \, U \, \langle ge| \, . \qquad (7.14)$$

Here, U is the electronic dipole coupling which can be calculated in the point-dipole approximation using the structural information for the dimer skeleton obtained using the HyperChem v.7 package (see last section). For this geometry, the calculated value of U is ≈ 820 cm^{-1}. The dimer Hamiltonian includes two vibrational modes each belonging to one monomer in the same way as the molecular Hamiltonian. Hence, $h_g^{(x=1,2)} = \Omega(b_x^\dagger b_x + 1/2)$ and $h_e^{(x)} = E + \Omega(b_x^\dagger b_x + 1/2) + \kappa(b_x^\dagger + b_x)$ for the ground and excited states, respectively. The total transition dipole moment is $\mu = \mu_1 + \mu_2$ with $\mu_1 = \hat{e}_x(|g_1\rangle\langle e_1| + |e_1\rangle\langle g_1|)$ and $\mu_2 = (\cos(\alpha)\hat{e}_x + \sin(\alpha)\hat{e}_y)(|g_2\rangle\langle e_2| + |e_2\rangle\langle g_2|)$ with angle α between the dipole moments and $\hat{e}_i$ the unit vectors in the coordinate system of the dimer. The dimer absorption spectrum is also calculated using Eq. (7.13). The excellent fit to the experimental spectrum is depicted in Fig. 7.3b. We used the parameters $E = 18700\ \mathrm{cm}^{-1}, U = 870\ \mathrm{cm}^{-1}, \Omega = 1230\ \mathrm{cm}^{-1}$, and $\kappa = 834\ \mathrm{cm}^{-1}$. The slight modification of the monomer parameters (which have been used as an initial guess in the fitting procedure) is reasonable and could be attributed to the presence of the butyl chains perturbing the wave functions of the monomers. We have used the same values for the damping parameters as for the monomer. The stick spectrum in Fig. 7.3b reveals a strong electron-vibrational coherent coupling. Different states have quite different vibrational/electronic contributions in the stick components. For example, the main peak labeled as A shows almost equal contributions from electronic and vibrational states. For peak C, the electronic contribution is dominant, whereas the vibrational contribution clearly dominates in the peak B. From the electronic and vibrational contributions to the eigenstates, depicted in the stick spectrum in Fig. 7.3b using different colors (see figure capture), one already could expect that the dephasing of the associated transitions, and consequently the damping of coherent oscillations in the 2D spectra, should be rather different since the dephasing of pure electronic transitions is in general much stronger than the vibrational dephasing. However, as we will demonstrate below, this is not the case.

7.4 Electronic and vibrational coherence

7.4.1 Short-lived vs. long-lived quantum coherence

We next address the coherent time evolution of the coupling of electronic and vibrational DOF in the artificial dimer. To that end, we consider the 2D photon echo spectrum [23, 127, 128] which can be calculated upon using the phase matching approach of Ref. [26] in combination with the time-convolutionless quantum master equation [66]. The doubly excited states (the excited-state absorption) with an exciton at each monomer were properly accounted for in the model calculation but doubly excited states within the same monomer were neglected. To match the experimental conditions, the carrier frequency of the laser pulse is set to 18520 cm^{-1} and its duration to a FWHM of 7 fs. The resulting 2D photon echo spectra at different waiting times T are shown in Fig. 7.4. We see clearly separated diagonal peaks which correspond to the peaks A, B and C in the linear absorption spectrum shown in Fig. 7.3b. We note that the peak A represents a strong electron-vibrationally superposed vibronic state. Also, well-separated cross peaks (labeled by D to I) appear. Peaks D

and G are the most intense and correspond to the interference between the diagonal peaks A and B.

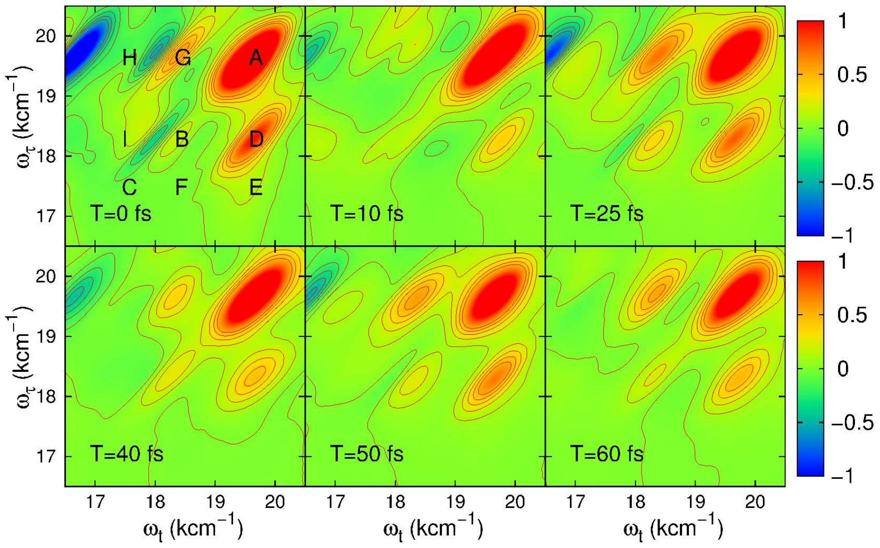

Figure 7.4: Real part of 2D photon echo spectra of the dimer at different waiting times (as indicated) calculated with the model parameters obtained from the fit of the dimer linear absorption spectrum. The diagonal as well as the cross peaks are labeled by capital letters in the frame $T = 0$ fs.

The strong vibronic coherent coupling is further illustrated in the sequence of 2D spectra for increasing waiting times with a step of 10 fs, shown in Fig. 7.4. We can clearly identify the oscillatory behavior of the amplitudes of the cross peaks 'by eye'. The calculations reproduce well the main features of the measured 2D spectra (Fig. 7.5) in Ref. [129, 130]. The slight underestimation of the excited state absorption is

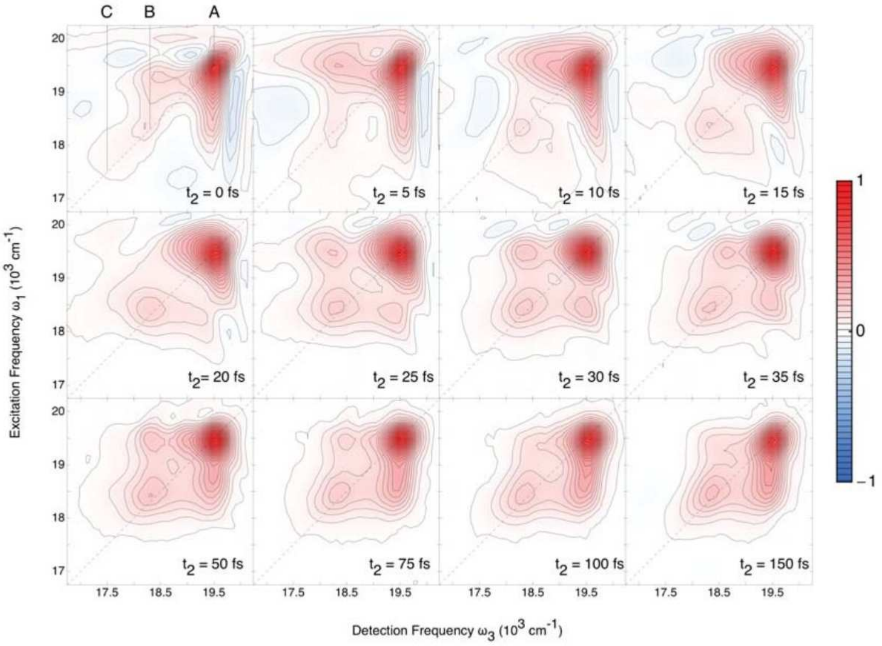

Figure 7.5: Measured absorptive 2D spectra of biscyanine at selected waiting times. The diagonal peaks and the well resolved cross peaks between the main transition and lower energy peaks are evident. The figure is taken from Ref. [129].

likely due to neglecting the higher excited states of the monomer.

To study the effect of the environment on the coherent coupling in more detail, we monitor the time evolution of the amplitude of the cross peaks as labeled in Fig. 7.4 for increasing waiting times. They can readily be extracted from the series of the 2D spectra (the calculations were performed with the waiting time step of 5 fs). The results are shown in Fig. 7.6 as symbols to which we fit a cosine function damped by a single exponential decay. This yields the oscillation periods and decay times which are summarized in Table 7.1 (first row).

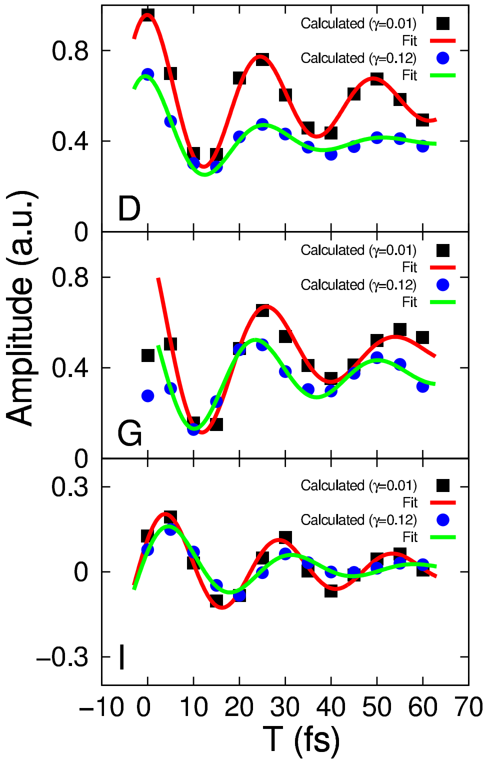

Figure 7.6: Amplitude of the spectral cross peaks D, G and I vs. the waiting time T. The symbols mark the cross peak maximum extracted from the real parts of the 2D spectra, while the solid lines represent a fit to an exponentially decaying oscillatory function. The oscillatory behavior of the cross peaks is shown for both the weakly ($\gamma_{\rm vib} = 0.01$) and the intermediately ($\gamma_{\rm vib} = 0.12$) damped vibrational modes (see text for details).

We find that the coherent oscillations appear with a period of around 25 fs and with decay times of $40 - 50$ fs. The latter are typical electronic dephasing times of organic dyes. The oscillation frequencies match the energy splittings between the main transitions A, B, and C in the dimer absorption spectrum (Fig. 7.3b) given by the stick components. Likewise, the coherence time (i.e., the decay time of the oscillations τ_D in Table 7.1) is clearly dominated by the electronic dephasing for all cross peaks. More importantly, these coherences are independent of the participation ratio between the electronic and vibrational contributions. This can be additionally verified by increasing the vibrational dephasing rate by one order of magnitude. The system then goes from the regime of weak damping with $\gamma_{\text{vib}} = 0.01$ to the regime of intermediate damping with $\gamma_{\text{vib}} = 0.12$. We find a proportional decrease of the vibrational coherence time from 2 ps to $\approx$ 200 fs. The extracted oscillations for both cases are also plotted in Fig. 7.6. For this intermediate damping, we find similar coherent oscillations decaying within a similar time window. The resulting fit parameters to the exponentially decaying cosine function are given in Table 7.1 (second row). Up to minor quantitative modifications, no significant impact of the increased vibrational damping is observed. This shows that the amplitude of the oscillating cross peaks is damped by the strong fluctuations acting on the electronic degree of freedom, i.e., electronic dephasing and, importantly, the weak vibration-bath coupling cannot reduce its damping.

A further proof can be obtained by changing the angle α between transition dipole moments of the monomers. This is readily possible in our accurate theoretical model

	D		G		I	
Damping	T_D/fs	τ_D/fs	T_G/fs	τ_G/fs	T_I/fs	τ_I/fs
weak	24.6	38.5	27.6	25.7	24.8	38.0
intermediate	25.8	18.9	26.7	30.5	26.8	23.6

Table 7.1: Oscillation periods T_X and decay times τ_X of the cross peak maxima for the peaks $X = D, G$ and I for a weakly damped vibrational mode with $\gamma_{\text{vib}} = 0.01$ and a intermediately damped vibrational mode with $\gamma_{\text{vib}} = 0.12$.

while it could be a great challenge in the experiment. Tuning of α modifies the exciton coupling between molecules, changes the relative intensities of the excitonic transitions, and induces a redistribution of the electronic contributions relative to the vibrational ones. For example, for $\alpha = 60°$, the ratio of the peak amplitudes of A and C in the absorption spectrum reaches $\approx 1/3$ vs. $1/60$ for $\alpha = 15°$. Thus, tweaking of α permits an easy control of the exciton transitions and of the contributions to both the electronic and vibrational sector. Some examples of calculated absorption and stick spectra with corresponding electronic and vibrational contributions for different angle α are given in Fig. 7.7.

We have calculated 2D spectra for various angles and waiting times increasing in steps of 5 fs. From there, the time dependence of the cross peaks was extracted and fitted to a single exponentially decaying cosine function as before. The results

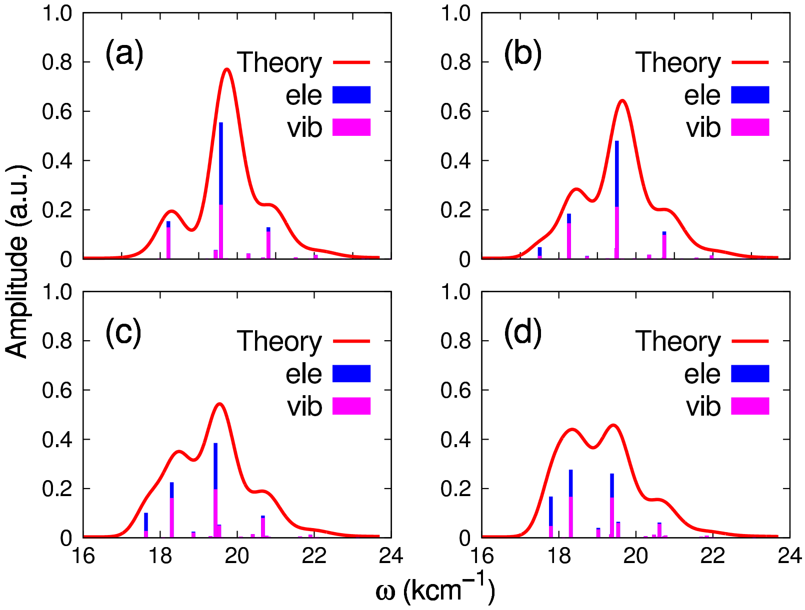

Figure 7.7: Absorption spectra of the dimer for different twist angle $\alpha = 0^o$, 30^o, 45^o, 60^o (a-d) between the two transition dipoles of monomers.

of this fitting for the cross peaks D and G are collected in Fig. 7.8. We find that despite small quantitative changes, the decay times are essentially independent from the angle α between the monomer transition dipole moments. This supports the previous conclusion that the quantum coherence of excitonic transitions is clearly dominated by the electronic dephasing.

It is well established that in some excitonically coupled systems the coherent oscillations in measured 2D spectra live sometimes significantly longer than primitively estimated from the magnitude of electronic dephasing. This is true even at room temperature (see, e.g., Refs.[100, 101, 131]). Nevertheless, their magnitudes are

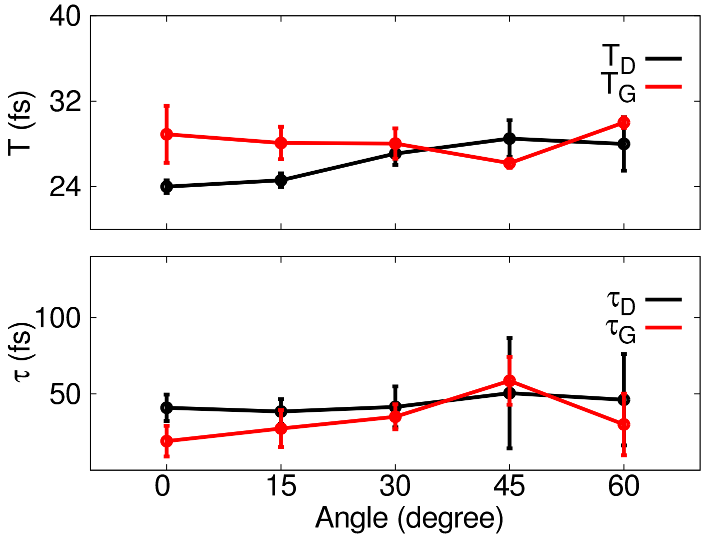

Figure 7.8: The oscillation periods $T_{x=D,G}$ and the decay rate $\tau_{x=D,G}$ for selected cross peaks as a function of twist angle α between the transition dipole moments of monomers evaluated at short times where the electronic dephasing prevails.

rather weak. In recent experimental study [132] of the oxidized reaction center from *Rhodobacter sphaeroides*, which can be considered as a good "natural" dimer model, the authors found in the 2D spectra weak oscillations lasting up to 1 ps at room temperature. Therefore, the origin and the physical mechanism of such long-lasting oscillations needs to be established.

In search for weak but long-lived oscillatory components, we have extended the waiting time window in our simulations to 400 fs and have found that, alongside with the short-lived oscillations in the cross peaks analyzed above (Fig. 7.6), there are much weaker long-lived oscillations. A typical example of these oscillations for our model dimer with $\alpha = 15^\circ$ and $\gamma_{\mathrm{vib}} = 0.01$ for the cross peak D is shown in Fig. 7.9. In this case, we fit this dynamics with two decaying cosine functions and find two similar yet distinguishable periods. The period of the strongly damped oscillation corresponds to the splitting between the interfering diagonal peaks A and B in the time domain, whereas the period of the long-lived oscillation precisely corresponds to the value of the vibrational frequency of $\Omega = 1230\ \mathrm{cm}^{-1}$. For this particular cross peak D, the ratio between their amplitudes is $44 : 1$ and is different for the other cross peaks. Notably different is the ratio for the imaginary part of the oscillations in the selected cross peak (see also Fig. 7.9). The long-lived component is stronger by about one order of magnitude. Since the overall amplitude of the real part dominates, the absolute 2D spectrum only shows a weak component of long-lived oscillations. Thus, it might be experimentally advantageous to study 2D spectra phase-resolved.

We observe a similar mixing of a strongly damped oscillation with a period corresponding to the splitting between peaks A and B and the long-lived vibrational frequency Ω (Fig. 7.9) for the position in the 2D spectra with $\omega_t = 17900\ \mathrm{cm}^{-1}$ and $\omega_\tau = 19720\ \mathrm{cm}^{-1}$, labeled in Ref. [129] as peak X. The calculated kinetics is in good agreement with the experimental observation (see Fig. 4d in [129]). The measurement along with its theoretical description in Ref. [129] was performed in a much smaller waiting time window (120 fs) than we used in our simulations (400 fs). Fig. 7.9 clearly resolves that at waiting times around 100 fs both contribution are of the

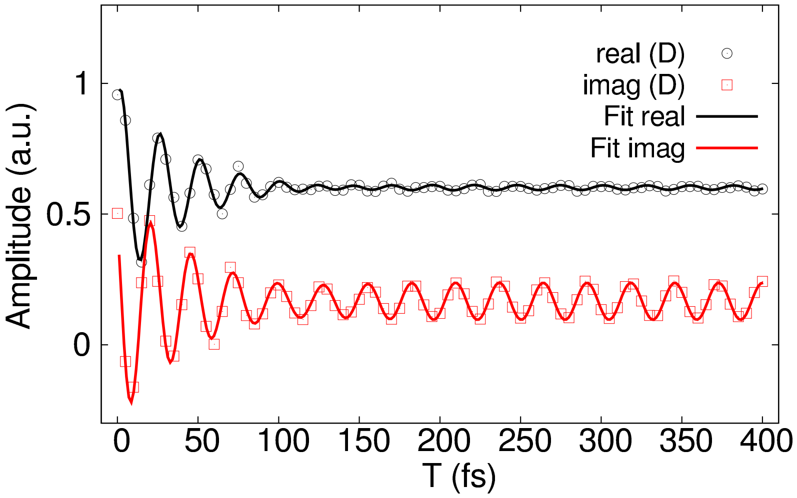

Figure 7.9: Oscillations in cross peaks D in a large waiting time window (symbols) and results of a two-component fit (see in text) revealing oscillatory frequencies 1235 ± 30 and 1350 ± 28 cm^{-1} corresponding to the vibrational frequency Ω and to the splitting between peaks A and B in the absorption spectrum of dimer, respectively.

same order of magnitude. Data up to this point do not justify a fit with two separate components and a fit with only a single component results only in a slightly longer dephasing time (as observed [129]) than in our analysis for the strong component obtained. Moreover, the polaron-like model used in Ref. [129] in which the vibrational mode has been integrated out generates an additional mixing of the contributions which renders the separation more difficult. Thus, our extended simulation (fully in line with experiments up to waiting times of $\sim$ 100 fs) reveals the long-lived weak component as a theoretical prediction to be tested in the experiment.

The nature of this long-lived oscillations becomes clear if we investigate more precisely the absorption stick spectrum as shown in the inset of Fig. 7.3b. The small satellite in the vicinity of the stick A has in essence a pure vibrational origin and the contribution of electronic transitions is very small. In turn, its decoherence is weak and the split between the stick component B and this satellite is precisely given by Ω. Therefore, their interference generates a long-lived oscillation with the frequency being equal to the vibrational frequency Ω and with a weak amplitude which is dictated by the small magnitude of that satellite.

To confirm this result, we have examined several additional parameter combinations. We have doubled the vibrational frequency and have kept all other model parameters unchanged. Similarly, we have decreased the excitonic coupling strength to $U = 250$ cm^{-1} and kept the vibrational frequency at the previous value of $\Omega = 1230$ cm^{-1} (Details in Appendix B). In all cases, we have found long-lasting oscillations with small amplitudes in the kinetics of the cross peaks in addition to the quickly decaying short-time oscillations. All results are consistent with those shown in Figs. 7.6 and 7.9. Importantly, the frequencies of the low-amplitude oscillations coincide with the vibrational frequency used. Whereas in the experimentally studied dimer both the energy difference between peak A and B and the vibrational frequency are very similar, in these theoretically designed dimers these energies differ strongly and, thus, this assignment is unambiguous.

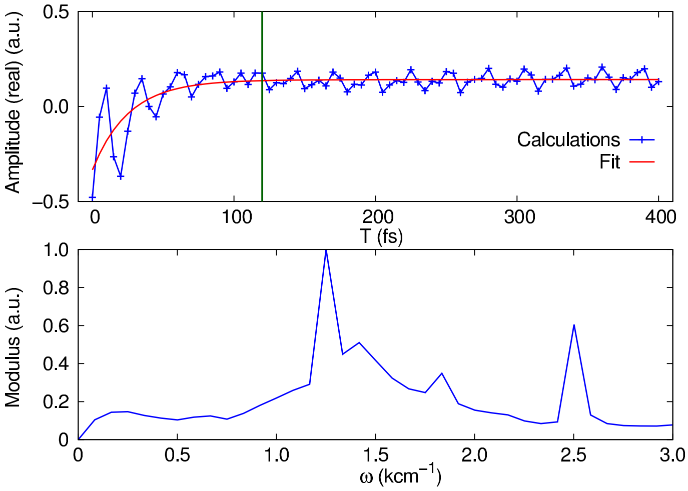

Figure 7.10: Kinetics of 2D spectra (top) for the peak position of $\omega_t = 17900$ cm^{-1} and $\omega_\tau = 19720$ cm^{-1}. The vertical line marks the time delay window used in the experiment of Ref. [129]. The Fourier transform of residuals (bottom) after a 3-exponential fit of kinetics reveals fast-decaying and long-lasting oscillations with the frequencies of ≈ 1400 cm^{-1}, a vibrational frequency ≈ 1230 cm^{-1}, and a high-frequency component ≈ 2500 cm^{-1} originating in the excited-state absorption. While the 1400 cm^{-1} - component has a rather broad spectral width, the accompanied vibrational component is very narrow.

This observation of an accurate coincidence of the frequencies of the long-lived oscillations and vibrational states can be understood using lowest-order perturbation theory. For the two equal monomers forming a dimer, standard perturbation theory for degenerate states yields a contribution in first order in U, while the electron-phonon coupling appears only in second order in κ. We find for the dimer energies of the state $|k = g/e, n = 0, 1, \ldots\rangle$ the expressions $E_{gn}^{(1)} = n\omega - U, E_{en}^{(1)} = E - \kappa^2/\omega + n\omega + U$, $E_{gn}^{(2)} = n\omega + U$ and $E_{en}^{(2)} = E - \kappa^2/\omega + n\omega - U$. Since these expressions only include the lowest order contributions, they can provide only the location of those peaks whose electronic or vibrational contribution is sizable. Inserting the values obtained from a fit to the linear absorption spectrum from above, we find the peaks at energies given by $E_{e0}^{(2)} = 17265$ cm^{-1}, $E_{e1}^{(2)} = 18495$ cm^{-1}, $E_{e2}^{(2)} = 19725$ cm^{-1} and $E_{e3}^{(2)} = 20955$ cm^{-1}. Also, the peaks at higher energies $E_{en}^{(1)} = E_{en}^{(2)} + 2U$ are present, although they are significantly smaller in amplitude. They follow as $E_{e0}^{(1)} = 19005$ cm^{-1}, $E_{e1}^{(1)} = 20235$ cm^{-1}, $E_{e2}^{(1)} = 21465$ cm^{-1} and $E_{e3}^{(1)} = 22695$ cm^{-1}. Fair enough, the accuracy of this lowest-order estimate is limited. Moreover, additional tiny peaks in the absorption spectrum are not covered by the lowest-order estimates of the energies and higher orders are required.

7.4.2 Controversy on the origin of the coherence

Over the last years, multidimensional ultrafast optical spectroscopy has been developed into a very successful probing tool [23, 58, 127, 128] aiming to reveal quantum coherent dynamics of excitonically coupled electronic states. The femtosecond time scale of the excitonic dynamics in photoactive molecular compounds and, especially, in natural photosynthetic units such as the antennae complexes and the reaction centers has become accessible (see, e.g., [49, 58, 59, 77, 101]).

While some 2D spectra at low temperature clearly display excitonic features in the form of well-resolved spectroscopic cross peaks [49, 58], at ambient temperature they are often fairly unstructured, and recovering of useful information about exciton states and their couplings is not possible. However, it has been reported that the measured sequences of 2D spectra taken at different "waiting" time delays T contain periodic oscillations in their amplitudes. Recent examples include the FMO complex [99, 100], photoactive marine cryptophyte algae [101], the bacterial reaction center and the light-harvesting complex LH2 of *Rhodobacter sphaeroides* [132, 133], the light-harvesting complex LHCII of the Photosystem II [49], and chlorosomes from the green sulfur bacterium *Chlorobaculum tepidum* [134]. Strong long-lived oscillatory components have been recently observed in the 2D photon echo spectra of artificial units at room temperature in J-aggregates [131]. These oscillations were initially attributed to the strong quantum coherent coupling between the excitonic states formed by interacting electronic states of the molecules [100, 101]. However, in addition to the purely electronic couplings [2], signatures of the vibrational DOF of the pigment-protein host [104] can also be accessed on the same spectroscopic footing. Any coherent coupling in general shows up in a sequence of 2D spectra in form of a coherent oscillatory time evolution of the amplitude of off-diagonal cross peaks. Long-lived electronic coherence are unexpected and have been proposed to affect the mechanism, the quantum yield, and the time scale of light harvesting [135, 136] in general. However, long-lived vibrational coherence are common and are not expected to strongly affect the light harvesting. Identifying the nature of this coherence, specifically the details of the involvement of vibrational effects into the excitonic dynamics, has thus become a hotly debated issue [88, 113, 114, 121, 137, 138, 139, 140, 141, 142, 143, 144, 145]. The decoherence rate reflects the magnitude of frequency fluctuations which arise from the coupling to the surroundings. Vibrational transitions have small fluctuations since the solvent interactions are not very sensitive to the vibrational state. However, electronic transitions show much stronger fluctuations, hence the faster decoherence (see Chapters 5 and 6 in Ref. [146]).

Natural molecular complexes are rather large and involve many neighboring excitonic states, broad spectral line shapes, and a complicated spectrum of vibrational modes. In turn, the ensuing strong spectral overlap of the excitonic and vibrational DOF renders it challenging to identify strongly overlapping cross peaks in the 2D-spectra. In addition, the complex protein environment could nebulize coherent electronic or vibrational transitions. Thus, to pinpoint the nature of the coherence, the artificial model dimer described in the Chapter which is much less complex in the electronic and vibrational structure and which can be chemically synthesized in a controlled way, is highly useful. Due to the strong excitonic coupling, small conformational variations lead to the well resolved peaks in 2D map shown in Fig. 7.4, which allow to study different dynamical behavior of electronic or vibrational originated peaks.

As shown above, we have rigorously established a vibronic exciton model, i.e., the need for a strong electron-vibration coupling in order to reproduce the experimentally measured absorption spectra of both the monomer and dimer. We found well separated peaks also in the calculated 2D photon echo spectra. These spectra agree well with experiment [129, 130]. On the basis of this accurate modeling of the real molecular complex, we have shown that the strong vibronic cross peaks, which occur in the 2D spectra, evolve in a quantum coherent manner over the *electronic* decoherence time (about of $\sim$ 50 fs). Their oscillation periods correspond to the vibronic splittings. Moreover, the theoretical model allows us to vary the angle between transition dipole moments of the two monomers “in theory” in a controlled way. This modifies the vibrational contributions to the exciton states and proves that the overall decoherence is dominated by the electronic dephasing. Likewise, it is essentially independent on the vibrational dephasing channel. These findings fully express the naive expectation that all vibronic states are subject to electronic dephasing and, thus, corresponding 2D signals must decay fast. Surprisingly, there is additionally a small slowly decaying oscillatory component which we observed by extending our simulations to delay times up to 400 fs. Its oscillation frequency exactly corresponds to the frequency of the vibrational transitions and their decay is caused by the weak vibrational decoherence and typically last up to several picoseconds for the C-C stretching mode. The associated frequency of $\simeq 1200$ cm^{-1} is determined by a weak delocalization with the electronic states. Thus, the overall kinetics of the spectral cross peaks has two clearly separated and distinguishable contributions: (i) The short lived and large-amplitude oscillations which are rapidly damped due to a strong electronic dephasing. The associated frequencies are determined by the vibronic splitting. In addition, (ii) there exist long-lasting, but small-amplitude oscillations whose life times and frequencies are determined by the inherent properties of the molecular vibrational states. Our results suggest a similar picture for the oscillatory behavior observed in photosynthetic complexes.

In the photosynthetic system, the intramolecular vibrational modes can be well resolved by a fluorescence or delta-fluorescence line-narrow experiment [147]. Vibrational frequencies and vibronic couplings (Huang-Rhys factor) can be estimated by fitting the data of the measured fluorescence spectrum. Relatively small Huang-Rhys factors were resolved, with a range of 0.01 to 0.05, which is much weaker than the vibronic coupling measured in current artificial dimer model (Huang-Rhys factor ~ 0.6). This may be caused by the correlation between the vibrational motion of the butyl chain and the molecular electronic wave function. It would be better for the study if molecule had a vibronic coupling comparable to the natural photosynthetic system. It could be an interesting challenge for the experiment to control the vibronic coupling strength. However, this is readily possible in the theoretical simulation. In Ref. [110], 2D spectra of the vibronic dimer model were calculated with weak, intermediate and strong vibronic couplings and it has been proved that the long-lived oscillations in the 2D experiment originate from the vibrational-assisted vibronic coherence.

Due to the complexity of the molecular structure in the photosynthetic system, theoretical predictions are always based on the system-bath model approach, in which the energetic structure is phenomenologically simplified as a quantum 'two-level system' and the environment is modeled as a reservoir of harmonic oscillators providing Gaussian quantum fluctuations. For an improved interpretation of the coherent coupling mechanism, an atomic view of the system should be developed for the study. For instance, the QM/MM approach is a molecular simulation method that combines the strengths of the QM (accuracy) and MM (speed) approaches, thus allowing for the study of photo-deactivation process in more complicated molecular structures [148]. However, it is still a challenge for this approach to study the nonequilibrium quantum dynamics with the laser-matter interactions included, especially, to deal with the feedback of the laser-induced dephasing between ground and excited states from the heat bath is challenging [149].

Chapter 8

The coherent modified Redfield quantum master equation

Due to the complexity of the natural photosynthetic systems and the artificial solar cells, the calculation of 2D electronic spectra is still a big challenge for the current computational resources. For instance, in order to properly include the laser-matter interaction, a rotational average and the averaging over static disorder has to be taken into account for the comparison between theory and experiment. For this, more than 6000 CPUs are used for the computation of the 2D spectra of the PSII reaction center in Chapter 5 for a given waiting time and it is not available for instance, for the study of the energy transfer or charge separation in the PSII core complex. It indeed requires one effective approach, which makes the simulation of large photosynthetic protein complexes accessible and, in the meantime, it should provide reliable results as well. In this chapter, we introduce a new efficient tool – the modified Redfield master equation to calculate 2D electronic spectra with relatively cheap calculations. In order to examine the reliability of the method, we compare its result to the numerically exact QUAPI method.

8.1 Available theoretical methods for dynamical simulations

To analyze the experimental findings in large and complex photoactive molecular complexes, a thorough comparison with theoretical calculations is essential, in order to arrive at a reliable interpretation of the measured 2D spectra. Since it is a difficult and computationally demanding task to determine 2D optical spectra, often only the population dynamics of exciton states is calculated. For the FMO complex, a rather small light-harvesting complex, the HEOM [109] was applied and quantum oscillations were observed on the time scale of the 2D experiments employing an environmental Debye model spectral density with rather small reorganization energy [110]. Employing the numerically exact quasi-adiabatic propagator path integral (QUAPI) allowed to use a more realistic measured environmental spectral density. This resulted in a decay of the decoherence faster than experimentally observed [112, 150]. This spectral density could, more recently, be used to calculate the 2D spectra of the FMO complex with the hierarchy equation [143] and a reasonable agreement between theory and experiment could be achieved. The calculations of QUAPI and the HEOM treated the coupling of the complex to environmental fluctuations numerically exactly. However, the computational effort is immense, which makes the simulation of larger light-harvesting molecular complexes (which contain, typically, dozens to hundreds of excitonic subunits) virtually impossible. The need for a highly efficient numerical tool to calculate 2D optical spectra of large molecular complexes with a reasonable numerical effort and a satisfactory accuracy still exists and it is expected to continue to increase.

Given their complex molecular structures, for the calculation of 2D spectra of large light-harvesters, approximate schemes are usually unavoidable. Standard Redfield equations [151], which invoke a lowest-order Born and a Markovian approximation, are good for weak system-bath coupling, but fail for strong coupling. The regime of intermediate system-bath coupling, as present for the exciton dynamics in photoactive complexes [55], is typically also not properly treated within Redfield equations [121, 152, 153]. Thus, the *modified* Redfield theory (MRT) has been widely used for the description of the energy transfer processes of large molecules [82, 154, 155, 156, 157, 158, 159]. In this approach, that contribution of the system-bath coupling Hamiltonian, which is diagonal in the eigenbasis of the system, is included fully, while a second-order perturbative approximation is used for the off-diagonal coupling terms. The equation of motion of the MRT includes a population transfer within the reduced density matrix, but the accompanying population-transfer induced dephasing is neglected. The accuracy of the MRT in view of the dynamics of the reduced density matrix has been analyzed in detail [160]. Moreover, MRT has been shown to have a somewhat wider range of applicability when compared to both the original Redfield and Förster theory [155]. Also, linear absorption spectra for an ensemble of B850 rings have been determined which shows that MRT includes non-Markovian effects which clearly show up in the high-energy part of the static absorption lineshapes [161]. Different energy transfer components of the LHCII trimer and phycoerythrin 545 have been revealed using MRT by simultaneous quantitative fits of the absorption, linear dichroism, steady-states fluorescence spectra, and transient absorption kinetics upon excitation at different wavelengths [52].

A more refined description of the quantum dissipative exciton dynamics is established in this chapter upon observing that the population-transfer induced electronic dephasing can be efficiently included in the quantum master equation. The off-diagonal terms in the quantum master equation now include the decoherence of excited states and electronic dephasing between ground and excited states by exploiting the relation $1/T_2 = 1/2T_1 + 1/T_2^*$ to estimate the different contributions to the dephasing rate, where T_2 is the transverse relaxation time and T_1, T_2^* are the longitudinal relaxation time and pure dephasing time, respectively. While working out the details with the results reported in this Chapter, this extended quantum master equation has also been independently put forward very recently in Ref. [162] and has been named the coherent modified Redfield theory (CMRT). To avoid confusion, we use this nomenclature also here.

For calculating 2D photon-echo spectra, essentially two different approaches are available. On the one hand, the response to the sequence of applied laser pulses can be calculated by evaluating the third-order optical response function [23]. Modified Redfield theory was successfully applied to simulate the 2D spectra of the double-ring LH2 aggregate of purple bacteria including both the B800 and the B850 ring [163]. An alternative approach to calculate 2D optical spectra, which is especially useful when finite durations of the laser pulses as well as pulse overlap effects are taken into account, is the equation of motion-phase matching approach (PMA) [87]. Using the PMA in combination with the conventional Redfield equations, 2D spectra of a single FMO subunit were studied, and the signature of energy transfer was revealed by well-resolved peaks in the simulation with adjustable pure dephasing of exciton states [164].

Although MRT is used to tackle many different problems in the study of energy transport in photosynthetic complexes, no investigation of its reliability in calculating nonlinear and, specifically, 2D optical spectra is at hand. In this Chapter, we first verify the CMRT approach by comparing the population dynamics of FMO exciton states with numerically exact results of the QUAPI approach. In addition, we combine the CMRT with the PMA to calculate 2D photon-echo spectra for a simple dimer model. Again, the results of CMRT+PMA are benchmarked against numerically exact results of the QUAPI approach. For the long-time steady state dynamics, the CMRT+PMA and QUAPI simulations show differences for intermediate and strong system-bath coupling. However, for intermediate coupling, as it is typical in photosynthetic complexes, the short time dynamics including dephasing times and coherent beating frequencies are well described by CMRT+PMA. Hence, an efficient numerical scheme to calculate 2D photon-echo spectra with a reasonable computational effort is now realized.

8.2 Coherent modified Redfield master equation

The coherent modified Redfield master equation can be derived from the Nakajima-Zwanzig equation [161] using a scheme for the separation of the total Hamiltonian which does not treat the whole system-bath interaction term H_{SB} perturbatively [152, 66]. Instead, the Hamiltonian is separated according to

$$\begin{aligned} H_0 &= H_S + H_B + \sum_{\mu} \left|\mu\right\rangle \left\langle\mu\right| H_{SB} \left|\mu\right\rangle \left\langle\mu\right| , \\ H' &= \sum_{\mu\nu,\mu\neq\nu} \left|\mu\right\rangle \left\langle\mu\right| H_{SB} \left|\nu\right\rangle \left\langle\nu\right| , \end{aligned} \tag{8.1}$$

where $|\mu\rangle$ are eigenstates of H_S and H' is the off-diagonal term of the system-bath interaction part in the exciton basis. In this basis, H_0 is diagonal and the matrix elements read

$$\langle\mu| H_0 |\mu\rangle = \epsilon_\mu - \lambda_{\mu\mu\mu\mu} + H_B(\mu), \tag{8.2}$$

where ϵ_μ is the μth excitonic level of the system Hamiltonian and

$$\lambda_{\mu\nu\mu'\nu'} = \sum_m \langle\mu| K_m |\nu\rangle \langle\mu'| K_m |\nu'\rangle \sum_j \frac{c_{mj}^2}{2m_{mj}\omega_{mj}^2}, \tag{8.3}$$

is the weighted reorganization energy. Moreover,

$$H_B(\mu) = \frac{1}{2}\sum_\xi \left[\frac{p_\xi^2}{m_\xi} + m_\xi\omega_\xi^2 \left(x_\xi + \sum_k \frac{\langle\mu| K_k |\mu\rangle}{m_\xi\omega_\xi^2}\right)^2\right], \tag{8.4}$$

describes a bath of harmonic oscillators with mass m_ξ, frequency ω_ξ and momentum p_ξ, shifted due to the coupling with the exciton state $|\mu\rangle$.

In addition to the redefinition of the system and the bath Hamiltonian, one has to define a different type of projection operator which only projects on the diagonal part of the system density matrix in the eigenstate basis. This is achieved by

$$\widetilde{P} = \sum_{\mu=0}^{N} P_\mu \quad \text{with} \quad P_\mu \cdot \ = R_{eq}^\mu \mathrm{tr}\{|\mu\rangle\langle\mu| \cdot\}, \tag{8.5}$$

where P_μ is the projector onto the μth excitonic state and $R_{eq}^\mu = \exp(-\beta H_B(\mu))/Z_{eq}^\mu$ is the equilibrium density matrix of the bath when the system is in the excitonic state $|\mu\rangle$. Here, $Z_{eq}^\mu = \mathrm{tr}\exp(-\beta \mathrm{H_B}(\mu))$ with $\beta = 1/(k_B T)$ and T being the temperature.

Inserting these definitions into the Nakajima-Zwanzig equation, determining H' up to second order and invoking the time-dependent population transfer rate, one obtains an equation of motion for the population transfer terms in the form

$$\frac{\partial}{\partial t}\rho_{\mu\mu}(t) \;=\; \sum_{\nu\neq\mu}[R_{\mu\mu\nu\nu}(t)\rho_{\nu\nu}(t) - R_{\nu\nu\mu\mu}(t)\rho_{\mu\mu}(t)], \tag{8.6}$$

with the population transfer rates [154]

$$\begin{aligned} R_{\mu\mu\nu\nu}(t) &= 2\,\mathrm{Re}\int_0^t d\tau \mathrm{tr}\{|\nu\rangle\langle\nu|\exp(-iH_0\tau)H'|\mu\rangle\langle\mu| \times R^{\mu}_{eq}\exp(iH_0\tau)H'\}, \\ &= 2\,\mathrm{Re}\int_0^t d\tau\exp[-i\omega_{\mu\nu}\tau - g_{\mu\mu\mu\mu}(\tau) - g_{\nu\nu\nu\nu}(\tau) \\ &+ g_{\nu\nu\mu\mu}(\tau) + g_{\mu\mu\nu\nu}(\tau) - 2i(\lambda_{\nu\nu\nu\nu} - \lambda_{\mu\mu\nu\nu})\tau] \\ &\times\{\ddot{g}_{\mu\nu\nu\mu}(\tau) - [\dot{g}_{\nu\mu\nu\nu}(\tau) - \dot{g}_{\nu\mu\mu\mu}(\tau) + 2i\lambda_{\nu\mu\nu\nu}] \\ &[\dot{g}_{\nu\nu\mu\nu}(\tau) - \dot{g}_{\mu\mu\mu\nu}(\tau) + 2i\lambda_{\mu\nu\nu\nu}]\}. \end{aligned} \tag{8.7}$$

Here, $\omega_{\mu\nu} = \epsilon_\mu - \epsilon_\nu$. The lineshape function $g_{\mu\nu\mu'\nu'}(t)$ can be written as the two-time integral of the bath correlation function according to

$$\begin{aligned} g_{\mu\nu\mu'\nu'}(t) &= \sum_k \langle\mu| K_k |\nu\rangle \langle\mu'| K_k |\nu'\rangle \int_0^t d\tau \int_0^\tau d\tau' C(\tau'), \\ \text{with } C(t) &= \int_{-\infty}^{\infty}\frac{d\omega}{\pi}J(\omega)\frac{e^{i\omega t}}{e^{\beta\omega}-1}. \end{aligned} \tag{8.8}$$

To obtain Eq. (8.7), we have used the cumulant expansion up to second order in the system-bath coupling and have taken the independent bath model into account. The absorption lineshape within the CMRT is given by

$$I(\omega) = \mathrm{Re}\sum_\mu d_\mu \int_0^\infty dt\exp\left[i(\omega-\omega_{\mu0})t - g_{\mu\mu\mu\mu}(t) - \frac{1}{2}\sum_{\nu\neq\mu}\int_0^t R_{\mu\mu\nu\nu}(\tau)\right]. \tag{8.9}$$

as detailed in Ref. [161].

Up to this point, Eq. (8.6) constitutes the modified Redfield theory, as developed and applied in Refs. [82, 154, 155, 156, 157, 158, 159]. Based on the population transfer term in Eq. (8.6), we extend the quantum master equation by including also the coherence (or, off-diagonal) terms of the reduced density matrix. The resulting coherent modified Redfield quantum master equation now reads

$$\frac{\partial}{\partial t}\rho(t) \quad = \quad -i[H+F(t),\rho(t)] - \Re\{\rho(t)\}\,, \tag{8.10}$$

where $F(t)$ is the time-dependent system-field interaction term.

The relaxation and dephasing operator $\Re\{\rho(t)\}$ now also includes diagonal and off-diagonal terms. The diagonal part of the relaxation operator, which was described in Ref. [165], reads

$$\Re\{\rho(t)\}_{\mu\mu} = \sum_{\nu\neq\mu}[R_{\mu\mu\nu\nu}(t)\rho_{\nu\nu} - R_{\nu\nu\mu\mu}(t)\rho_{\mu\mu}]\,. \tag{8.11}$$

The off-diagonal terms $\Re\{\rho(t)\}_{\mu\nu}$ are now included in order to describe decoherenece of excited states and electronic dephasing between the ground and excited states. Here, we use an efficient way to obtain the associated rates by exploiting the relation $1/T_2 = 1/2T_1 + 1/T_2^*$ to estimate the different contributions to the dephasing rate. T_2 is the transverse relaxation time, T_1, T_2^* are the longitudinal relaxation time and pure dephasing time, respectively [146]. In detail, $1/T_1 = \sum_{e\neq\mu} R_{\mu\mu ee} + \sum_{e\neq\nu} R_{\nu\nu ee}$ and $1/T_2^*$ is given by the first derivative of lineshape function $g_{\mu\mu\nu\nu}(t)$. Therefore, the off-diagonal terms of the excited states and between the ground and excited states can be written as

$$\begin{aligned}
\Re\{\rho(t)\}_{\mu\nu} &= \left[\frac{1}{2}\left(\sum_{e\neq\mu} R_{\mu\mu ee}(t) + \sum_{e\neq\nu} R_{\nu\nu ee}(t)\right) + \dot{g}_{\mu\mu\nu\nu}(t)\right]\rho_{\mu\nu}(t), \\
\Re\{\rho(t)\}_{\mu 0} &= \left[\frac{1}{2}(\sum_{m\neq n} R_{mmnn}(t) + \sum_{n\neq m} R_{nnmm}(t)) + \dot{g}_{\mu\mu\mu\mu}(t)\right]\rho_{\mu 0}(t).
\end{aligned} \tag{8.12}$$

This extended quantum master equation has also been independently put forward very recently in Ref. [162] and has been named the CMRT. It is an efficient, but approximate way to take into account population transfer and dephasing on the same footing.

8.3 Perturbative method versus iterative path-integral algorithm

In order to verify the reliability of the CMRT, we present the population dynamics of the FMO complex calculated by CMRT and compare the results to those obtained by the numerically exact QUAPI method. In Fig. 8.1, the population dynamics of selected FMO sites is shown for $T = 77$ K for two different initial conditions. In Fig. 8.1a), we assume the energy transfer to start from site 1. We monitor then the full transfer which involves all seven FMO sites. For simplicity, we only show the population dynamics of the sites 1, 2, and 3. Alternatively, the energy transfer may be assumed to start from site 6, see Fig. 8.1b). There, we depict the population dynamics of the relevant sites 3, 5, and 6. We observe that the oscillatory behavior of the populations is captured by both approaches. Both also yield the same decay rates and periods of oscillations. However, a phase shift of the oscillations occurs between the CMRT and QUAPI results. Energy transfer is believed to be related to the population of the FMO site 3 (green symbols and lines) which has the lowest energy in the FMO monomer. In our comparison, CMRT slightly overestimates the population transfer efficiency towards site 3. All in all, the CMRT results for the FMO exciton population dynamics are in good agreement to the numerically exact QUAPI results. Since the system-bath coupling parameters of the FMO complex are typical for natural photosynthetic units, we conclude that CMRT is a useful tool to study their exciton dynamics.

To obtain 2D spectra, we combine the CMRT next with the PMA. This constitutes a very efficient approximate numerical tool whose reliability is assessed by a comparison with 2D spectra obtained by QUAPI. Since 2D spectra involve extended numerical calculations, QUAPI results are available only for small model systems with present day hardware technology. For such a comparison, we present the calculated results for the dimer model. It allows us to study energy transfer and dephasing (homogeneous broadening) as building blocks of the exciton dynamics in larger molecular compounds. It can still be treated by QUAPI with reasonable numerical effort.

Fig. 8.2 (left) shows 2D spectra of the dimer calculated by CMRT+PMA for λ=50

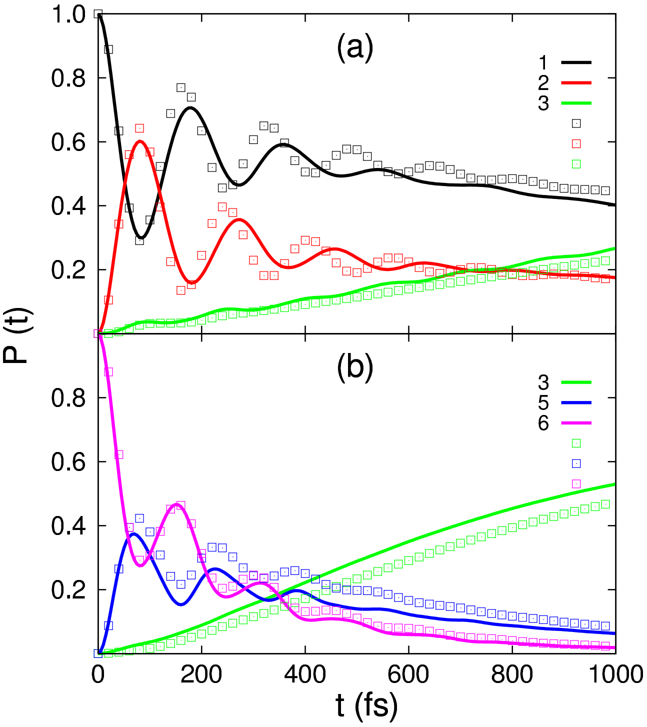

Figure 8.1: Population dynamics of selected FMO sites. In a), the population of sites 1 (black), 2 (red) and 3 (green) with the initial condition $\rho(1,1) = 1$ is shown, while in (b) the populations of sites 3 (green), 5 (blue) and 6 (magenta) with the initial condition $\rho(6,6) = 1$ is depicted (symbols: QUAPI, full lines: CMRT) for the parameters as given in the text.

cm^{-1} and the other parameters as indicated above. They are compared to QUAPI results (right column in Fig. 8.2) for waiting times $T = 0$ fs, 50 fs, 100 fs and 500 fs. These 2D spectra show two diagonal peaks (labeled A, B) which correspond to the two exciton states. Moreover, two cross peaks (labeled C and D) arise due to the excitonic coupling between them. For the sake of simplicity and clarity of the comparison, inhomogeneous broadening and the rotational averaging for different laser polarizations and molecular orientations are not performed here. Although this would be important to describe realistic experimental situations, the averaged results generally show smaller discrepancies (not shown).

At $T = 0$ fs, the two results show the same profile for diagonal and cross peaks and, indeed, the agreement is excellent. This shows that the CMRT correctly models the coherence times and the system-bath correlations created during the simulation. With increasing waiting time, the same coherent dynamics is found for both the diagonal and the cross peaks and even can be inspected by eye. However, some disagreement is observed for the long waiting time $T = 500$ fs. The diagonal peak B in the left figure (CMRT+PMA) shows a somewhat reduced amplitude as compared to the right figure (QUAPI).

For a more refined comparison, the amplitudes of the diagonal and cross peaks (A, B, C and D) are plotted against the waiting time in Fig. 8.3 and Fig. 8.4. In Fig. 8.3, the population dynamics of the diagonal peaks A (top) and B (bottom) calculated by CMRT+PMA from 0 to 1000 fs is shown and compared to the QUAPI result. We find that the CMRT+PMA provides reasonably accurate results for the population transfer and the oscillation period. However, the amplitude of peak B decays slightly faster in the approximate results as compared to the QUAPI data. Moreover, both

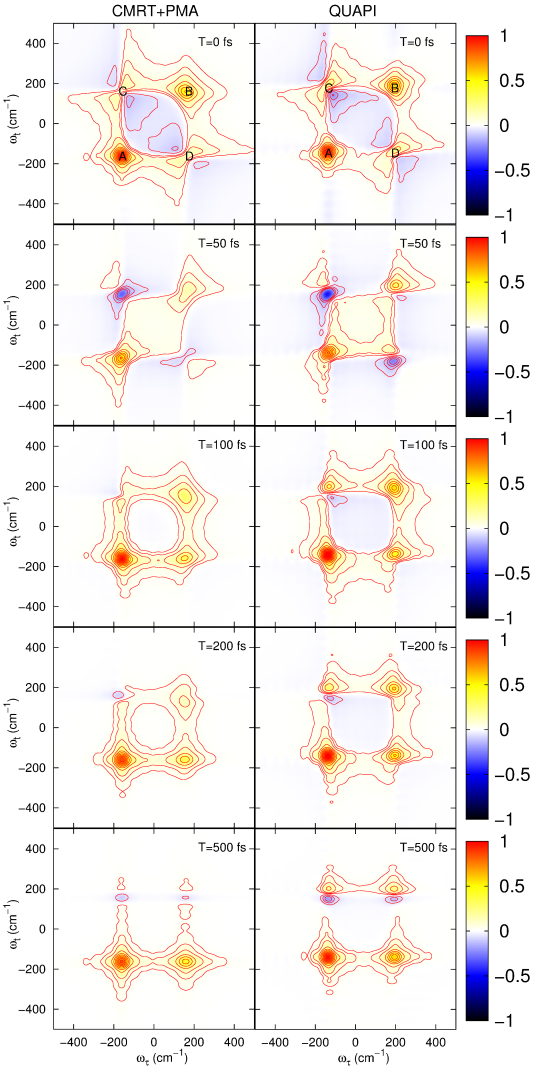

Figure 8.2: Two-dimensional photon-echo spectra (real part) of a dimer model calculated by CMRT+PMA (left) and QUAPI (right) for different waiting times as indicated. The Debye spectral density is used for the calculation with the parameters $\lambda = 50$ cm^{-1}, $\gamma = 100$ cm^{-1} and the temperature is set to $T = 77$ K.

yield different stationary states. In addition, the phase of the oscillations is slightly shifted. For the comparison of the cross peaks, the oscillatory behavior of peaks C and D is plotted in Fig. 8.4. Cross peak C shows a similar oscillatory behavior but the two approaches yield different stationary states. Peak D shows a only slightly shifted phase of the oscillatory behavior. Such a phase shift was also observed in the population dynamics of the FMO complex shown above. The phase shift might be due to the neglect of imaginary parts in the Redfield relaxation tensor.

In order to further assess the reliability of the CMRT+PMA, we have repeated the calculations for a larger reorganization energy, i.e., for λ=100 cm^{-1} (with γ=100 cm^{-1} kept unchanged). 2D spectra were again calculated by both approaches and the amplitude of the labeled peaks were extracted. Their time-dependence is plotted in Figs. 8.5 and 8.6. CMRT+PMA still yields quantitative agreement with the QUAPI result except for the behavior of the damping. The stronger system-bath coupling results in faster damping (diagonal peak A) and also in an increased difference between QUAPI and CMRT+PMA as compared to the weaker coupling with λ=50 cm^{-1}.

From the above comparison of the results obtained by both approaches, we observe that the discrepancies found in the 2D calculations are more pronounced than in the dynamics of the populations. Put differently, nonlinear 2D spectra are more sensitive to assess the performance and reliability of approximate theoretical approaches. In order to understand this, we point out two fundamental differences between 2D

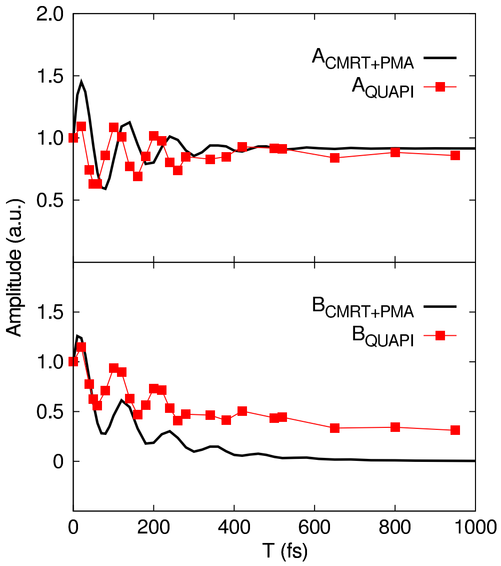

Figure 8.3: Population dynamics of the labeled diagonal peaks (A, B) extracted from the underlying sequence of 2D maps. The two approaches yield the same oscillation period. The diagonal peak B obtained from CMRT+PMA decays faster as compared to the QUAPI result. The oscillation periods can be extracted by data fitting and are: CMRT+PMA: 110fs, QUAPI: 99fs.

spectra and the population dynamics. First, entanglement between the system and the bath leads to initial correlations at the beginning of the waiting time window, which are absent in the calculation of the population dynamics. Second, two-exciton states contribute to the 2D spectra during the detection time, and interference between positive and negative peaks changes the observed amplitudes. This shows that one can not understand the reliability of a method to simulate correct 2D spectra by

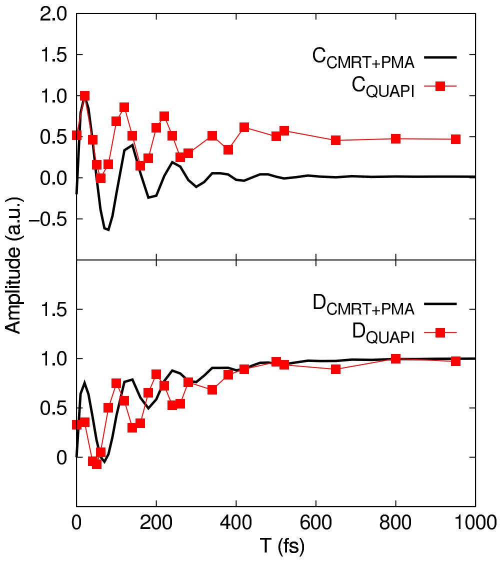

Figure 8.4: Coherent oscillations of labeled cross peaks (C, D) extracted from 2D maps. The cross peak C obtained by CMRT+PMA shows the same oscillatory behavior, but with a somewhat smaller amplitude.

calculating population dynamics alone. Our current framework, in which we use the combined CMRT+PMA and compare the results with QUAPI, is well suited to show the performance of these methods in understanding 2D spectra directly.

In more detail, we have observed three noticeable discrepancies of the CMRT+PMA as compared to QUAPI: i) A shifted oscillation phase of peak intensities, ii) a slightly faster decay, and, iii) a different amplitude of peaks B and C for long waiting times.

For the explanation of the shifted oscillation observed in 2D simulations of the CMRT+PMA, we need to notice that Eqs. (8.11) and (8.12) provide the analytic result for a monomer (two-level system), and that this has been proven by comparing to QUAPI [166]. However, CMRT yields a shifted period for the dimer model. The mismatch is mainly caused by the population transfer term $R(t)$ since there is no population transfer term in the monomer model. Here, the population transfer rate was calculated by the cumulant expansion in Eq. (8.7) [154] and we only took the real part. It is well known that the imaginary part dominates the phase of the oscillations [167]. So, most likely, the shifted oscillation is mainly caused by the real-valued approximation of the population transfer rates.

Then, the population transfer term is also derived based on the second-order perturbation approximation, which is one of the reasons for the explanation of the slightly too fast decay of the oscillations found in CMRT calculations. Furthermore, the secular approximation was used to separate the population dynamics and the dephasing process in Eqs. (8.11) and (8.12). This also contributes to the discrepancy in the decay rate, since it neglects the interference between population transfer and coherence dephasing.

A relatively small amplitude of peak B and C was found in Fig. 8.3 and Fig. 8.4 and it also can be observed by eye in the 2D map for the long waiting time $T = 500$ fs. We observe that peaks B and C are mainly formed by one positive (red) peak and the overlap with a negative (blue) peak in the 2D spectrum ($T = 500$ fs). Therefore, the amplitude of those peaks mainly depends on the overlap of two peaks. In the

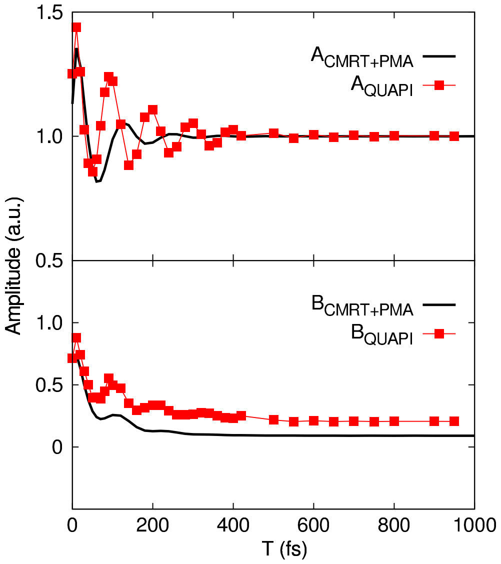

Figure 8.5: Amplitude of the diagonal peaks A and B for a stronger system-bath coupling λ=100 cm^{-1} (with γ=100 cm^{-1} unchanged). CMRT+PMA calculations yield a faster decay (A) as compared to the QUAPI result (decay time constants extracted from a fit: CMRT+PMA: 81 fs, QUAPI: 146 fs).

QUAPI result, the two peaks are clearly separated with a larger spectral distance than in the CMRT result and this leads to the larger amplitude of peaks B and C in the 2D spectrum calculated with QUAPI. It indicates that, besides the shifted oscillation and the faster decay of the oscillation, CMRT does not properly account for the reorganization energy by the heat bath (diagonal peaks show slightly different positions in the 2D map: -190 cm^{-1} and 190 cm^{-1} for CMRT and -180 cm^{-1} and 200 cm^{-1} for QUAPI). In the CMRT, the reorganization energy is included in the

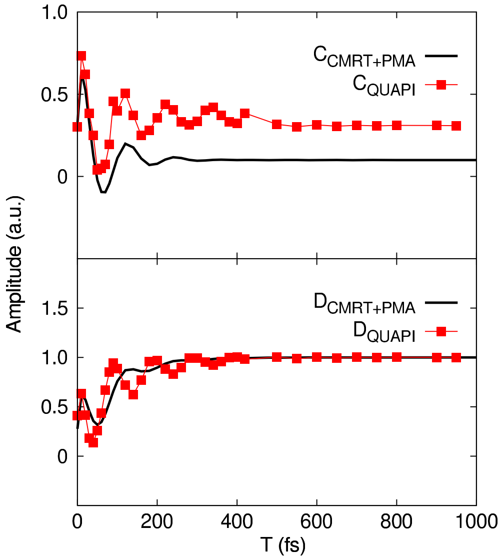

Figure 8.6: Oscillations of the cross peaks (C, D) with for a stronger system-bath interaction (same parameters as in Fig. 8.5). The cross-peak C calculated by CMRT+PMA yields a faster decay and a smaller amplitude (decay time constants as obtained from a fit: CMRT+PMA: 62 fs, QUAPI: 177 fs).

diagonal part of the Hamiltonian of Eq. (8.3), where it just brings in a shift of the excitonic transition frequency E_μ by the renormalization term Eq. (8.3) and does not affect the dynamics of the off-diagonal terms in the Hamiltonian of Eq. (8.1).

On the basis of a clear physical meaning (population transfer and dephasing terms) and for the purpose of an efficient and fast calculation, the secular approximation and the second-order perturbation theory were applied to construct the CMRT. On the one hand, the secular approximation leads to a separation of the population dynamics and dephasing process and avoids any complicated interaction terms between diagonal and off-diagonal parts in the equation. On the other hand, the second-order perturbation theory simplifies the population transfers. It is possible to improve the approach by including higher orders. However, this renders the practical calculation considerably more complicated and requires more computational resources for the simulation. It is a priori unclear how much this improves the accuracy at all.

Chapter 9

Quantum dynamics in the vicinity of conical intersection

In the last chapter, I have provided a simple scheme to calculate the 2D electronic spectrum for the study of the energy transport and the charge separation for complicated natural photosynthetic complexes. In this chapter, I provide one effective approach to significantly reduce the computation for the study of the dynamics of an electronic wave packet on the PESs in the vicinity of a conical intersection (CI), which is a degenerate point between PESs. The nonadiabatic coupling at the CI prevail and the Born-Oppenheimer approximation breaks down. This strong vibronic coupling provides a way to control the dynamics of electronic wave packet by the vibrational oscillations. Here, I study the impact of the vibrational coherence on the motion of the electronic wave packet at the CI. I find that the more coherent wave packet results in a higher quantum efficiency of photoisomerization. This study provides the background to support the quantum coherent-control experiments.

9.1 Introduction

A conical intersection is a degenerate point of two PESs in the configuration space of a polyatomic molecule. This degeneracy between two PESs induces a strong nonadiabatic coupling between the electronic states, such that the Born-Oppenheimer approximation breaks down and, in general, an ultrafast electronic and vibrational relaxation results [168, 169, 170, 171]. Due to the strong nonadiabatic coupling of the electronic to the vibrational DOF, the molecular electronic dynamics can be monitored by studying the vibrational coherence of the electronic wave packet along the reaction coordinates.

Various coherent spectroscopic techniques are useful tools to study the wave packet dynamics in the vicinity of the CI. Among them, the femtosecond stimulated Raman spectroscopy (FSRS) is one of the powerful tools to reveal the changes of the vibrational coherence in the molecule moving in the vicinity of the CI [172]. FSRS has been used to study the photoisomerization of rhodopsin, which was estimated to occur within a timescale of 200 fs or less [173]. The structural evolution of the stilbene photoisomerization has been tracked by the gradual shift of the associated vibrational frequency over time [174]. The proton transfer in the Green Fluorescent Protein has been revealed by FSRS [175]. More recently, two-dimensional time-resolved stimulated Raman spectroscopy has been applied to measure the vibrational coherence of a charge-transfer dimer. Thereby, the anharmonicity of the vibrational coherence on the excited PESs has been clearly revealed [176]. Moreover, the transient absorption spectroscopy is another diagnostic tool to uncover how the atom in the reactants moves during the formation of the product. The motion of the electronic wave packet in the primary photoisomerization reaction has been resolved by the transient absorption measurement [177]. A frequency shift due to the stimulated emission of the electronic wave packet on the excited state surface was observed. Furthermore, by tracking the vibrational coherence on the PESs, it was shown that the stretch mode in the retinal molecule is largely unaffected by the presence of the CI, while the hydrogen-out-of-plane (HOOP) mode is strongly damped after passing through the CI [178]. In addition, the high-order anharmonic couplings between different vibrational modes on the excited state surface have been well-resolved by the transient absorption spectroscopy [179]. Recently, using an ultrashort pulse and exploiting the sensitivity of the heterodyne detected transient grating approach, the local vibrational coherence of the effective modes has been identified to drive the primary photo-isomerization in vertebrate vision [180]. This measurement has refined the timescale of the primary step in vision and the passage through the CI was shown to occur within 50 fs. This has also been confirmed by the two-dimensional electronic spectroscopy [181], which indicates that the relevant reaction dynamics occurs under the vibrational coherent process before decoherence of the reaction coordinates sets in. This directly implies that the vibrational coherence can be used to control the dynamics and the efficiency of the photoisomerization. The coherent control of the primary step of the photoisomerization of rhodopsin has been demonstrated by modulating the phase and the amplitude of the excitation laser pulse in the transient absorption spectroscopy [182]. The isomerization efficiency has been increased and decreased by 20% by using the optimal or anti-optimal pulse shape. It was not possible to observe the same effects with all phase control only [183]. Although the phase-only aspect was only a few percent, it could be argued that the noise level of 4% in this experiment would make it difficult to observe such an effect. The question then is what is the physics at work and to what degree can the reaction dynamics be controlled at CIs.

Theoretically, in a minimal model, the physics of a CI can be described by the two-state two-mode model [184]. The transient absorption spectroscopy of the two-state two-mode model has been calculated for the cis-trans isomerization [185]. The wave packet on the PESs is projected onto the effective reaction coordinates of the tuning and coupling modes, respectively. Its dynamics was calculated by using quantum master equations, e.g., by the Redfield master equation [186] or the HEOM [187]. In this chapter, this model is now further simplified by transferring the tuning and coupling modes to the harmonic bath and solving the resulting non-Markovian dynamics by a numerically exact approach [188]. By this, the model, in principle, can describe the configuration with multiple CIs between the PESs, which is more close to a realistic situation. Moreover, 2D electronic spectroscopy has been applied to study the electronic wave packet dynamics in the vicinity of the CI [189, 190, 191]. It has been found that the excited-state absorption becomes significant when compared to the model where only vibrational coupling is present. In addition, it has been proposed to use vibrational coherence in 2D spectra to measure the interstate coupling near a CI [192]. More recently, a numerical calculation has shown that photorelaxation in Uracil can be fully modulated to form the long-lived excited state by a properly shaped laser pulse [193].

The kinetic energy of the wave packet on the PESs is considered as one tool to control the photoisomerization efficiency in the CI [194]. More details of the coherent control of the electron-nuclear dynamics at the CI have been provided recently [195]. In Ref. [196], the role of vibrational coherence of an electronic wave packet moving in the vicinity of a CI has been investigated. Evidence has been provided that the quantum yield and the isomerization rate both are strongly related to the vibrational coherence. This was shown by calculating the transient absorption and the 2D electronic spectra of the three-state two-mode model. The time evolution of the electronic wave packet in the transient absorption spectrum has been tracked and, counterintuitively, it was found that the more coherent wave packet results in a higher quantum yield, but with a larger isomerization time constant. However, the full picture of the nonadiabatic dynamics of an electronic wave packet near a CI is still unclear and the direct evidence of the impact of vibrational coherence on the quantum efficiency is still missing.

Then, we study the impact of vibrational coherence on the quantum yield and the isomerization rate of an electronic wave packet moving in the vicinity of a CI by monitoring the nonadiabatic dynamics of the wave packet projected onto the tuning and the coupling mode. This allows us to directly visualize the quantum yield and its isomerization time constant (or, rate). By varying the strength of the dissipative coupling of the vibrational modes to their respective baths, we find that the quantum yield can be significantly enhanced by an increased vibrational coherence of the wave packet. In fact, the generated quantum yield can reach up to 93% for the most coherent wave packet and it can be significantly reduced to 50% for an electronic wave packet which experiences strong vibrational damping. In addition, we find in the case of stronger damping that the electronic wave packet directly penetrates the higher-lying PES to the lower electronic state via tunneling, before the remaining parts of the wave packet reach the seam of the CI and can pass directly through. The direct tracking of the dissipative wave packet motion provides an elegant experimental tool to reveal the role of vibrational dissipation at a CI.

9.2 Reduced two-state two-mode model

We start with two-state two-mode model in which a molecule is assumed to possess a spectroscopically accessible CI between two PES associated to the ground ($|g\rangle$) and excited ($|e\rangle$) electronic state. In addition, we include a dissipative interaction of the standard harmonic environment. The total Hamiltonian can be written as $H = H_{\mathrm{mol}} + H_{\mathrm{env}}$. The molecular Hamiltonian is given by $H_{\mathrm{mol}} = H_g + H_e$, with $H_g = |g\rangle (h_1 - \epsilon/2) \langle g|$ and $H_e = |e\rangle (h_2 + \epsilon/2) \langle e| + (|e\rangle V \langle g| + h.c.)$. Here, ϵ is the energy gap between the ground and the excited state and $\hbar = 1$. The vibrational Hamiltonians h_1, h_2 are associated to the ground and excited electronic state, respectively. They include two vibrational modes, the coupling mode characterized by the reaction coordinate Q_{c}, and the tuning mode described by the reaction coordinate Q_{t}. They are given by $h_g = \frac{1}{2} \sum_{i=\mathrm{c/t}} \Omega_i (P_i^2 + Q_i^2)$ and $h_1 = h_g - \kappa Q_{\mathrm{t}}$, $h_2 = h_g + \kappa Q_{\mathrm{t}}$, where $\Omega_{i=\mathrm{c/t}}$ are the frequencies of the harmonic coupling and tuning mode, respectively. Moreover, κ is the vibronic coupling strength. The electronic coupling between the two PESs is assumed to linearly depend on Q_{c}, such that $V = \Lambda Q_{\mathrm{c}}$ with the electronic coupling strength Λ. Furthermore, we assume that all relevant interactions between the two electronic PESs are captured by the coupling mode which is explicitly included. Thus, the bath only couples vibrational states within the same electronic PES and we assume that the two vibrational modes are coupled to their own linear bath according to the

Hamiltonian [16]

$$
\begin{aligned}
H_{\mathrm{env}} =& \sum_{\alpha} \left[\frac{p_\alpha^2}{2m_\alpha} + \frac{m_\alpha \omega_\alpha^2}{2} \left(x_\alpha + \frac{c_\alpha Q_1}{m_\alpha \omega_\alpha^2} \right)^2 + \right. \\
& \left. \frac{q_\alpha^2}{2M_\alpha} + \frac{M_\alpha \nu_\alpha^2}{2} \left(y_\alpha + \frac{d_\alpha Q_2}{M_\alpha \nu_\alpha^2} \right)^2 \right].
\end{aligned}
\tag{9.1}
$$

Here, the momenta of the bath oscillators are denoted as p_α and q_α, while their coordinates, masses, and frequencies are denoted by $x_\alpha, m_\alpha, \omega_\alpha$, and $y_\alpha, M_\alpha, \nu_\alpha$. The respective coupling constants are c_α and d_α. The baths are characterized by the spectral densities $J_{\mathrm{c}}(\omega) = \frac{\pi}{2} \sum_\alpha \frac{c_\alpha^2}{m_\alpha \omega_\alpha} \delta(\omega - \omega_\alpha)$ and $J_{\mathrm{t}}(\omega) = \frac{\pi}{2} \sum_\alpha \frac{d_\alpha^2}{M_\alpha \nu_\alpha} \delta(\omega - \nu_\alpha)$. Throughout this work, we assume that both the tuning and coupling mode experience fluctuations with an Ohmic spectral distribution according to $J_{\mathrm{c/t}}(\omega) = \eta_{\mathrm{c/t}} \omega$. Here, $\eta_{\mathrm{c/t}}$ are the damping strengths for the coupling and tuning mode, respectively. The transition dipole moment is defined within the Condon approximation as $\mu = |e\rangle \langle g| + |g\rangle \langle e|$.

A well separated PES crossing can be induced by a large shift $\Delta = 2\sqrt{2}\kappa/\Omega_{\mathrm{t}}$ between the minima of the $|g\rangle$ and $|e\rangle$-PES. In order to obtain converged numerical results, a large number of vibrational states is required [189]. This is possible in the regime of a weakly damped vibrational dynamics within the Born-Markov approximation. Numerically exact methods such as, e.g., the quasiadiabatic propagator path integral [197, 198] or the hierarchy equation of motion (HEOM) [199, 200] technique are not applicable due to the large vibrational Hilbert space, especially when the vibrational damping is strong.

However, a numerically exact treatment becomes possible if the two modes Q_1 and Q_2 are transformed into the bath and treated as effective modes with their full non-Markovian dynamics.[198, 201] The unitary transformation of Ref. [201] is readily generalized to the two-mode case and yields the total Hamiltonian

$$\begin{aligned} H_{\rm M} = \frac{\epsilon}{2}\sigma_z \quad &- \quad \sigma_x \sum_\alpha c'_\alpha x'_\alpha + \sum_\alpha \left[\frac{p'^2_\alpha}{2m'_\alpha} + \frac{m'_\alpha \omega'^2_\alpha}{2} x'^2_\alpha \right] \\ &- \quad \sigma_z \sum_\alpha d'_\alpha y'_\alpha + \sum_\alpha \left[\frac{q'^2_\alpha}{2M'_\alpha} + \frac{M'_\alpha \nu'^2_\alpha}{2} y'^2_\alpha \right] . \end{aligned} \tag{9.2}$$

Here, $\sigma_z = |g\rangle\langle g| - |e\rangle\langle e|$ and $\sigma_x = |g\rangle\langle e| + |e\rangle\langle g|$ are Pauli matrices. The resulting effective spectral densities follow as

$$J^{\rm eff}_{\rm c/t}(\omega) = \lambda_{\rm c/t} \frac{\gamma_{\rm c/t}\Omega^2_{\rm c/t}\omega}{(\Omega^2_{\rm c/t} - \omega^2)^2 + \gamma^2_{\rm c/t}\omega^2}, \tag{9.3}$$

where $\lambda_{\rm c} = \Lambda^2/(2\Omega_{\rm c})$, $\lambda_{\rm t} = \kappa^2/(\Omega_{\rm t}) = \frac{1}{2}\Omega_{\rm t}(\Delta/2)^2$ are the reorganization energies for the coupling and tuning mode, respectively. They represent two effective structured harmonic reservoirs for the electronic dynamics, when both are assumed to initially be in thermal equilibrium at the same temperature $\mathcal{T}$. In this effective picture characterized by Eq. 9.2, the coupling strength between the ground and excited PES can be tuned by the reorganization energy λ_c. The shift between the ground and the excited PES is encoded in the magnitude of the reorganization energy λ_t [202]. We have assumed the shift Δ to be large, a large reorganization energy for tuning mode results and leads to the system-bath interaction of Eq. 9.2, valid in the strong coupling region. The structured environment is characterized by the two localized modes

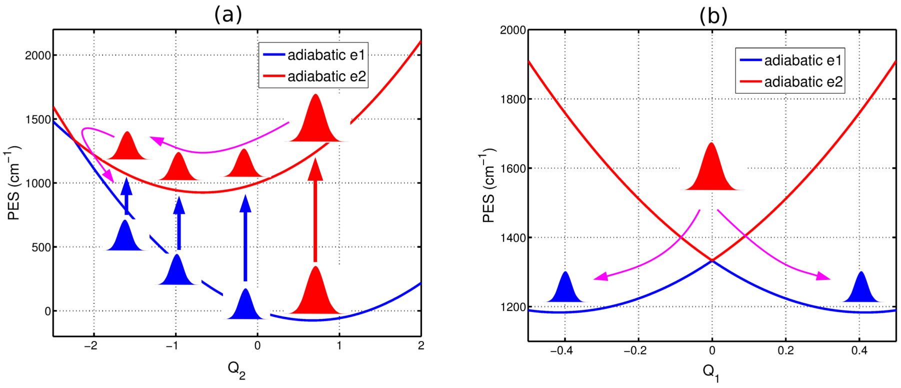

Figure 9.1: CI of two PESs illustrated along the tuning (Q_2 in (a)) and coupling (Q_1 in (b)) direction for the ground and excited states in the adiabatic basis, respectively.

which induce two spectral peaks at the frequencies Ω_i with the widths given by γ_i. In the present chapter, we are interested in the most difficult case when the vibrational relaxation of the two modes is overdamped. Hence, in the limit $\gamma_{\mathrm{c/t}} \gg \Omega_{\mathrm{c/t}}$, we obtain

$$J^{\mathrm{eff},\infty}_{\mathrm{c/t}}(\omega) = \lambda'_{\mathrm{c/t}} \frac{\gamma'_{\mathrm{c/t}}\omega}{\omega^2 + \gamma'^2_{\mathrm{c/t}}} \, . \tag{9.4}$$

The effective reorganization energies and damping constants in the overdamped limit follow as $\lambda'_{\mathrm{c/t}} = \lambda_{\mathrm{c/t}}$ and $\gamma'_{\mathrm{c/t}} = \Omega^2_{\mathrm{c/t}}/\gamma_{\mathrm{c/t}}$.

9.3 Signature of the conical intersection in the 2D spectrum

Based on the effective Hamiltonian of Eq. (9.2) of a quantum two-level system coupled to a non-standard structured environment, we have calculated the resulting non-Markovian dynamics by employing the numerically exact HEOM approach [200]. In particular, we are interested in the spectroscopic traces of a CI in 2D electronic spectra [203]. Therefore, we evaluate the total 2D electronic spectra (rephasing plus nonrephasing part) by Fourier transforming the third-order nonlinear response function. Further details are given in Ref. [23]. For the calculation, we have set the electronic gap in the Franck-Condon region to $\epsilon = 1000$ cm^{-1} after having performed the usual rotating wave approximation. The bath parameters are chosen as $\lambda'_{\mathrm{c}} = 150$ cm^{-1}, $\gamma'_{\mathrm{c}} = 150$ cm^{-1} and $\lambda'_{\mathrm{t}} = 150$ cm^{-1}, $\gamma'_{\mathrm{t}} = 20$ cm^{-1}, and the temperature was set to $\mathcal{T} = 300$ K.

In Figure 9.2, we show a collection of selected 2D electronic spectra for different waiting times T (left column). For $T = 300$ fs, we observe a split peak with one positive and one negative branch. Interestingly, the negative off-diagonal peak around $\omega_t = 1000$ cm^{-1} reaches its maximum magnitude at $T = 500$ fs. The negative branch decays rapidly with increasing waiting time and becomes almost invisible at $T = 1000$ fs. The negative peak is generated by a secondary excitation which lifts the wave packet from the ground state PES (blue arrows) to the excited state PES, as indicated by the blue arrow in Figure 9.1. This excited-state absorption process can only exist when the initially excited wave packet (indicated in red in Figure 9.1) has moved from the Franck-Condon region on the excited-state PES through the CI downhill, see the purple arrow in Figure 9.1. This can only occur in the presence of a CI and the negative cross peaks can thus serve as a unique identifier of it.

To verify this picture, a comparison with the model without a CI is helpful. This is realized by setting $\lambda'_{\mathrm{c}} = 0$ while keeping the strong vibrational dissipation with $\lambda'_{\mathrm{t}} = 150\ \mathrm{cm}^{-1}$ and $\gamma'_{\mathrm{t}} = 20\ \mathrm{cm}^{-1}$. The analogues sequence of 2D spectra is shown in the right column of Figure 9.2 (labeled as 'no CI'). It shows the typical relaxation dynamics in which negative peaks are completely missing. Besides, the maxima of the 2D spectra decay much slower than in the case with a CI being present. Clearly, the wave packet no longer can relax in a radiationless process to the electronic ground state PES via a funneling the CI.

In order to quantitatively compare both cases, the magnitudes of selected peaks are traced for increasing waiting times. The results are shown in Figure 9.3. We compare the maximal and minimal peak height of the case with a CI to the maximal peak height of the case without a CI. Clearly, for the model with CI, the extremal peaks of the 2D spectra decay very fast and reach zero at 1500 fs (left ordinate in Figure 9.3). In turn, in the case without a CI, such a rapid decay is not present.

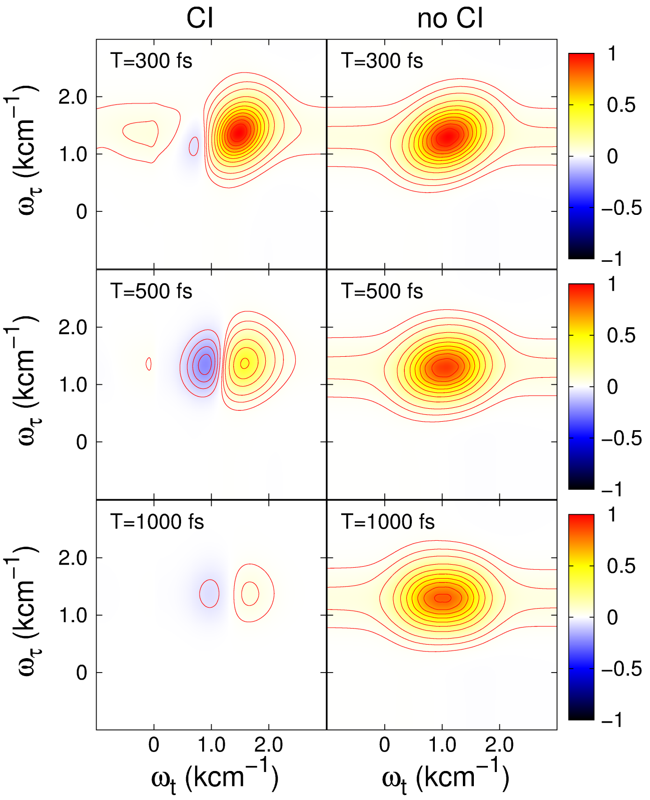

Figure 9.2: Selected 2D electronic spectra calculated for the effective quantum two-level model with the structured environment formed by the two baths. The left column shows 2D spectra calculated in presence of the CI, while the right column shows the results in absence of the CI with $\lambda_1' = 0$. The 2D electronic spectra are normalized separately according to their maximal peak in the 2D spectrum at $T = 300$ fs. Here, kcm^{-1}= 1000 cm^{-1}.

Instead, we find still a larger maximum of ~ 0.28 (in arbitrary units) for the longest waiting time of 1500 fs considered (right ordinate in Figure 9.3).

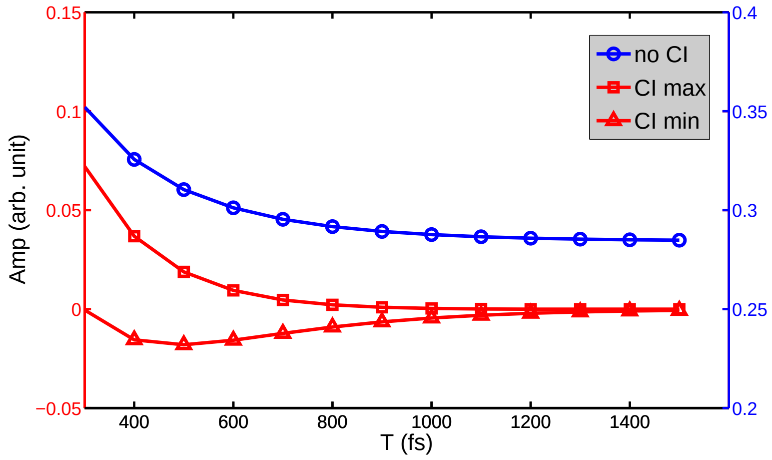

Figure 9.3: Extremal peak heights in the 2D spectra as a function of the waiting time. The red symbols (labeled ‘CI max’ and ‘CI min’) show the magnitude of the peaks at ($\omega_\tau = 1240$ cm^{-1}, $\omega_t = 1240$ cm^{-1}) and ($\omega_\tau = 1240$ cm^{-1}, $\omega_t = 880$ cm^{-1}) in the 2D spectra for the case with a CI, respectively. Moreover, the blue symbols (labeled ‘no CI’) show the magnitude of the peak at (ω_τ=1200 cm^{-1}, ω_t=1200 cm^{-1}) of the spectra for the case without a CI.

A further confirmation can be obtained from the time-evolved transition absorption spectrum shown in Figure 9.4. Two bands show up with positive and negative amplitudes. The time scales on which the dynamics of the wave packet around the CI occurs can be clearly distinguished by considering the dynamics associated to the positive and negative bands. After the initial photoexcitation, a part of the wave packet moves directly through the CI and reaches the ground state PES. This process

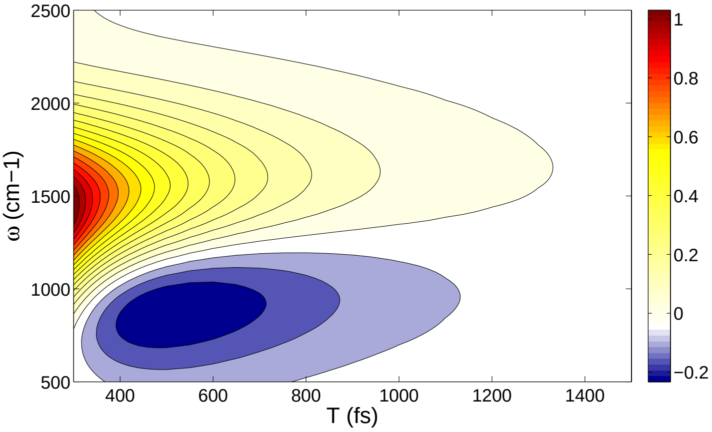

Figure 9.4: Transient absorption spectrum as a function of the waiting time in presence of a CI. It shows two clearly separated bands (positive and negative) centered at 1600 cm^{-1} and 850 cm^{-1}, respectively.

contributes significantly to the positive bands associated to the fast relaxation. In addition, the remaining part of the wave packet moves through the CI to the PES minimum. It can be identified with the starting point of the negative bands at $\sim$ 200 fs. This process reaches its maximum at $\sim$ 500 fs and is followed by a fast relaxation. This is caused by the secondary excitation and the backward motion to ground state PES through the CI. The entire relaxation process is completed within $\sim$ 1.2 ps.

In this section, we have established a reduced model for the nonadiabatic quantum dynamics of an electronic wave packet in the region of a conical intersection. It is obtained from the well-known two-state two-mode model by transforming the two harmonic potential energy surfaces to the harmonic bath. The resulting quantum mechanical two-level model with two highly structured harmonic baths can be solved by advanced numerically exact non-Markovian techniques, such as the hierarchy equation-of-motion approach. This greatly facilitates the numerical efforts. Most importantly, it allows to tackle the notoriously difficult case of strong vibrational damping. The signatures of the conical intersection show up in form of branches with negative peaks in optical 2D spectra. They clearly can be traced back to secondary excitations of wave packets which have moved through the conical intersection. Their ultrafast time scale is also revealed by the time dependence of the cross peaks in the 2D spectra. Finally, we note that negative amplitude cross peak could in principle also arise when an extremely large shift between the ground and the excited state potential energy surface exists. For this, the Huang-Rhys factor must be larger than $\epsilon/\Omega_{\mathrm{c/t}}$. For any realistic molecules, this factor will be unrealistically large.

After studying the wave packet in the overdamped limit (Eq. 9.4), we investigate next the impact of the vibrational coherence on the wave-packet dynamics in the vicinity of CI. For this, we return back to the spectral density with the underdamped form, Eq. 9.6 and reconstruct the new PESs and parameters for the study.

9.4 Vibrationally modulated quantum yield

In this section, we start with the three-state two-mode model (see Fig. 9.5) in which a molecule is assumed to have an electronic ground state $|\mathrm{g}\rangle$ and a CI between two PESs belonging to the excited states $|\mathrm{e1}\rangle$ and $|\mathrm{e2}\rangle$. In addition, we include a standard dissipative harmonic environment. The total Hamiltonian is $H = H_{\mathrm{mol}} + H_{\mathrm{env}}$. The molecular Hamiltonian is given by $H_{\mathrm{mol}} = H_{\mathrm{g}} + H_{\mathrm{e1}} + H_{\mathrm{e2}} + H_{\mathrm{int}}$ with $H_{\mathrm{g}} = |\mathrm{g}\rangle\,(h_{\mathrm{g}} + \epsilon_{\mathrm{g}})\,\langle\mathrm{g}|$, $H_{\mathrm{e1}} = |\mathrm{e1}\rangle\,(h_1 + \epsilon_1)\,\langle\mathrm{e1}|$ and $H_{\mathrm{e2}} = |\mathrm{e2}\rangle\,(h_2 + \epsilon_2)\,\langle\mathrm{e2}|$. The interaction Hamiltonian between two electronic states is $H_{\mathrm{int}} = |\mathrm{e1}\rangle\,V\,\langle\mathrm{e2}| + h.c.$ with the strength V of the electronic coupling. Here, ϵ_{g}, ϵ_1 and ϵ_2 are the energies of the ground and the electronic excited states, respectively. h_{g}, h_{e1} and h_{e2} are the vibrational Hamiltonians associated to the ground, first and second electronic excited states. They include two vibrational modes, the coupling mode characterized by the reaction coordinate Q_{c}, and the tuning mode described by the reaction coordinate Q_t. They are given by $h_{\mathrm{g}} = \frac{1}{2}\sum_{i=\mathrm{c,t}} \Omega_i\,(P_i^2 + Q_i^2)$ and $h_{\mathrm{e1}} = h_{\mathrm{g}} - \kappa Q_{\mathrm{t}}$, $h_{\mathrm{e2}} = h_{\mathrm{g}} + \kappa Q_{\mathrm{t}}$, where $\Omega_{i=\mathrm{c,t}}$ are the frequencies of the harmonic coupling and tuning mode, respectively. Moreover, κ is the vibronic coupling strength. The electronic coupling between two PESs is assumed to linearly depend on Q_{c}, such that $V = \Lambda Q_{\mathrm{c}}$ with the electronic coupling strength Λ. Furthermore, we assume that all relevant interactions between the two electronic PESs are captured by the coupling mode. Thus, the bath only couples vibrational states on the same electronic PES. We assume that the two vibrational modes are coupled to their own linear bath according to the Hamiltonian, Eq. 9.1. Again, we assume two Ohmic spectral densities $J_{\mathrm{c/t}}(\omega) = \eta_{\mathrm{c/t}}\omega$ with $\eta_{\mathrm{c/t}}$ being the vibrational damping strengths for the coupling and tuning mode, respectively. For the transition

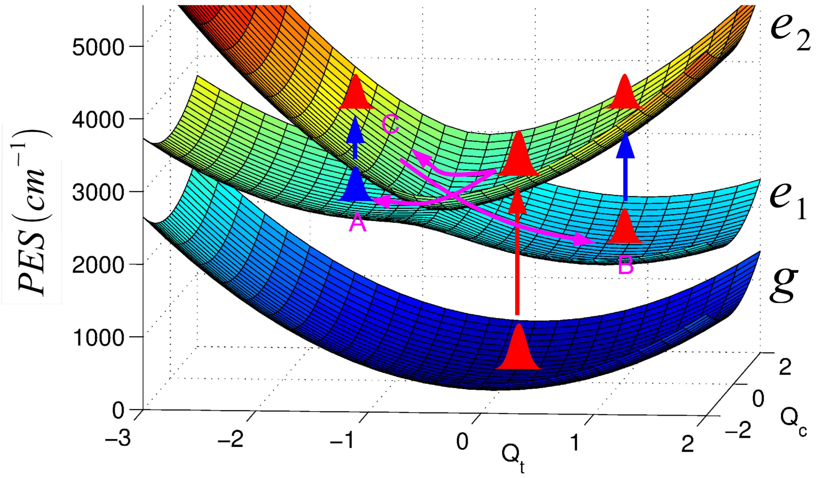

Figure 9.5: Energy diagram of the three-state two-mode model with an electronic ground and two excited states. The CI exists between the two excited states, $|e1\rangle$ and $|e2\rangle$. The initial optical excitation is indicated by the red vertical arrow and the two transitions yielding the second-excited-state absorption are marked by blue arrows. The magenta arrows show three different possible deactivation pathways.

dipole moment, we assume an allowed optical transition from the ground state to the electronic bright state $|e2\rangle$ in the Franck-Condon region. Moreover, we assume that the first excited state $|e1\rangle$ is dark with respect to the ground state. In addition, we assume a second allowed transition between the two electronic excited states. Therefore, the transition dipole moment is given by $\mu = |e2\rangle\langle g| + |g\rangle\langle e2| + |e1\rangle\langle e2| + |e2\rangle\langle e1|$, with all components being equally strong.

It turns out that it is technically beneficial to simplify the molecular Hamiltonian by again transforming the two modes Q_c and Q_t into the bath Hamiltonian and include their influence within a full non-Markovian treatment of the resulting structured environment [188]. A unitary transformation [201], generalized to two modes, yields the total Hamiltonian

$$\begin{aligned} H = H_\mathrm{el} \quad & - \quad \sigma_\mathrm{c} \sum_\alpha c'_\alpha x'_\alpha + \sum_\alpha \left[\frac{p'^2_\alpha}{2m'_\alpha} + \frac{m'_\alpha \omega'^2_\alpha}{2} x'^2_\alpha \right] \\ & - \quad \sigma_\mathrm{t} \sum_\alpha t'_\alpha y'_\alpha + \sum_\alpha \left[\frac{q'^2_\alpha}{2M'_\alpha} + \frac{M'_\alpha \nu'^2_\alpha}{2} y'^2_\alpha \right] . \end{aligned} \tag{9.5}$$

Here, the coupling matrices between system and bath for coupling and tuning mode follow as $\sigma_\mathrm{c} = |\mathrm{e1}\rangle \langle \mathrm{e2}| + |\mathrm{e2}\rangle \langle \mathrm{e1}|$ and $\sigma_\mathrm{t} = |\mathrm{e1}\rangle \langle \mathrm{e1}| + |\mathrm{e2}\rangle \langle \mathrm{e2}|$, respectively. The new effective system Hamiltonian with three electronic levels then is $H_\mathrm{el} = |\mathrm{g}\rangle \epsilon_\mathrm{g} \langle \mathrm{g}| + |\mathrm{e1}\rangle \epsilon_1 \langle \mathrm{e1}| + |\mathrm{e2}\rangle \epsilon_2 \langle \mathrm{e2}|$ (see Ref. [188] for details). The resulting effective spectral densities follow as

$$J^\mathrm{eff}_\mathrm{c/t}(\omega) = \lambda_\mathrm{c/t} \frac{\gamma_\mathrm{c/t} \Omega^2_\mathrm{c/t} \omega}{(\Omega^2_\mathrm{c/t} - \omega^2)^2 + \gamma^2_\mathrm{c/t} \omega^2}, \tag{9.6}$$

where $\lambda_\mathrm{c} = \Lambda^2/(2\Omega_\mathrm{c})$, $\lambda_\mathrm{t} = \kappa^2/(\Omega_\mathrm{t})$ are the reorganization energies for the coupling and tuning mode, respectively. We note that we previously [188] have used in Sec. 9.3 a further assumption of an overdamped vibrational dynamics, which we do not apply in this section. Instead, we study here the underdamped vibrational dynamics.

The three-state two-mode model is sketched in Fig. 9.5. The electronic coupling between the two electronic excited states $|\mathrm{e1}\rangle$ and $|\mathrm{e2}\rangle$ generates a CI of the two PESs. We assume that an electronic wave packet is initially photoexcited from the ground state. The three possible relaxation pathways of the wave packet on the bright excited state $|\mathrm{e2}\rangle$ are labeled by A, B and C. Along the path A, the wave packet is deactivated to the minimum position A on the excited state PES $|\mathrm{e1}\rangle$ by passing through the CI without changing its direction. Via the pathway B, the wave packet passes through the CI but changes its direction. A third pathway C that the wave packet remains with a finite probability on the excited state PES $|\mathrm{e2}\rangle$ is possible since we allow for an underdamped vibrational relaxation (see Eq. 9.6).

The dynamics of the electronic wave packet on the first excited state PES $|\mathrm{e1}\rangle$ can be measured by the second excited state absorption signal in a 2D spectrum after it has reached the PES minimum of $|\mathrm{e1}\rangle$. The second excited state absorption processes are marked by the blue arrows in Fig. 9.5. Within the three-state two-mode model, we can separate the information of the dynamics of the wave packet on the first excited state PES $|\mathrm{e1}\rangle$ from that of the vertical excitation between ground and second excited state PES $|\mathrm{e2}\rangle$ in the 2D and the transient absorption spectra by scanning the transition frequency corresponding to the transition from the $|g\rangle$ to the $|\mathrm{e2}\rangle$ state. In addition, we can distinguish the different channels of the second excitation process by the transition difference of the energy gap between $|\mathrm{e1}\rangle$ and $|\mathrm{e2}\rangle$ at the position A and B, respectively. To show this, we choose the parameters $\epsilon_g = 0\ \mathrm{cm}^{-1}$, $\epsilon_1 = 2000\ \mathrm{cm}^{-1}$ and $\epsilon_2 = 2600\ \mathrm{cm}^{-1}$. The vibrational frequencies of the tuning and coupling mode are set to $\Omega_\mathrm{t} = 500\ \mathrm{cm}^{-1}$ and $\Omega_\mathrm{c} = 200\ \mathrm{cm}^{-1}$ and the corresponding reorganization energy

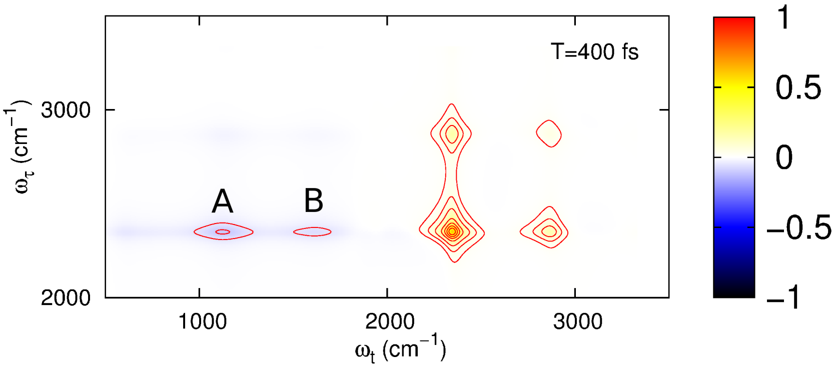

Figure 9.6: 2D electronic spectrum for the effective three-state model for the waiting time $T = 400$ fs. The two off-diagonal signals A and B are associated to the two relaxation pathways as indicated in Fig. 9.5. The damping constants are set to $\gamma_{c/t} = 30\ \text{cm}^{-1}$ (for the remaining parameters, see text).

and damping constants are fixed to $\lambda_c = 25\ \text{cm}^{-1}$, $\gamma_c = 30\ \text{cm}^{-1}$, $\lambda_t = 250\ \text{cm}^{-1}$, and $\gamma_t = 30\ \text{cm}^{-1}$. By applying the numerically exact hierarchy equation of motion approach [200] together with the phase-matching technique [87, 204], we calculate the 2D spectrum for different waiting times and show in Fig. 9.6 the result for the waiting time $T = 400$ fs. The excited state absorption peak (negative) is completely separated from the diagonal peak (positive). Furthermore, the different channels of the second excitation state absorption can be clearly distinguished as well (denoted as A and B in Fig. 9.6).

Since the different relaxation channels are clearly identified, we can now investigate the wave packet dynamics in the vicinity of the CI. In particular, we can easily evaluate the quantum yield and the rate of the isomerization reaction from the 2D and the transient absorption spectra by monitoring the second excited-state absorption peaks of the channels A and B. To investigate the impact of the vibrational coherence on the isomerization, we vary the vibrational coherence of the wave packet by changing the damping constant $\gamma_{\mathrm{c/t}}$. We consider the three cases (a) $\gamma_{\mathrm{c/t}} = 30$ cm^{-1}, (b) $\gamma_{\mathrm{c/t}} = 50$ cm^{-1} and (c) $\gamma_{\mathrm{c/t}} = 100$ cm^{-1}. Inspired by the experiment [182], we calculate the transient absorption spectra for these three cases. To be able to compare the same configuration of the PESs, we ensure that the reorganization energies are kept unchanged, i.e., $\lambda_{\mathrm{c}} = 25$ cm^{-1} and $\lambda_{\mathrm{t}} = 250$ cm^{-1}. The results of the transient absorption spectra are shown in Fig. 9.7. The electronic wave packet motion along the two pathways A and B of the excited state PES $|\mathrm{e1}\rangle$ are clearly distinguishable from each other in Fig. 9.7 (a) for the weakly damped vibrational coherence with $\gamma_{\mathrm{c/t}} = 30$ cm^{-1}. Clearly, the wave packet reaches the position A earlier than B by about 200 fs. This is expected due to the structure of the PESs shown in Fig. 9.5. For a more strongly damped vibrational motion, i.e., for $\gamma_{\mathrm{c/t}} = 50$ cm^{-1} as shown in Fig. 9.7(b), or for $\gamma_{\mathrm{c/t}} = 100$ cm^{-1} as shown in Fig. 9.7(c), the magnitude of the signal of the excited-state absorption channel A is smaller compared to the one in channel B. In addition, the time delays between the arrivals of the wave packet at the positions A and B decrease from $\gamma_{\mathrm{c/t}} = 30$ to 100 cm^{-1}. In fact, for $\gamma_{\mathrm{c/t}} = 100$ cm^{-1}, this delay is hardly resolvable in the transient absorption spectrum (Fig. 9.7(c)). Hence, the more coherent wave packet allows us to better identify the direction of the motion after the passage through the CI. In turn, a less coherent one rather shows the features of a classical motion. For a quantitative comparison, we report in Table 9.1 the quantum yield $A/(A+B)$ extracted from the transient absorption spectrum at $T = 5$ ps for $\gamma_{\mathrm{c/t}}$ between 30 and 150 cm^{-1}. It decreases from 0.614 to 0.540 in Table 9.1 and we may anticipate that this ratio reaches 0.5 for the classical (overdamped) case ($\gamma_{\mathrm{c/t}} \to \infty$).

A confirmation of this mechanism is obtained by recording the absorption signal of the channels A and B for varying waiting times T. The result is shown in Fig. 9.8 (a) for the underdamped case $\gamma_{\mathrm{c/t}} = 30\ \mathrm{cm}^{-1}$. We find an exponential decay with superposed fast coherent vibrational oscillations. From this, the isomerization rate can be extracted by fitting an exponential. The inverse isomerization rates are shown in Table 9.1. These results show quantitatively that the speed of the photoisomerization reaction increases when the wave packet is less coherent, i.e, experiences stronger damping by coupling to the bath. The effect is to truncate the wavepacket in the reaction coordinate without the prospect of recurrences. In turn, a more coherent wave packet oscillates on the same PES and has a smaller probability to pass through the CI. Some components of the wave packet remain on the excited state PES $|e2\rangle$ and continue their motion for the next round of traversal.

Further information on the wave packet dynamics can be obtained from the coherent oscillations of the transient excited state absorption signal. The Fourier trans-

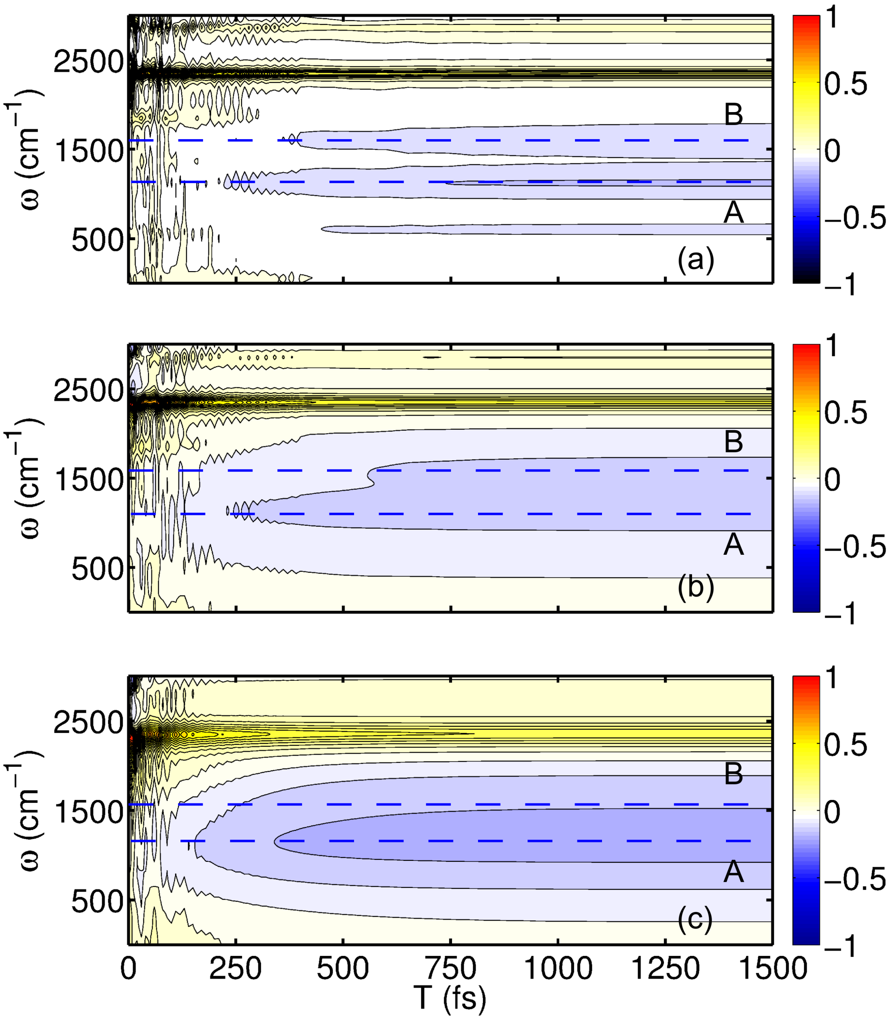

Figure 9.7: Transient absorption spectra of the three-state two-mode model with different damping constants (i.e., different vibrational lifetimes), (a) $\gamma_{\mathrm{c/t}} = 30$ cm^{-1}, (b) $\gamma_{\mathrm{c/t}} = 50$ cm^{-1} and (c) $\gamma_{\mathrm{c/t}} = 100$ cm^{-1}. All the other parameters are kept the same as in Fig. 9.6.

form of the residual, obtained after subtracting the exponential kinetics from the time-dependent signal, is shown in Fig. 9.8 (b) for $\gamma_{\mathrm{c/t}} = 30\ \mathrm{cm}^{-1}$. Several vibrational frequency components are resolved, with peaks at the frequencies 500 cm^{-1}, 1000 cm^{-1}, 1750 cm^{-1} and 2250 cm^{-1}. The component at 500 cm^{-1} demonstrates that the tuning mode component of the wave packet is largely unaffected after having passed through the CI. Interestingly, no evidence of the vibrational frequency of the coupling mode around the frequency of 200 cm^{-1} is found. Hence, only the vibrational coherence of the coupling mode component is strongly influenced in the vicinity of the CI, which is due to the wave packet being split into two parts along the reaction coordinate Q_{c} of the coupling mode (see Fig. 9.5). This effect has recently been observed experimentally in the transient absorption spectrum [178].

A further interesting conclusion can be drawn from the relatively weak vibrational component around $\sim 1000\ \mathrm{cm}^{-1}$, emphasized by the magenta box in Fig. 9.8(b). It is associated to a two-frequency beating of the vibrational coherence present for the case of the relatively long-lived coherence with $\gamma_{\mathrm{c/t}} = 30\ \mathrm{cm}^{-1}$. This beating is absent in the two less coherent cases of $\gamma_{\mathrm{c/t}} = 50\ \mathrm{cm}^{-1}$ and 100 cm^{-1}. The peaks originate from the coherent mixing of the tuning mode at the frequency 500 cm^{-1} and the recrossing components. The former components stem from the wave packet which goes through the CI and reaches the minimum position A, while the latter parts first follow the pathway C on the excited state PES $|e2\rangle$ in the underdamped case. Then, at the

$\gamma_{\mathrm{c/t}}$ (cm^{-1})	Magnitude A	Magnitude B	$A/(A+B)$	Γ_y^{-1} (fs)
30	-0.1001	-0.0630	0.614	285
40	-0.1065	-0.0690	0.607	268
50	-0.1143	-0.0767	0.598	240
100	-0.1601	-0.1206	0.570	200
150	-0.1961	-0.1672	0.540	195

Table 9.1: Magnitude for pathways A (1100 cm^{-1}) and B (1600 cm^{-1}) for the waiting time $T = 5$ ps in the transient absorption spectrum with the stable products A and B. The ratio $A/(A+B)$ shows that the more coherent wave packet produces a higher quantum yield than the less coherent one. In addition, we show the inverse of the isomerization rate Γ_y.

turning point (meant in the sense of a semiclassical wave packet) these components reverse their direction towards the CI and move back. After the following crossing of the CI, parts of the wave packet traverse to the lower lying PES and interfere with the former parts of the wave packet on the pathway A, such that a coherent mixing results. This interference signal generates Stueckelberg oscillations in the vicinity of the CI. In principle, they are discernible experimentally by transient absorption and 2D spectroscopy with sufficient time resolution [172]. Finally, the high-frequency components at 1750 and 2250 cm^{-1} are rooted in the transition interaction between the two PES at A and B due to the excited state $|e2\rangle$ in Fig. 9.5.

In this section, we have shown that the vibrational coherence of an electronic wave packet crucially determines the efficiency of the photoisomerization reaction. We have used a very efficient approach to simulate the nonadiabatic wave packet dynamics in which the coupling and the tuning modes are transformed to the bath Hamiltonian. The resulting structured environment can be treated by available non-Markovian techniques of which we have employed the HEOM. Despite the model based on the harmonic approximation of the PES and on the dipole approximation of the coupling to the tuning and coupling mode, ab-initio calculations [205] provide a computational justification of the simple two-state two-model model for the study of photoisomerization of rhodopsin, which significantly reduces the complexity of the theoretical investigation. Of course, more than one effective mode need to be

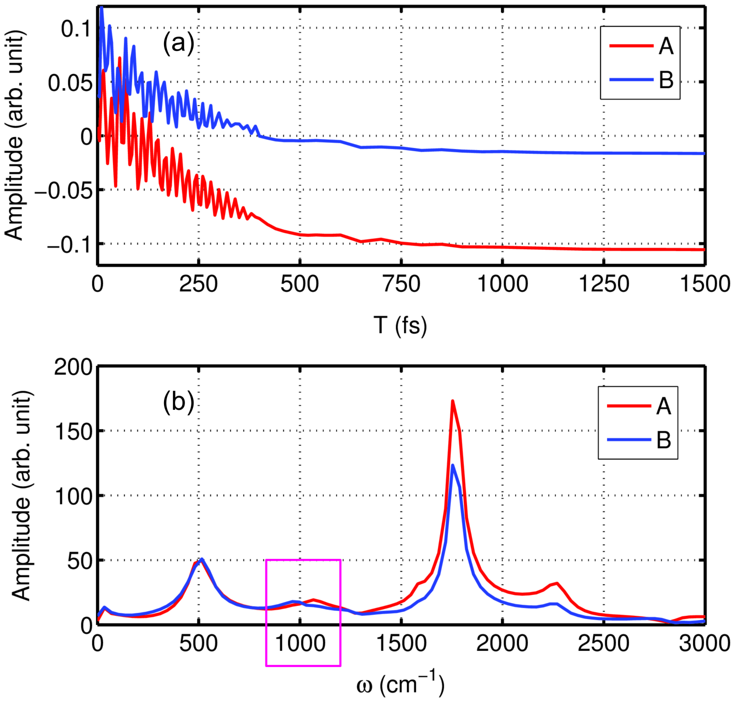

Figure 9.8: (a) Time-resolved vibrational dynamics of the wave packet along the relaxation pathways A (red) and B (blue) in the transient absorption spectrum for $\gamma_{\mathrm{c/t}} = 30\ \mathrm{cm}^{-1}$. For graphical reasons, the magnitude of B is shifted upwards by 0.05. (b) Vibrational frequencies in the transient absorption signal of pathway A (red) and B (blue) obtained after a Fourier transform of the vibrational residual after subtracting the exponential kinetics of the two signals A and B. The magenta box is associated to a beating due to repeated passages of the wave packet after returning from C.

properly accounted for in a quantitative comparison with the experiment. Yet, this is possible in our approach since only the spectral structure of the non-Markovian bath needs to be adopted, which significantly reduces the computational costs and makes the calculations tractable with GPU-based techniques [143]. When a vibrationally coherent wave packet moves in the vicinity of a conical intersection, it can follow different relaxation pathways which all can be identified in the transient absorption and the 2D spectra. We studied the kinetics around the conical intersection with different degrees of coherence for the wave packet using different degrees of damping. We have found that the more coherent wave packet results in a higher quantum yield. In the present combination of parameters, we find a gain of 7.4% for the more coherent motion as compared to the less coherent one. It already indicates a significant enhancement in general, since here, we have chosen a rather weak coupling between two PESs along the coupling mode (in fact, it is ten times smaller than the value of the tuning mode). We expect that the quantum efficiency could be enhanced further for stronger coupling modes. After passing through the CI, the vibrational coherence of the coupling mode component is significantly affected, while the tuning mode component is unaltered. A vibrationally coherent wave packet also can repeatedly cross a CI within its coherence time such that interference leads the Stueckelberg oscillations (see Fig. 9.9) which are manifest in mixing components in the excited state absorption. Our findings illustrate that the photoisomerization reaction

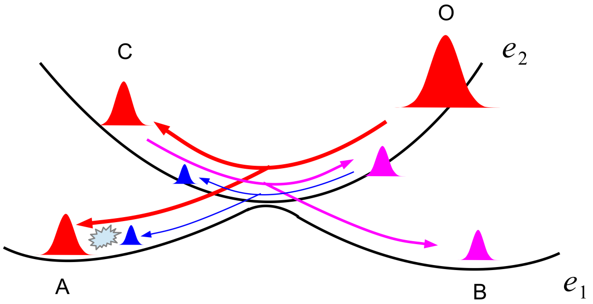

Figure 9.9: Schematic illustration of repeated passages of a wave packet in the vicinity of a CI to induce Stueckelberg oscillation.

can be controlled by tuning the vibrational coherence of the electronic wave packet.

9.5 Motion of the wave packet at the CI

In the last section, based on the calculation of the 2D and the transient absorption spectra, we revealed the impact of the vibrational coherence on the motion of the wave packet in the vicinity of the CI. However, the details of the motion of the wave packet are still unclear. In this section, we study the motion of the electronic wave packet at the CI and investigate the details how it affects the quantum yield.

We start with the the two-state two-mode model again, in which a spectroscopically accessible CI is assumed with two electronic excited states $|e1\rangle$ and $|e2\rangle$. The molecule couples to the dissipative bath, which is composed of the infinity number of harmonic oscillators. The total Hamiltonian can be written as $H = H_{\text{mol}} + H_{\text{env}}$. The system Hamiltonian is constructed by the electronic states vibronically couple to two effective modes, tuning Q_t and coupling mode Q_c. We again assume that both the tuning and coupling mode experience fluctuations with an Ohmic spectral density $J_{t/c}(\omega) = \eta_{t/c}\omega \exp(-\omega/\omega_c)$. In this part, we assume the initial wave packet to be prepared in the state $|e2, 0\rangle$, such that the density matrix at initial time $t = 0$ can be written as $\rho(0) = |e2, 0_c, 0_t\rangle \langle e2, 0_c, 0_t|$. Here, 0_c and 0_t are the vibrational ground states of the coupling and tuning mode, respectively. In order to obtain the time-dependent position of the electronic wave packet on the PES, we need to project the wave packet on the corresponding coordinates in the adiabatic basis. The projection yields the two reduced probability densities

$$\begin{aligned} P_k^{ad}(Q_c, t) &= \int dQ_t \, \langle Q_c| \langle Q_t| \langle \widetilde{e}_k| \, \rho(t) \, |\widetilde{e}_k\rangle \, |Q_t\rangle \, |Q_c\rangle \, , \\ P_k^{ad}(Q_t, t) &= \int dQ_c \, \langle Q_c| \langle Q_t| \langle \widetilde{e}_k| \, \rho(t) \, |\widetilde{e}_k\rangle \, |Q_t\rangle \, |Q_c\rangle \end{aligned} \tag{9.7}$$

of the coupling and the tuning mode, respectively. Here, $|\widetilde{e}_{k=1,2}\rangle$ denotes the electronic wave function in the adiabatic basis. The transformation of the wave function from the diabatic to the adiabatic basis is given by $|\widetilde{e}_k\rangle = \sum_{k'=e1,e2} S(Q_c, Q_t)_{kk'} \, |e_{k'}\rangle$ and the transfer matrix $S(Q_c, Q_t)$ can be found in Ref. [206]. We assume a vibronic coupling strength of $\kappa = 1000$ cm^{-1} of the tuning mode Q_t, and a vibronic coupling strength of $\Lambda = 200$ cm^{-1} of the coupling mode, $\Omega_t = 500$ cm^{-1} and $\Omega_c = 900$ cm^{-1}. The energy gap between the two PESs is set to $\epsilon = 2000$ cm^{-1}. In this part, all the calculations have been carried out at room temperature ($\mathcal{T} = 300$ K). In order to realize a sufficiently large eigenbasis of the molecular Hamiltonian for converged results, 30 and 6 vibrational levels are included for the tuning and coupling mode, respectively. The total molecular Hamiltonian matrix is 360 dimensional. We use the TNL quantum master equation [66, 67] for the calculation of the full dynamics of the electronic wave packet. Based on the above parameters, we plot the PES-configuration of the two electronic states in Fig. 9.10.

On the basis of this model, we study the impact of the vibrational coherence of the wave packet on the kinetics around the CI. For this, we vary the vibrational damping constants $\eta_{t/c}$. We begin with the weak damping case and choose $\eta_t = \eta_c = 0.5$ and $\omega_c = 50$ cm^{-1}. We calculate the dynamics of the wave packet and project it to the tuning and coupling coordinate. The results of the two reduced probability densities are shown in Fig. 9.11 in a color scale. In Fig. 9.11(a), the initial wave packet prepared in the state $\left|\widetilde{e2}\right\rangle$ was initially localized at $Q_t = 0$. It starts to move to the left side and passes through the CI (see Fig. 9.10(a), position at $Q_t = -1$) within the first 20 fs. Consequently, the wave packet of the state $\left|\widetilde{e2}\right\rangle$ completely disappears on the upper PES, while, at the same time, the wave packet starts to grow at $Q_t = -1$ on the $\left|\widetilde{e1}\right\rangle$-PES. With growing time, it continues to move further to the left side until it reaches its maximal displacement at $Q_t = -6$. Then, it turns around, moves towards the center again and penetrates the PES to come back to the upper electronic PES

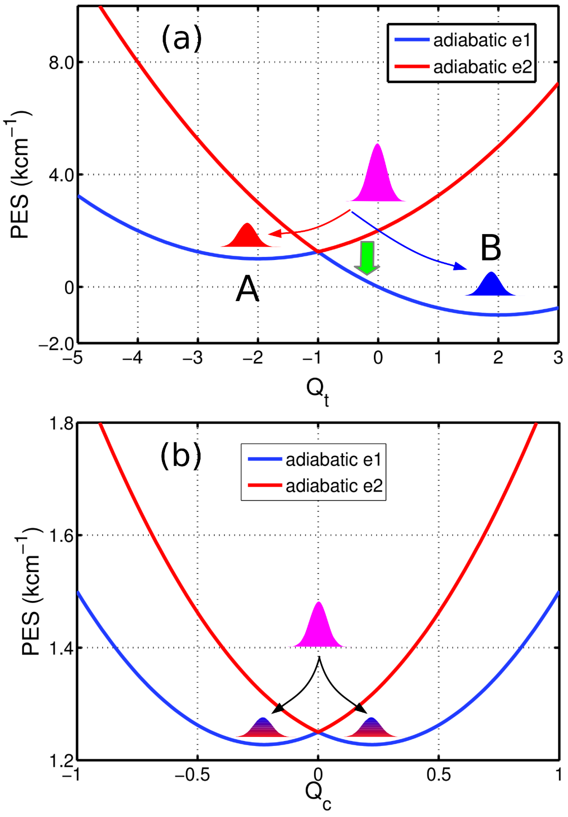

Figure 9.10: Configuration of the potential energy surfaces and the conical intersection along the tuning (a) and the coupling (b) mode. The conical intersection is located at the tuning coordinate $Q_t = -1$ and at the center of the coupling mode at $Q_c = 0$. The quantum yield is calculated by the magnitudes of the wave packets at A and B of the state $\left|\widetilde{e1}\right\rangle$ according to $Y = \frac{A}{A+B}$.

of $\left|\widetilde{e2}\right\rangle$. This can be observed in Fig. 9.11(a) to occur at $\sim$ 60 fs. After that, the wave packet moves towards the CI again and repeats the kinetics as described until the end of the considered time window of 500 fs. During this motion, vibrational coherence can be clearly identified and shows a period of ∼65 fs in the wave-packet dynamics on the $\left|\widetilde{e1}\right\rangle$-PES. This value coincides with the vibrational frequency of the tuning mode being set to 500 cm^{-1}. Moreover, the transfer time τ and the quantum yield Y of the wave packet between the two PESs can be clearly resolved. First, the quantum yield is quite high in this case of weak damping since the electronic wave packet is mostly located in the left region of the $\left|\widetilde{e1}\right\rangle$-PES in Fig. 9.11(b). Moreover, an effective potential barrier can be identified at $Q_t = -1$ which blocks the wave packet motion further to the right side. The transfer time of the wave packet can be easily determined by integrating over all the parts of the wave packet on the left side up to $Q_t = -1$. In the case of weak damping, we find $Y = 93\%$ and a transfer time $\tau = 920$ fs.

The wave packet also shows interesting dynamics along the coupling mode direction, see Figs. 9.11 (c) and (d). At the beginning, the wave packet is localized at the center $Q_c = 0$. It penetrates the CI and leaves the PES of $\left|\widetilde{e2}\right\rangle$ within 20 fs. At the same time, the wave packet appears on the $\left|\widetilde{e1}\right\rangle$-PES and reaches the maximum probability at 25 fs. Then, the wave packet starts to decay from the $\left|\widetilde{e1}\right\rangle$-PES and moves back to the $\left|\widetilde{e2}\right\rangle$-surface. Also these kinetics are repeated. The period of this oscillation is 65 fs which coincides with the period of the tuning mode. Interestingly, a coherent vibrational oscillation along the coupling mode direction can not be

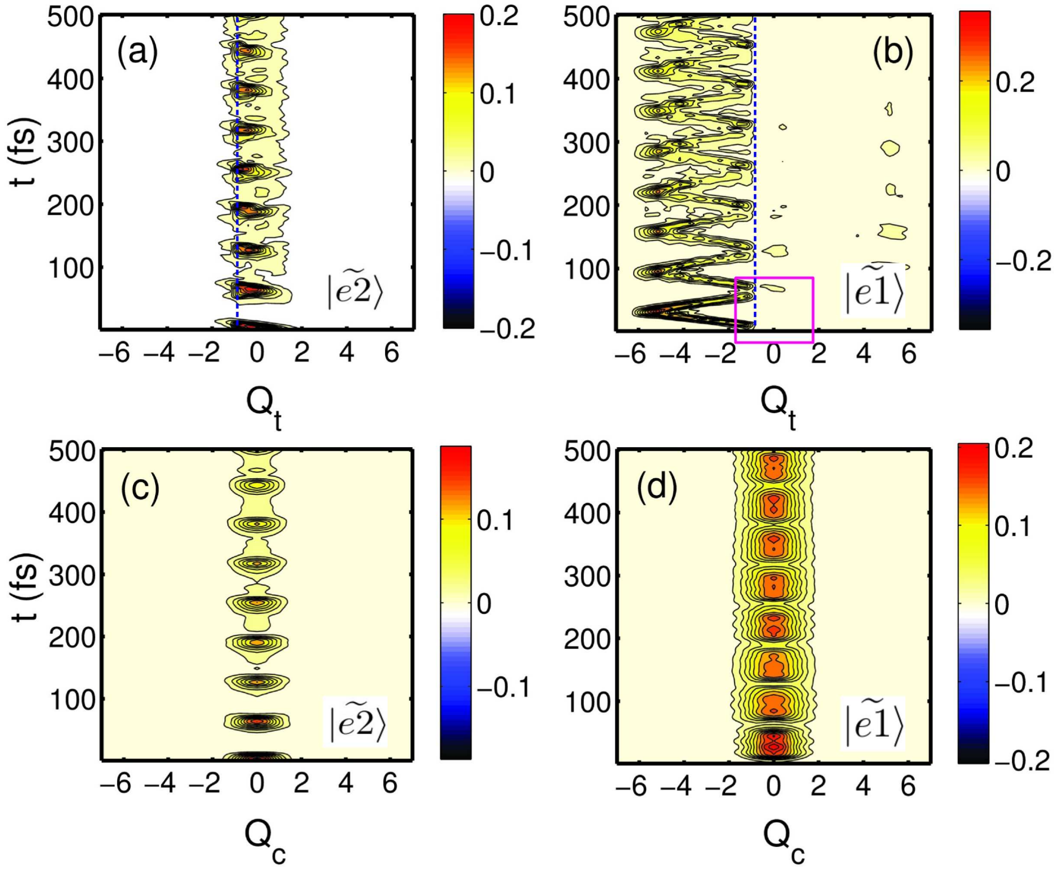

Figure 9.11: Time evolution of the probability densities of the underdamped electronic wave packet on the $\left|\widetilde{e2}\right\rangle$-PES and the $\left|\widetilde{e1}\right\rangle$-PES along the tuning mode Q_t and the coupling mode Q_c: (a) $P_2^{ad}(Q_t, t)$, (b) $P_1^{ad}(Q_t, t)$, (c) $P_2^{ad}(Q_c, t)$, and, (d) $P_1^{ad}(Q_c, t)$. The parameters are $\eta_t = \eta_c = 0.5$ and $\omega_c = 50$ cm^{-1} in the Ohmic spectral density.

identified since the wave packet splits into two parts and shows different frequencies of the oscillation on the $\left|\widetilde{e1}\right\rangle$-PES in the adiabatic basis (see Fig. 9.10(b)). This is consistent with the theoretical and experimental results of Refs. [178, 186, 196].

For the case of strong vibrational damping, we choose the parameters $\eta_t = \eta_c = 2$ and $\omega_c = 200$ cm^{-1}. The results for the wave-packet dynamics are shown in Fig. 9.12. In Fig. 9.12(a), the wave packet population on the $\left|\widetilde{e2}\right\rangle$-surface shows a much stronger damped dynamics. The wave packet only shows three clear oscillation periods up to ~ 120 fs and then disintegrates and disappears after 200 fs. This shows that the wave packet has completely passed through the CI to the PES of $\left|\widetilde{e1}\right\rangle$. In Fig. 9.12(b), the wave packet dynamics is similar to the one on the $\left|\widetilde{e2}\right\rangle$-PES and also shows three periods of vibrational coherence and gets completely disintegrated afterwards. Yet, it can be clearly observed that the transfer time is significantly shorter, but with a smaller efficiency in view of the quantum yield as compared to the weak damping case in Fig. 9.11. Similarly, for the wave packet dynamics along the coupling mode, we also observe that the transfer happens faster than before.

In Fig. 9.12(d), we see that the wave packet on the $\left|\widetilde{e1}\right\rangle$-surface is split into two parts at times > 400 fs. This is a clear signature of the geometric (or, Berry) phase [207, 208]. When the wave packet travels on the two opposite sides around the CI, it can interfere destructively at $Q_c = 0$ due to the phase difference of π acquired along the two different pathways. Thus, the probability density gets reduced at $Q_c = 0$ and the wave packet develops two maxima symmetrically located at $Q_c \neq 0$.

Clearly, the geometric phase does not occur in the weak damping case (Fig. 9.11 (d)) since the electronic wave packet is almost completely localized on the left side

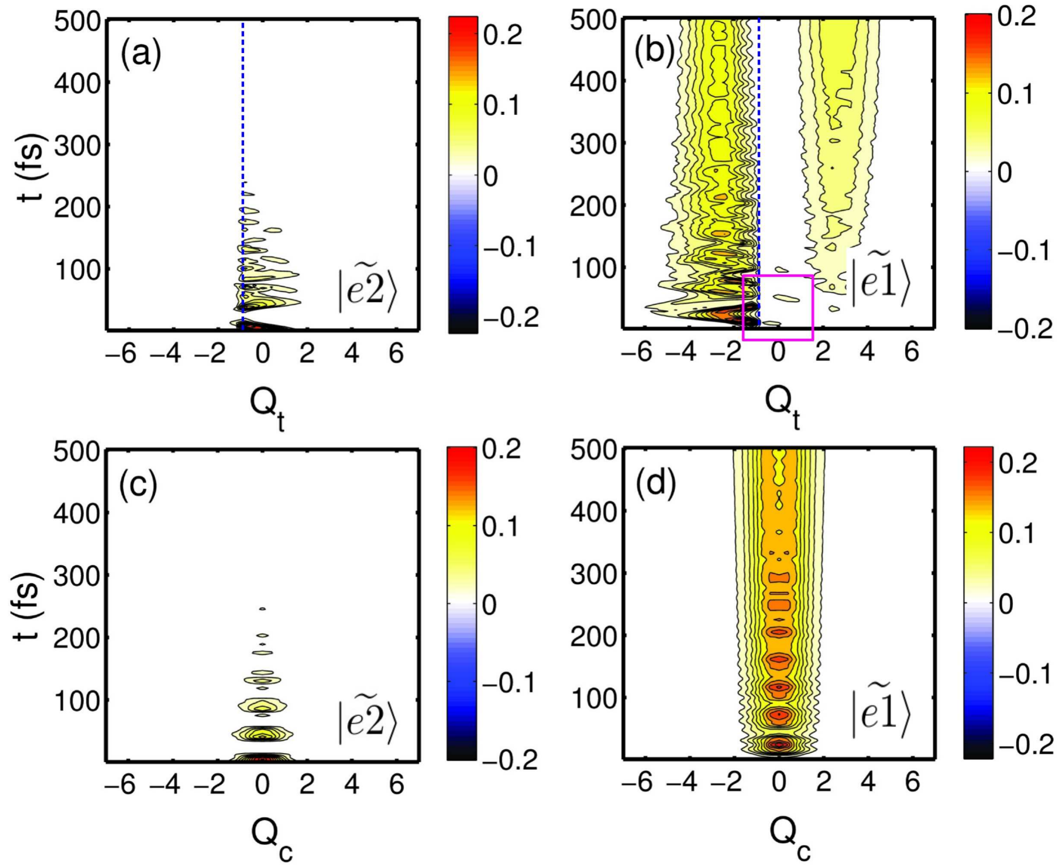

Figure 9.12: Same as Fig. 9.11, but for stronger vibrational damping. The parameters are $\eta_t = \eta_c = 2$ and $\omega_c = 200$ cm^{-1}.

of the $\left|\widetilde{e1}\right\rangle$-PES. In order to quantify this, we fit the kinetics of the electronic wave packet on the $\left|\widetilde{e1}\right\rangle$-surface to an exponential function and obtain the transfer time constant τ. The kinetics extracted from the left and the right side of the CI (which are separated by the barrier at $Q_t = -1$) show comparable magnitudes. Furthermore, we determine the quantum yield Y by integrating over the probability density (separated by the barrier line at $Q_t = -1$) at time $t = 500$ fs. The quantum yield decreases to $Y = 50.4\%$ in the case of strong damping as compared to $Y = 93\%$ in the weak damping case.

For a complete picture, we calculate the electronic wave packet dynamics for a wide range of damping parameters, $\eta_{t/c}$ and ω_c. The quantum yields and the associated transfer times are listed in Table 9.2. We find that both the transfer time and the quantum yield almost monotonously decrease with increasing damping. Thus, a less damped and hence a more coherent wave packet results in a higher quantum yield but with slower transfer process. This is in agreement with previous work [196], but we now prove the effect on the quantum yield from the viewpoint by explicitly tracking the wave packet motion in position space. Further, we illustrate that the spectroscopic approach is capable of revealing the dynamics in the vicinity of a CI, notwithstanding the experimental issue with rapidly changing spectra.

In addition, the significant difference of the wave-packet dynamics on the $\left|\widetilde{e1}\right\rangle$-surface at short times should be noticed between the weak (Fig. 9.11) and the strong damping case (Fig. 9.12). We highlight this by the magenta boxes. In the strong damping case, a small probability density of the wave packet appears at $Q_t = 0$ on the $\left|\widetilde{e1}\right\rangle$-surface. However, the wave packet on the upper $\left|\widetilde{e2}\right\rangle$-surface does not reach the seam within that time. This indicates that in the strong damping case, the electronic wave packet can penetrate the PES by tunneling when the two PESs are

$\eta_{t/c}$	ω_c [cm^{-1}]	$R_{t/c}$ [cm^{-1}]	Y [%]	τ [fs]
0.5	50	16	93	920
0.8	80	41	87	600
1.1	110	77	82	430
1.4	140	125	77	350
1.7	170	184	73	300
2.0	200	255	50	200

Table 9.2: The reorganization energy $R_{t/c}$, quantum yield Y and transfer time τ for the different cases of the damping parameters. We set $\eta_t = \eta_c$, such that $R_t = R_c$.

close together (the region is marked by the green arrow in Fig. 9.10). In contrast, there is no evidence of this tunneling process in the magenta box of the weak damping case in Fig. 9.11. To confirm this observation, we increase the electronic coupling between the two PESs to $\Lambda = 800$ cm^{-1} and calculate the wave packet dynamics up to $t = 500$ fs. We compare the time evolution of the probability density $P_1^{ad}(Q_t, t)$ of the wave packet on the $\left|\widetilde{e1}\right\rangle$-surface for the cases $\Lambda = 800$ cm^{-1} and $\Lambda = 200$ cm^{-1} in Fig. 9.13. In Fig. 9.13(a), we can clearly identify the tunneling of the wave packet at the coordinate $Q_t = 0$. Moreover, it also shows that the wave packet moves to the right side and to the minimum of the $\left|\widetilde{e1}\right\rangle$-surface. In contrast, we observe in Fig. 9.13(b) a much smaller magnitude of the wave packet at $Q_t = 0$ and no clear evidence of the movement towards the minimum at the position $Q_t = 2$. Based on

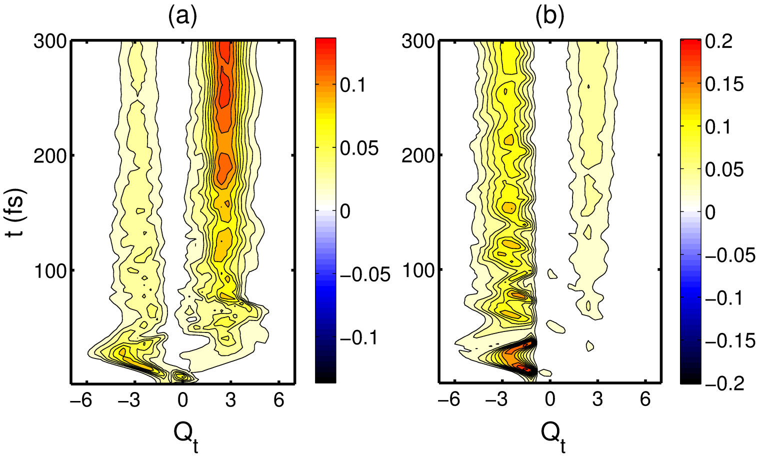

Figure 9.13: Time evolution of the probability density $P_1^{ad}(Q_t, t)$ of the wave packet on the $\left|\widetilde{e1}\right\rangle$ surface for (a) $\Lambda = 800$ cm^{-1}, and, (b) $\Lambda = 200$ cm^{-1}.

these calculations, we confirm that the less coherent wave packet does not show a net passage through the CI. Instead, it tunnels through the PESs when they are close together. In contrast, the more coherent wave packet shows an almost complete passage through the CI. We believe that this is the significant factor which ultimately determines the quantum efficiency of the isomerization and would provide a means for evolutionary optimization of the reaction coordinate.

In this section, we have studied the impact of vibrational damping on the dynamics of the electronic wave packet in the vicinity of a CI and its transfer between the potential energy surfaces. The projection of the dynamics onto the tuning and the coupling mode allows us to directly track the nonadiabatic dynamics of the wave packet on the PESs. By this, the direct visualization of the quantum transfer efficiency or the quantum yield and the associated transfer times becomes possible. The quantum yield is evaluated for different values of the vibrational damping strength of the tuning and the coupling mode. It shows that the quantum yield can be significantly enhanced by an increased vibrational coherence of the wave packet. It can reach more than 93% in the coherent or underdamped case and is reduced to 50% for the case of an incoherent wave packet. In addition, we find signatures of the geometric (or Berry) phase in the form of a destructive interference in the time-dependent probability density for the case of stronger damping. Moreover, in the case of stronger damping, we observe that the electronic wave packet directly penetrates the higher-lying PES to the lower electronic state $\left|\widetilde{e1}\right\rangle$ via tunneling, before the remaining parts of the wave packet can pass directly through the CI. Our work helps to clarify the details of the wave-packet dynamics at the seam of the CI and it provides new approaches for coherently controlling the wave packet traversal in the vicinity of the CI by tuning the vibrational coherence.

Chapter 10

Photo-induced dynamics in hybrid lead halide perovskites

In this chapter, we study the dynamics of excitons and free carriers in the hybrid lead halide perovskites by 2D electronic spectroscopy, which is one hot candidate functional material for technological application with solar cells. In the 2D spectra, the exciton peak is clearly resolved at room temperature and the exciton binding energy is precisely measured. Moreover, with the time evolution, we can detect the ultrafast exciton dissociation to the free carriers. It can be reasonably explained in terms of an entorpy-driven process. In addition, we observe the scattering of the free carriers for increasing excitation power.

10.1 Introduction

Hybrid lead halide perovskites (LHP) are known to have facile solution processability [209] and reasonably high charge carrier mobility [210, 211]. Therefore, they have become an attractive emerging material for solar cell, photodetector and lasing applications [212, 213, 214, 215, 216, 217]. Since Miyasaka and coworkers first realized perovskite-sensitized solar cells with a power conversion efficiency (PCE) of 3.8% [218] in 2009 and since the realization of highly efficient solid state perovskite cells in 2012 [212], the perovskite based photovoltaics has shown phenomenally rapid rise in PCE. With improved deposition methods and rational selection of device designs, the PCE has meteorically advanced to 22.1% based on a solid polycrystalline perovskite absorber layer sandwiched between charge selective contacts [215, 219, 220, 221]. For further rational tailoring of the device efficiency and stability, it is imperative to actively pursue the fundamental studies of underlying photophysical mechanisms for charge separation.

To advance the understanding of the basic photophysical processes, significant experimental and theoretical efforts have been expended focusing on different aspects of the problem [211, 222, 223, 224, 225, 226]. Recent studies have converged to the proposal that most elementary photoexcitations in perovskite are free charge carriers, which behave like III-V inorganic semiconductors. In addition, the significant role of bound electron-hole pairs, or excitons, has been realized. The exciton dissociation and the coupling of the exciton to the bath is the central important process in photovoltaics and the knowledge of the true exciton binding energy at room temperature is crucial for the further development of the technology. A wide range of exciton binding energies from 2 to 55 meV has been reported, based on steady state absorption, photocurrent and photoluminescence spectroscopy [227, 228, 229, 230, 231]. The fate of the exciton is also determined by the exciton-phonon coupling. The photoluminescence spectrum shows a narrow exciton peak at low temperature, which indicates quite weak exciton-phonon interactions in the LHP. Recent studies suggest that the exciton screening by the collective reorientation motion of the organic cations at room temperature weakens this interaction [232, 233, 234, 235]. In a recent study, using magneto optics measurements, the exciton binding energy $\mathrm{E_b}$ at low temperature has been determined to be ∼16 meV [230]. The value at room temperature could not be determined by magneto optics measurements due to thermal broadening. Knowledge of $\mathrm{E_b}$ at room temperature is important as photovoltaic cells operate in this temperature region. To gather a comprehensive understanding of the exciton dynamics at room temperature, it is imperative to directly observe the exciton. The free-exciton peak has been well-resolved at low temperature by the photocurrent, photoluminescence [227] and four-wave mixing spectroscopy [236]. However, at elevated temperature, the exciton peak shifts and is lost within the broad bandwidth of the free carrier transitions, which makes the detection of free excitons challenging [237].

Despite enormous experimental and theoretical efforts, there has been no report of the direct generation of free excitons after photoexcitation in LHP at room temperature [238] up to present.

2D electronic spectroscopy is one of the effective tools, which allows for direct mapping of the electronic dynamics as a function of the absorption and emission wavelength [36]. It is particularly useful for examining systems with manifolds of electronic states, i.e. solid-state materials with band structures, and of systems where static disorder induces strong spectral broadening and highly congested spectra. It has been successfully implemented to reveal the excitation energy transfer pathways in the photosynthetic protein complex [59, 90, 91, 85] and in inorganic semiconductors [239, 240]. Here we use 2D electronic spectroscopy to capture the electronic dynamics of sub-bandgap bulk excitons after optical excitation of a LHP thin film at room temperature and at 180 K. The high temporal resolution of 16 fs allows us to discriminate exciton and free carrier transitions and resolve the exciton binding energy of $E_b = 12$ meV at room temperature. Moreover, we observe the ultrafast dissociation dynamics of the free excitons within the electronic dephasing time scale of 47 fs at 296 K, resulting in primarily free charge carrier population after this process.

10.2 Sample preparation and measuring condition

Sample and the information in this section were provided by Dr. Pabitra Nayak and Prof. Herry J. Snaith from the University of Oxford. The precursor solution for the perovskite film was prepared by dissolving 442.2 mg of methylammonium iodide (Dyesol) and 351.2 mg of lead(II)acetate trihydrate (Sigma-Aldrich) in 4 ml of anhydrous N, N-dimethylformamide (Sigma-Aldrich). The perovskites films were prepared by spin-coating the precursor solution at 2000 r.p.m on quartz substrates for 45 s under a nitrogen atmosphere in a glove box. Then, the films were left for drying for 10 minutes followed by annealing at 100 °C for 5 minutes in the glove box. The UV-Vis spectrum of the thin film was taken on a Carry 300 UV-Vis spectrometer. The steady-state photoluminescence measurement was done on a Flourolog Horiba Jobin Yvon. A scanning electron microscope image was taken on a Hitachi S-4300.

10.3 Exciton binding energy

Figure 10.1(a) represents the absorption spectrum (red line) of the perovskite film. The shoulder at 13500 cm^{-1} corresponds to the bandgap transition (black arrow in Fig. 10.1(b)) from the valence band (VB) to the conduction band (CB). The laser spectrum (blue shaded region) used in the 2D optical measurements covers the bandgap transition as well as the proposed excitonic transition (red arrow in Fig.

10.1(b)) which can not be resolved at room temperature by steady state absorption measurements. To decipher the interplay of these transitions, we measured a series of photon-echo 2D electronic spectra of LHP at room temperature (296 K) and at 180 K for different waiting times. The measured 2D spectra at 296 K for the waiting times $T = 0, 20, 50$ and 200 fs are shown in Fig. 10.2. At $T = 0$ fs, the generated free carriers in LHP are associated to the central peak at $\omega_\tau = 13600$ cm^{-1}. This peak is significantly stretched along the diagonal direction which manifests a strong inhomogeneous broadening of the free carriers signal. Moreover, one additional diagonal peak as shoulder is well resolved at $\omega_\tau = 13100$ cm^{-1}, although with a lower intensity. This peak is in good agreement with the excitonic transition resolved by the Elliott model [229, 231, 241, 242, 243], which lies slightly below the free-carrier transition (described in Fig. 10.1(b)). Based on the central peak of the conduction band, we assign the bandgap of continuum transitions at $E_\mathrm{g} \sim 13200$ cm^{-1}, which is indicated in Fig. 10.1(a). Thus, the exciton binding energy, the difference in energy between the exciton and continuous transition, is obtained as $\mathrm{E_b}$12 meV, which is in the range of 5 to 55 meV of the previous measurements. Unlike the other approaches, the 2D spectroscopy allows us to directly measure the exciton binding energy in LHP. Thus, based on the observation of the 2D spectrum at $T = 0$ fs, it clearly demonstrates that the free carriers and the excitons are generated in LHP after the photo-excitation at room temperature, which is hard to be observed by other spectroscopic techniques

[228]. Based on the magnitude of the two diagonal peaks, we clearly observe that the free carriers dominate the photo-excitation process. In addition, it is known that the anti-diagonal bandwidth of the 2D spectrum at $T = 0$ fs reflects the time scale of electronic dephasing [129]. The lifetime of the electronic coherence generated by the coherent laser excitation is mainly determined by the electron-phonon and exciton-phonon interactions in LHP. Thus, the anti-diagonal bandwidth is directly determined by the strengths of these interactions. For a quantitative analysis, we fit the profile along the anti-diagonal direction for both peaks to Lorentzian lineshapes, see Fig. 10.2(b) and (c). We obtain the lifetimes of 41 fs and 47 fs for the electronic dephasing of the free carriers and the excitons, respectively. Interestingly, it is comparable to the values for a solved cyanine dye molecule [129], which is a rather small object dissolved in a solvent. Hence, the electron-phonon and exciton-phonon interactions in LHP appear to be quite weak. This is probably caused by the protection of free carriers and excitons in LHP by charge screening [232].

10.4 Exciton dissociation and carrier scattering

At $T = 20$ fs, the 2D spectrum is significantly shrinked along its diagonal direction which indicates a dramatically reduced inhomogeneous broadening. Moreover, many cross peaks appear in the frequency range of the free carriers above 13500 cm^{-1}. They stem from the dynamics of the excited-state absorption from the free-carrier band.

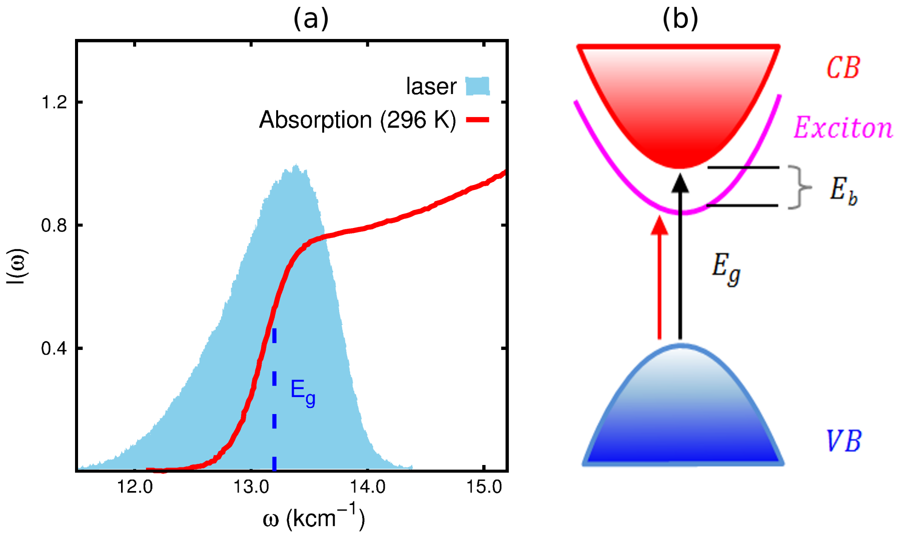

Figure 10.1: (a) Absorption (red line) and laser spectrum used in the measurement (blue curve). '$\mathrm{E_g}$' denotes the band gap in LHP. (b) Energy diagram of the exciton and conduction band in LHP. 'VB/CB' indicate the valence/conduction band, $\mathrm{E_b}$ the exciton binding energy.

The magnitude of the exciton peak at 13100 cm^{-1} significantly decays for increasing waiting times and is hard to be observed at $T = 50$ fs in Fig. 10.2. Meanwhile, one new cross peak appears at $(\omega_\tau, \omega_t) = (13500\ \mathrm{cm}^{-1},\ 12750\ \mathrm{cm}^{-1})$ which provides evidence of the electronic coupling between the excitons and the free carriers. To resolve the population dynamics, we extract the time evolution of selected peaks in the 2D spectra (marked as a red and blue square in the 2D spectra "T = 50" fs), the kinetics are shown in Fig. 10.2(d). We observe that the magnitude of the cross peak (red square) dramatically increases and reaches its maximum at 50 fs. This coincides with the time scale on which the free-exciton peak disappears in the 2D spectrum at T = 50 fs. Moreover, the time-dependent trace of the second off-diagonal peak (marked by a blue square in Fig. 10.2) clearly shows evidence of coherent oscillations within a time window of 50 fs. It is an important cross-check result that this value fully agrees with the time scale extracted from the anti-diagonal bandwidth discussed above. To ensure that the exciton decay has no contribution from exciton-exciton scattering, the energy of the pump beam has been tuned to generate the excitons well below their Mott density. Figures 10.3(c) and (d) represent exciton and charge carrier decays at different pump fluence, respectively. Unlike free carriers, excitons decay independently of the pump energy which demonstrates the linear regime of the exciton dynamics. The coincidence of the coherent dynamics and the disappearance of the exciton peak proves that the free excitons undergo an ultrafast dissociation process to free carriers within a time window of 50 fs. The energy transition from the excitonic to free-carrier band is within the time scale of the electronic dephasing, which is revealed by the anti-diagonal bandwidth of the 2D spectrum at $T = 0$ fs. Thus, this unusual energetically uphill transition is purely an electronic process which is entropically driven by the electronically coupled much higher density of states in the conduction band. For the analogy of this process, Zu and co-workers also observed coherent electronic coupling in tetracene molecules which overcome the energy barrier in singlet fission [244]. To verify this, we measure the 2D spectra at a different temperature 180 K and study the temperature-dependent dissociation process. The measured 2D spectrum at 180 K is shown in Fig. 10.4. At 180 K, the excitonic peak is better resolved from the peak related to the free carriers. In order to compare the dynamics of dissociation, kinetic traces of the exciton peak are plotted for different temperatures in Fig. 10.3(b). We do observe that the rate of exciton dissociation is not sensitive to temperature, which is strongly related to the acoustic phonons in the lattice. This temperature-independent dissociation validates our model of entropically driven coherent exciton decay. At $T = 200$ fs, the inhomogeneous broadening has completely vanished and only the free-carrier peak remains visible, as shown in Fig. 10.2.

To better resolve the exciton energy, we generate the three-dimensional matrix of time-evolved 2D electronic spectra and analyze the kinetics by the global fitting approach [69]. We perform the correlation analysis of the residuals obtained by subtracting the underlying global kinetics from the measured data and plot the correlation in the Fig. 10.3(a). We observe that the cross peaks in the correlation map can be generally divided into two parts along the diagonal direction. First, many cross peaks are present above 13500 cm^{-1} with positive and negative magnitude, which clearly shows the evidence of the associated vibrational oscillations during the free-carrier dynamics. The cross peaks are marked by the white dotted lines to illustrate the

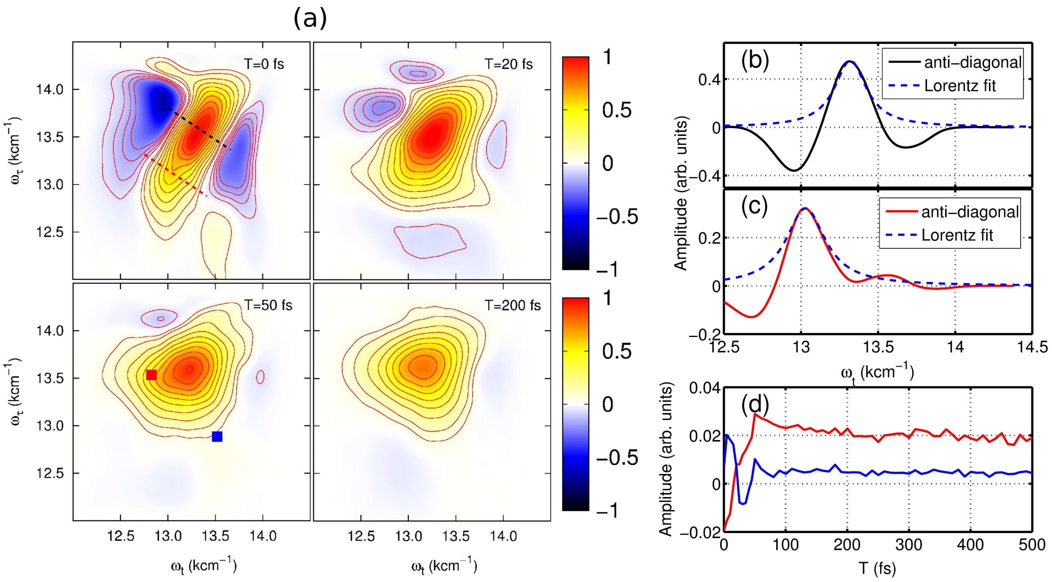

Figure 10.2: (a) Measured 2D electronic spectra with selected waiting times as indicated. The anti-diagonal profile is measured at the central peak in (b) and the exciton peak in (c). (d) Time traces of the selected peaks in the 2D spectrum at T=50 fs.

possible related eigenstates in the conduction band. Second, at least one cross peak can be resolved in the frequency region below 13500 cm^{-1}, which agrees with the transition frequency of the free exciton resolved by low-temperature photoluminescence spectroscopy [227].

In order to resolve the relative contributions of vibrational frequencies that produce the beating in the 2D spectra, a Fourier transform of the residuals of the global analysis has been performed. To visualize the spectral location of these vibrational modes, we plot the 2D vibrational map on the basis of the rephasing part of the

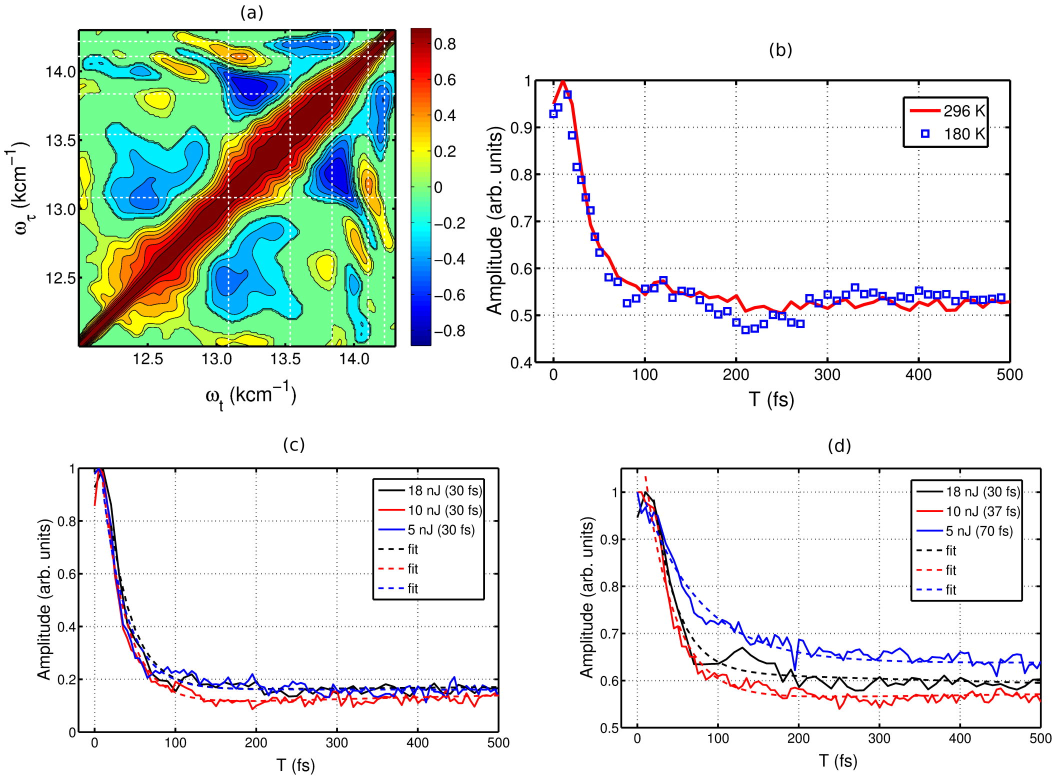

Figure 10.3: (a) 2D correlation spectrum analyzed by the residual after subtracting the kinetics in the time sequence of 2D spectra. (b) Temperature-dependent exciton dissociation dynamics. The scattering of excitons (c) and free carriers (d) is measured under different excitation conditions, i.e., different strength of the excitation laser.

2D correlation map [245]. Two low-frequency vibrational modes at 48 cm^{-1} and at 96 cm^{-1} are clearly resolved. Based on the theoretical calculations [246, 247], they are assigned to the “breathing” modes of the inorganic octrahedra, which have been suggested as the central important modes related to the charge-carrier dynamics in

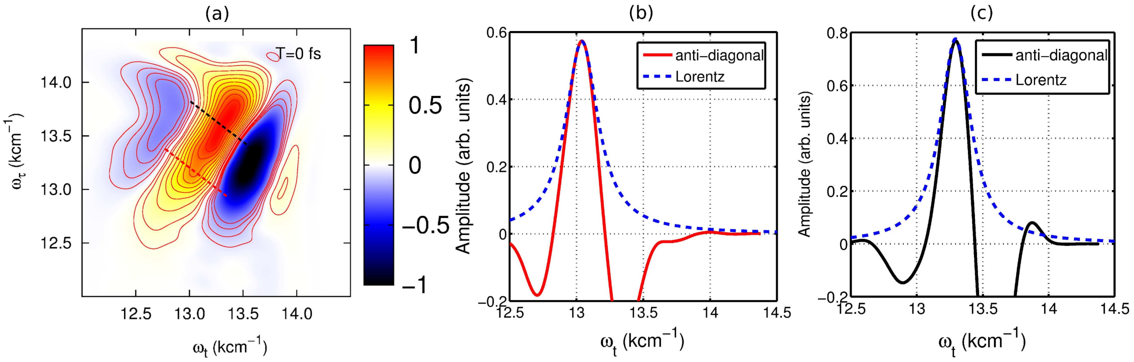

Figure 10.4: (a) Real part of the measured 2D electronic spectrum at T=0 fs at 180 K. The anti-diagonal profile of the exciton (red curve) and free-carrier (black curve) transitions are shown in (b) and (c), respectively. The associated linewidth is estimated by the fit to a Lorentzian lineshape function. This yields the linewidths of 210 and 200 cm^{-1}, which correspond to the time scales of the electronic dephasing of 49 and 51 fs, respectively.

LHP [248]. In the light of the weak electron-phonon coupling in perovskite, the role of these lattice modes should be revisited using other spectroscopic techniques. Finally, a few high-frequency modes associated with $CH_3NH_3^+$ have also been observed which are primarily centered on the conduction band and are in agreement with the reported literature [247, 249].

In conclusion, we have established direct spectroscopic evidence for the co-existence of excitons and free carriers in the LHP after optical excitation at room temperature and 180 K using 2D electronic spectroscopy. Direct observation of the exciton af-

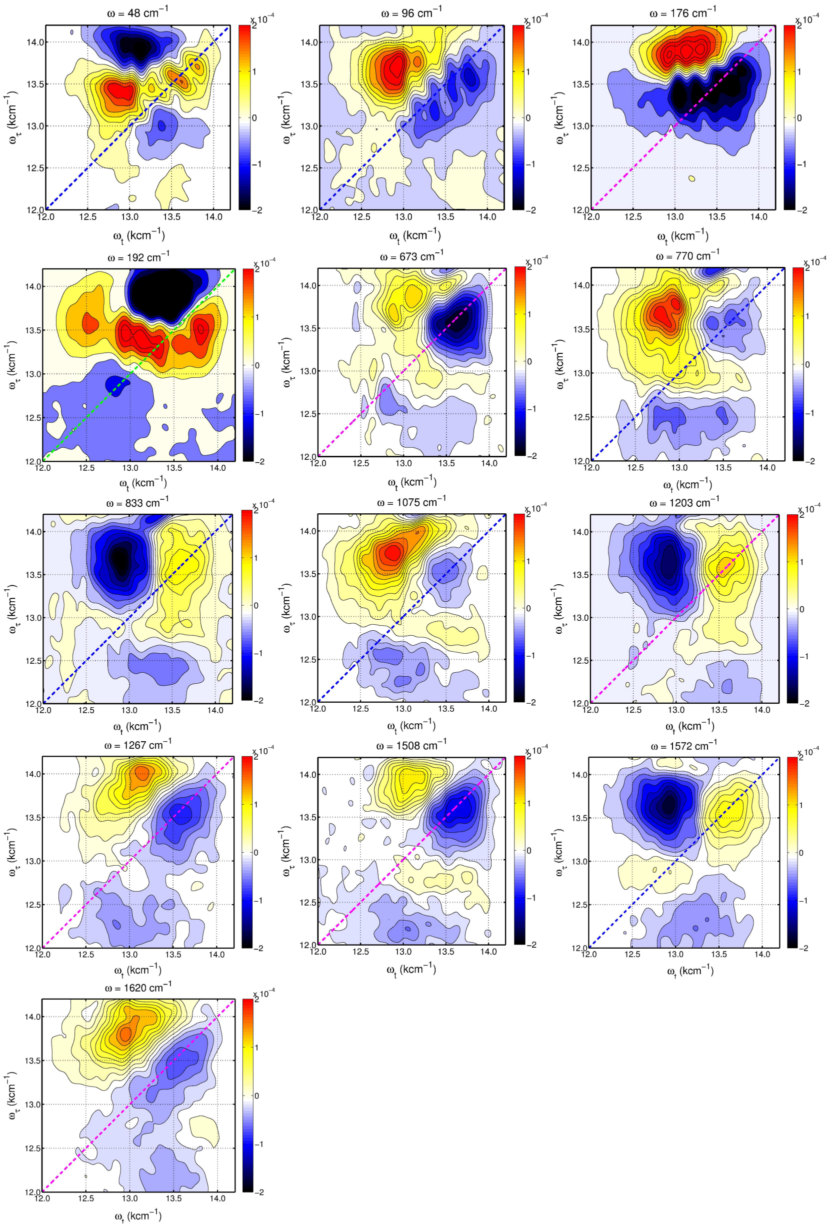

Figure 10.5: The observable vibrational modes resolved in the Fourier transform of the residual after subtracting the kinetics based on the global fitting approach.

ter optical excitation allows us to obtain the binding energy of $E_b = 12$ meV for LHP at room temperature. This shows that E_b does not completely collapse at room temperature, but retains a value similar to that determined at lower temperatures [230]. Additionally, the high temporal resolution enables us to capture the ultrafast decay of free excitons to the charge carriers occurring in a time span of 50 fs. This entropically driven uphill temperature-independent transition is favored by coherent electronic coupling between the excitonic and conduction band of states. The time scales of the electronic dephasing of 41 fs and 47 fs have been resolved by measuring the anti-diagonal bandwidth of the 2D spectrum at zero waiting time. This indicates the relatively weak exciton-phonon and electron-phonon interaction in the LHP. Moreover, it indirectly provides indication that excitons and electrons in LHP are possibly protected by charge screening effects [233]. This possibly provides a degree of immunity to mid-gap state trapping and associated non-radiative decay losses. Our results provide important fundamental insight into the nature of photogenerated species at the band-edge of LHP which elucidates the photophysical mechanisms underlying the remarkable performance of this material in optoelectronic devices.

Chapter 11

Conclusion and outlook

In this work, the photophyscial properties of biological photosynthetic complexes and of solar cell functional materials and the wave-packet dynamics in the vicinity of a conical intersection have been studied by optical 2D electronic spectroscopy. At the beginning, the molecular structures of the natural photosynthetic complexes were described. The basic concepts of the energy transfer, charge separation and electronic quantum coherence were introduced in the first chapter. In the second chapter, the physics of quantum dissipative systems has been briefly illustrated. The derivation of the quantum master equation has been obtained by the projection operator technique. The Frenkel exciton and the vibronic model have been shown to describe the energy transfer in photosynthetic protein complexes and the tight-binding model for the charge-separation process has been reviewed. The theoretical background of the spectroscopic calculation has been briefly described in the last section of the second chapter. The associated experimental techniques, the NOPA, pulse compression and the photo-echo spectrometer are illustrated in the third chapter.

In the fourth chapter, the exciton energy flow in the LHCII has been studied by 2D electronic spectroscopy at physiological temperature. It is one of the dominating antenna photosynthetic complex in higher plants. With the assistance of the global fitting approach, multiple pathways of the energy transport were clearly revealed by the time sequence of measured 2D spectra. Several timescales of the energy-transfer components have been identified from hundreds of femtoseconds to tens of picoseconds. Then, the dynamics of the charge separation in the PSII reaction center has been studied by 2D electronic spectroscopy, which is the unique natural protein complex capable of charge separation for water splitting. The signature of the primary charge separation in the reaction center is clearly resolved by the adjacent theoretical modeling and the global fitting analysis of the time sequence of the 2D spectra.

Recently, a controversy raised of whether the long-lived electronic coherence is present in the process of the primary energy transport of natural photosynthetic complexes and what would be the functional role if it exists? To answer this important question, we examine the energy-transfer process in the FMO complex by 2D electronic spectroscopy at physiological temperature. In Chapter 6, the energy transport in the FMO complex has been studied by 2D spectroscopy. It reveals several energy transfer components from hundreds of femtoseconds to tens of picoseconds. However, on the basis of careful theoretical and experimental analysis, it shows the electronic decoherence timescale of ∼60 fs, which is shorter than the timescale of the energy transport. This short electronic coherence hardly plays any functional role to impact the primary step of the energy transport in the FMO complex. The observed long-lived oscillations mainly originate from vibrational coherence. To further uncover the impact of the vibrational coherence on the timescale of the electronic coherence, especially, in the resonant case, the coherent dynamics of the excitonically-coupled indocarbocyanine dye molecule is studied in Chapter 7. It is one artificial synthetic molecule with strong electronic coupling. By this, the cross peaks are clearly separated in the 2D spectrum. Based on the modeling of the linear and 2D spectra, we demonstrate that the short-lived electronic coherence is not prolonged by the vibrational coherence.

Besides the experiments, theoretical simulations play the central important role for interpreting the 2D spectroscopic measurements. Due to the complicated molecular structures of the biological protein complexes, the system-bath model is the workhorse for the calculation of the excitonic dynamics in the photosynthetic complex, despite recent efforts on the quantum chemistry calculations with GPU techniques. In Chapter 8, the modified Redfield approach has been generalized to a master equation. 2D spectra were calculated with the combination of the modified Redfield master equation and the phase-matching approach. To examine its accuracy, the kinetics from the time sequence of 2D spectra were compared to the one calculated by the numerically exact method, QUAPI and it shows that the modified Redfield approach provides reliable results in the weak and intermediate region of the system-bath interaction. Thus, in this chapter, one possible and reliable method has been provided to study the excitonic dynamics in photosynthetic systems with rather cheap calculations.

A conical intersection is a degenerate point between two PESs and it is an important model to study the quantum dynamics of the photoisomerization reaction. With the strong nonadiabatic coupling, the electronic dynamics in the vicinity of the CI can be strongly influenced by the vibrational molecular dynamics. In Chapter 9, the established two-state two-mode model has been simplified by transforming the effective vibrational modes into the reservoir and treat their impact as part of a highly non-Markovian nonadiabatic quantum bath. HEOM has been used to calculate the electronic dynamics and the 2D electronic spectra. The signature of the CI is identified by the negative peak present in the 2D spectra, which comes from the excited-state absorption of the lower state after the wave packet have passed through the CI. Moreover, the impact of the vibrational coherence on the electronic wave packet in the vicinity of CI was studied and it shows that a more coherent wave packet results in a higher efficiency of quantum isomerization, but with slower transfer times.

In the Chapter 10, the excitonic and free carrier dynamics in perovskite have been studied by the 2D electronic spectroscopy. The exciton peak is clearly identified in the 2D spectra at the initial waiting time. The exciton binding energy is directly measured by the energy difference between the exciton and the bandgap. Ultrafast dissociation dynamics of the exciton to the free carriers is demonstrated to occur within 50 fs and it further demonstrates that this process is entropy-driven. In addition, the carrier scattering dynamics is shown in the measurements with different pulse energies.

Based on all the 2D spectroscopic studies, it becomes clear that 2D electronic spectroscopy is a powerful tool to investigate the molecular electronic dynamics at the ultrafast time scale. By projecting the absorption and emission signal onto two dimensions, the measured spectrum presents the full information of the ground state bleaching, stimulated emission and the excited state absorption. However, it still contains potential of improvals. (a). 2D electronic spectroscopy is one optical technique based on the third-order photon-echo signal, but it seems still hard to read all the information barely based on the 2D spectrum due to the overlap of the different components (ground state bleaching, stimulated emission and excited state absorption). (b). Up to now, all the 2D spectra are obtained from the ensemble-averaged signal. In principle, the 2D spectroscopy can be also applied to a single-molecule experiment, which was recently only successfully used in the optical region based on the emission spectroscopy. (c). The bandwidth of the 2D spectrum is determined by the spectrum amplified by NOPA, for instance, in the optical range (550nm to 800 nm) and the associated pulse duration of ∼5 fs. However, in some measurements, the knowledge of the deep UV, near IR and the deep IR region also contains useful information. For instance, the charge separation in the PSII reaction center and the polaron dynamics in the polymer solar cell materials are of interest. (d). 2D electronic spectroscopy is capable to fully reveal the electronic dynamics. However, the associated molecular structural dynamics are missing. Thus, the combination of the spectroscopy and a microscopy technique should be one way to solve the problem [250, 251]. At the moment, the spatial resolution is limited to ∼5 nm. For the development of (a) and (b), the 2D spectroscopy based on the phase-cycling technique [252] would be a good way to achieve these goals. On one hand, different components (ground state bleaching, stimulated emission and excited state absorption) of the 2D spectrum can be separated by locking under different phase relations of the pulse sequence. On the other hand, phase-cycling provides a much better signal-noise ratio, which makes it possible to detect the photon-echo signal from a single molecule. The problem of the broadband pulse can be overcome by the direct compression of the white light, which has been achieved by Ref. [253]. By this, the spectroscopic signal in the optical, near IR region can be obtained simultaneously.

For the theoretical studies, the system-bath model has been used for all the spectroscopic calculations in this work. It provides the workhouse for the study of the energy transfer and charge separation in the photosynthetic biological complexes and some solar cell functional materials. It definitely helps to interpret the exciton, charge and free-carrier dynamics. However, the system-bath model has limitations: (a). Simplified system, bath and system-bath interactions are usually considered. The optical transition in the polyatomic molecule is commonly approximated by a two-level model. Fluctuations in the bath are simplified as harmonic oscillations and linearly coupled to the system in order to achieve the description of the bath effect in the form of the spectral density. For this, the quantum chemistry calculations (ab initio, semiempirical) should be one alternative approach to be included, which provide the atomic picture of the study of the electronic dynamics in the polyatomic molecules. (b). Super-large molecular structures of the natural photosynthetic complexes are apparently too large for the current computer hardware for an accurate simulation. For this, on the one hand, molecular simulations would be one way to calculate the noise from the bath (for instance, thermal fluctuations and structural variations from proteins, water and vibrations from pigments). On the other hand, simplified quantum master equations, for instance, modified Redfield master equation, would provide one way to study one of the most relevant super-large complexes, PSII core complex [254]. For the study of the interaction between system and bath, the quantum chemistry/molecular dynamics [149, 255, 256] provides one way to focus on the atomic details of the interaction between system and bath. In any case, the technology of nonlinear 2D spectroscopy seems to have an exciting bright further ahead.

Appendices

Appendix A

Model Hamiltonian for LHCII

In Chapter 4, we have studied the photophysics of the LHCII. Here, we provide the details of the Hamiltonian of the LHCII.

A.1 Hamiltonian Matrix

The LHCII model includes spectroscopically relevant 8 chlorophyll-a (Chla) and 6 chlorophyll-b (Chlb). No carotenoids are accounted for. The 14-dimensional model Hamiltonian and its matrix elements have been determined as follows: First, we start with the excitonic couplings which were taken from Ref. [65] where they had been calculated by the transition density cube method. Second, the vertical excitation energies of the chlorophylls were initially pre-calculated by quantum chemistry methods. We have used both time-dependent density functional theory (B3LYP/6-31G) and ZINDO/S [257]. Then, the site energies were further optimized by fitting the resulting absorption and circular dichroism (CD) spectra simultaneously to the available experimental data. The Hamiltonian obtained as such was then used to calculate the 2D spectra. Inhomogeneous broadening and the strength of the system-bath interaction were extracted by a simultaneous fit of the linear spectra (absorption and CD) and the cuts through the 2D spectra along the anti-diagonal. After several refining loops, the final Hamiltonian was obtained in the optimized form as the matrix

$$\left[\begin{array}{cccccccccccccc}
15410 & 47.1 & -6.1 & -2.7 & 0.5 & -2.0 & -2.6 & 3.3 & 4.4 & -4.5 & 24.5 & 2.3 & -8.4 & 2.9 \\
47.1 & 14790 & 17.4 & 5.5 & -0.2 & 4.9 & 6.2 & -5.8 & -21.9 & -5.4 & 0.7 & 10.1 & -1.9 & 0.1 \\
-6.1 & 17.4 & 14904 & -0.5 & -0.2 & -2.1 & 8.2 & 4.2 & 71.6 & 8.4 & -0.7 & -0.6 & 2.4 & -5.7 \\
-2.7 & 5.5 & -0.5 & 15032 & 5.4 & 80.8 & 26.0 & -5.7 & -1.5 & -0.2 & -3.3 & 3.7 & 2.2 & -2.8 \\
0.5 & -0.2 & -0.2 & 5.4 & 15186 & 11.5 & -5.2 & -3.7 & -0.1 & 0.8 & 1.1 & -2.2 & -1.2 & 0.0 \\
-2.0 & 4.9 & -2.1 & 80.8 & 11.5 & 15348 & 23.7 & -6.7 & -11.8 & -0.6 & -2.0 & 2.1 & 1.2 & -1.8 \\
-2.6 & 6.2 & 8.2 & 26.0 & -5.2 & 23.7 & 15240 & -3.5 & -1.7 & -0.4 & -2.1 & 2.2 & 2.7 & -2.4 \\
3.3 & -5.8 & 4.2 & -5.7 & -3.7 & -6.7 & -3.5 & 15360 & 26.1 & 57.0 & 4.8 & -1.3 & -2.2 & 1.4 \\
4.4 & -21.9 & 71.6 & -1.5 & -0.1 & -11.8 & -1.7 & 26.1 & 15180 & 1.1 & 3.3 & -0.2 & -2.5 & 2.0 \\
-4.5 & -5.4 & 8.4 & -0.2 & 0.8 & -0.6 & -0.4 & 57.0 & 1.1 & 14680 & -26.4 & 12.4 & 6.0 & -1.2 \\
24.5 & 0.7 & -0.7 & -3.3 & 1.1 & -2.0 & -2.1 & 4.8 & 3.3 & -26.4 & 14880 & 105.0 & -0.8 & 0.6 \\
2.3 & 10.1 & -0.6 & 3.7 & -2.2 & 2.1 & 2.2 & -1.3 & -0.2 & 12.4 & 105.0 & 14880 & -1.0 & -0.2 \\
-8.4 & -1.9 & 2.4 & 2.2 & -1.2 & 1.2 & 2.7 & -2.2 & -2.5 & 6.0 & -0.8 & -1.0 & 14802 & -28.0 \\
2.9 & 0.1 & -5.7 & -2.8 & 0.0 & -1.8 & -2.4 & 1.4 & 2.0 & -1.2 & 0.6 & -0.2 & -28.0 & 14860
\end{array}\right] \tag{A.1}$$

All entries are given in units of cm^{-1}.

Appendix B

Vibronic dimer

In Chapter 7, we have studied the indocyanine dimer which shows a strong vibronic coupling. Here, we study other parameters and configurations to thoroughly investigated its quantum coherence properties.

B.1 Other parameters of the vibronic dimer

In order to underpin further our conclusion drawn in Chapter 7, our accurate theoretical model which has been validated against precise experimental data, allows us to study further parameter constellations in theory. We have carried out additional calculations for two different cases, which are (i) a vibrational frequency of $\omega = 2460$ cm^{-1}, and, (ii) an excitonic coupling of $J = 250$ cm^{-1}. The stick spectra with the electronic and the vibrational components and the corresponding absorption spectra are shown in Fig. B.1 and Fig. B.2, respectively.

Large frequency gaps between the sticks are observed in Fig. B.1 for the vibrational frequency of $\omega = 2460$ cm^{-1}. In turn, for the modified excitonic coupling of $J = 250$ cm^{-1}, we find congested sticks as shown in Fig. B.2.

Then, the resulting 2D spectra of the two cases (i) and (ii) have been again calculated upon applying the time-nonlocal quantum master equation approach in combination with the EOM-PMA [87]. The results are shown in Fig. B.3. Again, well separated diagonal and cross peaks appear.

In order to analyze the coherence properties of the cross peaks, the amplitude of the cross-peak D is extracted. Its evolution for growing waiting times is shown in Fig. B.4 for both cases (i) and (ii). As before, we have fitted the data points by two decaying cosine functions at long time, similarly as described in Chapter 7. We find two clearly separated oscillation frequencies in the data fit, which exactly coincide with the energy gaps between the stick B and the two sticks of peak A in the absorption spectrum, see Fig. B.4 for the precise values. More interestingly, the decay rate of the initial short-time oscillations and the asymptotic long-time oscillations do not change very much in the considered cases. This provides a further proof that the electronic dephasing cannot be improved by the long-lived vibrational oscillations via the vibronic molecular coupling.

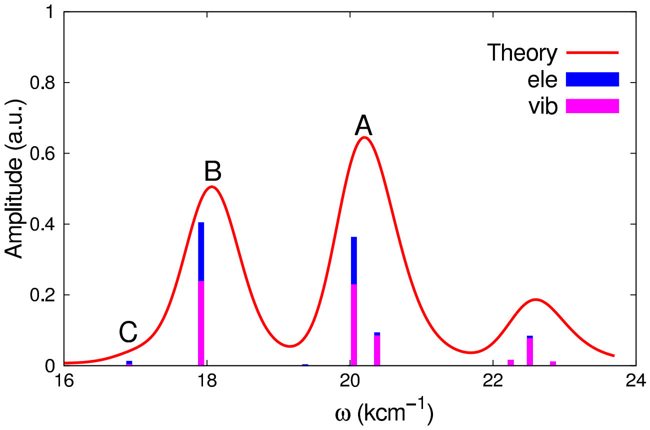

Figure B.1: Absorption spectrum of the dimer with a modified vibrational frequency of $\omega = 2460$ cm^{-1} (all the other parameters are kept unchanged and are as given in Chapter 7). The large spectral distances between the stick of peak B and the two sticks of peak A are 2136 cm^{-1} and 2460 cm^{-1}, respectively.

B.2 Global fitting analysis of 2D spectra

In this part, we describe further details of the fitting procedure carried out to analyze the 2D spectra. To obtain the “background-free” oscillatory components from the sequence of the 2D spectra calculated at the different waiting times at each spectral position ω_t, ω_τ, we have applied the recently developed multi-dimensional global fitting procedure [69] to the 3D data array formed by a series of 2D spectra. This technique has already been successfully applied to the analysis of the 2D photon-echo experimental data of tubular J-aggregates [131]. The detailed description of the method can be found elsewhere [69]. This fitting approach provides the

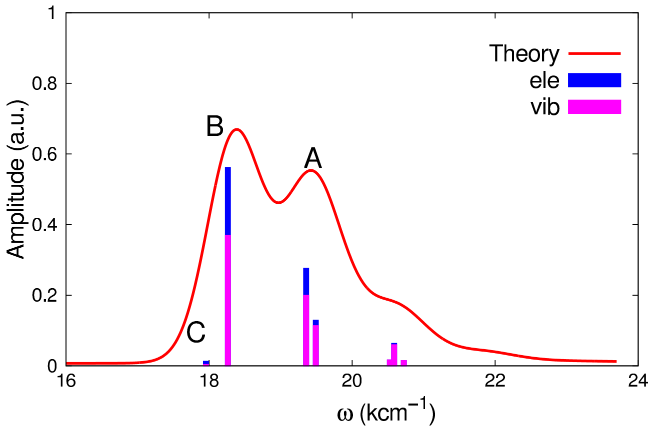

Figure B.2: Absorption spectrum of the dimer with the weaker electronic coupling $J = 250$ cm^{-1} (all other parameters remain unchanged and are given in Chapter 7). The spectral distances between the stick of peak B and the two sticks of peak A are 1095 cm^{-1} and 1230 cm^{-1}, respectively.

two-dimensional decay-associated spectra (2DDAS) from which the energy transfer pathways between different excitonic levels can be reconstructed.

We have performed the two-dimensional global fit of the calculated 2D spectra in a range of waiting times $[0, 400]$ fs and have found a satisfactory fit upon using the three lifetimes 25 fs, 90 fs, and an infinitely long relaxation component (at zero frequency) whose time constant cannot be resolved within a 400 fs-time window. The 2DDAS (real part) for each lifetime is plotted in Fig. B.5 together with the distribution of standard deviations (STD) of residuals which is a good measure of the intensity of the oscillations in the sequence of 2D spectra. The quality of the fit can be estimated

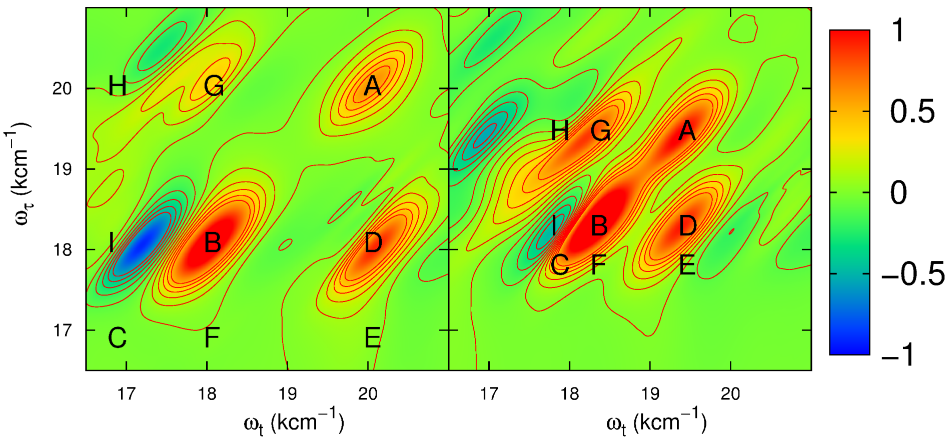

Figure B.3: 2D spectra of the dimer with the vibrational frequency $\omega = 2460$ cm^{-1} (left, all the other parameters are as given in Chapter 7) and with a weaker excitonic coupling $J = 250$ cm^{-1} (right, all the other parameters are as given in Chapter 7) for the waiting time $T = 0$ fs.

from Fig. 7.10 in the main text.

In the next step, we have performed the Fourier transform for the residuals and have, by this, obtained a "truly" three-dimensional spectrum in the frequency space $[\omega_t, \omega_\tau, \omega_T]$. We note that due to a relatively small waiting time window, the resolution in this 3D spectrum along the coordinate ω_T is 83 cm^{-1}.

Figures B.6 shows the spectra of the oscillation amplitudes for the three most intense frequencies in the 3D spectrum, which are 1251 cm^{-1}, 1334 cm^{-1}, and 2502 cm^{-1}. They are associated to the vibrational frequency, the beating frequency between the excitonic states A and B. The oscillations originate from the excited state

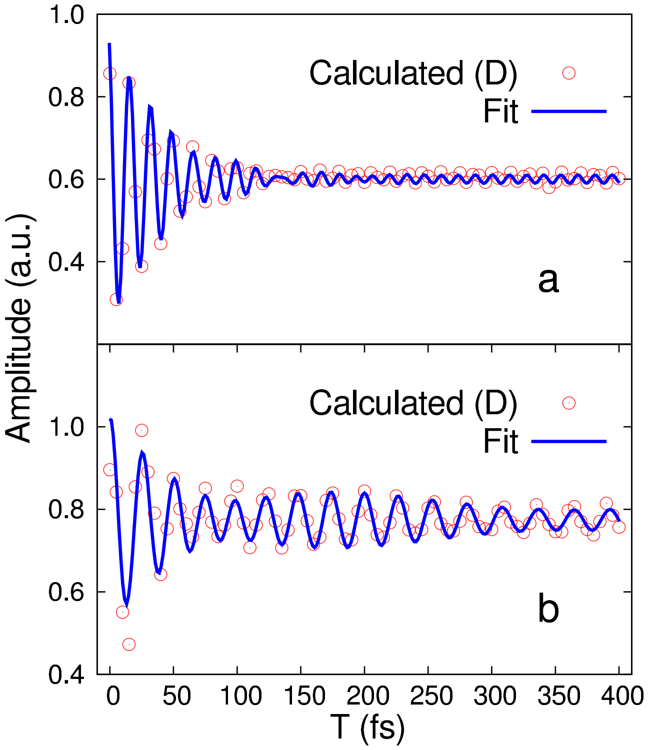

Figure B.4: Evolution of the amplitude of cross-peak D for growing waiting times for the two cases (i) with the vibrational frequency $\omega = 2460$ cm^{-1} (a), and (ii) with the excitonic coupling 250 cm^{-1} (b). The data are again fitted to two cosine functions (see the fitting function part) and we obtain the fit parameters for (a) as $\omega_{D1} = 1989$ (1974, 2003) cm^{-1} and $\omega_{D2} = 2484$ (2461, 2507) cm^{-1}, and, for (b) as $\omega_{D1} = 1208$ (1191, 1225) cm^{-1} and $\omega_{D2} = 1324$ (1306, 1343) cm^{-1}. The numbers in brackets indicate the 95% confidence bounds.

absorption, respectively.

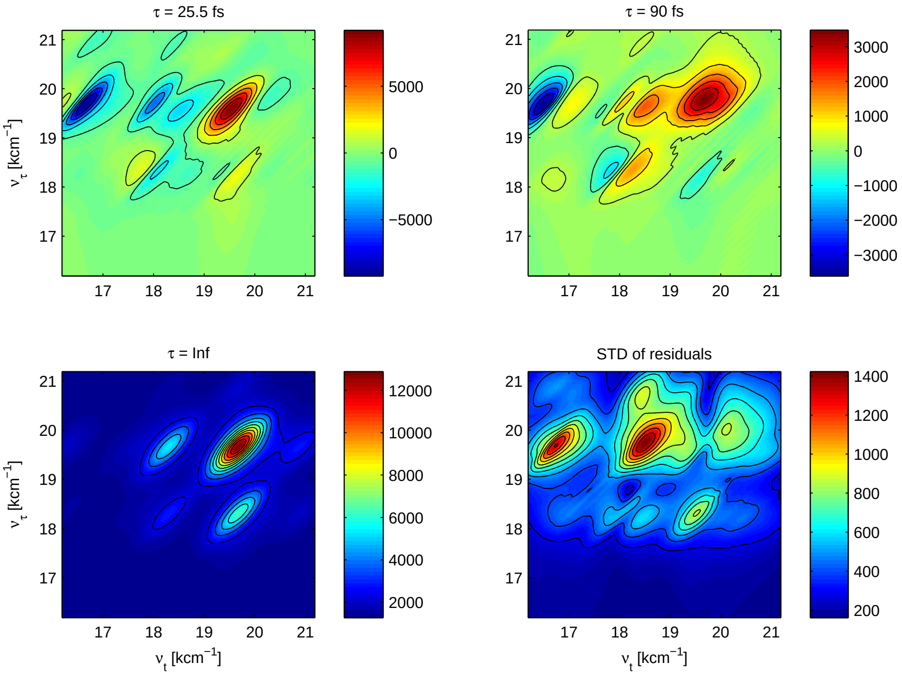

Figure B.5: Two-dimensional decay-associated spectra obtained after a 2D global analysis of 2D spectra, calculated in the waiting time range of $[0, 400]$ fs for the lifetimes $\tau = 25.5$ fs (top left), $\tau = 90$ fs (top right) and $\tau = \infty$ (bottom left). The bottom-right plot shows the standard deviations of residuals.

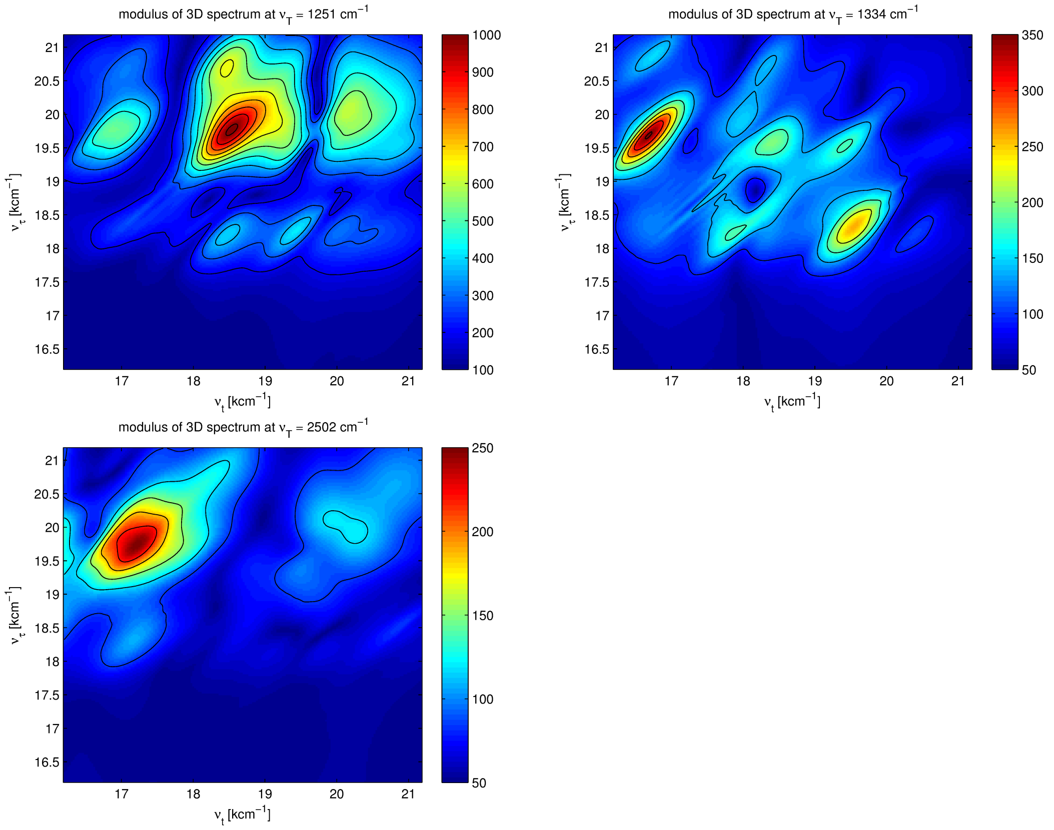

Figure B.6: Slice of the 3D spectrum showing the amplitude spectral distribution at $\omega_T = 1251\ \mathrm{cm}^{-1}$, $1334\ \mathrm{cm}^{-1}$ and $2502\ \mathrm{cm}^{-1}$, respectively.

Appendix C

Quasiadiabatic propagator path integral

Here, we provide the details of the Quasiadiabatic path integral approach and follow Ref. [258, 259]. In absence of external field, the system-bath model (see Chapter 1) is given by the Hamiltonian

$$H_{tot} = H_S + \sum_j \left(\frac{p_j^2}{2m_j} + \frac{1}{2} m_j \omega_j^2 \left(x_j - \frac{c_j x}{m_j \omega_j^2} \right)^2 \right). \tag{C.1}$$

Here, we assume the linear type of system-bath interaction $c_j x$. It is common to assume that the bath is initially at thermal equilibrium and the system-bath interaction switched on at t=0. Therefore, the initial total density operator can be factorized as

$$W(0) = \rho(0) \bigotimes e^{-\beta H_B}, \tag{C.2}$$

where H_B is Hamiltonian for isolated bath, $\rho(0)$ is the initial density matrix of system and $\beta = 1/k_B T$, k_B is Boltzmann constant. The total density operator is propagated with time according to

$$\rho(t) = Tr_B \left[e^{-iHt/\hbar} W(0) e^{iHt/\hbar} \right], \tag{C.3}$$

where Tr_B denotes the trace with respect to all the bath DOF. Discretization of the path integral representation of Eq. C.3 by N time steps of length $\Delta t = t/N$ yields the form

$$\begin{aligned}
\rho(t) &= \langle s''| \, \rho(0) \, |s'\rangle , \\
&= \int ds_0^+ \int ds_1^+ \ldots \int ds_{N-1}^+ \int ds_0^- \int ds_1^- \ldots \int ds_{N-1}^- \, \langle s''| \, e^{-iH_S \Delta t/\hbar} \left| s_{N-1}^+ \right\rangle \ldots \\
&\quad \left\langle s_1^+ \right| e^{-iH_S \Delta t/\hbar} \left| s_0^+ \right\rangle \left\langle s_0^+ \right| \rho_s(0) \left| s_0^- \right\rangle \left\langle s_0^- \right| e^{iH_S \Delta t/\hbar} \left| s_1^- \right\rangle \ldots \left\langle s_{N-1}^- \right| e^{iH_S \Delta t/\hbar} \left| s' \right\rangle \\
&\quad I(s_0^+, s_1^+, \ldots, s_{N-1}^+, s'', s_0^-, s_1^-, \ldots, s_{N-1}^-, s'; \Delta t).
\end{aligned} \tag{C.4}$$

Here, $s_k^\pm$ denotes the coordinates at time $k\Delta t$ on the forward discretized Feynman path. $I(s_0^+, s_1^+, \ldots,$
$s_{N-1}^+, s'', s_0^-, s_1^-, \ldots, s_{N-1}^-, s'; \Delta t)$ is an influence functional that arises from the coupling to the environment, which has the form

$$\begin{aligned}
I(s_0^+, s_1^+, \ldots, s_{N-1}^+, s'', s_0^-, s_1^-, \ldots, s_{N-1}^-, s'; \Delta t) &= Tr_B [e^{-iH_B(s'')\Delta t/2\hbar} e^{-iH_B(s_{N-1}^+)\Delta t/\hbar} \ldots \\
&\quad \times e^{-iH_B(s_0^+)\Delta t/2\hbar} \rho_B(0) e^{iH_B(s_0^-)\Delta t/2\hbar} \ldots \\
&\quad \times e^{iH_B(s_{N-1}^-)\Delta t/\hbar} e^{iH_B(s')\Delta t/2\hbar}],
\end{aligned} \tag{C.5}$$

which is simplified by the spectral density $J(\omega)$,

$$\begin{aligned} I(s_0^+, s_1^+, \ldots, s_{N-1}^+, s'', s_0^-, s_1^-, \ldots, s_{N-1}^-, s'; \Delta t) \qquad & = \\ \exp\left(-\frac{1}{\hbar} \sum_{k=0}^{N} \sum_{k'=0}^{k} (s_k^+ - s_k^-)(\eta_{kk'} s_{k'}^+ - \eta *_{kk'} s_{k'}^-) \right), & \end{aligned} \tag{C.6}$$

where $s_N^+ = s''$ and $s_N^- = s'$ and the different types of coefficients $\eta_{kk'}$ read

$$\begin{aligned} \eta_{kk'} &= \frac{2}{\pi} \int_{-\infty}^{\infty} d\omega \frac{J(\omega)}{\omega^2} \frac{\exp(\beta\hbar\omega/2)}{\sinh(\beta\hbar\omega/2)} \times \sin^2(\omega\Delta t/2) e^{-i\omega\Delta t(k-k')}, \qquad 0 < k' < k < N, \\ \eta_{kk} &= \frac{1}{\pi} \int_{-\infty}^{\infty} d\omega \frac{J(\omega)}{\omega^2} \frac{\exp(\beta\hbar\omega/2)}{\sinh(\beta\hbar\omega/2)} \times (1 - e^{-i\omega\Delta t}), \qquad 0 < k < N, \\ \eta_{N0} &= \frac{2}{\pi} \int_{-\infty}^{\infty} d\omega \frac{J(\omega)}{\omega^2} \frac{\exp(\beta\hbar\omega/2)}{\sinh(\beta\hbar\omega/2)} \times \sin^2(\omega\Delta t/4) e^{-i\omega(t-\Delta t/2)}, \\ \eta_{00} = \eta_{NN} &= \frac{1}{2\pi} \int_{-\infty}^{\infty} d\omega \frac{J(\omega)}{\omega^2} \frac{\exp(\beta\hbar\omega/2)}{\sinh(\beta\hbar\omega/2)} \times (1 - e^{-i\omega\Delta t/2}), \\ \eta_{k0} &= \frac{2}{\pi} \int_{-\infty}^{\infty} d\omega \frac{J(\omega)}{\omega^2} \frac{\exp(\beta\hbar\omega/2)}{\sinh(\beta\hbar\omega/2)} \times \sin(\omega\Delta t/4) \sin(\omega\Delta t/2) e^{-i\omega(k\Delta t-\Delta t/4)}, \qquad 0 < k < N, \\ \eta_{Nk} &= \frac{2}{\pi} \int_{-\infty}^{\infty} d\omega \frac{J(\omega)}{\omega^2} \frac{\exp(\beta\hbar\omega/2)}{\sinh(\beta\hbar\omega/2)} \times \sin(\omega\Delta t/4) \sin(\omega\Delta t/2), \qquad 0 < k < N. \end{aligned} \tag{C.7}$$

Here, spectral density for the negative part is formally defined as $J(-\omega) = -J(\omega)$.

Iterative propagation. To derive the iterative propagation, we rewrite the influence functional Eq. C.6 as a product of subterms

$$\begin{aligned} I = \prod_{k=0}^{N} I_0(s_k^\pm) \prod_{k=0}^{N-1} I_1(s_k^\pm, s_{k+1}^\pm) \ldots \prod_{k=0}^{N-\Delta k} I_{\Delta k}(s_k^\pm, s_{k+\Delta k}^\pm) \ldots \times \\ \prod_{k=0}^{N-\Delta k_{max}} I_{\Delta k_{max}}(s_k^\pm, s_{k+\Delta k_{max}}^\pm), \end{aligned} \tag{C.8}$$

where

$$\begin{aligned} I_0(s_k^\pm) &= \exp\big\{ -\frac{1}{\hbar}(s_k^+ - s_k^-)(\eta_{kk} s_k^+ - \eta_{kk}^* s_k^-) \big\}, \\ I_{\Delta k}(s_k^\pm, s_{k+\Delta k}^\pm) &= \exp\big\{ -\frac{1}{\hbar}(s_{k+\Delta k}^+ - s_{k+\Delta k}^-)(\eta_{k+\Delta k,k} s_k^+ - \eta_{k+\Delta k,k}^* s_k^-) \big\}, \qquad \Delta k \geq 1. \end{aligned} \tag{C.9}$$

For the iterative propagation, we define a new propagation tensor Λ of rank $\Delta k_{max}+1$,

$$\Lambda^{\Delta k_{max}+1}(s_k^\pm, s_{k+1}^\pm, \ldots, s_{k+\Delta k_{max}}^\pm) = K(s_k^\pm, s_{k+1}^\pm) I_0(s_k^\pm) I_1(s_k^\pm, s_{k+1}^\pm) I_2(s_k^\pm, s_{k+2}^\pm) \times \ldots \\ \times I_{\Delta k_{max}}(s_k^\pm, s_{k+\Delta k_{max}}^\pm). \tag{C.10}$$

Here, $K(s_k^\pm, s_{k+1}^\pm)$ is the propagator for the system part, which is given as

$$K(s_k^\pm, s_{k+1}^\pm) = \left\langle s_{k+1}^+ \right| e^{-iH_S\Delta t/\hbar} \left| s_k^+ \right\rangle \left\langle s_k^- \right| e^{iH_S\Delta t/\hbar} \left| s_{k+1}^- \right\rangle. \tag{C.11}$$

We also define the reduced density tensor $A^{\Delta k_{max}}$ with the initial value obtained from initial density matrix,

$$A^{\Delta k_{max}}(s_0^\pm, s_1^\pm, \ldots, s_{\Delta k_{max}-1}^\pm) = \left\langle s_0^+ \right| \rho_S(0) \left| s_0^- \right\rangle. \tag{C.12}$$

We propagate $A^{\Delta k_{max}}$ to time Δt according to the relation

$$A^{\Delta k_{max}}(s_{k+1}^\pm, \ldots, s_{k+\Delta k_{max}}^\pm; (k+1)\Delta t) = \int ds_k^\pm \Lambda^{\Delta k_{max}+1}(s_k^\pm, \ldots, s_{k+\Delta k_{max}}^\pm) \times \\ A^{\Delta k_{max}}(s_k^\pm, \ldots, s_{k+\Delta k_{max}-1}^\pm; k\Delta t). \tag{C.13}$$

The final reduced density matrix at time $t = N\Delta t$ is calculated by the terminal iterations

$$\rho(s_N^\pm; N\Delta t) = A^{\Delta k_{max}}(s_k^\pm, s_{N+1}^\pm = \ldots = s_{N+\Delta k_{max}}^\pm = 0; N\Delta t). \tag{C.14}$$

Convergence of memory parameters. The quasiadiabatic propagator path integral (QUAPI) is a numerical exact approach to determine the influence of environmental fluctuations on the system dynamics within a open quantum systems approach. Specifically, QUAPI determines the time dependent reduced density operator $\rho(t)$ of the system. It is well established in the literature and we only briefly summarize the central features in the following. The algorithm is based on a symmetric Trotter splitting of the short-time propagator $K(t_{k+1}, t_k)$ for the full Hamiltonian into two parts, one depending on the system Hamiltonian, and one involving the bath and the coupling term. The short-time propagator determines the time evolution over a Trotter time slice Δt. The discrete time evolution becomes exact in the limit $\Delta t \to 0$. For any finite Δt, a finite Trotter error occurs which has to be eliminated by choosing Δt small enough to achieve convergence. On the other side, the environmental DOF generate correlations which are non-local in time. For any finite temperature, these correlations decay on a time scale denoted as the memory time scale. The QUAPI scheme defines an augmented reduced density tensor, which lives on this full memory time window. Then, the iteration scheme described above is established in order to extract the time evolution of this object. All correlations are completely included over the finite memory time $\tau_{\mathrm{mem}} = K\Delta t$ but are neglected for times beyond τ_{mem}. One increases the memory parameter K until convergence is found. The two strategies to achieve convergence, i.e., minimize Δt but maximize $\tau_{\mathrm{mem}} = K\Delta t$, are naturally counter-current, but nevertheless convergent results can be obtained in a wide range of parameters, including the cases presented in this work.

Bibliography

[1] R. E. Blankenship, *Molecular mechanisms of photosynthesis*; Blackwell Science: Oxford; Malden, MA, 2002.

[2] G. D. Scholes, G. R. Fleming, A. Olaya-Castro, and R. van Grodelle, Nat. Chem. **3**, 763 (2011).

[3] Z. F. Liu, H. C. Yan, K. B. Wang, T. Y. Kuang, J. P. Zhang, L. L. Gui, X. M. An, and W. R. Chang, Nature **428**, 287 (2004).

[4] R. Standfuss, A. C. T. van Scheltinga, M. Lamborghini, and W. Kuhlbrandt, EMBO J. **24**, 919 (2005).

[5] B. A. Diner, and F. Rappaport, Annu. Rev. Plant Biol. **53**, 551 (2002).

[6] R. E. Fenna, and B. W. Matthews, Nature **258**, 573 (1975).

[7] J. Dostál, J. Pšenčík, and D. Zigmantas, Nat. Chem. **8**, 705 (2016).

[8] D. E. Tronrud, J. Z. Wen, L. Gay, and R. E. Blankenship, Photosynth. Res. **100**, 79 (2009).

[9] W. Humphrey, A. Dalke, and K. Schulten, “VMD - Visual Molecular Dynamics”, J. Molec. Graphics, **14**, 33 (1996).

[10] H. Gaffron, and K. Wohl, Naturwissenschaften **24**, 81 (1936).

[11] T. Förster, In: *Modern Quantum Chemistry Istanbul Lectures*, Academic Press, New York, pp. 93137 (1965).

[12] R. S. Knox, and D. Gülen, Photochem. Photobiol. **57**, 40 (1993).

[13] J. Frenkel, Phys. Rev. **37**, 17 (1931).

[14] D. L. Dexter, J. Chem. Phys. **101**, 7211 (1953).

[15] S. Gröblacher, A. Trubarov, N. Prigge, G. D. Cole, M. Aspelmeyer, and J. Eisert, Nat. Comm. **6**, 7606 (2015).

[16] U. Weiss, *Quantum Dissipative Systems*, 3rd ed. (World Scientific, Singapore 2008).

[17] P. Ullersma, Physica (Utrecht) **32**, 27 (1966).

[18] R. Zwanzig, J. Stat. Phys. **9**, 215 (1973).

[19] A. J. Leggett, S. Chakravarty, A. T. Dorsey, M. P. A. Fisher, A. Garg, and W. Zwerger, Rev. Mod. Phys. **59**, 1 (1987).

[20] A. G. Redfield, IBM J. Res. Dev. **1**, 19 (1957); Adv. Magn, Reson. **1**, 1 (1965).

[21] M. Morillo, and R. I. Cukier, Phys. Rev. B **54**, 13962 (1997).

[22] D. Abramavicius, and S. Mukamel, J. Chem. Phys. **133**, 184501 (2010).

[23] S. Mukamel, *Principles of Nonlinear Optics and Spectroscopy* (Oxford University Press, New York 1995).

[24] M. F. Gelin, D. Egorova, and W. Domcke, J. Phys. Chem. Lett. **2**, 114 (2011).

[25] G. S. Schlau-Cohen, A. Ishizaki, and G. R. Fleming, Chem. Phys. **386**, 1 (2011).

[26] M. F. Gelin, D. Egorova, and W. Domcke, Chem. Phys. **312**, 135 (2005).

[27] L. De Boni, C. Toro, and F. E. Hernandez, Opt. Exp. **16**, 957 (2008).

[28] H. Hundertmark, S. Rammler, T. Wilken, R. Holzwarth, T. W. Hänsch, and P. S. J. Russell, Opt. Exp. **17**, 1919 (2009).

[29] G. M. Gale, M. Cavallari, T. J. Driscoll, and F. Hache, Opt. Lett. **20**, 1562 (1995).

[30] G. Cerullo, and S. D. Silvestri, Review of Scientific Instruments **74**, 1 (2003).

[31] A. V. Smith. How to select nonlinear crystals and model their performance using snlo software.

[32] R. L. Fork, C. H. Cruz, P. C. Becker, and C. V. Shank, Opt. Lett. **12**, 483 (1987).

[33] E. H. G. Backus, S. Garret-Roe, and P. Hamm, Opt. Lett. **33**, 2665 (2008).

[34] A. D. Bristow, D. Karaiskaj, X. Dai, and S. T. Cundiff, Opt. Exp. **16**, 1807 (2008).

[35] S. M. G. Faeder, and D. M. Jonas, J. Phys. Chem. B **103**, 10489 (1999).

[36] V. I. Prokhorenko, A. Halpin, and R. J. D. Miller, Opt. Exp. **17**, 9764 (2009).

[37] P. W. Hemelrijk, S. L. S. Kwa, R. van Grondelle, and J. P. Dekker, Biochim. Biophys. Acta **1098**, 159 (1992).

[38] S. Nussberger, J. P. Dekker, W. Kunhlbrandt, B. M. van Bolhuis, R. van Grondelle, and H. van Amerongen, Biochemistry **33**, 14775 (1994).

[39] E. J. G. Peterman, S. Hobe, F. Calkoen, R. van Grondelle, H. Paulsen, and H. van Amerongen, Biochim. Biophys. Acta **1273**, 171 (1994).

[40] C. Tieta, F. Jelezko, U. Gerken, S. Schuler, A. Schubert, H. Rogl, and J. Wrachtrup, Biophys. J. **81**, 556 (2001).

[41] D. Olszowka, S. Krawczyk, and W. Maksymiee, Biochim. Biophys. Acta **1657**, 61 (2004).

[42] J. Piper, M. Ratsep, R. Jankowiak, K. D. Irrgang, J. Voigt, T. Renger, and G. J. Small, J. Phys. Chem. A **103**, 2412 (1999).

[43] C. C. Gradinaru, S. Özdemir, D. Gülen, I. H. M. Stokkum, R. van Grondelle, and H. van Amerongen, Biophys. J. **75**, 3064 (1998).

[44] J. P. Connelly, M. G. Müller, M. Hucke, G. Gatzen, C. W. Mullineaux, A. V. Ruban, P. Horton, and A. R. Holzwarth, J. Phys. Chem. B **101**, 1902 (1997).

[45] R. Croce, M. G. Müller, R. Bassi, and A. R. Holzwarth, Biophys. J. **80**, 901 (2001).

[46] R. Agarmal, B. P. Krueger, G. D. Scholes, M. Yang, J. Yom, L. Mets, and G. R. Fleming, J. Phys. Chem. B **104**, 2908 (2000).

[47] J. M. Salverda, M. Vengris, B. P. Krueger, G. D. Scholaes, A. R. Czamoleski, V. I. Novoderezhkin, H. van Amerongen, and R. van Grondelle, Biophys. J. **84**, 450 (2003).

[48] G. S. Schlau-Cohen, T. R. Calhoun, N. S. Ginsberg. E. L. Read, M. Ballottari, R. Bassi, R. van Grondelle, and G. R. Fleming, J. Phys. Chem. B **113**, 15352 (2009).

[49] T. R. Calhoun, N. S. Ginsberg, G. S. Schlau-Cohen, Y. -C. Cheng, M. Ballottar, R. Bassi, and G. R. Fleming, J. Phys. Chem. B **113**, 16291 (2009).

[50] K. L. Wells, P. H. Lambrev, Z. -Y. Zhang, G. Garab, and H. -S. Tan, Phys. Chem. Chem. Phys. **16**, 11640 (2014).

[51] H. van Amerongen, and R. Croce, *Primary Processes of Photosynthesis: Basic Principles and Apparatus*, RSC Publ. Cambridge, UK Vol. I, p. 329, 2008.

[52] R. van Grondelle, and V. I. Novoderezhkin, Phys. Chem. Chem. Phys. **8**, 793 (2006).

[53] V. I. Novoderezhkin, M. A. Palacios, H. van Amerongen, and R. van Grondelle, J. Phys. Chem. B **109**, 10493 (2005).

[54] B. P. Krueger, G. D. Scholes, and G. R. Fleming, J. Phys. Chem. B **102**, 5378 (1998).

[55] J. Adolphs, and T. Renger, Biophys. J. **91**, 2778 (2006).

[56] J. D. Hybl, A. W. Albrecht, S. M. G. Faeder, and D. M. Jonas, Chem. Phys. Lett. **297**, 307 (1998).

[57] D. M. Jonas, Annu. Rev. Phys. Chem. **54**, 425 (2003).

[58] T. Brixner, J. Stenger, H. M. Vaswani, M. Cho, R. E. Blankenship, and G. R. Fleming, Nature **434**, 625 (2005).

[59] D. Zigmantas, E. L. Read, T. Mančal, T. Brixner, A. T. Gardiner, R. J. Cogdell, and G. R. Fleming, Proc. Natl. Acad. Sci. (USA) **103**, 12672 (2006).

[60] V. I. Novoderezhkin, A. Marin, and R. van Grondelle, Phys. Chem. Chem. Phys. **13**, 17093 (2011).

[61] G. S. Schlau-Cohen, T. R. Calhoun, N. S. Ginsberg, M. Ballottari, R. Bassi, and G. R. Fleming, Proc. Natl. Acad. Sci. (USA) **107**, 13276 (2010).

[62] M. T. Zanni, N. H. Ge, Y. S. Kim, and R. M. Hochstrasser, Proc. Natl. Acad. Sci. (USA) **98**, 11265 (2001).

[63] G. S. Schlau-Cohen, A. Ishizaki, T. R. Calhoun, N. S. Ginsberg, M. Ballottari, R. Bassi, and G. R. Fleming, Nat. Chem. **4**, 389 (2012).

[64] Z. Liu, and W. Chang, in *Biophysical Techniques in Photosynthesis II*, Eds. T.J. Aartsma and J. Matysik, Springer, pp. 77-96 (2008).

[65] J. S. Frähmcke, and P. J. Walla, Chem. Phys. Lett. **430**, 397 (2006).

[66] C. Meier, and D. J. Tannor, J. Chem. Phys. **111**, 3365 (1999).

[67] U. Kleinekathöfer, J. Chem. Phys. **121**, 2505 (2004).

[68] M. B. Oviedo, and C. G. Sánchez, J. Phys. Chem. A **115**, 12280 (2011).

[69] V. I. Prokhorenko, *European Photochemistry Association Newletter*, issue June 2012, page 21.

[70] A. V. Pisliakov, T. Mančal, and G. R. Fleming, J. Chem. Phys. **124**, 234505 (2006).

[71] Y. Umena, K. Kawakami, J. R. Shen, and N. Kamiya, Nature **473**, 55 (2011).

[72] W. R. Newell, H. van Amerongen, R. van Grondelle, J. W. Aalberts, A. F. Drake, P. Udvarhelyi, and J. Barber, FEBS Lett. **228**, 162 (1988).

[73] S. L. Hammes, L. Mazzola, S. G. Boxer, D. F. Gaul, and C. C. Schenck, Proc. Natl. Acad. Sci. (USA) **87**, 5682, (1990).

[74] V. I. Prokhorenko, and A. R. Holzwarth, J. Phys. Chem. B **104**, 11563 (2000).

[75] A. R. Holzwarth, M. G. Müller, M. Reus, M. Nowaczyk, J. Sander, and M. Rögner, Proc. Natl. Acad. Sci. (USA) **103**, 6895 (2006).

[76] E. Romero, I. H. M. van Stokkum, V. I. Novoderezhkin, J. P. Dekker, and R. van Grondelle, Biochem. **49**, 4300 (2010).

[77] J. A. Myers, K. L. M. lewis, F. D. Fuller, P. F. Tekavec, C. F. Yocum, and J. P. Ogilvie, J. Phys. Chem. Lett. **1**, 2774 (2010).

[78] V. I. Novoderezhkin, E. G. Andrizhiyevskaya, J. P. Dekker, and R. van Grondelle, Biophys. J. **89**, 1464 (2005).

[79] V. I. Novoderezhkin, J. P. Dekker, and R. van Grondelle, Biophys. J. **93**, 1293 (2007).

[80] G. Raszewski, B. A. Diner, E. Schlodder, and T. Renger, Biophys. J. **95**, 105 (2008).

[81] V. I. Novoderezhkin, E. Romero, J. P. Dekker, and R. van Grondelle, Chem. Phys. Chem. **12**, 681 (2011).

[82] A. Gelzinis, L. Valkunas, F. D. Fuller, J. P. Ogilvie, S. Mukamel, and D. Abramavicius, New J. Phys. **15**, 075013 (2013).

[83] S. Caffarri, R. Kouřil, S. Kereïche, E. J. Boekema, and R. Croce, EMOB J. **28**, 3052 (2009).

[84] S. Caffarri, R. Croce, L. Cattivelli, and R. Bassi, Biochem. **43**, 9467 (2004).

[85] H. -G. Duan, A. L. Stevens, P. Nalbach, M. Thorwart, V. I. Prokhorenko, and R. J. D. Miller, J. Phys. Chem. B **119**, 12017 (2015).

[86] A. G. Dijkstra, C. Wang, J. S. Cao, and G. R. Fleming, J. Phys. Chem. Lett. **6**, 627 (2015).

[87] M. F. Gelin, D. Egorova, and W. Domcke, J. Chem. Phys. **123**, 164112 (2005).

[88] A. W. Chin, J. Prior, R. Rosenbach, F. Caycedo-Soler, S. F. Huelga, and M. B. Plenio, Nat. Phys. **9**, 113 (2013).

[89] H. -G. Duan, P. Nalbach, V. I. Prokhorenko, S. Mukamel, and M. Thorwart, New J. Phys. **17**, 072002 (2015).

[90] F. D. Fuller, J. Pan, A. Gelzinis, V. Butkus, S. S. Senlik, D. E. Wilcox, C. F. Yocum, L. Valkunas, D. Abramavicius, and J. P. Ogilvie, Nat. Chem. **6**, 706 (2014).

[91] E. Romero, R. Augulis, V. I. Novoderezhkin, M. Ferretti, J. Thieme, D. Zigmantas, and R. van Grondelle, Nat. Phys. **10**, 676 (2014).

[92] B. W. Matthews, R. E. Fenna, M. C. Bolognesi, M. E. Schmid, and J. M. Olson, J. Mol. Biol. **131**, 259 (1979).

[93] D. E. Tronrud, M. F. Schmid, and B. W. Matthews, J. Mol. Biol. **188**, 443 (1986).

[94] Y. F. Li, W. Zhou, R. E. Blankenship, and J. P. Allen, J. Mol. Biol. **271**, 456 (1997).

[95] A. Camara-Artigas, R. E. Blankenship, and J. P. Allen, J. Mol. Biol. **75**, 49 (2002).

[96] J. M. Olson, Photosynth. Res. **80**, 181 (2004).

[97] J. Wen, H. Zhang, M. L. Gross, and R. E. Blankenship, Proc. Natl. Acad. Sci. (USA) **106**, 6134 (2008).

[98] S. Savikhin, D. R. Buck, and W. S. Struve, Chem. Phys. **223**, 303 (1997).

[99] G. S. Engel, T. R. Calhoun, E. L. Read, T. -K. Ahn, T. Mančal, Y. -C. Cheng, R. E. Blankenship, and G. R. Fleming, Nature **446**, 782 (2007).

[100] G. Panitchayangkoon, D. Hayes, K. A. Fransted, J. R. Caram, E. Harel, J. Wen, R. E. Blankenship, and G. S. Engel, Proc. Natl. Acad. Sci. (USA) **107**, 12766 (2010).

[101] E. Collini, C. Y. Wong, K. E. Wilk, P. M. G. Curmi, P. Brumer, and G. D. Scholes, Nature **463**, 644 (2010).

[102] P. Ball, Nature **474**, 272 (2011).

[103] N. Lambert, Y. -N. Chen, Y. -C. Cheng, C. -M. Li, G. -Y. Chen, and F. Nori, Nat. Phys. **9**, 10 (2013).

[104] S. F. Huelga, and M. B. Plenio, Contemporary Physics **54**, 181 (2013).

[105] M. Mohseni, Y. Omar, G. S. Engel, and M. Plenio, *Quantum Effects in Biology*, (Cambridge University Press, Cambridge, MA).

[106] D. Abbott, P. Davies, and A. Pati, *Quantum Aspects of life*, (World Scientific, Singapore).

[107] A. Olaya-Castro, A. Nazir, and G. R. Fleming, Philos. T. Roy. Soc. A **370**, 3613 (2012).

[108] E. Thyrhaug, K. Žídek, J. Dostál, D. Bína, and D. Zigmantas, J. Phys. Chem. Lett. **7**, 1653 (2016).

[109] A. Ishizaki, and G. R. Fleming, Proc. Natl. Acad. Sci. (USA) **106**, 17255 (2009).

[110] M. B. Plenio, J. Almeida, and S. F. Huelga, J. Chem. Phys. **139**, 235102 (2013).

[111] L. -P. Chen, R. Zheng, Y. -Y. Jing, and Q. Shi, J. Chem. Phys. **134**, 194508 (2011).

[112] P. Nalbach, D. Braun, and M. Thorwart, Phys. Rev. E **84**, 041926 (2011).

[113] N. Christensson, H. F. Kauffmann, T. Pullerits, and T. Mančal, J. Phys. Chem. B **116**, 7449 (2012).

[114] V. Tiwari, W. K. Peters, and D. M. Jonas, Proc. Natl. Acad. Sci. (USA) **110**, 1203 (2013).

[115] C. Olbrich, T. L. C. Jansen, J. Liebers, M. Aghtar, J. Strümpfer, K. Schulten, J. Knoester, and U. Kleinekathöfer, J. Phys. Chem. B **115**, 8609 (2011).

[116] M. S. am Busch, F. Müh, M. E. Madjet, and T. Renger, J. Phys. Chem. Lett. **2**, 93 (2011).

[117] A. N. Melkozernov, J. M. Olson, Y. Li, J. P. Allen and R. E. Blankenship, Photosyn. Res. **56**, 315 (1998).

[118] V. Butkus, D. Zigmantas, L. Valkunas, and D. Abramavicius, Chem. Phys. Lett. **545**, 40 (2012).

[119] P. Hamm, and M. Zanni, *Concepts and Methods of 2D Infrared Spectroscopy*; Cambridge University Press: New York, 2011.

[120] K. Lazonder, M. S. Pshenichnikov, and D. A. Wiersma, Ultrafast Phenomena XV, **88**, 356-358 (2007).

[121] C. A. Mujica-Martinez, P. Nalbach, and M. Thorwart, Phys. Rev. E **88**, 062719 (2013).

[122] F. Müh, M. E. Madjet, J. Adolphs, A. Abdurahman, B. Rabenstein, H. Ishikita, E. Knapp, and T. Renger, Proc. Natl. Acad. Sci. (USA) **104**, 16862 (2007).

[123] A. K. Chibisov, G. V. Zakharova, H. Görner, Y. A. Sogulyaev, I. L. Mushkalo, and A. I. Tolmachev, J. Phys. Chem. **99**, 886 (1995).

[124] C. Houssier, and K. Sauer, J. Am. Chem. Soc. **92**, 779 (1970).

[125] V. M. Agranovich, and M. D. Galanin, *In Electronic Excitation Energy Transfer in Condensed Matter*, chapter 4. Edited by V. M. Agranovich, and M. D. Galanin (North-Holland, Amsterdam, 1962), p. 81-170.

[126] B. J. Berne, and G. D. Harp, Adv. Chem. Phys. v. XVII, 63 (1970).

[127] S. Mukamel, Annu. Rev. Phys. Chem. **51**, 691 (2000).

[128] M. Cho, *Two-Dimensional Optical Spectroscopy* (CRC Press, Boca Raton, 2009).

[129] A. Halpin, P. J. M. Johnson, R. Tempelaar, R. S. Murphy, J. Knoester, T. L. C. Jansen, and R. J. D. Miller, Nat. Chem. **6**, 196 (2014).

[130] A. Halpin, P. J. M. Johnson, R. S. Murphy, V. I. Prokhorenko, and R. J. D. Miller, Proc. of Ultrafast Phenomena XVIII, in Eur. Phys. J. **41**, 05032 (2013).

[131] F. Minlota, V. I. Prokhorenko, T. Mančal, H. von Berlepsch, O. Bixner, H. F. Kauffmann and J. Hauer, J. Phys. Chem. A **117**, 6007 (2013).

[132] S. Westenhoff, D. Paleček, P. Edlund, P. Smith, and D. Zigmantas, J. Am. Chem. Soc. **134**, 16484 (2012).

[133] A. F. Fidler, V. P. Singh, P. D. Long, P. D. Dahlberg, and G. S. Engel, J. Phys. Chem. Lett. **4**, 1404 (2013).

[134] J. Dostál, T. Mančal, R. Augulis, F. Vácha, J. Pšenčík, and D. Zigmantas, J. Am. Chem. Soc. **134**, 11611 (2012).

[135] K. E. Dorfman, D. V. Voronine, S. Mukamel, and M. O. Scully, Proc. Natl. Acad. Sci. (USA) **110**, 2746 (2013).

[136] P. Nalbach, and M. Thorwart, Proc. Natl. Acad. Sci. (USA) **110**, 2693 (2013).

[137] M. Womick, and A. M. Moran, J. Phys. Chem. B **113**, 15747 (2009).

[138] M. Womick, and A. M. Moran, J. Phys. Chem. B **115**, 1347 (2011).

[139] G. Ritschel, J. Roden, W. T. Strunz, and A. Eisfeld, New J. Phys. **13**, 113034 (2011).

[140] A. Kolli, E. J. O'Reily, G. D. Scholes, and A. Olaya-Castro, J. Chem. Phys. **137**, 174109 (2012).

[141] P. Nalbach, and M. Thorwart, J. Phys. B **45**, 154009 (2012).

[142] G. H. Richards, K. E. Wilk, P. M. G. Curmi, H. M. Quiney, and J. A. Davis, J. Phys. Chem. Lett. **3**, 272 (2012).

[143] C. Kreisbeck, and T. Kramer, J. Phys. Chem. Lett. **3**, 2828 (2012).

[144] E. J. O'Reilly, and A. Olaya-Castro, Nat. Comm. **5**, 3012 (2014).

[145] P. Nalbach, C. A. Mujica-Martinez, and M. Thorwart, Phys. Rev. E **91**, 022706 (2015).

[146] V. May, and O. Kühn, *Charge and Energy Transfer Dynamics in Molecular Systems*, 3rd ed. (Wiley-VCH, Weinheim 2011).

[147] M. Rätsep, Z. L. Cai, J. R. Reimers, and A. Freiberg, J. Chem. Phys. **134**, 024506 (2011).

[148] M. Aghtar, J. Strümpfer, C. Olbrich, K. Schulten, U. Kleinekathöfer, J. Phys. Chem. B **117**, 7157 (2012).

[149] C. P. van der Vegte, J. D. Prajapati, U. Kleinekathöfer, J. Knoester, and T. L. C. Jansen, J. Phys. Chem. B **119**, 1302 (2015).

[150] M. Thorwart, J. Eckel, J. H. Rina, P. Nalbach, and S. Weiss, Chem. Phys. Lett. **478**, 234 (2009).

[151] A. G. Redfield, Adv. Magn. Reson. **1**, 1 (1965).

[152] A. Ishizaki, and G. R. Fleming, J. Chem. Phys. **130**, 234110 (2009).

[153] P. Nalbach, and M. Thorwart, J. Chem. Phys. **132**, 194111 (2010).

[154] W. M. Zhang, T. Meier, V. Chernyak, and S. Mukamel, J. Chem. Phys. **108**, 7763 (1998).

[155] M. Yang, and G. R. Fleming, Chem. Phys. **275**, 355 (2002).

[156] V. I. Novoderezhkin, A. G. Yakovlev, R. van Grondelle, and V. A. Shuvalov, J. Phys. Chem. B **108**, 7445 (2004).

[157] Q. Ai, T. -C. Yen, B. -Y. Jin. and Y. -C. Cheng, J. Phys. Chem. Lett. **4**, 2577 (2013).

[158] M. Cho, H. M. Vaswani, T. Brixner, J. Stenger, and G. R. Fleming, J. Phys. Chem. B **109**, 10542 (2005).

[159] K. L. M. Lewis, F. D. Fuller, J. A. Myers, C. F. Yocum, S. Mukamel, D. Abramavicius, and J. P. Ogilvie, J. Phys. Chem. A **117**, 34 (2013).

[160] Y. Chang, and Y. -C. Cheng, J. Chem. Phys. **142**, 034109 (2015).

[161] M. Schröder, U. Kleinekathöfer and M. Schreiber, J. Chem. Phys. **124**, 084903 (2006).

[162] Y. -H. Hwang-Fu, W. Chen, and Y.-C. Cheng, Chem. Phys. **447**, 46 (2015).

[163] O. Rancova, and D. Abramavicius, J. Phys. Chem. B **118**, 7533 (2014).

[164] L. Z. Sharp, D. Egorova, and W. Domcke, J. Chem. Phys. **132**, 014501 (2010).

[165] M. Schröder, M. Schreiber, and U. Kleinekathöfer, J. Luminescence, **125**, 126 (2007).

[166] We compare the absorption lineshape calculated by MRT and QUAPI. They are shown exactly same result.

[167] A. Ishizaki, and G. R. Fleming, J. Chem. Phys. **130**, 234111 (2009).

[168] W. Domcke, D. R. Yarkony, and H. Köppel, *Conical Intersection: Electronic Structure, Dynamics and Spectroscopy* (World Scientific: Singapore, 2004).

[169] W. Domcke, D. R. Yarkony, and H. Köppel, *Conical Intersection: Theory, Computation and Experiment* (World Scientific: Singapore, 2011).

[170] W. Domcke, and D. R. Yarkony, Annu. Rev. Phys. Chem. **63**, 325 (2012).

[171] P. Hamm, and G. Stock, Phys. Rev. Lett. **109**, 173201 (2012).

[172] D. P. Hoffman, and R. A. Mathies, Acc. Chem. Res. **49**, 616 (2016).

[173] P. Kukura, D. W. McCamant, S. Yoon, D. B. Wandschnedier, and R. A. Mathies, Science **310**, 1006 (2005).

[174] S. Takeuchi, S. Ruhman, T. Tsuneda, M. Chiba, T. Taketsugu, and T. Tahara, Science **322**, 1073 (2008).

[175] C. Fang, R. R. Frontiera, R. Tran and R. A. Mathies, Nature **462**, 200 (2009).

[176] D. P. Hoffman, S. R. Ellis, and R. A. Mathies, J. Phys. Chem. A **118**, 4955 (2014).

[177] D. Polli, P. Altoé, O. Weingart, K. M. Spillane, C. Manzoni, D. Brida, G. Tomasello, G. Orlandi, P. Kukura, R. A. Mathies, M. Garavelli, and G. Cerullo, Nature **467**, 440 (2010).

[178] C. Schnedermann, M. Liebel, and P. Kukura, J. Am. Chem. Soc. **137**, 2886 (2015).

[179] M. Liebel, C. Schnedermann, G. Bassolino, G. Taylor, A. Watts, and P. Kukura, Phys. Rev. Lett. **112**, 238301 (2014).

[180] P. J. M. Johnson, A. Halpin, T. Morizumi, V. I. Prokhorenko, O. P. Ernst, and R. J. D. Miller, Nat. Chem. **7**, 980 (2015).

[181] P. J. M. Johnson, M. H. Farag, A. Halpin, T. Morizumi, V. I. Prokhorenko, J. Knoester, T. L. C. Jansen, O. P. Ernst, and R. J. D. Miller, J. Phys. Chem. B **121**, 4040 (2017).

[182] V. I. Prokhorenko, A. M. Nagy, S. A. Waschuk, L. S. Brown, R. R. Birge, and R. J. D. Miller, Science **313**, 1257 (2006).

[183] M. Liebel, and P. Kukura, Nat. Chem. **9**, 45 (2017).

[184] W. Domcke, and G. Stock, Adv. Chem. Phys. **100**, 1 (1997).

[185] S. Hahn, and G. Stock, J. Phys. Chem. B **104**, 1146 (2000).

[186] A. Kühl, and W. Domcke, J. Chem. Phys. **116**, 263 (2002).

[187] L. Chen, M. F. Gelin, V. Y. Chernyak, W. Domcke, and Y. Zhao, Fara. Dis. **194**, 61 (2016).

[188] H. -G. Duan, and M. Thorwart, J. Phys. Chem. Lett. **7**, 382 (2016).

[189] J. Krčmář, M. F. Gelin, D. Egorova, and W. Domcke, J. Phys. B **47**, 124019 (2014).

[190] J. Krčmář, M. F. Gelin, and W. Domcke, J. Chem. Phys. **143**, 074308 (2015).

[191] M. Sala, and D. Egorova, Chem. Phys. **481**, 206 (2016).

[192] M. H. Farag, T. C. Jansen, and J. Knoester, J. Phys. Chem. Lett. **7**, 3328 (2016).

[193] D. Keefer, S. Thallmair, S. Matsika, and R. de Vivie-Riedle, J. Am. Chem. Soc. **139**, 5061 (2017).

[194] C. Liekhus-Schmaltz, G. A. McCracken, A. Kaldun, J. P. Cryan, and P. H. Bucksbaum, J. Chem. Phys. **145**, 144304 (2016).

[195] M. Richter, F. Bouakline, J. Gonzălez-Vázquez, L. Martínez-Fernández, I. Corral, S. Patchkovskii, F. Morales, M. Ivanov, F. Martín, and O. Smirnova, New J. Phys. **17**, 113023 (2015).

[196] H. -G. Duan, R. J. D. Miller, and M. Thorwart, J. Phys. Chem. Lett. **7**, 3491 (2016).

[197] N. Makri, J. Math. Phys. **36**, 2430 (1995).

[198] M. Thorwart, E. Paladino, and M. Grifoni, Chem. Phys. **296**, 333 (2004).

[199] A. Ishizaki, and Y. Tanimura, J. Phys. Soc. Jpn. **74**, 3131 (2005).

[200] Y. Tanimura, J. Phys. Soc. Jpn. **75**, 082001 (2006).

[201] A. Garg, J. N. Onuchic, and V. Ambegaokar, J. Chem. Phys. **83**, 4491 (1985).

[202] Y. Tanimura, J. Chem. Phys. **137**, 22A550 (2012).

[203] A. Ishizaki, and Y. Tanimura, Chem. Phys. **347**, 185 (2008).

[204] M. F. Gelin, D. Egorova, and W. Domcke, Acc. Chem. Res. **42**, 1290 (2009).

[205] R. González-Luque, M. Garavelli, F. Bernardi, M. Merchán, M. A. Robb, and M. Olivucci, Proc. Natl. Acad. Sci. (USA) **97**, 9379 (2000).

[206] U. Manthe, and H. Köppel, J. Chem. Phys. **93**, 1658 (1990).

[207] M. V. Berry, Proc. Roy. Soc. A **392**, 45 (1984).

[208] I. G. Ryabinkin, and A. F. Izmaylov, Phys. Rev. Lett. **111**, 220406 (2013).

[209] J. Burschka, N. Pellet, S. Moon, R. Humphry-Baker, P. Gao, M. K. Nazeeruddin, and M. Grätzel, Nature **499**, 316 (2013).

[210] S. D. Stranks, G. E. Eperon, G. Grancini, C. Menelaou, M. J. P. Alcocer, T. Leijtens, L. M. Herz, A. Petrozza, and H. J. Snaith, Science **342**, 341 (2013).

[211] G. Xing, N. Mathews, S. Sun, S. S. Lim, Y. M. Lam, M. Grätzel, Subodh Mhaisalkar, and T. C. Sum, Science **342**, 344 (2013).

[212] M. M. Lee, J. Teuscher, T. Miyasaka, T. N. Murakami, and H. J. Snaith, Science **338**, 643 (2012).

[213] H. -S. Kim, C. Lee, J. -H. Im, K. -B. Lee, T. Moehl, A. Marchioro, S. -J. Moon, R. Humphry-Baker, J. Yum, J. E. Moser, M. Grätzel and N. Park, Sci. Rep. **2**, 591 (2012).

[214] L. Etgar, P. Gao, Z. Xue, Q. Peng, A. K. Chandiran, B. Liu, M. K. Nazeeruddin, and M. Grätzel, J. Am. Chem. Soc. **134**, 17396 (2012).

[215] W. S. Yang, J. H. Noh, N. J. Jeon, Y. C. Kim, S. Ryu, J. Seo, S. I. Seok, Science **348**, 1234 (2015).

[216] H. Zhu, Y. Fu, F. Meng, X. Wu, Z. Gong, Q. Ding, M. V. Gustafsson, M. T. Trinh, S. Ji, and X. -Y. Zhu, Nat. Mater. **14**, 636 (2015).

[217] Q. Lin, A. Armin, P. L. Burn and P. Meredith, Nat. Photon. **9**, 687 (2015).

[218] A. Kojima, K. Teshima, Y. Shirai, and T. Miyasaka, J. Am. Chem. Soc. **131**, 6050 (2009).

[219] N. J. Jeon, J. H. Noh, W. S. Yang, Y. C. Kim, S. Ryu, J. Seo and S. I. Seok, Nature **517**, 476 (2015).

[220] for record cell efficiencies, see: Best Research-Cell Efficiencies. http://www.nrel.gov/ncpv/images/efficiency-chart.jpg (2016).

[221] J. M. Ball, M. M. Lee, A. Heya, and H. J. Snaith, Ener. Envir. Sci. **6**, 1739 (2013).

[222] K. G. Stamplecoskie, J. S. Manser, and P. V. Kamat, Ener. Environ. Sci. **8**, 208 (2014).

[223] C. S. Ponseca Jr, and V. Sundströma, Nanoscale, **8**, 6249 (2016).

[224] M. Saba, F. Quochi, A. Mura, and G. Bongiovanni, Acc. Chem. Res. **49**, 166 (2016).

[225] X. Wu, M. T. Trinh, D. Niesner, H. Zhu, Z. Norman, J. S. Owen, O. Yaffe, B. J. Kudisch, and X.-Y. Zhu, J. Am. Chem. Soc. **137**, 2089 (2015).

[226] J. S. Manser, and P. V. Kamat, Nat. Photon. **8**, 737 (2014).

[227] L. Q. Phuong, Y. Nakaike, A. Wakamiya, and Y. Kanemitsu, J. Phys. Chem. Lett. **7**, 2316 (2016).

[228] V. D'Innocenzo, G. Grancini, M. J. P. Alcocer, A. R. S. Kandada, S. D. Stranks, M. M. Lee, G. Lanzani, H. J. Snaith, and A. Petrozza, Nat. Comm. **5**, 3586 (2014).

[229] N. Sestu, M. Cadelano, V. Sarritzu, F. Chen, D. Marongiu, R. Piras, M. Mainas, F. Quochi, M. Saba, A. Mura, and G. Bongiovanni, J. Phys. Chem. Lett. **6**, 45566 (2015).

[230] A. Miyata, A. Mitioglu, P. Plochocka, O. Portugall, J. T. Wang, S. D. Stranks, H. J. Snaith, and R. J. Nicholas, Nat. Phys. **11**, 582 (2015).

[231] Y. Yang, D. P. Ostrowski, R. M. France, K. Zhu, J. van de Lagemaat, J. M. Luther, and M. C. Beard, Nat. Photon. **10**, 53 (2016).

[232] J. Even, L. Pedesseau, and C. Katan, J. Phys. Chem. C **118**, 11566 (2014).

[233] H. Zhu, K. Miyata, Y. Fu, J. Wang, P. P. Joshi, D. Niesner, K. W. Williams, Song Jin, and X. -Y. Zhu, Science **353**, 1409 (2016).

[234] A. A. Bakulin, O. Selig, H. J. Bakker, Y. L. A. Rezus, C. Mller, T. Glaser, R. Lovrincic, Z. Sun, Z. Chen, A. Walsh, J. M. Frost, and T. L. C. Jansen, J. Phys. Chem. Lett. **6**, 3663 (2015).

[235] X. -Y. Zhu, and V. Podzorov, J. Phys. Chem. Lett. **6**, 4758 (2015).

[236] S. A. March, C. Clegg, D. B. Riley, D. Webber, I. G. Hill, and K. C. Hall, Sci. Rep. **6**, 39139 (2016).

[237] H. Diab, G. Trippé-Allard, F. Lédée, K. Jemli, C. Vilar, G. Bouchez, V. L. R. Jacques, A. Tejeda, J. Even, J. Lauret, E. Deleporte, and D. Garrot, J. Phys. Chem. Lett. **7**, 5093 (2016).

[238] J. S. Manser, J. A. Christians, and P. V. Kamat, Chem. Rev. **116**, 12956 (2016).

[239] A. A. Bakulin, S. E. Morgan, T. B. Kehoe, M. W. B. Wilson, A. W. Chin, D. Zigmantas, D. Egorova, and A. Rao, Nat. Chem. **8**, 16 (2016).

[240] J. Lim, D. Paleček, F. Caycedo-Soler, C. N. Lincoln, J. Prior, H. von Berlepsch, S. F. Huelga, M. B. Plenio, D. Zigmantas, and J. Hauer, Nat. Comm. **6**, 7755 (2015).

[241] R. J. Elliott, Phys. Rev. **108**, 1384 (1957).

[242] Y. Yang, M. Yang, K. Zhu, J. C. Johnson, J. J. Berry, J. van de Lagemaat, and M. C. Beard, Nat. Comm. **7**, 12613 (2016).

[243] M. Saba, M. Cadelano, D. Marongiu, F. Chen, V. Sarritzu, N. Sestu, C. Figus, M. Aresti, R. Piras, A. G. Lehmann, C. Cannas, A. Musinu, F. Quochi, A. Mura, and G. Bongiovanni, Nat. Comm. **5**, 5049 (2014).

[244] W. -L. Chan, M. Ligges, and X. -Y. Zhu, Nat. Chem. **4**, 840 (2012).

[245] D. Egorova, J. Phys. Chem. A **118**, 10259 (2014).

[246] L. -Q. Xie, T. -Y. Zhang, L. Chen, N. Guo, Yu Wang, G. Liu, J, -R. Wang, J. Zhou, J. Yan, Y. Zhao, B. Mao, and Z. Tiana, Phys. Chem. Chem. Phys. **18**, 18112 (2016).

[247] F. Brivio, J. M. Frost, J. M. Skelton, A. J. Jackson, O. J. Weber, M. T. Weller, A. R. Goi, A. M. A. Leguy, P. R. F. Barnes, and A. Walsh, Phys. Rev. B **92**, 144308 (2015).

[248] B. Park, S. M. Jain, X. Zhang, A. Hagfeldt, G. Boschloo, and T. Edvinsson, ACS Nano **9**, 2088 (2015).

[249] T. Glaser, C. Müller, M. Sendner, C. Krekeler, O. E. Semonin, T. D. Hull, O. Yaffe, J. S. Owen, W. Kowalsky, A. Pucci, and R. Lovrinčić, J. Phys. Chem. Lett. **6**, 2913 (2015).

[250] C. Schnedermann, J. M. Lim, T. Wende, A. S. Duarte, L. Ni, Q. Gu, A. Sadhanala, A. Rao, and P. Kukura, J. Phys. Chem. Lett. **7**, 4854 (2016).

[251] S. Nah, B. Spokoyny, C. Stoumpos, C. M. M. Soe, M. Kanatzidis, and E. Harel, Nat. Photon. **11**, 285 (2017).

[252] Z. Zhang, K. L. Wells, E. W. J. Hyland, H. -S. Tan, Chem. Phys. Lett. **550**, 156 (2012).

[253] R. D. Mehlenbacher, T. J. McDonough, M. Grechko, M. -Y. Wu, M. S. Arnold, and M. T. Zanni, Nature Comm. **6**, 6732 (2015).

[254] Y. Shibata, S. Nishi, K. Kawakami, J. -R. Shen, and T. Renger, J. Am. Chem. Soc. **135**, 6903 (2013).

[255] J. Gao, W. Shi, J. Ye, X. Wang, H. Hirao, and Y. Zhao, J. Phys. Chem. B **117**, 3488 (2013).

[256] X. Wang, G. Ritschel, S. Wüster, and A. Eisfeld, Phys. Chem. Chem. Phys. **17**, 25629 (2015).

[257] M. J. Frisch, G. W. Trucks, H. B. Schlegel, G. E. Scuseria, M. A. Robb, J. R. Cheeseman, G. Scalmani, V. Barone, B. Mennucci, G. A. Petersson, H. Nakatsuji, M. Caricato, X. Li, H. P. Hratchian, A. F. Izmaylov, J. Bloino, G. Zheng, J. L. Sonnenberg, M. Hada, M. Ehara, K. Toyota, R. Fukuda, J. Hasegawa, M. Ishida, T. Nakajima, Y. Honda, O. Kitao, H. Nakai, T. Vreven, J. A. Montgomery, Jr., J. E. Peralta, F. Ogliaro, M. Bearpark, J. J. Heyd, E. Brothers, K. N. Kudin, V. N. Staroverov, R. Kobayashi, J. Normand, K. Raghavachari, A. Rendell, J. C. Burant, S. S. Iyengar, J. Tomasi, M. Cossi, N. Rega, J. M. Millam, M. Klene, J. E. Knox, J. B. Cross, V. Bakken, C. Adamo, J. Jaramillo, R. Gomperts, R. E. Stratmann, O. Yazyev, A. J. Austin, R. Cammi, C. Pomelli, J. W. Ochterski, R. L. Martin, K. Morokuma, V. G. Zakrzewski, G. A. Voth, P. Salvador, J. J.

Dannenberg, S. Dapprich, A. D. Daniels, . Farkas, J. B. Foresman, J. V. Ortiz, J. Cioslowski, and D. J. Fox, Gaussian, Inc., Wallingford CT, 2009.

[258] N. Makri, and D. E. Makarov, J. Chem. Phys. **102**, 4600 (1995).

[259] N. Makri, and D. E. Makarov, J. Chem. Phys. **102**, 4611 (1995).

Publication List

- H. -G. Duan, A. G. Dijkstra, P. Nalbach, and Michael Thorwart, Efficient Tool to Calcualte Two-dimensional optical spectra for photoactive molecular complexes. Phys. Rev. E **92**, 042708 (2015).

- H. -G. Duan, P. Nalbach, V. I. Prokhorenko, S. Mukamel, and Michael Thorwart. On the origin of oscillation in two-dimensional spectra of excitonically-coupled molecular systems. New J. Phys. **17**, 072002 (2015).

- H. -G. Duan, A. L. Stevens, P. Nalbach, M. Thorwart, V. I. Prokhorenko, and R. J. D. Miller, Two-dimensional Electronic Spectroscopy of Light-Harvesting Complex II at Ambient Temperature: A Joint Experimental and Theoretical Study. J. Phys. Chem. B **119**, 12017 (2015).

- H. -G. Duan, and M. Thorwart, Quantum Mechanical Wave Packet Dynamics at a Conical Intersection with Strong Vibrational Dissipation. J. Phys. Chem. Lett. **7**, 382 (2016).

- A. G. Dijkstra, H. -G. Duan, J. Knoester, K. A. Nelson, and J. -S. Cao, How two-dimensional brick layer J-aggregates Differ from Linear ones: Excitonic Properties and Line Broadening Mechanisms. J. Chem. Phys. **144**, 134310 (2016).
- H. -G. Duan, R. J. D. Miller, and M. Thorwart, Impact of Vibrational Coherence on the Quantum Yield at a Conical Intersection. J. Chem. Phys. Lett. **7**, 3491 (2016).
- H. -G. Duan, M. Frey, M. Thorwart, and P. Nalbach, Two-dimensional Photon Echoes Reveal Non-Markovian Energy Transfer in an Excitonic Dimer. Phys. Rev. E **94**, 052146 (2016).
- H. -G. Duan, V. I. Prokhorenko, R. J. Cogdell, K. Ashraf, A. L. Stevens, M. Thorwart, and R. J. D. Miller, Nature does not Rely on Long-lived Electronic Quantum Coherence for Photosynthetic Energy Transfer. Proc. Natl. Am. Soc. (USA) **114**, 8493 (2017).
- D. -L. Qi, H. -G. Duan, Z. -R. Sun, R. J. D. Miller, and M. Thorwart, Tracking an Electronic Wave Packet in the Vicinity of a Conical Intersection. J. Chem. Phys. **147**, 074101 (2017).
- H. -G. Duan, V. I. Prokhorenko, E. Wientjes, R. Croce, M. Thorwart, and R. J. D. Miller, Primary charge separation in the reaction center revealed by

two-dimensional electronic spectroscopy. Sci. Rep. **7**, 12347 (2017).

- A. Jha, H. -G. Duan, V. Tiwari, P. Nayak, H. J. Snaith, M. Thorwart, and R. J. D. Miller, Direct Observation of the Coherent Exciton Dissociation in Lead-iodide Perovskite by 2D Electronic Spectroscopy. ACS Photonics **5**, 852 (2017).

- A. Jha, Hong-Guang Duan, Vandana Tiwari, Michael Thorwart, and R. J. Dwayne Miller, Origin of poor doping efficiency in solution processed organic semiconductors. Chem. Sci. **9**, 4468 (2018).

- Hong-Guang Duan, Peter Nalbach, R. J. Dwayne Miller, and Michael Thorwart, Ultrafast Energy Transfer in Excitonically Coupled Molecules Induced by a Nonlocal Peierls Phonon. submitted.

- Hong-Guang Duan, Michael Thorwart, R. J. Dwayne Miller, Do Anticorrelated Pigment Vibrations Enhance Electronic Quantum Coherence? submitted.

- Hong-Guang Duan, Da-Long Qi, Zhen-Rong Sun, R. J. Dwayne Miller, and Michael Thorwart, Signature of the geometric phase in the wave packet dynamics on hypersurfaces. submitted.

Conference

- ‘Hands-On’ Workshop on Computational Biophysics at Bremen, June, 2014, Bremen, Germany.

- 7th CMDS conference, poster: On the nature of short-lived and long-lasting oscillations in 2D spectra of excitonic systems. June, 2014, Oregon, United States.

- 12th Femto conference, July, 2015, Hamburg, Germany.

- 8th CMDS conference, poster 1: Two-dimensional Electronic Spectroscopy of Fenna-Matthews- Olson Complex at Ambient Temperature. poster 2: Charge separation signature in reaction center revealed by 2D electronic spectroscopy. June, 2016, Groningen, Netherlands.

- Workshop of Quantum Dynamics: From Algorithms to Applications, oral presentation: Signature of charge transfer in the PSII reaction center. September 2016, Greifswald, Germany.

- DPG meeting, Oral presentation: Effective Treatment of Quantum Dissipation at a Conical Intersection. March 2017, Dresden, Germany.
- Workshop in Munich, poster: vibrationally modulated quantum yield in the vicinity of conical intersection. Oct 2017, Munich, Germany.
- CFEL Symposium 2017, Oral presentation: Nature does not rely on long-lived quantum coherence for photosynthetic energy transfer. Oct 2017, Timmendorf, Germany.
- Invited talk, oral presenatation: Exciton dissociation in Perovskites. Nov 2017, Ludwig-Maximilians Universität München, Germany.

Curriculum vitae

Name: Hong-Guang Duan

Date and place of birth:	06. November 1986, Hunan Provence, China
School education:	
1992-2005	Hong-Jiang, Hunan Provence, China
Study:	
Sep. 2005-Jun. 2009	Bachlor in Physics, Sichuan Normal University, Sichuan Provence, China
Sep. 2009-Jun. 2012	Master in Physics, Ningbo Unversity, Zhejiang Provence, China
Nov. 2012-now	PhD in Physics, I. Institute for Theoretical Physics, University Hamburg, Hamburg, Germany Max-Planck Institute for the Structure and Dynamics of Matter, Hamburg, Germany.

Erklärung

Die hier vorgelegte Dissertation habe ich eigenständig und ohne unerlaubte Hilfe angefertigt. Die Dissertation wurde in der vorgelegten oder in ähnlicher Form noch bei keiner anderen Institution eingereicht. Ich habe bisher keine erfolglosen Promotionversuche unternommen.

Hong-Guang Duan

Hamburg, den 26.09.2017